STAB

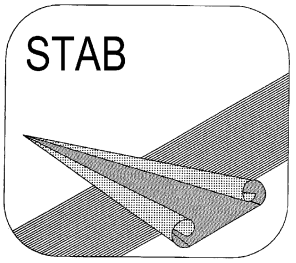

J A H R E S B E R I C H T

2023

zum

21. STAB-Workshop

7. - 8. November 2023

Göttingen

„Deutsche Strömungsmechanische Arbeitsgemeinschaft, STAB“

INHALT

Mitteilungen der Geschäftsstelle

Die STAB-Jahresberichte werden als Sammlung der Kurzfassungen der Vorträge an die Teilnehmer der abwechselnd stattfindenden Symposien und Workshops verteilt. So erscheint der vorliegende STAB-Jahresbericht 2023 anlässlich des 21. STAB-Workshops, der am 7. und 8. November 2023 in Göttingen stattfinden wird.

Der Bericht enthält 77 „Mitteilungen“ über Arbeiten aus den Fachgruppen, die auf dem Workshop vorgestellt werden. Den „Mitteilungen“ ist ein Inhaltsverzeichnis (Seite 14 bis Seite 19) vorangestellt, das nach Fachgruppen gegliedert ist. Innerhalb der Fachgruppen sind die Beiträge alphabetisch nach Autoren geordnet. Die Beiträge verteilen sich (bezogen auf die Erstautoren) zu 4 % auf die Industrie, zu 39 % auf Hochschulen und zu 57 % auf Forschungseinrichtungen (DLR, DNW, ISL). Die Autoren und Koautoren dieses Berichts sind auf den Seiten 174 und 175 aufgeführt.

Die Jahresberichte werden nur an den tatsächlich daran interessierten Personenkreis verteilt und können auch von der Webseite (siehe Link/Adresse unten) heruntergeladen werden. Alle Teilnehmer des diesjährigen STAB-Workshops erhalten ein Exemplar zur Veranstaltung. Darüber hinaus wird der Jahresbericht an die Mitglieder der STAB-Gremien und weitere Interessierte versandt.

Dieser Jahresbericht erscheint in einer Auflage von 140 Exemplaren. Erfahrungsgemäß sind einige Restexemplare bis zum Ende des jeweiligen Jahres verfügbar.

Aktualisierte Informationen über STAB finden Sie auch unter: www.dlr.de/agstab

Göttingen, im Oktober 2023

Zielsetzungen, chronologische Entwicklung und Organisation

Die Arbeitsgemeinschaft „Strömungen mit Ablösung“ (STAB) wurde 1979 auf Initiative der Deutschen Gesellschaft für Luft- und Raumfahrt (DGLR) - Lilienthal-Oberth, e.V. - von Strömungsforschern, Aerodynamikern und Luftfahrtingenieuren des DLR, der Hochschulen und der Industrie gegründet.

Sie entstand aus „dem gemeinschaftlichen Bestreben, die Strömungsforschung in Deutschland generell zu fördern und durch Konzentration auf ein wirtschaftlich und forschungspolitisch zukunftsträchtiges Teilgebiet zu vertiefen“ (Auszug aus der Präambel der Verfahrensordnung der STAB).

In Zeiten knapper werdender Budgets bei gleichzeitig massiv steigendem Wettbewerbsdruck sind diese Ansätze notwendiger denn je. Aber auch die öffentlichen Geldgeber setzen diese Kooperationsbereitschaft inzwischen voraus. Da dieser Leitgedanke von STAB inzwischen in anderer Weise verfolgt wird, konzentriert sich STAB verstärkt auf Fachveranstaltungen.

Die STAB ist der DGLR als ‚Kompetenznetzwerk’ angegliedert. Auf der Homepage der DGLR ist die STAB zu finden unter:
https://www.dglr.de/vernetzen/fachbereiche/kompetenznetzwerk-stab/

Die STAB vereint alle wichtigen Gebiete der Strömungsmechanik - insbesondere der Luft- und Raumfahrt - aus Grundlagenforschung, Großforschung und Industrie in Deutschland. Die Gründung basierte auf der Idee, Forschungsverbünde aus Industrie, Hochschulen und Großforschung zu einem hochaktuellen Fachthema zu organisieren, das damals als „Strömungen mit Ablösungen“ identifiziert wurde. In den Folgejahren wurden weitere strömungsmechanische Fragestellungen aufgegriffen, die STAB zu einem in der Fachwelt bekannten Namen werden ließen. Dabei werden nicht nur die klassischen Themen der Strömungsmechanik angesprochen, sondern auch Probleme aus dem Automobilbau, der Gebäudeaerodynamik, der Verfahrenstechnik, dem Motorenbau usw. diskutiert.

Die Programmleitung hat im November 2000 beschlossen, in Zukunft auf den Zusatz „AG“ im Namen zu verzichten.

Die für die Öffentlichkeit relevanten wissenschaftlichen Aktivitäten spiegeln sich in der folgenden chronologischen Entwicklung wider:

DGLR-Symposium „Forschung und Entwicklung auf dem Gebiet der Strömungsmechanik und Aerodynamik in der Bundesrepublik Deutschland“	Bonn, 29.11.-01.12.1978
„Gespräch über Strömungsforschung in Deutschland“	Ottobrunn, 30.01.1979
„Memorandum über zukünftige nationale Zusammenarbeit in der Strömungsforschung, insbesondere der Aerodynamik auf dem Gebiet der Strömungen mit Ablösung“	Oktober 1979
Programmpräsentation anlässlich der BDLI-Jahrestagung	Bonn, 01.07.1980

Programm der Arbeitsgemeinschaft „Strömungen mit Ablösung“	September 1980
Programmpräsentation im Bundesministerium für Forschung und Technologie	Bonn, 19.03.1981
Konstituierung des Kuratoriums und Neuorganisation der Arbeitsgemeinschaft „Strömungen mit Ablösung" (AG STAB)	Köln-Porz, 23.02.1982
Konstituierung von Programmleitung/Programmausschuss	Göttingen, 24.03.1982
Erfassung STAB-relevanter Aktivitäten in der Bundesrepublik Deutschland (Stand Mitte 1981)	April 1982
Fachtagung anlässlich der ILA '82 „Strömungen mit Ablösung“	Hannover, 19.05.1982
Neue Impulse für die Strömungsforschung- und Aerodynamik; Vortrag von H.-G. Knoche, DGLR-Jahrestagung	Hamburg, 01.-03.10.1984
DGLR Workshop „2D-Messtechnik“	Markdorf, 18.-19.10.1988

Symposium

1. DGLR-Fachsymposium	München, 19.-20.09.1979
2. DGLR- Fachsymposium	Bonn, 30.06.-01.07.1980
3. DGLR- Fachsymposium	Stuttgart, 23.-25.11.1981
4. DGLR- Fachsymposium	Göttingen, 10.-12.10.1983
5. DGLR- Fachsymposium	München, 09.-10.10.1986
6. DGLR-Fach-Symposium	Braunschweig,08.-10.11.1988
7. DGLR- Fachsymposium	Aachen, 07.-09.11.1990
8. DGLR- Fachsymposium	Köln-Porz, 10.-12.11.1992
9. DGLR- Fachsymposium	Erlangen, 04.-07.10.1994
10. DGLR- Fachsymposium	Braunschweig,11.-13.11.1996
11. DGLR- Fachsymposium	Berlin, 10.-12.11.1998
12. DGLR- Fachsymposium	Stuttgart, 15.-17.11.2000
13. DGLR- Fachsymposium	München, 13.-15.11.2002
14. DGLR- Fachsymposium	Bremen, 16.-18.11.2004
15. DGLR- Fachsymposium	Darmstadt, 29.11.-01.12.2006
16. DGLR- Fachsymposium	Aachen, 03.-04.11.2008
17. DGLR- Fachsymposium	Berlin, 09.-10.11.2010

18. DGLR- Fachsymposium	Stuttgart, 06.-07.11.2012
19. DGLR- Fachsymposium	München, 04.-05.11.2014
20. DGLR- Fachsymposium	Braunschweig,08.-09.11.2016
21. DGLR- Fachsymposium	Darmstadt, 06.-07.11.2018
22. DGLR- Fachsymposium	Präsenzveranstaltung aufgrund der Corona-Pandemie abgesagt
23. DGLR-Fachsymposium	Berlin, 09.-10.11.2022

Workshop

1. STAB-Workshop	Göttingen, 07.-08.03.1983
2. STAB-Workshop	Köln-Porz, 18.-20.09.1984
3. STAB-Workshop	Göttingen, 10.-11.11.1987
4. STAB-Workshop	Göttingen, 08.-10.11.1989
5. STAB-Workshop	Göttingen, 13.-15.11.1991
6. STAB-Workshop	Göttingen, 10.-12.11.1993
7. STAB-Workshop	Göttingen, 14.-16.11.1995
8. STAB-Workshop	Göttingen, 11.-13.11.1997
9. STAB-Workshop	Göttingen, 09.-11.11.1999
10. STAB-Workshop	Göttingen, 14.-16.11.2001
11. STAB-Workshop	Göttingen, 04.-06.11.2003
12. STAB-Workshop	Göttingen, 08.-09.11.2005
13. STAB-Workshop	Göttingen, 14.-15.11.2007
14. STAB-Workshop	Göttingen, 11.-12.11.2009
15. STAB-Workshop	Göttingen, 09.-10.11.2011
16. STAB-Workshop	Göttingen, 12.-13.11.2013
17. STAB-Workshop	Göttingen, 10.-11.11.2015
18. STAB-Workshop	Göttingen, 07.- 08.11.2017
19. STAB-Workshop	Göttingen, 05.-06.11.2019
20. STAB-Workshop	Göttingen, 16.-17.11.2021

Ein Kurs über „Application of Particle Image Velocimetry, PIV“
findet seit 1993 regelmäßig im DLR in Göttingen statt,
letztmalig am: 20.03. – 24.03.2023

Die Symposiums-Tagungsbände durchlaufen einen Begutachtungsprozess.
Die Bände der letzten Jahre finden Sie hier aufgelistet.

- Notes on Numerical Fluid Mechanics, Vol. 60; Eds.: H. Körner, R. Hilbig; Friedr. Vieweg & Sohn Verlagsgesellschaft mbH, Braunschweig/Wiesbaden, 1997
- Notes on Numerical Fluid Mechanics, Vol. 72; Eds.: W. Nitsche, H.-J. Heinemann, R. Hilbig; Springer-Verlag Berlin Heidelberg
- Notes on Numerical Fluid Mechanics, Vol. 77; Eds.: S. Wagner, U. Rist, H.-J. Heinemann, R. Hilbig; Springer-Verlag Berlin Heidelberg 2002
- Notes on Numerical Fluid Mechanics and Multidisciplinary Design, Vol. 87; Eds.: Chr. Breitsamter, B. Laschka, H.-J. Heinemann, R. Hilbig; Springer-Verlag Berlin Heidelberg 2004
- Notes on Numerical Fluid Mechanics and Multidisciplinary Design, Vol. 92; Eds.: H. J. Rath, C. Holze, H.-J. Heinemann, R. Henke, H. Hönlinger; Springer-Verlag, Berlin Heidelberg 2006
- Notes on Numerical Fluid Mechanics and Multidisciplinary Design, Vol. 96; Eds.: C. Tropea, S. Jakirlic, H.-J. Heinemann, R. Henke, H. Hönlinger; Springer-Verlag Berlin Heidelberg 2008
- Notes on Numerical Fluid Mechanics and Multidisciplinary Design, Vol. 112; Eds.: A. Dillmann, G. Heller, M. Klaas, H.-P. Kreplin, W. Nitsche, W. Schröder; Springer Berlin Heidelberg 2010
- Notes on Numerical Fluid Mechanics and Multidisciplinary Design, Vol. 121; Eds.: A. Dillmann, G. Heller, H.-P. Kreplin, W. Nitsche, I. Peltzer; Springer-Verlag Berlin Heidelberg 2013
- Notes on Numerical Fluid Mechanics and Multidisciplinary Design, Vol. 124; Eds.: A. Dillmann, G. Heller, E. Krämer, H.-P. Kreplin, W. Nitsche, U. Rist; Springer International Publishing Switzerland, 2014
- Notes on Numerical Fluid Mechanics and Multidisciplinary Design, Vol. 132; Eds.: A. Dillmann, G. Heller, E. Krämer, C. Wagner, C. Breitsamter; Springer International Publishing Switzerland 2016
- Notes on Numerical Fluid Mechanics and Multidisciplinary Design, Vol. 136; Eds.: A. Dillmann, G. Heller, E. Krämer, C. Wagner, S. Bansmer, R. Radespiel, R. Semaan; Springer International Publishing AG 2018
- Notes on Numerical Fluid Mechanics and Multidisciplinary Design, Vol. 142; Eds.: A. Dillmann, G. Heller, E. Krämer, C. Wagner, C. Tropea, S. Jakirlic; Springer Nature Switzerland AG 2020
- Notes on Numerical Fluid Mechanics and Multidisciplinary Design, Vol. 151, Eds.: A. Dillmann, G. Heller, E. Krämer, C. Wagner; Springer Nature Switzerland AG 2021
- Notes on Numerical Fluid Mechanics and Multidisciplinary Design, Vol. 154 Eds.: A. Dillmann, G. Heller, E. Krämer, C. Wagner, J. Weiss; Springer Nature Switzerland AG 2024

Vorschau:

24. DGLR-Fachsymposium	Regensburg, 13. - 14.11.2024
30. Kurs „PIV“	Göttingen, 19.- 22.03.2024

Programmleitung

Prof. Dr. C. Breitsamter (Technische Universität München)
christian.breitsamter@aer.mw.tum.de Tel.: 089 289-16137

Prof. Dr. A. Dillmann (Sprecher) (DLR, Göttingen)
andreas.dillmann@dlr.de Tel.: 0551 709-2177

Prof. Dr. J. Fröhlich (TU Dresden)
jochen.froehlich@tu-dresden.de Tel.: 0351 463-37607

Dr. R. Höld (MBDA Deutschland GmbH,
roland.hoeld@mbda-systems.de Schrobenhausen)
Tel.: 08252 99-8845

Dr. G. Heller (Sprecher) (Airbus, Manching)
gerd.heller@airbus.com Tel.: 8459-8112582

Prof. Dr. E. Krämer (Sprecher) (Universität Stuttgart)
kraemer@iag.uni-stuttgart.de Tel.: 0711 685-63401

Prof. C. Stemmer (Universität Stuttgart)
christian.stemmer@tum.de Tel.: 089 289-16142

Prof. Dr. W. Schröder (RWTH, Aachen)
office@aia.rwth-aachen.de Tel.: 0241 80-95410

Prof. Dr. L. Tichy (DLR, Göttingen)
lorenz.tichy@dlr.de Tel.: 0551 709-2341

Fachgruppen[1]	**Sprecher:**
Aeroelastik und Strukturdynamik*	Prof. Dr. L. Tichy (DLR, Göttingen) Tel.: 0551 709-2341 E-Mail: Lorenz.Tichy@dlr.de
Experimentelle Aerodynamik*	Prof. Dr. C. Breitsamter (Technische Universität München) Tel.: 089 289-16137 E-Mail: Christian.Breitsamter@aer.mw.tum.de
Hyperschallaerothermodynamik	Dr. T. Eggers (DLR, Braunschweig) Tel.: 0531 295-2436 E-Mail: Thino.Eggers@dlr.de
Multidisziplinäre Optimierung	Dr. M. Hepperle (DLR, Braunschweig) Tel.: 0531 295-3337 E-Mail: Martin.Hepperle@dlr.de und Dipl.-Ing. D. Reckzeh (Airbus, Bremen) Tel.: 0421 538-2136 E-Mail: Daniel.Reckzeh@airbus.com
Numerische Aerodynamik*	Dr. C. Grabe (DLR, Göttingen) Tel.: 0551 709-2628 E-Mail: Cornelia.Grabe@dlr.de
Strömungsakustik*	Prof. Dr. J. Delfs (DLR, Braunschweig) Tel.: 0531 295-2170 E-Mail: Jan.Delfs@dlr.de
Strömungsbeeinflussung	Dr. A. Büscher (Airbus, Bremen) Tel.: 0421 538-4268 E-Mail: Alexander.Buescher@airbus.com
Turbulenz und Transition	Prof. Dr. W. Schröder (RWTH Aachen) Tel.: 0241 80-95410 E-Mail: office@aia.rwth-aachen.de und Prof. Dr. N. Adams (Technische Universität München) Tel.: 089 289-16120 E-Mail: Nikolaus.Adams@tum.de

*assoziierte DGLR-Fachkreise
[1]grundlagenorientiert

Fachgruppen[2]	**Sprecher:**
Allgemeine Strömungstechnik	Prof. Dr. C. Wagner (DLR, Göttingen) Tel.: 0551 709-2261 E-Mail: Claus.Wagner@dlr.de
Aerodynamik bodengebundener Fahrzeuge	Dr. A. Wäschle (Mercedes-Benz AG, Sindelfingen) Tel: 0151 586-26046 E-Mail: alexander.waeschle@mercedes-benz.com
Bio- und Mikrofluidmechanik	Prof. Dr. L. Krenkel (OTH Regensburg) Tel.: 0941 943-9689 E-Mail: lars.krenkel@oth-regensburg.de
Drehflügler	Dr. A. Gardner (DLR, Göttingen) Tel.: 0551 709-2267 E-Mail: Anthony.Gardner@dlr.de
Hochagile Konfigurationen	Dr. R. Höld (MBDA Deutschland GmbH, Schrobenhausen) Tel.: 08252 99-8845 E-Mail: Roland.Hoeld@mbda-systems.de
Transportflugzeugkonfigurationen	Dr. A. Seitz (DLR, Braunschweig) Tel.: 0531 295-2888 E-Mail: Arne.Seitz@dlr.de
Versuchsanlagen	Dr. G. Dietz (European Transonic Windtunnel GmbH, Köln) Tel.: 02203 609-110 E-Mail: gd@etw.de
Windenergie	Dr. T. Lutz (Universität Stuttgart) Tel.: 0711 685-63406 E-Mail: lutz@iag.uni-stuttgart.de
Wissenschaftlicher Koordinator	Prof. Dr. C. Wagner (DLR, Göttingen) Tel.: 0551 709-2261 E-Mail: Claus.Wagner@dlr.de

[2]anwendungsorientiert

Stand: Oktober 2023

Verfassen von „Mitteilungen“:

Die Anmeldungen zum STAB-Symposium bzw. STAB-Workshop werden bei der jeweiligen Veranstaltung als Bericht/Proceedings an die Teilnehmer verteilt.

Die Mitteilung ist eine zweiseitige Kurzfassung des Beitrags, bei der nur der unten dargestellte Kopf vorgegeben ist.

Mitteilung

Fachgruppe:

Thema/Titel des Beitrags

Autor(en)
Institution
Adresse
E-Mail

Bitte halten Sie sich bei der Anmeldung zur STAB-Veranstaltung unbedingt an die vorgegebenen zwei Seiten pro „Mitteilung“. Tragen Sie bitte keine Seitenzahlen ein.

Der Druck erfolgt weiterhin ausschließlich in schwarz/weiß.

Für Rückfragen steht Ihnen die Geschäftsstelle gerne zur Verfügung:

Tel.: 0551 709 - 2464
Fax: 0551 709 - 2241
E-Mail: stab@dlr.de

Mit freundlichen Grüßen
Ihre Fachgruppenleiter/innen und Ihre Geschäftsstelle

The **CEAS Aeronautical Journal** and the **CEAS Space Journal** have been created under the umbrella of CEAS to provide an appropriate platform for excellent scientific publications submitted by scientists and engineers. The German Aerospace Center (DLR) and the European Space Agency (ESA) support the journals.

CEAS Aeronautical Journal

An Official Journal of the Council of European Aerospace Societies
ISSN: 1869-5582 (Print), 1869-5590 (Online)
Springer
http://www.springer.com/13272

Editor-in-Chief: M. Fischer, DLR, Cologne, Germany
Managing Editors: C. Hillenherms, A. Dieball,
DLR, Cologne, Germany

The Journal is devoted to publishing results and findings in all areas of aeronautics-related science and technology as well as reports on new developments in design and manufacturing of aircraft, rotorcraft, and unmanned aerial vehicles. Of interest are also (invited) in-depth reviews of the status of development in specific areas of relevance to aeronautics, and descriptions of the potential way forward. Typical disciplines of interest include flight physics and aerodynamics, aeroelasticity and structural mechanics, aeroacoustics, structures and materials, flight mechanics and flight control, systems, flight guidance, air traffic management, communication, navigation and surveillance, aircraft and aircraft design, rotorcraft and propulsion.

The Journal publishes peer-reviewed original articles, (invited) reviews and short communications.

CEAS Space Journal

An Official Journal of the Council of European Aerospace Societies
ISSN: 1868-2502 (Print), 1868-2510 (Online)
Springer
http://www.springer.com/12567

Editor-in-Chief: H. Dittus (Universität Bremen, Germany)
Managing Editors: W. Kordulla (DLR, Cologne, Germany),
S. Leuko (DLR, Cologne, Germany),
J. Steelant (ESA/ESTEC, Noordwijk, The Netherlands)
Honorary Editor: C. Stavrinidis (Imperial College, London, UK)

The Journal is devoted to new developments and results in all areas of space-related science and technology, including important spin-off capabilities and applications as well as ground-based support systems and manufacturing advancements. Of interest are also (invited) in-depth reviews of the status of development in specific areas of relevance to space, and descriptions of the potential way forward. Typical disciplines of interest include mission design and space systems, satellite communications, aerothermodynamics (including physical fluid dynamics), environmental control and life support systems, materials, operations, space debris, optics, optoelectronics and photonics, guidance, navigation and control, mechanisms, propulsion, power, robotics, structures, testing, thermal issues, and small satellites.

The Journal publishes peer-reviewed original articles, (invited) reviews and short communications.

5. Fachgruppe „Drehflügler“

6. Fachgruppe “Experimentelle Aerodynamik”

7. Fachgruppe „Hochagile Konfigurationen“

8. Fachgruppe „Hyperschallaerothermodynamik“

9. Fachgruppe „Multidisziplinäre Optimierung“

10. Fachgruppe „Numerische Aerodynamik“

11. Fachgruppe „Strömungsakustik“

12. Fachgruppe „Strömungsbeeinflussung“

13. Fachgruppe „Transportflugzeugkonfigurationen“

14. Fachgruppe „Turbulenz und Transition“

Mitteilung

Fachgruppe: Aerodynamik bodengebundener Fahrzeuge

Über die Messung von Kraftschwankungen an einem Windkanalmodell

Klaus Ehrenfried und Daniela Heine

Institut für Aerodynamik und Strömungstechnik, DLR
Bunsenstraße 10, 37073 Göttingen
klaus.ehrenfried@dlr.de

Bei der Zulassung neuer Schnellzüge muss deren Seitenwindstabilität nachgewiesen werden. Die Details dieser Prozedur sind in verschiedenen nationalen und europäischen Normen vorgeschrieben. Ausgangspunkt sind Windkanalmessungen an einem Modell des Zugs. bei denen die Kräfte auf das Modell gemessen werden. Es sind Fälle bekannt, bei denen starke Windböen zu dem Umkippen eines Zugs geführt haben. Bei den Windkanalversuchen nach den geltenden Normen werden die Modelle allerdings keinen Böen ausgesetzt, sondern quasi-stationär aus unterschiedlichen Winkeln angeströmt. Es stellt sich hier die Frage, ob die geltenden Normen die realen Risiken wirklich gut abdecken.
In anderen Bereichen, wie zum Beispiel der Gebäudeaerodynamik, wird schon seit Jahrzehnten die Auswirkung von Windböen auf die Stabilität von Gebäuden untersucht. Dazu werden unter anderem Böen-Generatoren in Windkanälen eingesetzt, um eine gestörte Anströmung der Bauwerke zu erzeugen. Auch in der Flugzeugaerodynamik werden Modelle in Windkanälen Böen ausgesetzt. Bei Lancelot et al. [1] ist eine Auflistung von Windkanälen mit entsprechenden Möglichkeiten zu finden. Im Bereich der Fahrzeugaerodynamik wurden von Schröck et al. [2] Untersuchungen an einem Automodell im Windkanal bei gestörter Anströmung durchgeführt. Mit einem Klappensystem wurde eine periodisch schwankende Querkomponente der Strömung aufgeprägt. Es konnte gezeigt werden, dass es in einem bestimmten Frequenzbereich zu einer deutlichen Überhöhung der Querkraft kommt. Das bedeutet, die Querkraft ist bei wechselnder Anströmrichtung höher als bei stationärer Anströmung mit gleicher Geschwindigkeit. Um zu überprüfen, ob es auch bei Schienenfahrzeugen zu solchen Kraftüberhöhungen kommen kann, wurden in der Seitenwindversuchsanlage Göttingen (SWG) Experimente mit einem 1:25 Modell des NGT-Cargos durchgeführt.

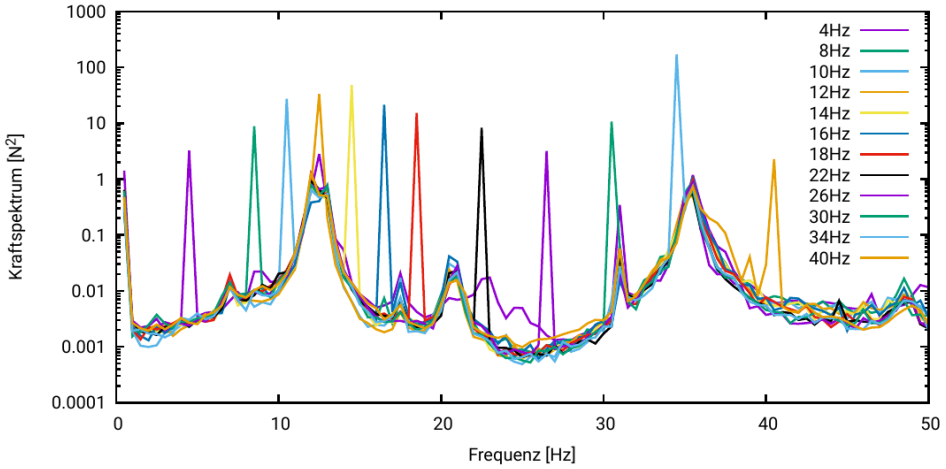

Abb. 1: Spektren der Seitenkraft auf das Zugmodell bei Störung der Anströmung mit unterschiedlichen Frequenzen.

Ein wichtiger und nicht ganz unproblematischer Punkt bei den Windkanaluntersuchungen ist die Halterung des Modells. Sie soll die Strömung möglichst wenig stören. Zudem soll das Modell über einem bewegten Band gehalten werden, um eine realistischere Strömung im

Unterbodenbereich zu bekommen. Für die Versuche im SWG wurde das Modell in der Mitte von oben an einem so genannten Schwert befestigt. Eine solche Befestigung ist bei Untersuchungen an Automodellen ebenfalls üblich und wurde so auch von Schröck et al. [2] verwendet. Die Waage zur Kraftmessung befindet sich dabei im Modell. Da die Halterung nicht komplett steif ist, besitzt die Anordnung Eigenschwingungen, welche das Ergebnis der Kraftmessung verfälschen können. Abbildung 1 zeigt die im SWG am Zugmodell gemessenen Spektren der Seitenkraft bei Störung der Anströmung mit unterschiedlichen Frequenzen. Deutlich sind die Peaks bei der Anregungsfrequenz zu erkennen. Daneben sind breitere Maxima im Spektrum zu sehen, die auf mechanische Eigenschwingungen hindeuten. Idealerweise ist die Halterung so steif ausgelegt, dass die Frequenzen der Eigenschwingungen oberhalb des Frequenzbereichs liegen, der strömungstechnisch von Interesse ist. Eine steifere Halterung ist jedoch massiver und führt zu mehr Störungen der Strömung.

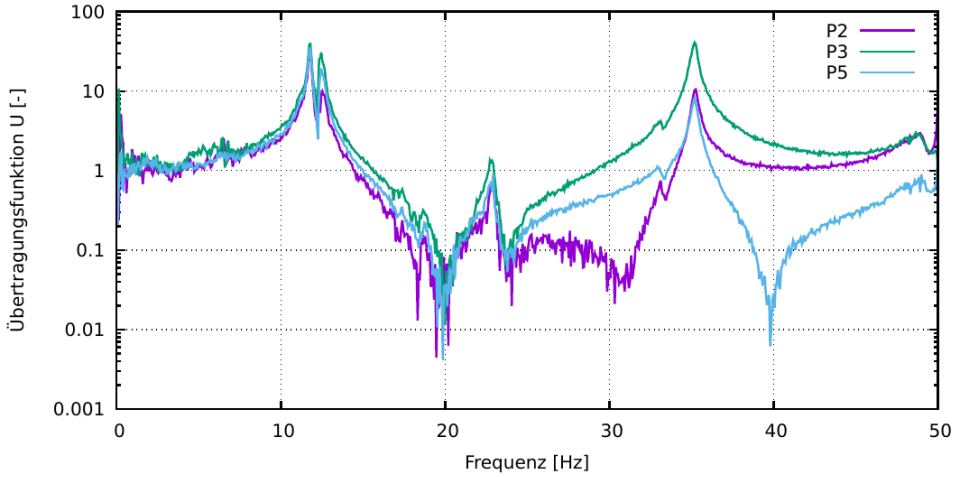

Abb. 2: Mit der Impulshammermethode an drei verschiedenen Positionen am Modell gemessene Übertragungsfunktion für die Querkraft.

Ein Ausweg aus diesem Dilemma ist die Korrektur der Kraftmessung mit einer Übertragungsfunktion, die zum Beispiel mit der Impulshammermethode ermittelt wird. In Abbildung 2 ist die an drei Unterschiedlichen Positionen am Modell gemessene Übertragungsfunktion dargestellt. Ab einer Frequenz von ca. 24 Hz weichen die Kurven deutlich voneinander ab. Das heißt die Übertragungsfunktion hängt von der Position ab, an der die Kraft am Modell angreift. Dies lässt sich durch die Anregung von einer Drehschwingung des Modells an der Halterung erklären. Auffällig ist auch der Einbruch der Übertragungsfunktionen bei ca. 20 Hz. Anscheinend gibt es Frequenzen, bei denen die Waage die äußeren Kräfte nur sehr abgeschwächt registriert. Dieser Effekt lässt sich anhand eines einfachen mechanischen Modells erklären. Dieses Modell wird hier erläutert und es werden Wege vorgestellt, wie auch oberhalb der ersten Resonanzfrequenz noch die Kraftmessungen ausgewertet werden können. So werden die mechanischen Schwingungen mit zusätzlichen Beschleunigungssensoren an geeigneten Positionen in der Halterung erfasst. Es wird gezeigt, wie eine Übertragungsmatrix aufgestellt werden kann, um auch bei der Anregung mehrerer Freiheitsgrade in der Aufhängung die Kräfte ermitteln zu können.

Literatur:

[1] Lancelot, P., Sodja, J., Werter, N., De Breuker, R.: (2017). Design and testing of a low subsonic wind tunnel gust generator. Advances in Aircraft and Spacecraft Science. 4. 125-144. 10.12989/aas.2017.4.2.125.

[2]. Schröck, D., Widdecke, N., Wiedemann, J.: On-road wind conditions experienced by a moving vehicle. In: Wiedemann, J. (ed.) Progress in Vehicle Aerodynamics and Thermal Management V, Expert, Renningen (2008). ISBN 978-3-8169-2771-6

Mitteilung

Fachgruppe: Aerodynamik bodengebundener Fahrzeuge

Untersuchung von Verformungseffekten am Gesamtfahrzeug mittels stationären Strömungssimulationen

Philipp Renz
Mercedes-Benz AG, Group Research & MBC Development
Bela-Barenyi-Straße, 71063 Sindelfingen
Philipp.renz@mercedes-benz.com

Motivation und Zielsetzung

Innerhalb des Entwicklungsprozesses bei Mercedes-Benz werden Unterschiede zwischen frühen Aerodynamik-Prototypen - den sogenannten Aerohartmodellen - und Serienfahrzeugen festgestellt. Aerohartmodelle sind detaillierte Modellaufbauten in vollem Maßstab, die bereits eine Motorraumdurchströmung, einfederbare Achsen mit drehbaren Rädern und im Entwicklungsprozess aktuelle Unterbodenverkleidungen besitzen. Die Außenhaut dieser Modelle ist allerdings im Unterschied zum Serienfahrzeug aus dem Vollen gefräst und demnach nicht verformbar. Dass Serienfahrzeuge tendenziell höhere c_w-Werte besitzen als deren Prototypen-Pendants wird auch von weiteren Herstellern berichtet, [1]. Innerhalb dieser Untersuchung wird der Einfluss von Verformungen an der Außenhaut eines Serienfahrzeugs der 2018 A-Klasse im Abgleich zum entsprechenden Aerohartmodell analysiert. Der Fokus liegt hierbei auf der Front- und Heckschürze.

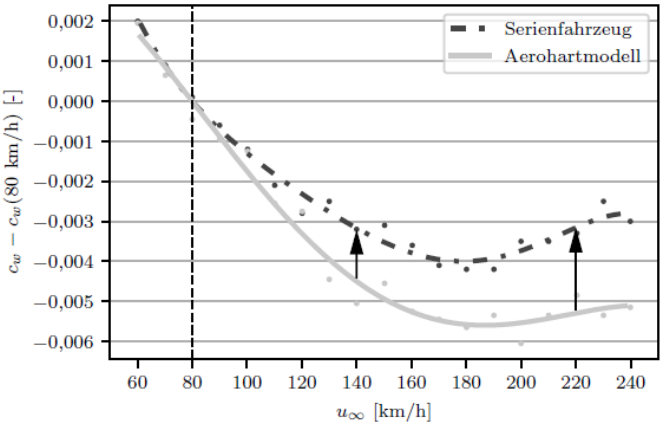

Abbildung 1: Entwicklung des Widerstandsbeiwerts über der Geschwindigkeit für Aerohartmodell und Serienfahrzeug, normalisiert

Eine Voruntersuchung im Windkanal zeigt für steigende Geschwindigkeiten zunächst für beide Fahrzeuge eine Verbesserung des integralen c_w-Wertes, siehe Abbildung 1. Dies ist hauptsächlich durch die Zentrifugalkraft an den drehenden Rädern begründet: Diese federn für steigende Geschwindigkeiten weiter in die Radhäuser ein und die Reifen werden im Latschbereich schmaler, [2]. Allerdings ist die c_w-Verbesserung am Serienfahrzeug nicht so groß wie am Aerohartmodell.

Methode

Grundlage der Untersuchung sind das Aerohartmodell und das Serienfahrzeug der 2018 A-Klasse im geometrisch angeglichenen Zustand. Dabei sind am Aerohartmodell sämtliche Vorserienstände von Anbauteilen durch Serienteile ersetzt und am Serienfahrzeug zusätzliche Durchströmungen unterbunden, die es am Aerohartmodell konstruktionsbedingt nicht gibt. Zur Messung der gemittelten Verformung von Front- und Heckschürze wird eine Photogrammetrie eingesetzt, [3]. Durch das Erzeugen von Bildern von diversen Positionen und Winkeln können mittels Triangulation kodierte und unkodierte Punkte auf der Fahrzeugoberfläche im Raum erfasst werden. Wird dieser Vorgang bei jeweils 0 km/h, 140km/h und 220 km/h durchgeführt, kann durch die Information der Verschiebung der Punkte auf die Verformung der Anbauteile bei 140km/h und 220 km/h zurück geschlossen werden. Als Basis für die Aufbereitung der Front- und Heckschürze wird die mit dem ATOS-System der Firma Carl Zeiss GOM Metrology GmbH aufgenommene Scan-Geometrie der Anbauteile verwendet. Dieser Ausgangsgeometrie kann in einem zweiten Schritt die Verformung aufgeprägt wer-

den. In Abbildung 2 ist die Verformung der Frontschürze bei 140 km/h visualisiert. Zu erkennen ist ein Aufweiten an allen vier umströmten Kanten, welches durch lokale Unterdruckgebiete verursacht wird. Ein ähnliches seitliches Aufweiten ist an der Heckschürze erkennbar.

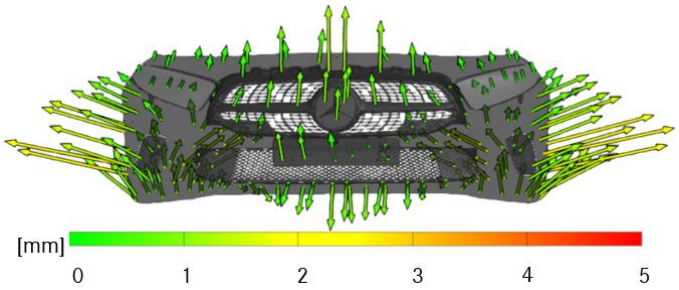

Abbildung 2: Verformung der Frontschürze bei 140 km/h

Analyse der Verformung mittels Strömungssimulationen

Zur numerischen Bewertung der Einflüsse der Verformung wird Simcenter STAR-CCM+ 2020.1 verwendet. Das Simulationssetup verwendet eine freie Anströmbedingung, modelliert durch eine rechteckige Box mit komplett bewegtem Boden, rotierenden Wandbedingungen für die Räder und Felgen sowie einer MRF-Modellierung für die Felgendurchströmung. Für die stationäre Simulation hat sich als Turbulenzmodell das *realizable* k-ε Modell mit dem „*Two-Layer All y*$^+$“-Ansatz bewährt. Weitere Details können [4] entnommen werden.

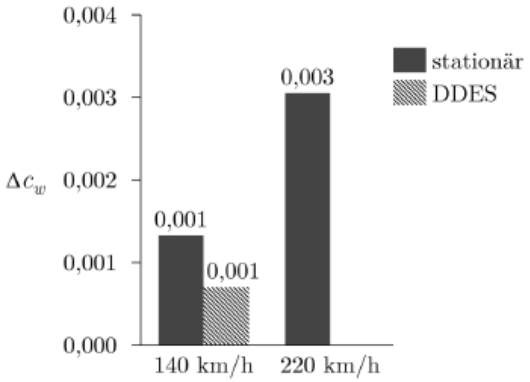

Abbildung 3: Widerstandsaufschlag durch verformte Geometrie in Simulation

Für den integralen Widerstandsbeiwert zeigt sich durch die Verformung in der stationären Simulation eine Verschlechterung von etwa 1 c_w-Punkt bei 140 km/h und von etwa 3 c_w-Punkten bei 220 km/h, siehe Abbildung 3. Im Feld liegt die Begründung dafür in lokal größeren Nachlaufgebieten an Front- und Heckschürze wie es in Abbildung 4 bei 140 km/h zu sehen ist. Bei 220 km/h sind die Änderungen in ähnlichen Regionen sichtbar, wenn auch deutlich markanter. Da die stationäre Simulation vor allem bei Betrachtung kleiner Deltas in Radnähe Unsicherheiten birgt, wurde eine zusätzliche Validierung durch eine instationäre DDES für den 140 km/h Fall durchgeführt.

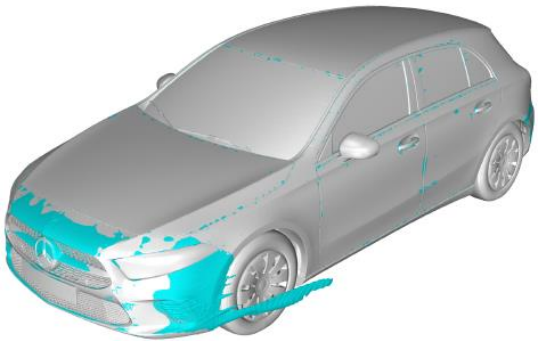
Abbildung 4: Darstellung Flächen verringerter Geschwindigkeit Δc_v=-0,125 bei 140 km/h durch die Verformung in der stationären Simulation

Hierbei zeigen sich ähnliche Effekte sowohl bei integraler Kraftbetrachtung als auch bei den Effekten im Feld, was den Ergebnissen der stationären Simulation Sicherheit gibt. Die mit der Simulation analysierte Verschlechterung im Widerstandsbeiwert durch die Verformung stimmt in der Größenordnung mit dem unterschiedlichen Verhalten bei steigenden Geschwindigkeiten von Aerohartmodell und Serienfahrzeug überein.

Literatur

[1] Blacha, T. und M. Islam (2017). The Aerodynamic Concept of the Audi Q5. In: ATZ worldwide 119.3, S. 42–47

[2] Landstrom, C., L. Josefsson, T. Walker und L. Lofdahl (2012). Aerodynamic Effects of Different Tire Models on a Sedan Type Passenger Car. In: SAE International Journal of Passenger Cars: Mechanical Systems 5.1, S. 136–151

[3] Dannhäuser, P. (2005). Use of 3D Measuring Techniques in the Aerodynamic Development. In: 6th Stuttgart International Symposium Automotive and Engine Technology. Renningen: Expert, S. 490–504

[4] Renz, P. und E. Krämer (2021). Experimental and Numerical Investigation of a Full-Sized Aerodynamic Vehicle Model in Relation to Its Production Car. In: SAE International Journal of Advances and Current Practices in Mobility 4.1, S. 236–248

Mitteilung

Fachgruppe: Aerodynamik bodengebundener Fahrzeuge

Development of a Computational Model for the NGT-Cargo Model based on Wind-Tunnel Data

K. A. Weinman[1*], Müller, T. S[1]., Fey, U[1], K. Ehrenfried[1] & C. Wagner[1,2]
[1]DLR Göttingen, Institut für Aerodynamik und Strömungstechnik
Bunsenstr. 10, 37073 Göttingen, Germany
[2]Technische Universität Ilmenau, Institut für Thermo- und Fluiddynamik
Am Helmholtzring 1, 98693 Ilmenau, Germany
*keith.weinman@dlr.de

The flow about a train is characterized by a large range of energetically significant flow scales which challenge accurate simulations using CFD methods. Nevertheless, the use of CFD methods for certification of trains is accepted with some restrictions by the transport industry. For example, the EN 14067-6 [1] standard permits evaluation of aerodynamic forces by means of computational fluid dynamics (CFD) simulations for full-scale or reduced model geometries under constant cross-wind conditions. At the present time there is no acknowledged international standard concerned with CFD drag prediction under unsteady on-flow conditions for rail vehicles. It is cost effective to develop sufficiently accurate CFD models to assist in the construction of appropriate standards.

The NGT-Cargo [2] is a DLR concept study examining methods of improving rail transport of cargo with the aim of increasing the volume of European rail freight traffic. Initial CFD validations against wind tunnel measurements for the NGT-Cargo concept vehicle have been presented in [3]. In that work both steady and unsteady on-flow conditions were examined. Results suggested the presence of systematic errors when drag values were compared across different configurations of the wind-tunnel model setup and their matched CFD calculations. A feature of the experimental setup that was not included in the initial CFD analysis is the removal of the boundary layer attached to the test section floor upstream of the moving belt by the use of both active and passive suction. The influence of active and passive suction on the computational drag assessment of the NGT-Cargo concept is discussed in the current work. The computational geometry is matched to the experimental geometry more accurately by constructing a catalog of CAD parts that precisely mimic wind tunnel components. Figure 1 illustrates a selection of the components from the parts catalog from which the wind tunnel geometry was constructed for this work.

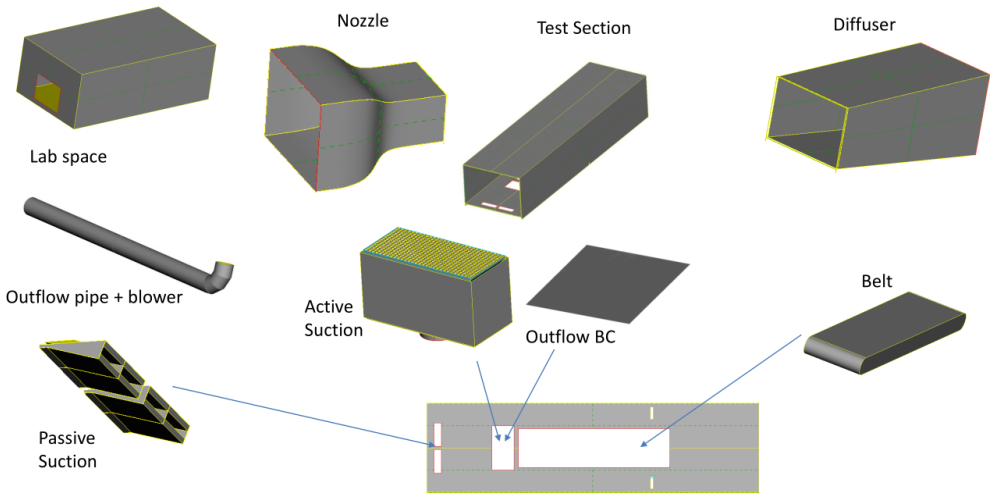

Figure 1: Some components of the CAD catalog.

The catalog simplifies the task of creating computational geometries which model a range of wind tunnel configurations. For our application the onflow to a model inside a wind-tunnel test section should correspond to

the situation of a vehicle moving at a constant relative velocity (U_b) to the stationary ground. Figure 2 demonstrates that the CFD model achieves this goal using passive/active suction and a moving belt under the model. In particular this corrected velocity profile mimics that of a top hat velocity profile containing more energy in the lower boundary layer which interacts directly with the model. RANS calculations completed with the moving belt and with both active and passive suction return a difference between

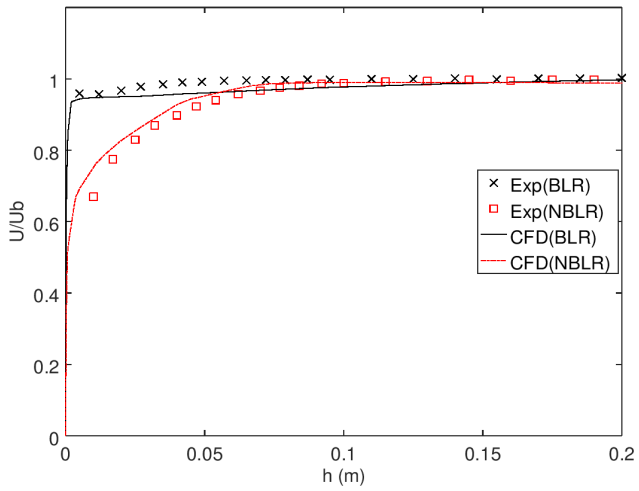

Figure 2: Wall normal velocity profiles. Exp: Experimental data [4]; CFD: Menter-SST turbulent transport model; BLR: boundary layer removal (BLR); NBLR: no boundary layer removal; U/U_b: velocity normalized with the tunnel bulk velocity (U_b); h: height above the wind tunnel floor.

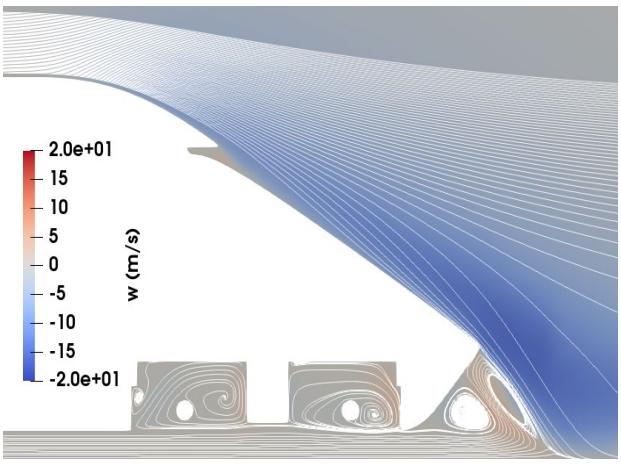

Figure 3: Contour plot of the w velocity component and streamlines about the trailing head of the NGT-Cargo vehicle obtained with upstream boundary layer removal (symmetry plane of model). Differences against the case without upstream boundary layer removal will be discussed in the paper.

computed and measured drag of four (4) drag counts. This can be compared with a difference of nine (9) drag counts using an intact upstream boundary layer [3]. The analysis presented in [3] demonstrated that further reductions in error are achieved when non-resolving hybrid methods are used – at present these calculations have not been completed and results should be available for presentation and detailed discussion in this STAB symposium. Figure [3] illustrates a contour plot of the *w* velocity component about the rear train head along the model's symmetry axis. The corrected onflow velocity profile results in velocity distributions which share the same characteristics as those obtained in [3], however there are differences which will be discussed in the presentation.

[1] DIN EN 14067-6:2018, Railway applications – Aerodynamics - Part 6: Requirements and test procedures for cross wind assessment, September 2018

[2] https://verkehrsforschung.dlr.de/en/projects/ngt-cargo,

[3] K.A. Weinman and Ehrenfried, K. (2022) *Unsteady onflow effects on model train drag.* In: New Results in Numerical and Experimental Fluid Mechanics XIV, Contributions to the 23rd STAB/DGLR Symposium Berlin, Germany 2022. A. Dillmann, G. Heller, E. Krämer, C. Wagner and J. Weiss (Ed.), Springer, 2024

[4] DLR-Projekt „Next-Generation-Train", AP 0410, Meilenstein 04101912, Fey, U.: Inbetriebnahme des Laufbandes im SWG und Vermessung der Strömung, 2020

Mitteilung

Fachgruppe: Aeroelastik und Strukturdynamik:

Experimental and Numerical Analysis of Aeroservoelastic Phenomena
on a Structurally Dynamic Scaled Delta Wing

Konstantin Bantscheff, Christian Breitsamter
Chair of Aerodynamics and Fluid Mechanics, Technical University of Munich,
Boltzmannstr. 15, 85748 Garching bei München, konstantin.bantscheff@tum.de

Introduction

The enhancement of computational capabilities in the recent years allowed a development of high-fidelity computational approaches for fluid structure interactions (FSI) to capture the coupling effects between aerodynamic loads and elastic structures. The use of FSI simulations in the field of aircraft aerodynamics is of major interest for cases with medium to large deformations to account for significant changes in the aerodynamic load with respect to a rigid assumption [1]. In this regard the validation of those simulations by means of experimental analyses plays an important role in aircraft design processes. For both, the simulation approach, and the experimental analysis using scaled models, it is essential to provide a realistic structural behavior of the investigated model with respect to a full-scale equivalent.

Model Design

The main objective of this work is the conduction of experimental investigations of an aeroelastically scaled delta wing, considering flap deflections and their effect on the occurring flow phenomena for low Mach numbers and steady cruise conditions. These data are used for validation purposes regarding computational results. The scaling of the model is conducted according to previous work [2].

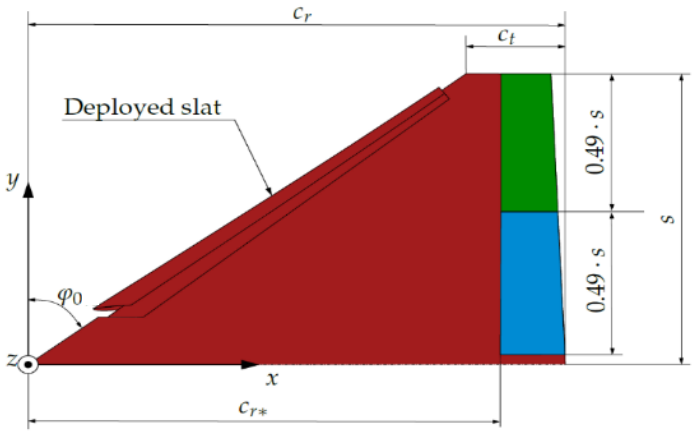

Figure 1: Geometry of the Model53

For the manufacturing of the scaled wind tunnel model, named Model53, 3D printing technology is applied. The utilized delta wing model features a leading edge sweep of $\varphi_0 = 53°$ and a taper ratio of $\lambda = 0.159$. The model is downscaled by a factor of 11.2 with respect to a fictitious full-scale wing and has a root chord length of $c_r = 0.75\ m$ [3]. A leading edge slat is deployed at a fixed angle of $20°$. The inner and outer trailing edge flaps are screwed to the main wing and can be exchanged by flaps with different deflection angles. Figure 1 shows a sketch of the wing geometry and its trailing edge flaps.

Experimental Analysis

For the experimental investigation in the wind tunnel facility A of the Technical University of Munich the global mean forces and moments are evaluated. Furthermore, multiple transient pressure transducers (Kulite XCQ-093 series) and accelerometers (PCB 352C22/NC) are installed in the model. This instrumentation is applied to evaluate the global and local influence of flap deflections on the aerodynamics of the wing. Figure 2 shows a plot of multiple lift polars, resulting from the conducted experiments. As depicted in the plot, a positive or negative flap deflection leads to a shift of the lift polar to higher or lower values, respectively. Furthermore, the elasticity of the model also has a visible effect on the course of the lift curve. As a higher

dynamic pressure leads to an increased deformation of the wing, a tendency of reduced aerodynamic efficiency is observable for the higher dynamic pressure.

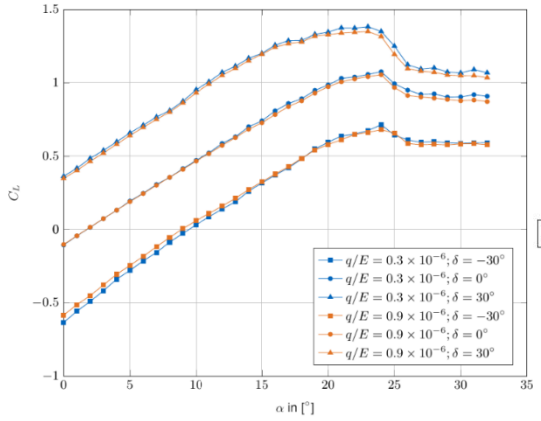

Figure 2: Lift polar for three flap deflection angles and two dynamic pressures (Experiment)

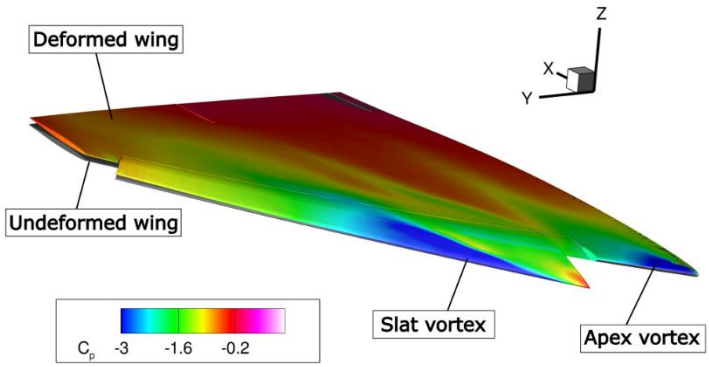

Figure 3: Pressure coefficient distribution of the Model53 at $\alpha = 20°$ and $q = 1570\ Pa$ ($\frac{q}{E} = 0.9 \cdot 10^{-6}$) (Simulation)

Computational Approach

For the simulation task, the elasticity of the model is considered as well. As a result, a two-way FSI simulation is performed by utilizing the ANSYS tools Fluent, transient Mechanical and System Coupling. A transient simulation is performed. In the beginning of each physical time step a transfer of the surface pressure forces from the Computational Fluid Dynamics (CFD) mesh onto the structural mesh is conducted. For the CFD simulations the unsteady Reynolds-averaged Navier-Stokes (U-RANS) equations are solved. The U-RANS equations are closed using the $SST\ k-\omega$ turbulence model. The resulting deformation of the FEM mesh is transferred back to the CFD grid. The deformation of the wing model is propagated into the volume mesh of the grid. Furthermore, for each time step three exchange cycles between the two meshes are performed. For the first step of the simulation a large time step is used to achieve an appropriate starting point with an already deformed geometry. This initial condition is then used to calculate the results for further refined time steps. Figure 3 presents the results of the calculated pressure coefficient distribution of the Model53 at an angle of attack of $\alpha = 53°$ and at a dynamic pressure of $q = 1570\ Pa$. The two occurring vortices originating from the apex and the slat are indicated by the two suction regions in the plot. Additionally, the deformation of the wing for the aerodynamic loading is visualized.

Acknowledgement

The authors want to thank ANSYS for providing the simulation software used for the numerical investigations and the Gauss Centre for Supercomputing e.V. (www.gausscentre.eu) for funding this project by providing computing time on the GCS Supercomputer SuperMUC at Leibniz Supercomputing Center (LRZ, www.lrz.de).

Literaturverzeichnis

[1] C. Reinbold, K. Sørensen und C. Breitsamter, „Aeroelastic simulations of a delta wing with a Chimera approach for deflected control surfaces," *CEAS Aeronautical Journal,* Bd. 13, Nr. 1, pp. 237-250, 2021, doi: 10.1007/s13272-021-00561-3.

[2] K. Bantscheff und C. Breitsamter, „Dynamic Structural Scaling Concept for a DeltaWing Wind," *Aerospace,* Bd. 10, Nr. 7, pp. 581, 2023, doi: 10.3390/aerospace10070581.

[3] M. Moioli, C. Reinbold, K. Sørensen und C. Breitsamter, „Investigation of Additively Manufactured Wind Tunnel Models with Integrated Pressure Taps for Vortex Flow Analysis," *Aerospace,* Bd. 6, Nr. 10, pp. 113, 2019, doi: 10.3390/aerospace6100113.

Mitteilung

Fachgruppe: Aeroelastik und Strukturdynamik

Unsteady RANS simulations of two dimensional separated wake flows

Kristopher Davies
DLR, Institut für Aeroelastik, Bunsenstr. 10, 37073 Göttingen, kristopher-marc.davies@dlr.de

Background

The prediction of unsteady loads occurring at the edges of the flight envelope remain a challenge due to complex flow phenomena. For instance, flow separation on the wing causes the formation of turbulent structures in the wake, which can potentially lead to vibrations on the horizontal tail plane (HTP) [1]. This phenomenon is referred to as *HTP buffet*. While high-fidelity CFD methods based on scale resolved turblence models, such as large eddy simulations (LES) or detached eddy simulations (DES) can be considered as promising to capture all relevant flow mechanisms, their requirement on computational effort are still too demanding for industrial applications. Methods based on the unsteady Reynolds-averaged Navier-Stokes (URANS) equations may provide a compromise between computational effort and the modeling of the most relevant flow phenomena in the wake of the wing causing HTP buffet.

Objective

This study aims to further explore the applicability of RANS methods in highly unsteady flows with distinct separation. For this purpose, a variation of the turbulence model is performed for flight conditions beyond the maximum lift coefficient. The development of the wake flow of an airfoil is analysed and discrepancies between the turbulence models are identified. The presented study is a prerequisite to understand similar flow effects on more complex industrial-relevant configurations.

Approach

In order to assess the accuracy of the RANS models, experimental data from Seifert and Pack [2] are consulted for the NACA0012 profile. Unsteady RANS simulations are performed with the DLR TAU code and compared to the experimental data.

Preliminary Results

Fig. 1 shows the spectra of the fluctuating pressure component $C_{p'}=p'/q_\infty$ as a function of the dimensionless Strouhal number obtained at a specific point in the wake of the airfoil by Seifert and Pack [2] in a low-speed stall condition. The boundary layer is fully separated on the upper surface for this condition. However, numerical results for the same angle of attack reveal partially attached flow, for which reason a correction of the angle of attack is required in order to reproduce a similar condition as for the experiment. This is the case for angles of $\alpha\approx19.0°$. The numerical results presented in Fig. 1 obtained by the SSG/LRR-ln(ω) Reynolds stress model for the angle of attack $\alpha\approx19.0°$show a good agreement to the experimental results. Similar trends are also observed for eddy viscosity models, such as the Spalart-Allmaras or Menter-

SST k-ω turbulence models. The differences between the turbulence models in the spectra and development of the wake flow are further investigated in this study.

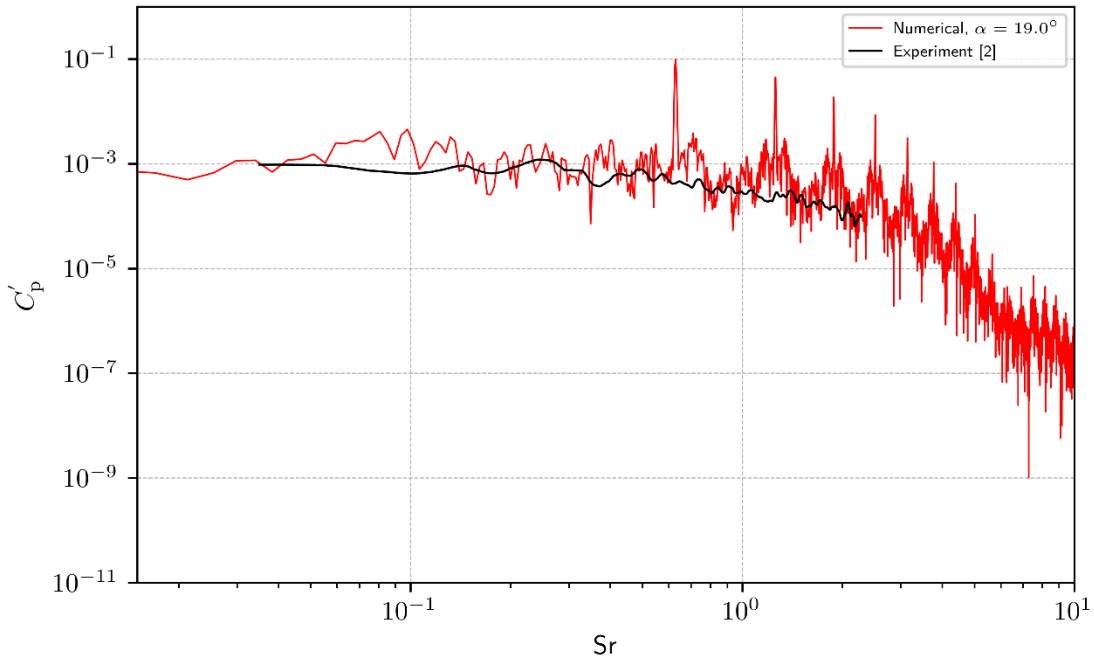

Figure 1: Pressure spectra in the separated wake at M=0.30, Re=6·10⁶, α=16.0° (experimental) and α=19.0° (numerical)

References

[1] Koopmans, W., Klabes, A., and Gojny, M. H. (2022). Wing-Tailplane Flow Interaction: Flight Test Data Analysis from Stall Flights. In: Proceedings International Forum on Aeroelasticity and Structural Dynamics (IFASD), Madrid.

[2] Seifert, A., and Pack, L. G. (1999). Oscillatory Excitation of Unsteady Compressible Flows over Airfoils at Flight Reynolds Numbers. In: 37th AIAA Aerospace Sciences Meeting and Exhibit, AIAA, 99-0925, Reno.

Mitteilung

Fachgruppe: Aeroelastik und Strukturdynamik

DLR Contributions to the 3rd Aeroelastic Prediction Workshop

Markus Ritter, Jonathan Hilger, Michael Fehrs
DLR Institut für Aeroelastik, Bunsenstraße 10, 37073 Göttingen
markus.ritter@dlr.de, jonathan.hilger@dlr.de, michael.fehrs@dlr.de

In this work we give an overview of the activities of the *Large Deflection Working Group* (LDWG) of the 3rd *Aeroelastic Prediction Workshop* (AePW3) and present DLR's contributions to this working group.

The AePW3[1] took place in conjunction with the 2023 AIAA SciTech Forum. The Large Deflection Working Group was one of the sub-groups of AePW3 and its purposes were to research in the static and dynamic aeroelastic behavior of aircraft structures undergoing geometrically large deformations in order to gain deeper understanding of the physical mechanisms involved. This particular objective was sparked by the current trend in transport aircraft design towards slender, high aspect ratio wings which reduce induced drag but yield high flexibility. Then, the question, which particular features an aeroelastic solver requires for the analysis of aircraft structures with geometrical nonlinearities was to be answered. Unfortunately, comprehensive and publicly available experimental data sets of highly flexible test cases are scarce. The Pazy Wing was designed and tested by Technion - Israel Institute of Technology as a benchmark to provide experimental data of a highly flexible aeroelastic test case for the validation of nonlinear aeroelastic simulation methods. Tip deformations in the order of 50% half-span were measured in wind tunnel tests. Particular features make this model highly attractive for a broad audience: A simple wing with rectangular planform, no taper, no sweep, and a symmetrical airfoil operating in incompressible flow. The Pazy Wing model from Technion is shown in Figure 1, its main dimensions are listed in Table 1.

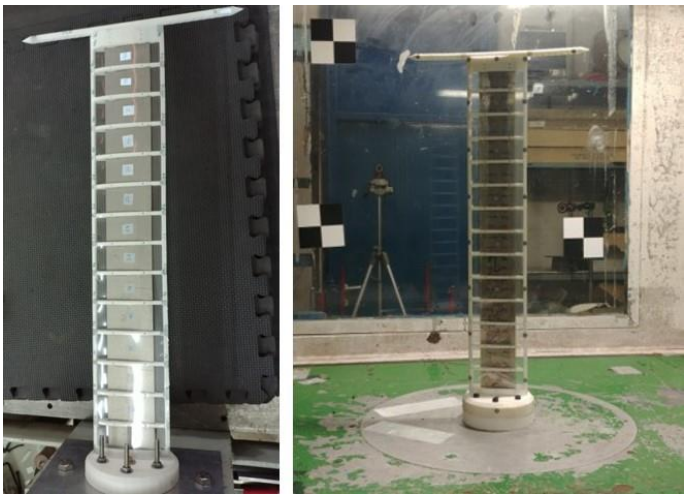

Figure 1 Pazy Wing benchmark model in Technion Wind Tunnel

Property	Unit	Pazy Wing
Span	m	0.56
Chord	m	0.1
Taper ratio	-	1
Sweep angle	deg	0
Tip rod length	m	0.3
Tip rod diameter	m	0.01
Airfoil	-	NACA0018
Covering	-	Oralight

Table 1 Dimensions of the Pazy Wing

For AePW3, the participants of the LDWG had to work on three different test cases. First, static coupling simulations for root angles of attack of 3°, 5°, and 7° at dynamic pressures ranging from zero to 1800 Pa. Second, the calculation of structural modal data (eigenvalues) as function of the static deformation of the wing. Third, flutter speeds, also for 3°, 5°, and 7° root angle of attack of the wing. All simulations of DLR are based on an in-house steady and unsteady Vortex Lattice Method coupled with a nonlinear structural solver. For the stability analysis, the whole aeroelastic system (aerodynamic and structure) was linearized about the particular static equilibrium conditions (in steps of 2 m/s airspeed) and the poles were obtained from an eigenvalue analysis of the Jacobian of the linearized system. Results for the

[1] https://nescacademy.nasa.gov/workshops/AePW3/public

static coupling simulation at 5° root angle of attack in terms of the wing tip displacement as function of the dynamic pressure are shown in Figure 2.

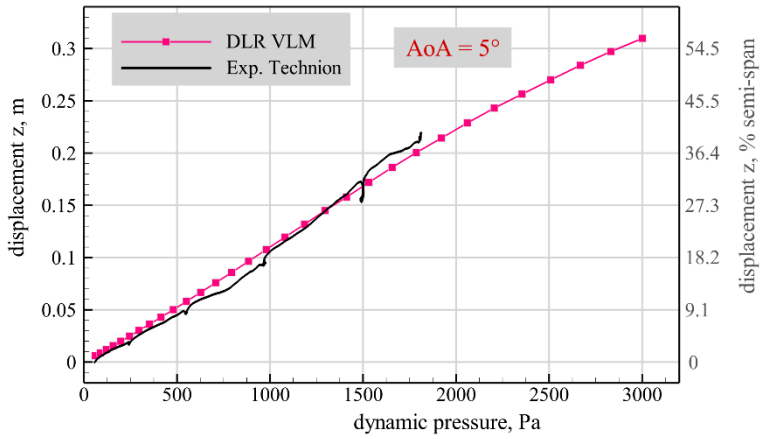

Figure 2 Pazy Wing static tip displacement as function of dynamic pressure calculated by VLM

The stability (flutter) regions of the Pazy Wing as function of the steady root angle of attack and the airspeed are plotted in Figure 3.

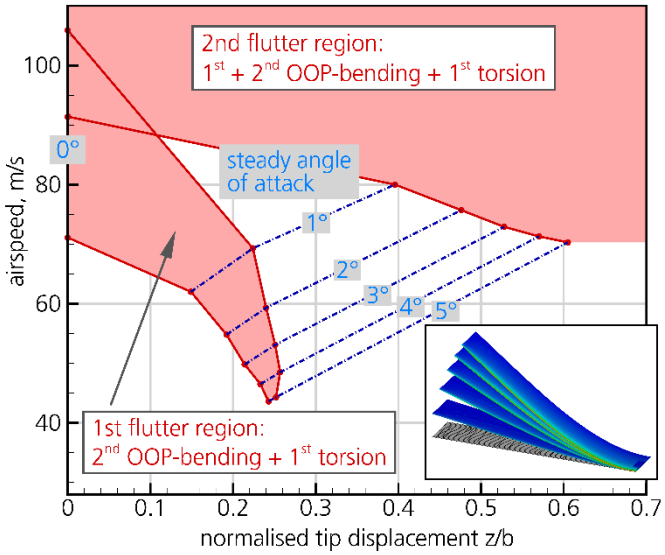

Figure 3 Flutter regions of the Pazy Wing as function of airspeed and steady angle of attack calculated by UVLM

In addition, DLR also applied a CFD method (TAU) with free transition modelling for the static coupling simulations. An unstructured CFD grid based on a geometry that includes the ribs and the sagging of the foil covering between the ribs was used. Exemplary results of the CFD simulations for various root angles of attack and 50 m/s airspeed are shown in Figure 4.

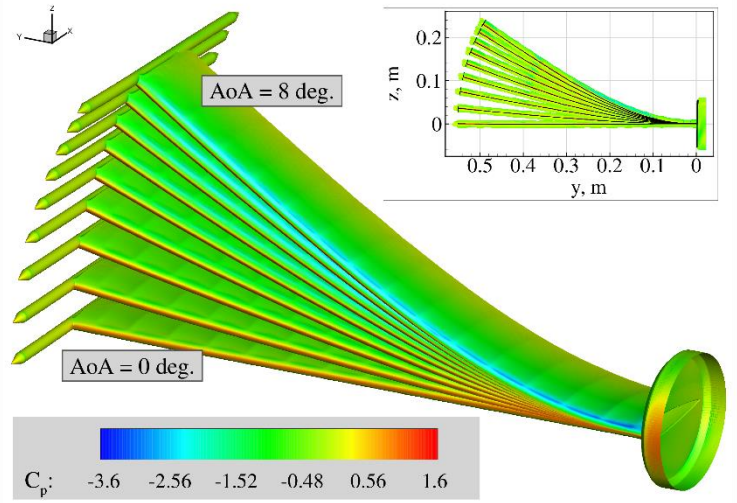

Figure 4 Static coupling results from a CFD method based on a realistic geometry (rib and sagged regions)

Mitteilung

Fachgruppe: Aeroelastik und Strukturdynamik

Extended CFD-CSD Coupling Featuring Elastic Airframes

Oskar Wengrzyn

Institut für Aerodynamik und Gasdynamik - Universität Stuttgart, Pfaffenwaldring 21, 70569 Stuttgart, oskar.wengrzyn@iag.uni-stuttgart.de

Current industrial state-of-the-art in aeromechanical CFD-CSD coupling consists of coupling a rigid airframe with aeroelastic rotor models. Furthermore, the rigid airframe does not incorporate unsteady motions in terms of blade passage frequency (b/rev) vibrations. While this set-up is perfectly suited to answer relevant aerodynamics and flight mechanics issues on high fidelity level, this approach needs to be refined in view of unsteady airframe loads, motions and vibrations.

This research project is dedicated to the vibration prediction challenge in the airframe. In this context, a comprehensive approach with respect to a CFD-CSD tool chain shall be realized for solving the combination of an (aero-)elastic airframe combined with aeroelastic rotor systems for vibration prediction in the frequency domain. Main industrial driver is the predictability of airframe vibrations at b/rev of the main rotor system. Elements to be added to the existing tool chain for the extended CFD-CSD coupling for the kinematic path from CSD to CFD are:

- Vibratory rotor hub motions to be considered by the CFD solver package
- Vibratory drive train motions to be considered by the CFD solver package
- Vibratory airframe motions (rigid body and elastic) to be considered by the CFD solver package for airframe surface loads analysis

On the other hand, aerodynamic loads need to be supplied to elastic model components representing the loads part from CFD to CSD for the full coupling scenario:

- CFD rotor loads to be transferred to the airframe system of motion equations
- CFD rotor loads to be transferred to the drive train system of motion equations
- Vibratory CFD airframe surface loads to be considered by the CSD solution of the elastic airframe

In the exploration of rotorcraft dynamics, two distinct approaches have been extensively examined: the loose coupling and strong coupling. Within the framework of the loose coupling approach, the elastic deformations of the main rotor hub are updated systematically using a CFD-CSD coupling toolchain. This process involves establishing an interface between CFD and CSD. The exchange of the surface load data derived from CFD simulations with the CSD solver is taking place over the interface. The said CSD solver calculates the elastic deformations of the rotor hub. Subsequently, these deformation values are incorporated into the CFD kinematic chain. This iterative process takes place every two full revolutions of the main rotor - hence the term "loose coupling methodology."

A part of this toolchain is CAMRADII - comprehensive tool. This polar-based comprehensive tool uses loads directly calculated by the CFD for the main rotor blades. For fuselage loads, the tool shifts the polars to align with the CFD-derived loads under specified control at-

titudes. Notably, CAMRADII serves a dual purpose by also being employed for the task of trimming.

Presently, the focal point of the project is to obtain a converged CFD simulation with correct control angle attitudes. Investigations have been conducted to scrutinize the stability of the CFD-CSD interface, involving a comparison between the polar-based Jacobian and its CFD-computed counterpart. Despite the efforts, achieving convergence remains an ongoing challenge.

However, it's worth noting that CAMRADII doesn't encompass an integrated Finite Element Method (FEM) solver. Instead, it assembles beams into a system representing the helicopter's structure. Then it solves these interconnected beams, linked through joints. This approach sufficiently addresses most scenarios, yet its accuracy might not be enough when predicting vibrations at blade-passing frequency. Consequently, the project also investigates strong coupling.

The strong coupling methodology introduces an in-house library, a derivative of the CFD tool FLOWer, called FEMLib. Operating as a CSD solver, FEMLib uses the Newmark method, a second-order technique noted for its robustnes. The FEMLib library is tightly integrated into FLOWer code – making the usage relatively easy and calculations fast. The integration is carried out in modal space to enable the flexibility of modal reduction if complex structural model with massive degree of freedom are solved.

Unquestionably, the CSD model has a considerable number of degrees of freedom. While the IAG has expertise in the CFD and aerodynamics, modal reduction for CSD has not been explored in-house. This led to a collaboration between IAG and the Institute of Technical Mechanics (ITM). ITM is currently working the modal reduction for the helicopter's CSD model.

However, the modal reduction process advocated by ITM requires the solution of a rigid CFD simulation. Regrettably, due to persistent convergence issues with control angle attitudes, the exchange of CFD data and the CSD model has not taken place.

Notably, FEMLib has demonstrated its efficacy in a different project that examined the phenomenon of tailshake with success.

Currently, the researcher under this project is investigating the loosely coupled methodology. The extraction of hub motions from comprehensive tool and insertion of the motions to the kinematic chain of CFD is nearly done. Finding the correct control angles proves to be the most difficult task yet. Comparison of Jacobians from polar based models and CFD calculations showed that some stability criteria are not satisfied. As a result oscillations of residual forces are present, making it difficult to find the correct control angles.

Mitteilung

Fachgruppe: Allgemeine Strömungstechnik

Calculation of the three-point contact angle for water droplets on a surface from a rearward droplet observation

Rupert Anschütz, Andreas Westhoff and Konstantin Niehaus
German Aerospace Center (DLR), Institute of Aerodynamics and Flow Technology, Göttingen, Germany, Rupert.Anschuetz@dlr.de

Droplet condensation on cooled surfaces is a phenomenon that occurs in a variety of technical applications and in nature. For example, the condensation of droplets on camera lenses leads to aberration [1] or droplets on surfaces can increase the effectiveness of heat exchangers [2]. With the objective to determine the impact of droplet formation on optical properties or on the heat transfer an accurate detection of droplet distributions on surfaces is of utmost importance. Therefore, we have been developing a non-invasive measurement and evaluation method to characterise droplet ensembles on a surface by means of diameter and contact angle. In this conference contribution, we focus on the evaluation method to determine the three-phase contact angle from microscope images using a tray-tracing algorithm.

An important aspect for understanding droplet condensation is the quantification of mass transfer rates and the resulting water mass on the surface. For the determination of the local water mass on a surface, we have developed an automated measurement method [3] to determine the droplet diameters that can be used to calculate the water mass assuming a constant contact angle. However, when droplets grow or shrink during condensation or evaporation, the contact angle often changes while the radius remains almost constant as shown by Parisse et al.[4]. Therefore, a method which allows to measure the contact angle and the droplet diameter simultaneously is highly desirable. However, it is difficult to detect the three-phase contact point from a lateral perspective due to the small droplet size and limited lines of sight due to obstruction by neighbouring droplets at a high droplet density. Therefore, a direct measurement of the contact angle is often not possible. To overcome this issue, we propose a non-invasive experimental method for the detection of droplets involving the simulation of the contact angle.

Figure 1b shows a photo of the experimental set-up for droplet investigation. The set-up consists of a cooling plate, two cameras equipped with far field microscopes to record the droplets on the cooling plate, and a ring light to illuminate the droplets from the flipside as illustrated in figure 1b. The rear camera is parallel oriented to the cooling plate in order to observe the contact area of the droplets, while the lateral camera observes the contact angle.

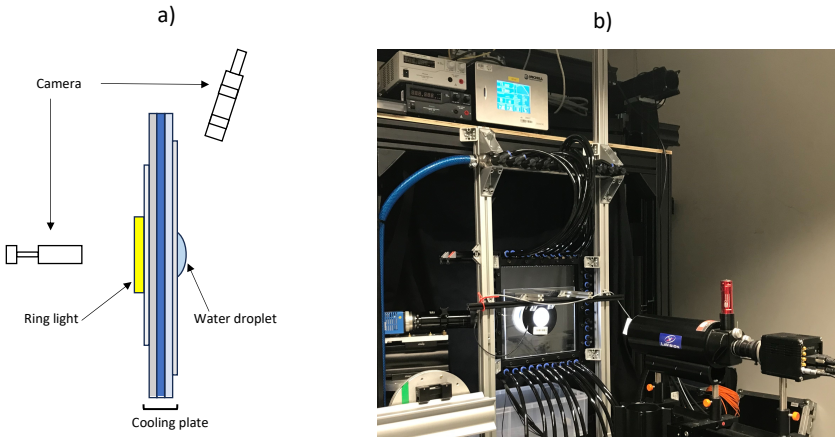

Figure 1: (a) Sketch of the cooling plate with the positions of the camera with the far-field microscopes. (b) Photo of the experimental set-up (front view).

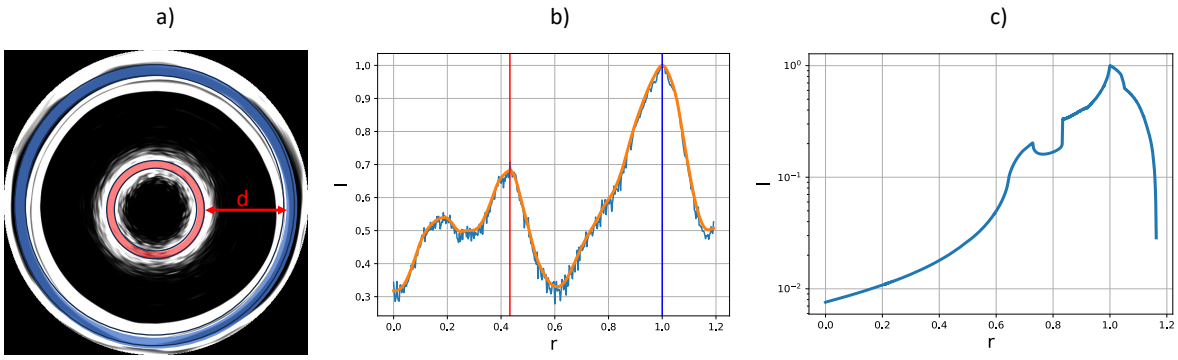

Figure 2: (a) Images showing the inner (red) and outer (blue) reflection ring of a single droplet. (b) Averaged intensity I as a function of the normalised radius r with centre position r=0. (c) Model of the averaged intensity I as a function of the normalised radius r with the same radius and contact angle as the droplet in figure 2b).

Figure 2a depicts a sample result of a single droplet recorded by the rear camera with a diameter of 400μm after image postprocessing. The image reveals the inner (red) and the outer (blue) reflection rings. Here, the outer ring is the result of enhanced light reflections at the boundary of the droplet, while the internal reflection depends on the geometric properties of the droplet. In addition, the radius of the outer ring represents the radius of the droplet. The distance of these two rings dependents on the contact angle of the droplet. Figure 2b shows the corresponding over four axis averaged radial intensity distribution, where the centre of the droplet is $r = 0$. The plot depicts two local maxima representing the centre radius of the inner and outer ring, respectively. In the following, the distance between these maxima is $d = r_o - r_i$.

By means of the distance d and the droplet radius r_o we can calculate the contagt angle. Therefore, we implemented a geometric ray-tracing algorithm to calculate the light intensity of the droplet as a function of the radius, assuming the shape of the droplet is a perfect sphere. Initially, the possible angles of incidence are checked for the first reflection point on the airside surface of the droplet. This is calculated for points at a regular distance along the radius on the airside surface of the droplet. Each of the possible incident rays are traced through the droplet until it hits the liquid-gas surface. Further, the intensity loss due to transmission at each reflection point is taken into account, as well as the loss through the different layers of the cooling plate. To obtain the intensity distribution on the rear side of the cooling plate, the sum of the intensities is calculated. Figure 2c shows the intensity as the function of the radius r from the ray-tracing calculations where the y-axis is scaled logarithmically. Based on an ensemble of these calculations for the here investigated parameter range a functional relation $\alpha = f(d, \theta_C)$ is formalised to determine the contact angle alpha by means of the droplet diameter r_o and the distance d.

At the workshop we will present the experimental set-up, introduce the ray-tracing algorithm, the method to calculate the contact angle and a discussion of the accuracy of this evaluation procedure as well as the limitations of this method.

References

[1] F. Secci und A. Ceccarelli, „On failures of RGB cameras and their effects in autonomous driving applications“, *2020 IEEE 31st Int. Symp. Softw. Reliab. Eng. ISSRE*, S. 13–24, Okt. 2020, doi: 10.1109/ISSRE5003.2020.00011.

[2] H. Nguyen und H. S. Ahn, „A comprehensive review on micro/nanoscale surface modification techniques for heat transfer enhancement in heat exchanger“, *Int. J. Heat Mass Transf.*, Bd. 178, S. 121601, Okt. 2021, doi: 10.1016/j.ijheatmasstransfer.2021.121601.

[3] K. A. Niehaus, M.-C. Volk, A. Westhoff, und C. Wagner, „Evaluation of three measurement techniques for water-vapor mass transfer in case of droplet condensation“, in *8th Thermal and Fluids Engineering Conference, TFEC 2023*, College Park, MD, USA: ASTFE Digital Library, März 2023, S. 1525–1536. doi: 10.1615/TFEC2023.the.046304.

[4] F. Parisse und C. Allain, „Shape Changes of Colloidal Suspension Droplets during Drying“, *J. Phys. II*, Bd. 6, Nr. 7, S. 1111–1119, Juli 1996, doi: 10.1051/jp2:1996119.

Mitteilung

Fachgruppe: Allgemeine Strömungstechnik

DNS study of the dispersion of cough-induced particles and their interaction with a large-scale circulation

Ege Batmaz[1,2], Daniel Schmeling[1] and Claus Wagner[1,2]
[1] DLR Göttingen, Institut für Aerodynamik und Strömungstechnik,
Bunsenstraße 10, 37073 Göttingen,
[2]Technische Universität Ilmenau, Institut für Thermo- und Fluiddynamik,
Am Helmholtzring 1, 98996 Ilmenau
ege.batmaz@dlr.de

The ventilation of train compartments, aircraft cabins or other confined spaces is mainly characterised by a large-scale circulation (LSC). Extending previous research on droplet dispersion in unventilated environments [1], this study focuses on aerosols within a turbulent cough-generated jet, analysing their interaction with a LSC and comparing trajectories. The mean paths of the particles in the horizontal direction are further analysed and compared using the centroid and the dynamic time warping (DTW) methods.

We performed a direct numerical simulation (DNS) using a second-order accurate finite volume method in combination with a projection method for the velocity-pressure coupling and an explicit second-order accurate Euler-Leapfrog time step. The transport equations for temperature and vapour concentration are coupled to the momentum equations using the Boussinesq approximation to account for the buoyancy effect. The exhaled particles are assumed to have spherical shape with constant mass and are tracked using a Lagrangian approach. Prior to this DNS, a separate DNS of a turbulent lid-driven cavity flow was performed using a semi-implicit time integration scheme to obtain an initial flow field for the former DNS.

Figure 1 shows the velocity magnitude field and the predicted particle cloud at the end of the jet phase of a single cough (t = 0.9 s) in a LSC environment. Particles larger than 100 µm have already detached from the jet cloud due to gravitational forces and are approaching the ground with ballistic (semi-ballistic) behaviour. Figure2 shows the particle cloud propagation from the top and side, 6 s after the start of exhalation, for the quiescent and the LSC cases. The particle cloud in the LSC case spreads 16% farther in the horizontal direction than the particles in the quiescent case. In addition to the increased horizontal propagation, the overall lateral dispersion (z-direction) becomes more uniform due to the stretching of the cloud by shear forces from the circulating flow, resulting in a narrower and more elongated cloud shape compared to the quiescent scenario (see top views in Fig. 2).

Figure 3 shows the horizontal coordinates of the mean trajectories computed in the LSC case using the centroid and DTW methods. As can be seen on the left hand side of the figure, the horizontal advancement decreases with increasing particle size. Particles of size $d_{50\text{-}60\mu m}$ experience a horizontal acceleration after t = 16 s as they enter the strong near-surface wind of the LSC. In contrast, Fig. 3 (right) shows a twisted DTW mean trajectory of the particles and, in contrast to the centroid method, the particle size is not directly correlated with the horizontal advancement. Compared to the results of the centroid method, the influence of the strong LSC wind near the ground is evident not only for particles larger than 50 µm, but also for particles larger than 30 µm.

References

[1] E. Batmaz, P. Bahavar, D. Schmeling and C. Wagner. DNS of aerosol particle spreading emitted by coughing and breathing in a simplified room. Accepted for publication in New Results in Numerical and Experimental Fluid Mechanics XIV., Notes on Numerical Fluid Mechanics and Multidisciplinary Design, Springer, 2023.

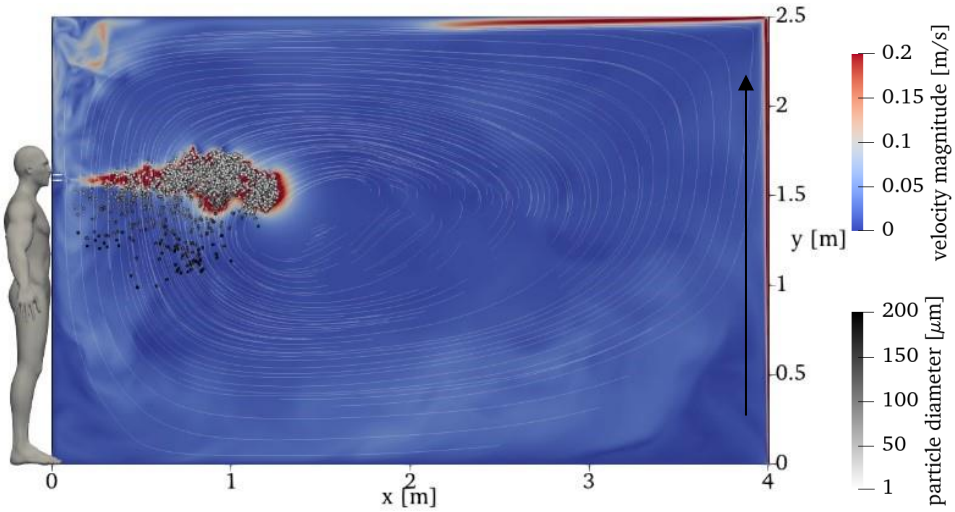

Figure 1: Instantaneous field of the velocity magnitude and particle distribution under the influence of a LSC at t = 1 s. The semi-transparent streamlines represent the initial time-averaged LSC field. The arrow indicates the flow orientation at the wall.

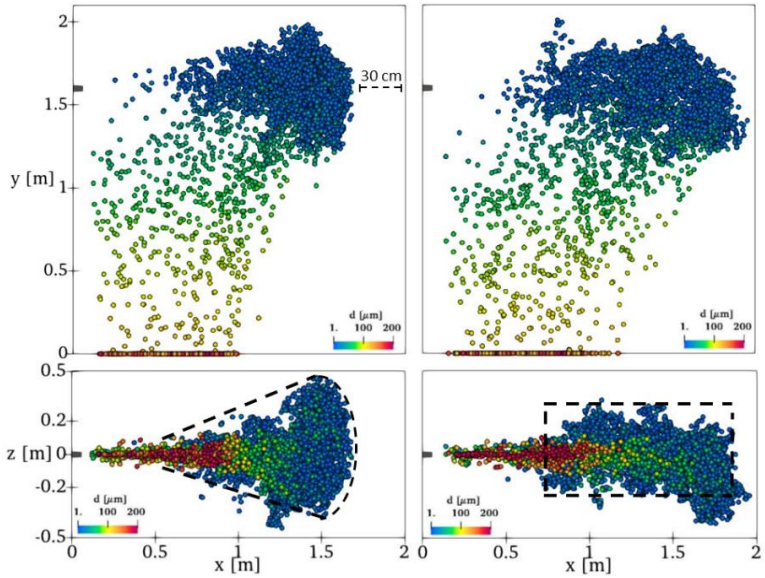

Figure 2: Particle distribution induced by a cough in the room without (left) and with (right) LSC from the side view (top) and from the top view (bottom) during the puff phase (t = 6 s).

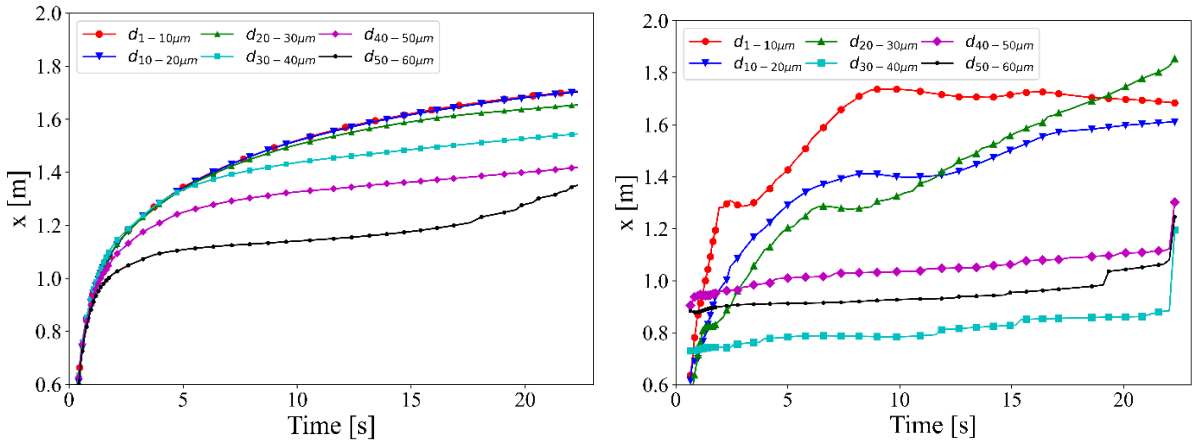

Figure 3: Horizontal coordinates of the mean trajectories of particles with sizes belonging to different bins in the LSC case, analysed by the centroid (left) and DTW (right) methods for 22 s.

Mitteilung

Fachgruppe: Allgemeine Strömungstechnik

Wechselwirkung von ausgeatmeten Aerosolpartikeln mit dem Strömungsfeld eines Luftvorhangs

Andreas Kohl, Daniel Schmeling, Claus Wagner
Deutsches Zentrum für Luft- und Raumfahrt e.V. (DLR),
Institut für Aerodynamik und Strömungstechnik
Bunsenstraße 10, 37073 Göttingen, E-mail: andreas.kohl@dlr.de

Ein wesentliches Merkmal moderner Belüftungskonzepten ist die effektive Reduzierung der Ausbreitung luftgetragener Krankheitserreger. Ein vielversprechender Ansatz zur Kontrolle und Verhinderung der Ausbreitung von pathogenbeladenen Aerosolen in Innenräumen ist der Luftvorhang, ein planarer turbulenter Freistrahl der den Luftaustausch zwischen zwei Volumina minimiert. Ein großes Anwendungsgebiet hierfür ist bisher der Gebäudesektor, wo hochfrequentierte Durchgänge in Kaufhäusern oder Kühllagern mit einem Luftvorhang ausgestattet werden um einen Temperaturausgleich zu verhindern und somit Energiekosten zu minimieren. In dieser Arbeit soll die Wechselwirkung von Aerosolpartikeln mit dem turbulenten Strömungsfeld des Luftvorhangs untersucht werden. Ein Thema, das auch im Zuge der Corona Pandemie an Interesse gewonnen hat [1]. Die Aerosolpartikel liegen im Größenbereich des menschlichen Atemaerosols und der Großteil der Partikel besitzt einen mittleren Durchmesser zwischen D_m=0,3 und 2,8µm. In diesem Größenbereich konnte ebenfalls ein Großteil der ausgeatmeten SARS-CoV-2 RNA beim Singen, Sprechen und Atmen einer infizierten Person nachgewiesen werden [2].

In der hier vorgestellten Arbeit werden zunächst das Geschwindigkeitsfeld und die erzeugte Turbulenzintensitätsverteilung für zwei unterschiedliche Volumenstrom-Konfigurationen AC_P des vertikalen Luftvorhanges mit einer Düsenbreite b_0=42mm und Länge L_0=900mm ($AC_P = 50\% \approx 320\mathrm{m^3/h}$, $AC_P = 100\% \approx 560\mathrm{m^3/h}$) vermessen. Dies erfolgt mit Hilfe von 11 Luftstrom-Sonden (Dantec 54T33), die auf zwei Linearachsen im Strömungsfeld des Luftvorhangs verfahren werden (siehe Abbildung 1 (links)). Anschließend wird der Aerosolgenerator aktiviert und ein laminarer Aerosolfreistrahl (Re_{jet}=1385) tritt mit einem konstanten Volumenstrom von 12l/min aus dem horizontalen Aerosolauslass aus (siehe Abbildung 1 (links) & (rechts, C)). Dieser hat einen Rohrdurchmesser von 12mm, so dass ein Freistrahl entsteht, dessen Impuls dem mittlere Atemimpuls eines ausatmenden Menschen gleicht.

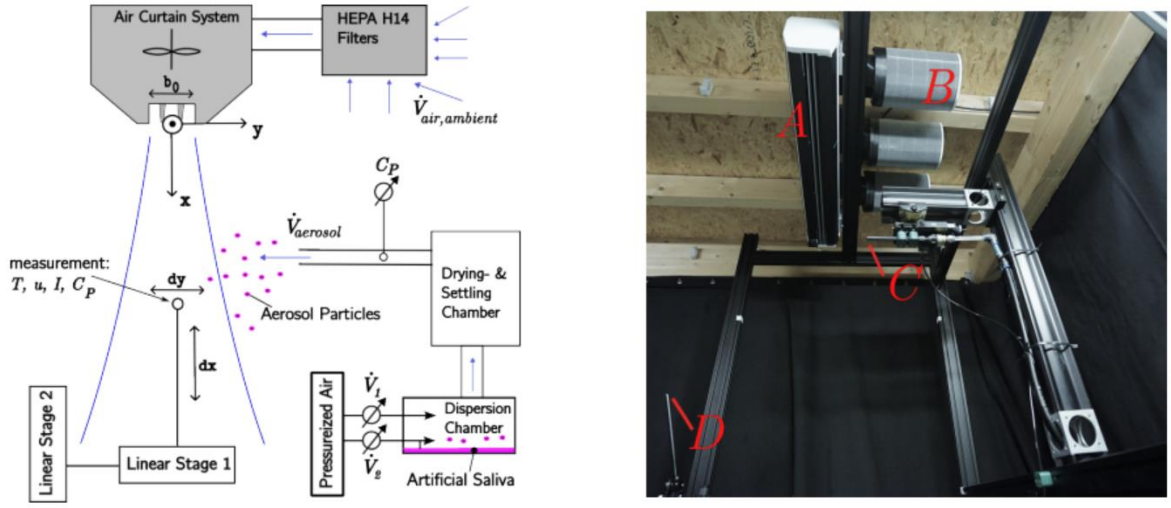

Abbildung 1: Skizze des Versuchsaufbaus mit Luftvorhang, Aerosolgenerator & Aerosolauslass, HEPA Filtern, Lineartischen und Messpositionen (links) und Bild des Versuchsaufbaus mit A) Luftvorhangsystem, B) HEPA-Filtern, C) Aerosolauslass und D) Aerosol-Probenahmerohr (rechts).

Die resultierende Partikelkonzentration wird zeitaufgelöst im Aerosolauslass und orts- und zeitaufgelöst im Luftvorhang gemessen (siehe Abbildung 1 (links)). Dazu werden zwei optische Partikelzähler (OPS3300, TSI) mit entsprechenden Verdünnungsstufen (Aerosol Diluter 3332, TSI) eingesetzt. Die ortsaufgelöste Aerosolmessung erfolgt über das Probenahmerohr in Abbildung 1 (rechts, D), welches ebenfalls über Linearführungen im Luftvorhang in x- und y-Richtung verfahren wird. Die Wirksamkeit der beiden Volumenstrom-Konfigurationen gegen Aerosolpartikeldurchdringung (in Abbildung 1 von rechts nach links) wird mit Hilfe eines von uns entwickelten partikelbasierten Luftvorhang-Effizienzmodells evaluiert. Hierbei vergleichen wir die zeitliche und räumliche mittlere Partikelkonzentration $\overline{C}_p$ vor dem Luftvorhang (y>0) mit der Konzentration hinter dem Luftvorhang (y<0):

(1)
$$\boldsymbol{E_p = 1 - \overline{C}_{p,y<0} / \overline{C}_{p,y>0}}$$

Wie in der Forschung zu planaren Freistrahlen und Luftvorhängen üblich, werden alle Längeneinheiten auf die Düsenbreite b_0 des Luftvorhanges normiert. Die Ergebnisse für die partikelbasierte Luftvorhangeffizienz E_p sind in Abbildung 2 für drei Abstände x/b_0 und die untersuchten Partikeldurchmesser D_m dargestellt. Dabei zeigt sich, dass der Luftvorhang $AC_P = 100\%$ mit dem größeren Volumenstrom eine jeweils höhere Effizienz E_p besitzt für alle Abstände x als dies für $AC_P = 50\%$ der Fall ist. Für beide AC_P −Konfigurationen nimmt E_p mit steigendem x-Abstand ab, was durch die Querdispersion der Partikel aufgrund der Turbulenzeigenschaften des Luftvorhanges erklärt werden kann. Abbildung 2 zeigt auch eine positive Korrelation zwischen dem Partikeldurchmesser D_m und E_p bei gleichem Abstand x/b_0. Mit zunehmendem Partikeldurchmesser nimmt die Wirksamkeit des Luftvorhanges gegen dessen Durchdringen durch die Mittelebene bei y=0 zu. Diese und weitere Messergebnisse, wie die Geschwindigkeits-, Turbulenz- und Partikelverteilungen im Luftvorhang, werden auf dem Workshop ausführlich vorgestellt und diskutiert.

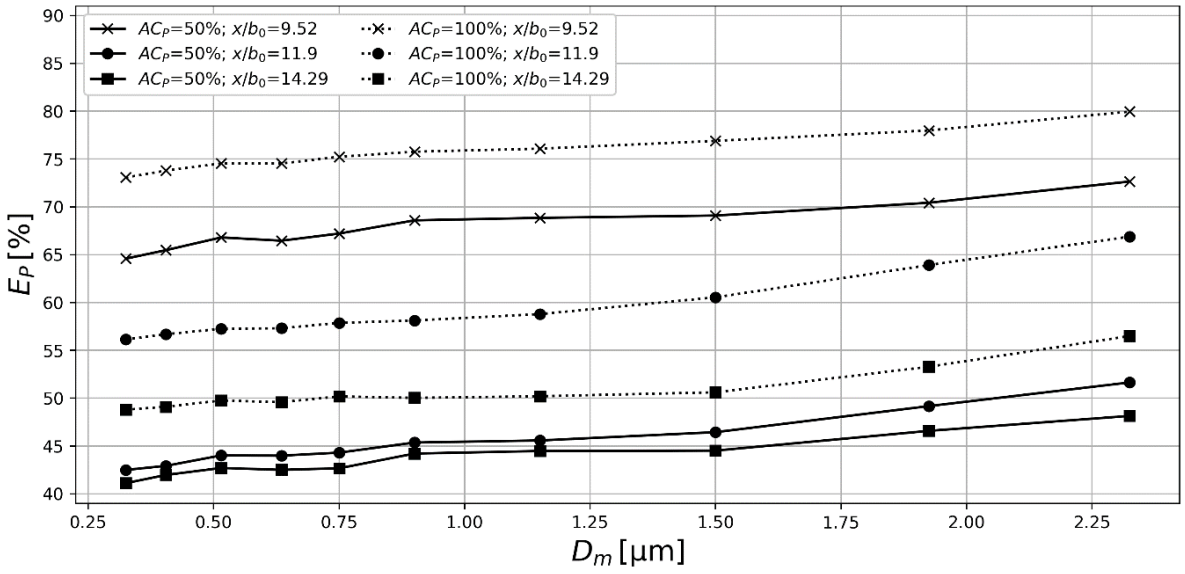

Abbildung 2: Partikelbasierte Luftvorhangeffizienz E_p für beide Luftvorhangkonfigurationen (AC_P) für drei verschiedene Abstände x/b_0 von der Düse des Luftvorhanges und variierende Partikeldurchmesser D_M.

Referenzen:

[1] Kurec K., Olszański, B; Gumowski, K; Klamka, M; Remer, M; Piechna, J.; Kubacki, S (2023): Air curtain as a SARS-CoV-2 spreading mitigation method in a small aircraft cabin. In: *Proceedings of the Institution of Mechanical Engineers, Part G: Journal of Aerospace Engineering,* 095441002311537.

[2] Alsved M., Nygren D., Thuresson S., Fraenkel C., Medstrand P., Löndahl J. (2023): Size distribution of exhaled aerosol particles containing SARS-CoV-2 RNA. In: *Infectious diseases (London, England)* 55 (2), S. 158–163.

Mitteilung

Fachgruppe: Allgemeine Strömungstechnik

Reynolds number and humidity dependency of dropwise condensation in moist convective air flows

Andreas Westhoff[1], Konstantin Niehaus[1,2], Marie Volk[1] and Claus Wagner[1,2]

[1]Institute of Aerodynamics and Flow Technology, German Aerospace Center (DLR), Göttingen (Germany)
[2]Institute of Thermodynamics and Fluid Mechanics, Technische Universität Ilmenau, Ilmenau (Germany)

Condensation and evaporation on surfaces in moist convective air flows are phase transition phenomena that occur in many technical application or in nature. An example of condensation known from our everyday life is fogging of cold surfaces such as panes or glasses, where condensation usually occurs dropwise. The water droplets lead to a change in the optical properties, which can cause problems in situations where optical transparency is significant. For instance, condensation on vehicle windows, in headlamps, or on sensors leads to safety-relevant functional restrictions [1]. Moreover, due to the strong dipole moment of the water molecules condensation and evaporation have a significant influence on the heat transfer. For heat exchangers dropwise condensation is used to enhance the heat transfer performance [2]. Furthermore, defogging of a wind shield in an electronic vehicle requires a large amount of electric energy which results in a shorter driving range [3].
In such flows, as mentioned above, the process of phase transition and the convective flow is strongly influenced by the sensible and the latent heat transfer. Additionally, the droplet shape (contact angle), the surface properties and the spatial distribution of the droplets also have a strong influence. Hence, empirical models or numerical calculations often fail to predict the heat and mass transfer due to the large number of parameters and the mutual interplay of the different heat transport mechanisms. To obtain a reliable prediction of the mass and the heat transfer, time-consuming and cost-intensive experiments or computationally expensive numerical simulations are necessary. Neither is feasible in the development and design process for industrial applications. It would be too costly and time consuming. Therefore, the method of predicting the droplet size distribution and the corresponding heat transfer by means of a scalar model is of vital interest. To overcome this issue we have been developing a prediction model based on the scaling of system characteristic numbers. Part of this approach is to investigate the effect of large-scale flow structures on the dynamics of the droplet size distribution and the corresponding sensible heat transfer and the condensation mass transfer.

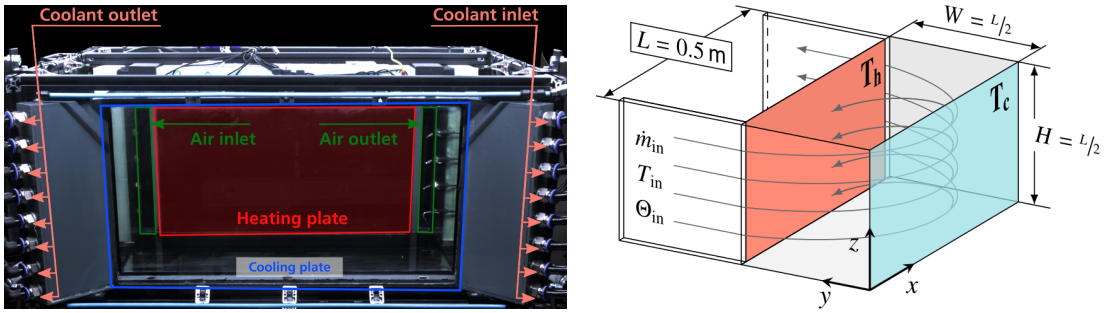

(a) photograph (front view)

(b) sketch of the container and the air flow

Figure 1: Experimental set-up: (a) photograph of the configuration with: cold wall (front), warm wall (back), air inlet (left), and air outlet (right). (b) visualisation of the primary air flow with the corresponding boundary conditions for the isothermal side walls and at the air inlet.

Therefore, measurements of dropwise condensation on a cooled surface in moist convective air flows were performed. Figure 2 shows: a photo of the setup (figure 1a) and a sketch of the container geometry with a visualisation of the bulk air flow (figure 1b). The setup consists of a rectangular box with the dimensions: length $L = 0.5\,\mathrm{m}$, width $W = 0.5 \times L$, and height $H = 0.5 \times L$ with an isothermally cooled front wall and a heated rear wall. All other side walls are adiabatic. The forced flow is supplied

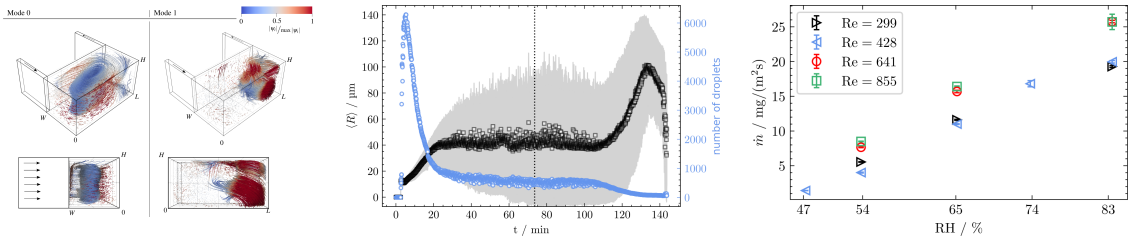

(a) coherent structures (b) particle size (c) mass flow

Figure 2: Topology of the first two POD modes revealing the predominant coherent flow structures. (b) Mean size and standard deviation of the particle size distribution and the corresponding number of droplets as a function of time for condensation and evaporation. (c) Mass flow of water due to phase transition as a function of time.

by an air inlet on the left and an outlet on the right side. Both slots span the full height and have a width of $W_{\text{slot}} = 0.05 \times L$. The inflow conditions are constant in terms of moist air mass flow $\dot{m}_{\text{in}}$, temperature $\dot{T}_{\text{in}}$ and dew point $\dot{\Theta}_{\text{in}}$. In order to measure the system relevant properties the setup is equipped with a plethora of temperature and humidity sensors. Furthermore, time-resolved velocity measurements for the three-dimensional flow field as well as optical measurements for the droplet size distribution on the cold surface were applied. Details of both measurement configurations can be found in Niehaus et al. [4] and Volk et al. [5].

Figure 1 depicts sample results of the flow and particle size measurements. With the objective to characterise the large-scale flow structures and to identify the influence of these structures on the heat and mass transfer an analysis of the velocity vector fields is performed by means of a proper orthonormal decomposition (POD). The topology from the POD calculation for the first two modes is imaged in figure 2a for $\mathcal{R}e = 254$, where the Reynolds number is defined as $\mathcal{R}e = \dot{m}_{\text{in}}/\nu H$ and ν is the dynamic viscosity. The mode $n = 0$ represents the dominant flow structure resulting from the forced convection. Air enters the container through the inlet follows the left wall, detaches, flows over the cold front, and detaches again. The flow then splits into two parts: one part leaves the container through the outlet and the other part flows along the heating plate, detaches and mixes with the air from the inlet. As a result, a large-scale circulation is developed in the bulk. Further, a second large-scale coherent structure is identified. Here, mode $n = 1$ is associated with the vortex located in the right front corner. These two structures have a significant impact on the vapour mass transfer $\dot{m}_v$ as well as on the particle size distribution, while the structure itself depends on $\mathcal{R}e$. Figure 2b shows the mean particle size (black squares) and the corresponding standard deviation (grey) of the particle size distribution for an evaluation area of $3.97\,\text{mm} \times 3.29\,\text{mm}$ for condensation (left of the dashed line) and evaporation (right side). Finally, figure 2c depicts the mass flow as a function of the relative humidity $RH = p_v/p_s$, where p_v and p_s denote the partial and the saturation vapour pressure, respectively. Here, the plot clearly reveals a scaling of the latent heat transfer and a $\mathcal{R}e$-dependency.

Based on these analyses, we will present a discussion on the scaling of sensible and latent heat transfer for dropwise condensation as a function of $\mathcal{R}e$ and RH. In addition, we will provide a brief introduction to the measurement techniques used.

[1] Matthias G Ehrnsperger, Uwe Siart, Michael Moosbühler, Emil Daporta, and Thomas F Eibert. Signal degradation through sediments on safety-critical radar sensors. *Advances in Radio Science*, 17:91–100, 2019.

[2] Dong Ho Nguyen and Ho Seon Ahn. A comprehensive review on micro/nanoscale surface modification techniques for heat transfer enhancement in heat exchanger. *International Journal of Heat and Mass Transfer*, 178:121601, 2021.

[3] Sun-Ik Na, Yoong Chung, and Min Soo Kim. Performance analysis of an electric vehicle heat pump system with a desiccant dehumidifier. *Energy Conversion and Management*, 236:114083, 2021.

[4] Konstantin A Niehaus, Andreas Westhoff, and Claus Wagner. Characterization of a mixed convection cell designed for phase transition studies in moist air. In *New Results in Numerical and Experimental Fluid Mechanics XIII: Contributions to the 22nd STAB/DGLR Symposium*, pages 483–493. Springer, 2021.

[5] Marie-Christine Volk, Konstantin A Niehaus, Andreas Westhoff, and Claus Wagner. Automated measurement of the number and growth of water droplets in mixed convection. In *23rd STAB/DGLR Symposium on New Results in Numerical and Experimental Fluid Mechanics*, 2022.

Mitteilung

Fachgruppe: Bio- und Mikrofluidmechanik

Einfluss der rheologischen Eigenschaften des respiratorischen Mukus auf die scherinduzierte Erzeugung von Aerosolpartikeln in den Atemwegen

Johanna Michel, Sandra Melina Tauwald, Lars Krenkel
johanna.michel@oth-regensburg.de
Ostbayerische Technische Hochschule Regensburg, Labor für Biofluidmechanik, Galgenbergstr. 30, 93053 Regensburg
Regensburg Center of Health Sciences and Technology (OTH Regensburg) und
Regensburg Center of Biomedical Engineering (OTH und Universität Regensburg)

Über die Entstehung von Aerosolen im menschlichen Atemtrakt ist trotz ihrer großen Bedeutung als potenzielle Träger von Infektionskrankheiten wenig bekannt. Die Partikel haben ihren Ursprung in den Flüssigkeiten, die die Oberflächen der elastischen luftleitenden Atemwege auskleiden. In der Luftröhre und bis zur 17. Verzweigung der Lunge ist dies eine komplexe, nicht-Newton'sche, viskoelastische Flüssigkeit, die als respiratorischer Mukus oder Airway Surface Liquid bezeichnet wird.
In den oberen Atemwegen entsteht Aerosol bei Husten und forciertem Ausatmen über einen scherinduzierten Mechanismus. Hierbei induziert der Luftstrom Scherspannungen im Mukus. Dies führt zur Bildung von Wellen und löst Aerosolpartikel aus der Mukusoberfläche [1]. Hierbei scheinen neben der anliegenden Scherrate auch die rheologischen Eigenschaften und Oberflächeneigenschaften des Mukus einen entscheidenden Einfluss auf die Partikelentstehung zu haben [2]–[4].

Ziel des vorgestellten Projektes ist die systematische Untersuchung des Einflusses der rheologischen Eigenschaften des Mukus auf die Größe und Menge der Aerosolpartikel, die durch die Scherströmung aus dem Mukus an den Oberflächen der oberen Atemwege erzeugt werden. Um den Einfluss der Rheologie des Mukus von der Vielzahl anderer im Körper vorherrschender Einflussfaktoren zu trennen, wird die Entstehung von Aerosolpartikeln isoliert experimentell betrachtet. Hierfür wird eine Luftströmung über eine isolierte, benetzte Oberfläche geleitet. Herausgelöste Aerosole werden bezüglich ihrer Menge und Größenverteilung analysiert.

Da es nicht möglich ist, ausreichend große Mengen humanen Mukus mit konsistenten, homogenen Eigenschaften zu sammeln, wird zunächst ein Ersatzfluid für humanen Mukus ent-

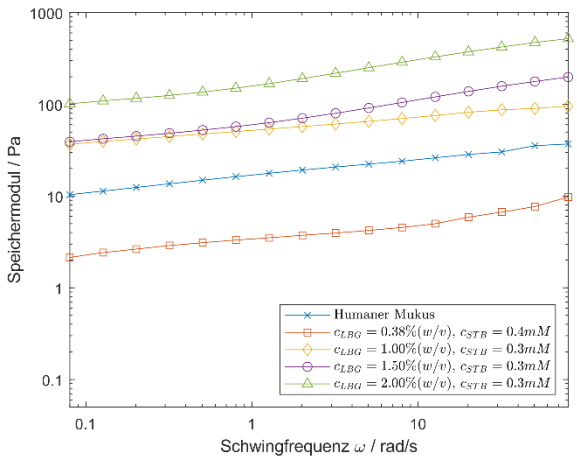

Abb. 1a) Speichermoduli

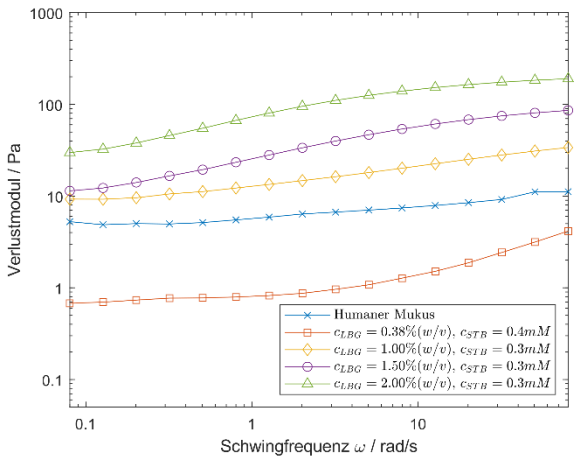

Abb. 1b) Verlustmoduli

Abb. 1 Verhalten von Mukus-Ersatzfluiden mit unterschiedlicher Konzentration der Einzelbestandteile (cLBG: Konzentration Johannisbrotkernmehl, cSTB: Konzentration Natriumtetraborat) im Vergleich zum Verhalten von humanem Mukus im Frequenz-Sweep Test

Abb. 2 Schematische Darstellung des Aufbaus zur Analyse der scherinduzierten Erzeugung von Aerosolpartikeln

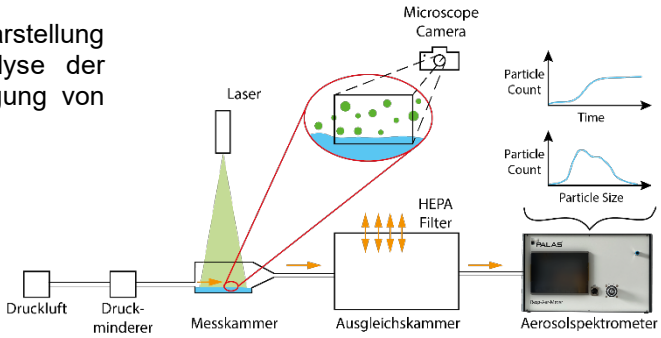

wickelt. Dieses Ersatzfluid besteht aus destilliertem Wasser, Johannisbrotkernmehl und Natriumtetraborat ([2], [5], [6]). Zur Einstellung der rheologischen Eigenschaften des Ersatzfluides werden die Konzentrationen von Johannisbrotkernmehl (c_{LBG}) und Natriumtetraborat (c_{STB}) variiert. Zur Einstellung der Oberflächenspannung werden Tenside zugegeben. Die Eigenschaften des Ersatzfluides werden anschließend in einem Rheometer (Discovery HR 30, TA Instruments, New Castle, USA) vermessen. Referenz für die Entwicklung des Ersatzfluides sind Daten aus der Charakterisierung von physiologischem, humanen Mukus aus Vorarbeiten unserer Gruppe. Durch die Variation der Konzentration der Einzelbestandteile kann das rheologische Verhalten der Ersatzfluide erfolgreich angepasst und so an das Verhalten von humanem Mukus angenähert werden. Abb. 1 zeigt das Verhalten von Ersatzfluiden mit unterschiedlichen Konzentrationen im Vergleich zum Verhalten von humanem Mukus im Frequenz-Sweep Test.

Abb. 2 zeigt den experimentellen Aufbau zur Analyse der scherinduzierten Aerosolentstehung. Hierfür wird das Ersatzfluid auf die Bodenfläche einer Messkammer aufgebracht. Eine Luftströmung über die Fluidoberfläche simuliert den Luftstrom während der Atmung. Die Messkammer und ihre Zu- und Abläufe werden optimiert mit dem Ziel, Ablösungen an der Probenoberfläche zu vermeiden. Der Druck vor der Messkammer wird mit einem Druckminderer so eingestellt, dass die Strömung an der Probenoberfläche ähnliche Scherraten aufweist, wie sie in den menschlichen Atemwegen auftreten. Aus dem Ersatzfluid ausgelöste Partikel werden mit einem Aerosolspektrometer (Resp-Aer-Meter Scientific, Palas GmbH, Karlsruhe, Deutschland) bezüglich ihrer Größe und ihrer Anzahl über den Verlauf der Messung analysiert. Das Aerosolspektrometer saugt dabei Luft mit einem Volumenstrom an, der sich in der Regel von dem Volumenstrom unterscheidet, mit dem die Strömung die Messkammer passiert. Um diese unterschiedlichen Volumenströme auszugleichen, ist zwischen der Messkammer und dem Aerosolspektrometer eine Ausgleichskammer angeordnet. In dieser kann ein Ausgleich mit der Umgebung über HEPA-Filter erfolgen, ohne dass zusätzliche Partikel in das System eingebracht werden.

Die in den Versuchsaufbau integrierte optische Messtechnik ermöglicht es, den scherinduzierten Entstehungsvorgang der Partikel aus dem Ersatzfluid zu analysieren. Dabei spannt ein Laser, ausgestattet mit einer Lichtschnittoptik, eine vertikale Ebene innerhalb der Messkammer auf. Die durch die Partikel erzeugten Reflektionen werden anschließend während ihres Entstehungsvorgang in der Ebene über ein Mikroskop unter 250-facher Vergrößerung sichtbar gemacht.

[1] P. J. Basser, T. A. McMahon, and P. Griffith, “The Mechanism of Mucus Clearance in Cough,” *J. Biomech. Eng.*, vol. 111, no. 4, pp. 288–297, Nov. 1989, doi: 10.1115/1.3168381.

[2] A. Hasan, C. F. Lange, and M. L. King, “Effect of artificial mucus properties on the characteristics of airborne bioaerosol droplets generated during simulated coughing,” *J. Non-Newton. Fluid Mech.*, vol. 165, no. 21, pp. 1431–1441, Nov. 2010, doi: 10.1016/j.jnnfm.2010.07.005.

[3] R. Hamed, D. M. Schenck, and J. Fiegel, “Surface rheological properties alter aerosol formation from mucus mimetic surfaces,” *Soft Matter*, vol. 16, no. 33, pp. 7823–7834, Aug. 2020, doi: 10.1039/D0SM01232G.

[4] M. Vasudevan and C. F. Lange, “Property dependence of onset of instability in viscoelastic respiratory fluids,” *Int. J. Eng. Sci.*, vol. 43, no. 15, pp. 1292–1298, Oct. 2005, doi: 10.1016/j.ijengsci.2005.05.004.

[5] A. J. Ragavan, C. A. Evrensel, and P. Krumpe, “Interactions of Airflow Oscillation, Tracheal Inclination, and Mucus Elasticity Significantly Improve Simulated Cough Clearance,” *Chest*, vol. 137, no. 2, pp. 355–361, Feb. 2010, doi: 10.1378/chest.08-2096.

[6] W. Watanabe *et al.*, “Why inhaling salt water changes what we exhale,” *J. Colloid Interface Sci.*, vol. 307, no. 1, pp. 71–78, Mar. 2007, doi: 10.1016/j.jcis.2006.11.017.

Mitteilung

Fachgruppe: Bio- und Mikrofluidmechanik

CFD-basierte Modellierung des absoluten Infektionsrisikos durch aerosolübertragene Krankheitserreger

Florian Webner[1], Daniel Schmeling[1], Claus Wagner[1,2]
1) Deutsches Zentrum für Luft und Raumfahrt e.V.,
Institut für Aerodynamik und Strömungstechnik, Göttingen
2) Technische Universität Ilmenau,
Institut für Thermo- und Fluiddynamik, Ilmenau

Florian.Webner@dlr.de

Die COVID-19-Pandemie hat in den Jahren 2020 - 2023 enorme menschliche und finanzielle Verluste verursacht. Zudem haben die Schutzmaßnahmen zur Eindämmung des Infektionsgeschehens die Freiheit der Bevölkerung im Alltag eingeschränkt. Auch wenn die Immunisierung der Bevölkerung durch Infektionen und Impfungen die Krankheitslast zuletzt deutlich reduziert hat, muss mit neuen Mutationen oder gänzlich neuen Erregern gerechnet werden, die erneut eine Pandemie auslösen können. Um dann Schutzmaßnahmen gezielt einsetzen zu können, müssen zunächst die Hotspots der Übertragungen identifiziert werden. In einem zweiten Schritt können dann technische Hilfsmittel oder Verhaltensregeln eingesetzt werden. Da technische Hilfsmittel teuer sein können und Verhaltensregeln möglicherweise die Freiheit der Betroffenen einschränken, sollte die Wirksamkeit dieser Maßnahmen überprüft werden, bevor sie für Millionen von Menschen verpflichtend eingeführt werden.
Mit Hilfe von Infektionsrisikomodellen, kann das Infektionsrisiko in verschiedenen Situationen – z. B. in einer Bar und in einem Fernzug – verglichen werden, um Hotspots der Übertragungen zu identifizieren. Darüber hinaus können Infektionsrisikomodelle verwendet werden, um die Wirksamkeit von Gegenmaßnahmen abzuschätzen.
Im Workshop wird vorgestellt, wie das Infektionsrisiko durch Aerosole modelliert werden kann. Dabei werden relevante Prozesse wie Exhalation, Transport, und Inhalation von Viren erläutert, die in *Abbildung 1* dargestellt sind.

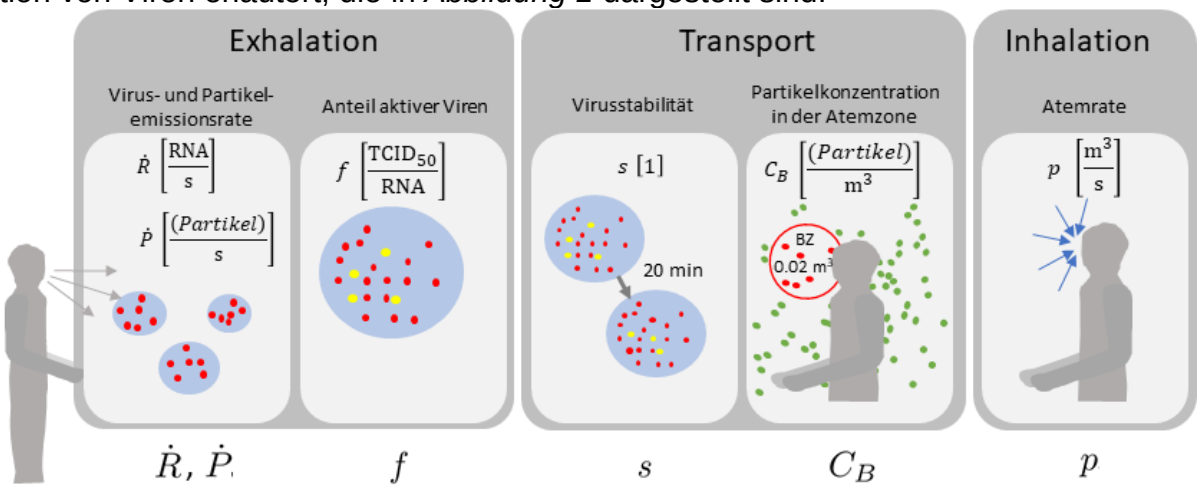

Abbildung 1: Prozesse zur Bestimmung der inhalierten infektiösen Dosis.

Mit der Virus-Emissionsrate $\dot{R}$ und der Partikel-Emissionsrate $\dot{P}$, kann die Anzahl der Viren pro Partikel bestimmt werden. Mit dem Anteil aktiver Viren *f* kann dann die Anzahl aktiver Viren pro Partikel nach der Exhalation berechnet werden.
Eine weitere Multiplikation mit der der Virusstabilität *s* ergibt die Anzahl aktiver Viren pro Partikel nach dem Transport in die Atemzone des Empfängers. Die Partikelkonzentration in der Atemzone C_B multipliziert mit der Atemrate des Empfängers *p*, ergibt die Inhalationsrate der Partikel. Multipliziert mit der zuvor bestimmten Anzahl aktiver Viren pro Partikel, ergibt sich die Inhalationsrate aktiver Viren. Eine weitere Multiplikation mit der Zeit, ergibt schließlich die inhalierte Dosis aktiver Viren.
Zur Bestimmung von C_B und *s* wird eine stationäre Reynolds-Averaged Navier-Stoke (RANS)-Simulation durchgeführt. Ausgangspunkt ist die Geometrie einer vollbesetzten Do728 Flugzeugkabine einschließlich Geschwindigkeits- und Temperaturrandbedingungen, auf deren Basis das statistisch gemittelte Strömungsfeld berechnet wird. Anschließend wird in einer instationären Simulation der Partikeltransport unter Berücksichtigung von Gewichtskraft, Trägheitskraft, turbulenter kinetischer Energie und strömungsmechanischem Widerstand der Aerosolpartikel vorhergesagt. Die Zeit, die die Partikel benötigen, um die Atemzone zu erreichen, wird ebenfalls bewertet, um schließlich die Inaktivierung der Viren als Funktion der Zeit zu modellieren.
Mit Hilfe einer Dosis-Wirkungs-Beziehung kann aus der inhalierten Dosis das Infektionsrisiko abgeschätzt werden. Die Dosis-Wirkungs-Beziehung wird hier aus den Daten einer Human Challenge, d.h. einer Studie, in der Freiwillige kontrolliert infiziert werden, konstruiert. Die Human Challenge wurde von Killingley et al. (2022)[1] durchgeführt, bei der 34 junge, gesunde Personen mit einer Dosis von zehn 50 % Tissue Culture Infectious Dose ($TCID_{50}$) SARS-CoV-2 inokuliert wurden. 18 der 34 Teilnehmenden (52,9 %) infizierten sich. Unter der Annahme, dass jedes aktive Virus die gleiche Wahrscheinlichkeit hat, jemanden zu infizieren, ergibt sich folgendes Infektionsrisiko *I*:

$$I = 1 - e^{-0.0754 D_{in}} \quad (1)$$

Abbildung 2 zeigt das vorhergesagte Infektionsrisiko in der Flugzeugkabine der Do728, für $\dot{R} = 500$ RNA/s, $f = 10^{-6}$ $TCID_{50}$/RNA, $p = 10^{-4}$ m^3/s (=6 l/min) und $t = 120$ min. Die Ergebnisse zeigen, dass die Infektionsrate der Human Challenge zur Modellierung des Infektionsrisikos verwendet werden kann. Darüber hinaus wird gezeigt, dass, obwohl Infektionen in der Kabine auch in größerer Entfernung von der Indexperson (IP) möglich sind, das Infektionsrisiko in der Nähe der IP jedoch signifikant erhöht ist.

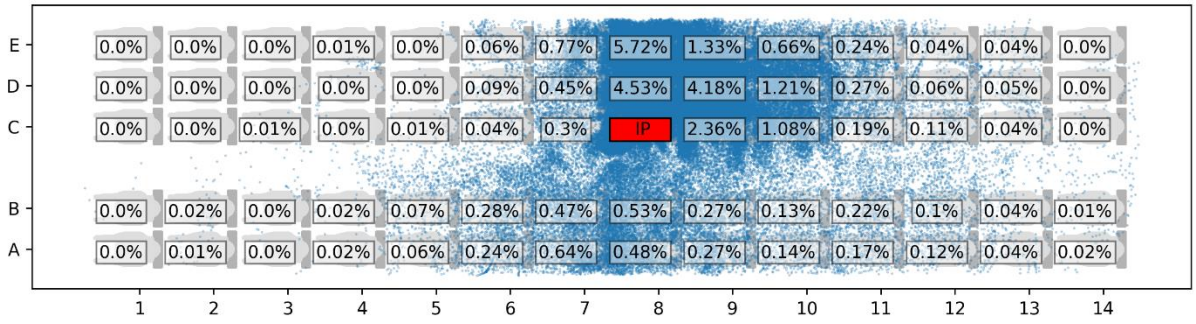

Abbildung 2: Infektionsrisiko für einzelne Passagiere nach 120 min mit der Indexperson (IP) auf Sitz 8C.

Referenzen

[1] B. Killingley, A. J. Mann, M. Kalinova, A. Boyers et al. „Safety, Tolerability and Viral Kinetics during SARS-CoV-2 Human Challenge in Young Adults", Nature Medicine, vol. 28, no 5, pp. 1031-1041, 2022.

Mitteilung

Fachgruppe: Drehflügler

Aeroelastic Dynamic Stall Computations of Double-Swept Rotor Blade Using a Weak Coupling Scheme

Georg Babij
German Aerospace Center (DLR), Institute of Aeroelasticity, 37073 Göttingen
georg.babij@dlr.de

Figure 1: Rotor Test Facility Göttingen with four-bladed rotor

High-fidelity aeroelastic simulations of rotor systems are carried out at the Institute of Aeroelasticity at the German Aerospace Center (DLR) by coupling numerical solvers for computational fluid dynamics (CFD) and multibody systems (MBS) with each other, namely the DLR TAU-Code on CFD side as well as Simpack on MBS side. In order to achieve this, data is exchanged between both solvers including in general aerodynamic forces and structural displacements. In the past, previous simulations utilized a strong coupling scheme [1] which denotes in the terminology used within the rotorcraft community an exchange of data in each physical time step and is mainly suited for time accurate simulations. While seeking for a periodic steady state solution, e.g. a helicopter in forward or hovering flight, the precise simulation of transients is of minor importance and the minimisation of wall-clock time in the simulation chain comes to the fore. Without affecting the solvers' algorithms, the latter is achieved first and foremost by reducing the overhead resulting from frequent data exchange and extensive switching between both solvers. Therefore, a weak coupling scheme for rotor sytems between CFD and MBS is presented and applied to a model rotor with double swept blades. The term denotes in the terminology used within the rotorcraft community an exchange of data being collected over one rotor revolution. For this purpose, an iteration step includes the calculation of the aerodynamic forces as well as the structural displacements and rigid body motions for an entire rotor revolution, respectively with TAU and Simpack. On MBS side, a periodic steady-state is ensured in the solution by performing a time integration over multiple revolutions. By this means, transients have been decayed towards the last calculated period which is taken for evaluation. Against this background, data transmission now takes places in a bundled form in order to reduce function calls serving initialisation purposes in the CFD and MBS solver.
In addition to the aeroelastic simulations with the aforementioned weak coupling scheme, a comparison with a strong coupling scheme is intended. For this purpose, strongly coupled simulations have already been performed for a model rotor with a double-swept blade in four-bladed configuration [1]. They are related to dynamic stall experiments being carried out at the Rotor Test Facility Göttingen (RTG) [2] which is depicted in Fig. 1. The rotor radius amounts to 652 mm. The blades measure 541 mm and 72 mm in length and chord at the root, respectively [3]. Due to an axial inflow to the rotor the dynamic stall phenomenon is triggered once per revolution by a sinusoidal variation in pitch angle Θ. This results in a periodic steady state in the fields of aerodynamics and structural dynamics involving strong non-linearities.

Numerical modelling

The weak coupling scheme is a partitioned approach based on a data exchange of an entire rotor revolution. In detail, over one rotor revolution gathered aerodynamic forces being calculated by TAU are transferred to Simpack and, vice versa, gathered structural displacements along with rigid body motions are transferred from Simpack back to TAU. In order to exchange this data between both differently discretized domains, i.e. between the CFD surface grids and the markers of the MBS substructures, scattered data interpolation methods based on radial basis functions are exploited. The entire procedure is illustrated by means of the eXtended

Strucure Design Matrix (XDSM) in Fig. 2. Furthermore, an azimuthal discretization of $\Delta\Psi = 1°$ is chosen in this study which results in a physical time step approximately $\Delta t \approx 1.177 \cdot 10^{-4}$ s for a rotor speed of $f = 23.6$ Hz.

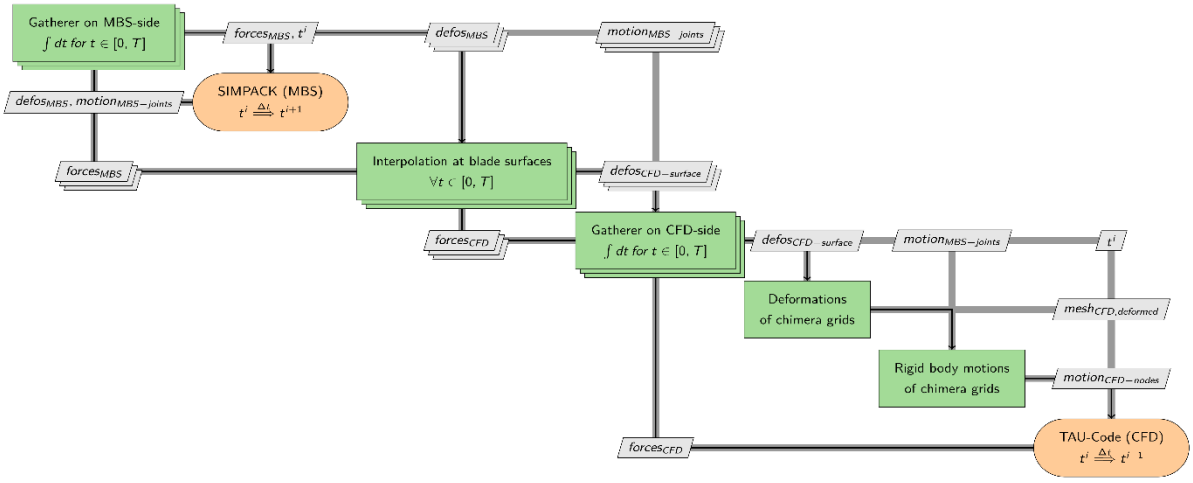

Figure 2:Weak coupling scheme (eXtended Design Structure Matrix)

Simpack is used to describe the structural dynamics of the entire rotor by means of a multibody system. In order to take flexible blades into account, their structural displacements are described in a modal representation with an underlying linear elastic material behaviour. Stiffening effects occurring due to centrifugal forces are considered by a geometric stiffness matrix. The entire MBS configuration of the rotor modelled in Simpack can be seen in Fig. 3.

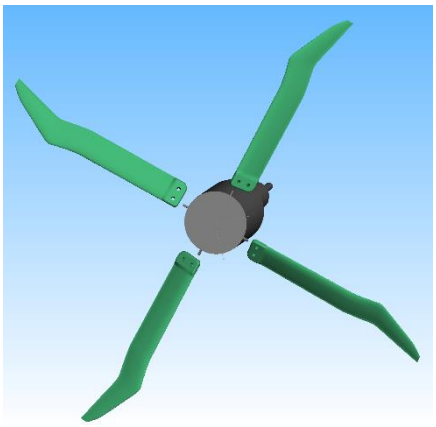

Figure 3: Modelling of structural dynamics in Simpack

TAU utilizes the Reynolds-Averaged-Navier-Stokes equations to model fluid flow by means of a vertex-centered finite volume method implemented for unstructured grids. Due to the unknown Reynolds stresses turbulence models are applied, such as the SST-k-ω-model according to Menter in this study. Taking into account grid motion and deformation, the Chimera technique as well as the geometric conservation law are exploited. The primary grid contains approximately 13.555 million nodes and it consists of a background grid as well as four chimera grids representing the blades.

Numerical investigations and comparison with results of a strong coupling scheme

Several test cases with a rotor speed of $f = 23.6$ Hz will be presented comprising operating conditions with a collective pitch angle $\Theta_{coll} \in \{17°, 24°, 27°\}$ superposed by a cyclic sinusoidal variation in pitch angle $\Theta_{cyc} \in \{6°, 8°\}$. Thereby, the dynamic stall phenomenon is induced and gradually strengthened which consequently results in increasing non-linearities in the periodic solutions. Forces acting normal to the planform of a blade F_n as well as pitch moments M_y are monitored and the structural displacements are extracted at the blade tips. They serve as a comparison to previous simulations based on a strong coupling scheme. Finally, the performance of the weak coupling scheme will be discussed regarding convergence behaviour and other criteria.

References

1. Babij, G.: *Dynamic Stall Computations of a Double-Swept Rotor Blade with Rigid and Elastic Modelling.* 23rd STAB-Symposium 2022, 9.-10. Nov 2022, Berlin, Germany, https://elib.dlr.de/190997/
2. Schwermer, T., Richter, K., Raffel, M.: *Development of a Rotor Test Facility for the Investigation of Dynamic Stall (2016)*, https://elib.dlr.de/91322
3. Müller, M.M., Schwermer, T., Mai, H., Stieg, C.: *Development of an innovative double-swept rotor blade tip for the rotor test facility Goettingen*. In: DLRK 2018 Deutscher Luft- und Raumfahrtkongress (Sep 2018), https://elib.dlr.de/122702

Mitteilung

Fachgruppe: Drehflügler

Towards Tip Vortex Measurements on Rotors in the
High Pressure Wind Tunnel Göttingen (HDG) of the DLR

Hauke T. Bartzsch, C. Christian Wolf, Anthony Gardner, Marc Braune, Markus Löhr
German Aerospace Center, Bunsenstr. 10, 37073 Göttingen, Germany, hauke.bartzsch@dlr.de

Introduction

The wake of a helicopter rotor features vortices originating from the blade tips. The vortices are relevant for the rotor noise and rotor performance, hence, the analysis of their propagation, growth and decay is of particular interest. It is widely believed that the vortex Reynolds number, defined as the ratio of the vortex circulation to the fluid viscosity, is an important factor in this process. Being related to turbulence and instability mechanisms, the Reynolds number effect on the vortex evolution is difficult to capture in numerical simulations. Therefore, experiments with a variation of the Reynolds number are required.
Atmospheric subscale test facilities cannot reproduce the Reynolds numbers encountered on full-size helicopter rotors due to size limitations, whereas field measurements on free-flying helicopters are affected by the engine exhaust flow, wind gusts, blockage of the fuselage, tail rotor, etc. Furthermore, neither approach enables a variation of the Reynolds number independently of the rotational speed and the rotor dimensions. Therefore, we chose DLR's High Pressure Wind Tunnel Göttingen (HDG) for measurements with a varying Reynolds number. The current work discusses the experimental methodology and sample results from a pretest.

Experimental Setup

The HDG is a closed-loop wind tunnel which can be pressurized up to 100 bar. The test section has a 0.6 m x 0.6 m cross-section and can be accessed through an air lock while keeping the tunnel itself pressurized. Optical access is given by two portholes in the sidewall and one porthole in the ceiling of the test section. A "C"-shaped support structure is placed in the test section, with a cylindrical tube stretching in upstream direction and serving as a rotor mount. The tube has an outer diameter of 75 mm and a length of 750 mm. It is equipped with load cell with thermal insulation, a 4.5 kW motor, and temperature/vibration monitoring.
The tip vortices were visualized using Background Oriented Schlieren (BOS). The system consists of a pressure-resistant LED array mounted on top of the test section and inside the pressure hull, a retroreflective background with a random dot pattern (D = 0.1 mm) on the floor of the test section, and two cameras (pco.panda 26, f = 85 mm, sampled at 6 fps, 0.2 m x 0.4 m combined field of view) outside of the pressure hull and close to the top porthole, see Fig.1.

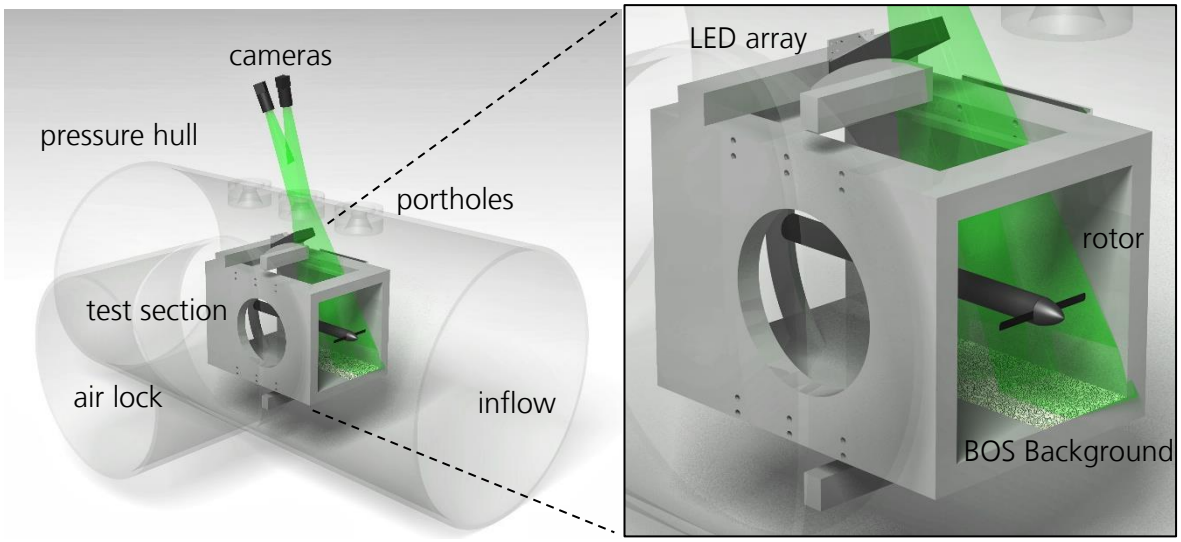

Figure 1: HDG test section with rotor assembly and instrumentation; camera view field in green

In the current pretests, the wind tunnel flow was switched off, and the rotors were operated in hover-like conditions. Due to safety concerns, the rotor was placed upstream of the glass windows. Hence, the cameras had to be slightly tilted in forward direction, viewing the wake downstream of the rotor plane. The BOS cameras were triggered by a light barrier for phase-locked Schlieren images of the vortex

system. The BOS sensitivity, defined as the relation of pixelwise displacement on the camera sensor to an observed density gradient, is approximately proportional to $(1/Z_D + 1/Z_A)^{-1} L_{Fov}^{-1}$. Z_D and Z_A are the camera-to-density-object and density-object-to-background distances, respectively. L_{Fov} is the size of the field of view. In the current setup, the sensitivity is limited by the short observation distances, and the tip vortices could only be visualized with a sufficient signal-to-noise ratio for tunnel pressures of about 14 bar and above. Higher tunnel pressures also lead to higher thrust values, which increases the accuracy of the thrust measurement.

Sample Results and Discussion

Data was taken at 16 bar, 32 bar and 64 bar and rotational speeds between 1000 rpm and 5000 rpm. For the current pretests, three different off-the-shelf model airscrews with a radius of R = 0.15 m, a chord length of C = 25 mm at a radial position of r/R = 0.75 and different blade pitch angles were selected as rotors (Master Airscrew Carbon 12x4″, 12x6″ and 12x8″). Operation at high tunnel pressures led to a strong deformation of the rotors. Later tests will use much stiffer DLR-designed model rotors milled from aluminum.

The blade tip vortices were remarkably stable even for the highest tunnel pressure, yielding a chord-based Reynolds number of $Re_{C,0.75}$ = 7x10^6 at r/R = 0.75. For the observed vortex ages from ζ = 0° to about ζ = 1200°, no pronounced vortex instabilities were identified, see Fig. 2.

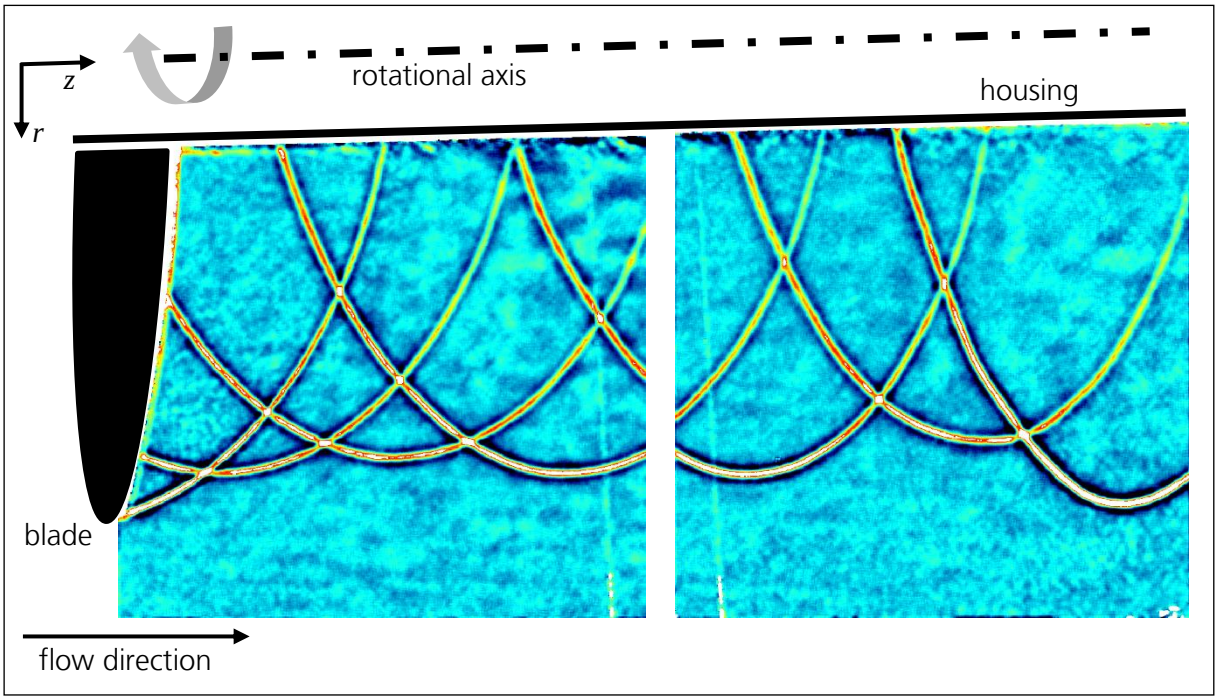

Figure 2: BOS sample result, 2D-Divergence of the BOS displacement; Master Airscrew Carbon 12x6″ at 5000 rpm, wind tunnel pressure of 16 bar

Fig. 3 shows the rotor thrust coefficient, C_T, as a function of the chord-based Reynolds number. The data comprises the different tunnel pressures and different rotor rpm for the lowest-pitch rotor, 12x4″. The deformation of the higher-pitched rotors, 12x6″ and 12x8″, was too large to result in meaningful and reliable thrust data.

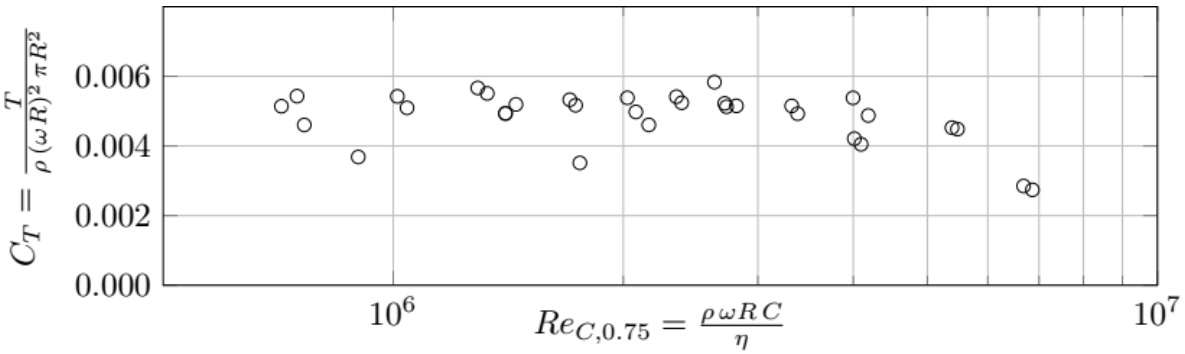

Figure 3: Thrust coefficient over $Re_{C,0.75}$, for the 12x4″ rotor

Mitteilung

Fachgruppe: Drehflügler

Analysis of Configurational Parameters on the Vortex System of a Rotor

Alexander Heintz, Clemens Schwarz, C. Christian Wolf and Markus Raffel
German Aerospace Center, Bunsenstr. 10, 37073 Göttingen,
alexander.heintz@dlr.de, clemens_a.schwarz@web.de, christian.wolf@dlr.de,
markus.raffel@dlr.de

Introduction

The wake of a rotor is a complex three-dimensional flow, which is dominated by unsteady aerodynamic effects. In general, the wake is characterized by the helix-shaped trailing blade tip vortices, the blade shear layers, the rotor-induced downwash velocity field and the external flow conditions. The interaction of these mechanisms results in the breakdown of the vortex system with its downward propagation. The blade tip vortices, which are initially well defined, begin to decompose with increasing wake age. Due to its complexity, the numerical simulation of this breakdown is still challenging and therefore part of current research activities. The vortex interaction and decomposition are highly relevant to the efficiency and noise development of rotors, especially for hover flight cases. Accordingly, these effects need to be investigated in detail. In recent publications additional s-shaped vortex worms, in between the blade tip vortices, were observed. A so formed vortex system is sketched in Fig. 1a. This presentation will also focus on their contribution to vortex breakdown.

Experimental Setup

The experiments were conducted at the Hover Test Stand (HVG) of the German Aerospace Center in Göttingen. It was designed to investigate the aerodynamics of an isolated rotor in hover out of ground effect. This facilitates an easier comparability with numerical methods, in particular for a detailed comparison of the vortex decomposition.
The rotor is mounted on a solid support structure with a built-in electric traverse system to change the height of the rotor plane, see Fig. 1b label 2. This allows for a measurement in different axial distances from the rotor without changing the PIV setup. In order to change the tip vortex spacing, the mounted rotor head allows to vary the blade number to one, two and four blade configurations. For force and torque measurements a six-component piezoelectric balance is mounted directly below the propulsion system.
To measure both, primary and secondary vortices, instantaneous flow fields were acquired in two perpendicular PIV planes, as sketched in Fig. 1b with the corresponding laser light sheets. As shown in Fig. 1a, the secondary structures

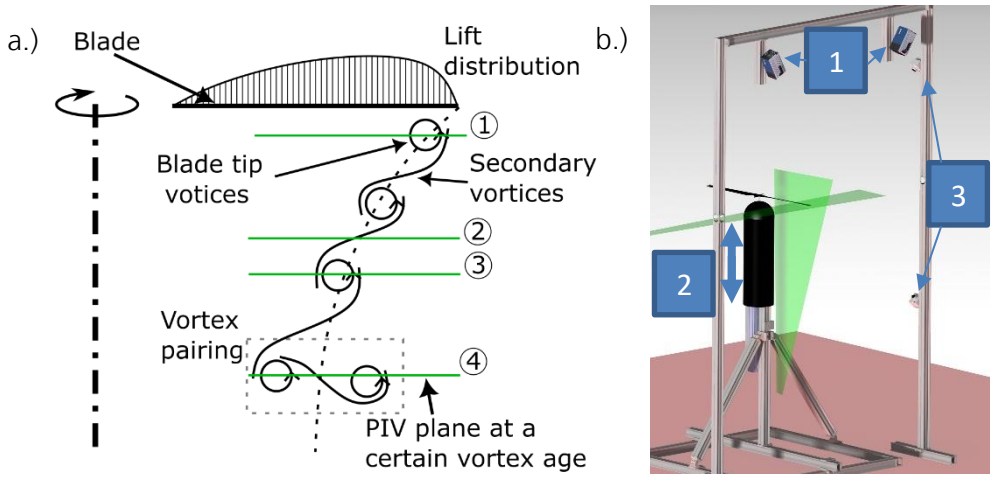

Fig 1: An example overview over the vortex system with secondary vortices and vortex pairing (left), and a sketch of the test stand with the PIV planes (right).

should be visible in the horizontal FOVs as their axis is perpendicular to the PIV plane and the primary blade tip vortices. A high-speed PIV system was used in the horizontal plane, to allow a temporal and statistical evaluation of the secondary vortex structures. It consists of a camera system (two Phantom VEO640L, see Fig. 1b label 3) with an acquisition frequency of 950 Hz, to acquire 50 images per rotor revolution. In addition, a low-speed PIV system was used to investigate the primary blade tip vortices and the overall wake structure in the vertical plane. Two pco DIMAX S4 cameras were used for imaging, see Fig. 1b label 1.
In addition to PIV, we also used a high-speed camera to track the position of the blade tips and conducted hotwire measurements at up to 588 points in a vertical plane. Both methods were only used for selected cases. The setup of this system will be explained in detail in the final presentation.

The following table lists the variation of configurational parameters of the current study:

Number of blades n_B	Frequency f	Blade loading C_T/σ	Blade-to-blade pitch offset $\Delta\theta$
1	$f = 19\ Hz, \sqrt{2}f, f/\sqrt{2}, f/2$	$0.059, 0.071, 0.085, 0.098, 0.106$	-
2	$f = 19\ Hz, \sqrt{2}f, f/\sqrt{2}, f/2$	0.085	$0°, 0.2°, 0.5°. 1°$
4	$f = 19\ Hz$	0.085	$0°, 0.2°, 0.5°. 1°$

Additionally, different blade shapes were studied (constant radius of 0.76m, constant thickness of 15% and constant chord length of 0.061m):

Name	Airfoil	Twist	Blade tip shape	Origin
SpinBlades BlackBelt	Symmetric	0°	Parabolic	Commercial
SpinBlades BlackBelt	Symmetric	0°	Rectangular	Commercial modified
DLR HEL-0	NACA23015	0°	Rectangular	Own design
DLR HEL-18	NACA23015	−18°	Rectangular	Own design

Sample Results and Discussion

In the following, a few sample results are shown. The PIV data from the vertical FOV were used to extract the primary tip vortices and will be shown in connection with the horizontal FOV data in the final presentation.

In this abstract, however, we will focus on some results of the evaluation of the secondary structures. An instantaneous sample of the flow field in the horizontal PIV plane is shown in Fig. 2. The secondary structures are marked by red

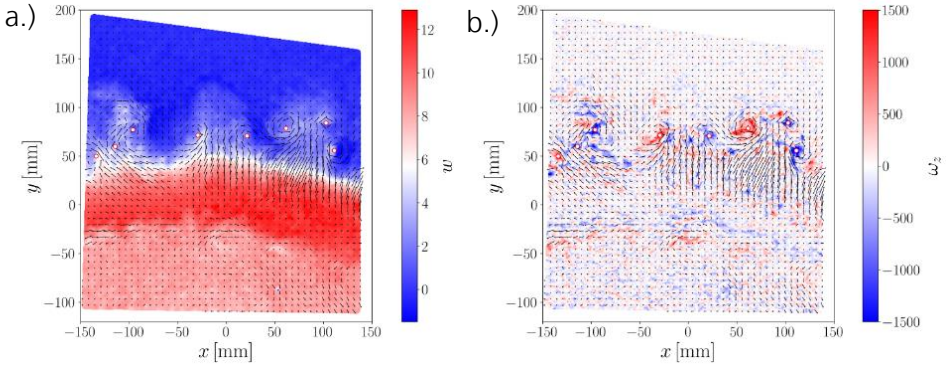

Fig 2: Sample PIV fields from the horizontal PIV plane together with the detected secondary vortices

circles in both pictures. These data are used to quantify the secondary structures in terms of wake age, respectively distance from the rotor. Owing to the high spatial resolution, the field of view is limited to an azimuthal range of 22.5°. Therefore, the average number of secondary vortices over the entire azimuth is calculated by:

$$n_{v,mean} = Avg\left(\frac{n_{sec,i} \cdot 360°}{22{,}5°}\right)$$

While the number of vortices detected in the ith sample is given as $n_{sec,i}$. Thus, the average number of secondary vortices in a certain distance from the rotor could be extracted. The evolution of $n_{v,mean}$versus the distance $-z/R$ is shown in Fig. 3. In a similar experiment Schwarz et. al. (2022) suspected an influence of the pitch offset on secondary

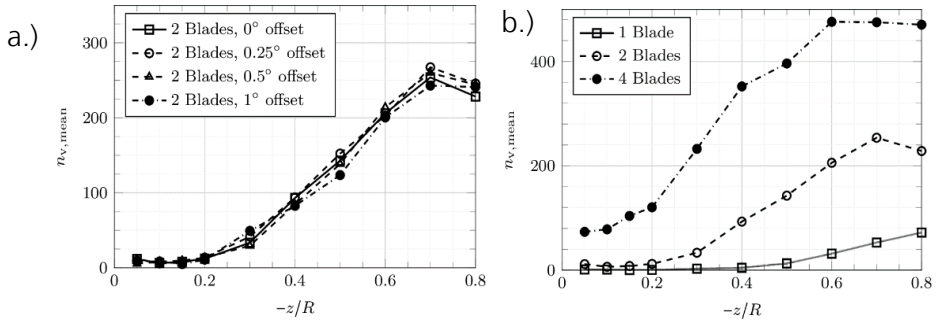

Fig 3: Development of the number of secondary structures per rotation over the distance to the rotor plane

structures. As can be seen in Fig. 3a this theory cannot be confirmed by this experiment. Nevertheless, it can be shown, that other factors such as the number of blades, see Fig. 3b, have a significant influence. In the final presentation we will discuss additional configurational parameters, which mainly effect the occurrence of secondary structures, e.g. the influence of the blade passing frequency. Moreover, the circulation and statistical characteristics were studied and evaluated. These results will then be combined to get a show how secondary vortices influence blade tip vortex break-down.

Schwarz et. al. (2022): Schwarz, C., Bodling, A., Wolf, C. C., Brinkema, R., Potsdam, M., and Gardner, A. D., "Development of Secondary Vortex Structures in Rotor Wakes," Experiments in Fluids, Vol. 63, No. 1, 2022, p. 4. https://doi.org/10.1007/s00348-021-03348-8.

Mitteilung

Fachgruppe: Drehflügleraerodynamik

Validation of a turbulent boundary layer method for fuselages of helicopters

Hilal Inac, Dr. Walid Khier
Deutsches Zentrum für Luft- und Raumfahrt e. V. (DLR),
Institut für Aerodynamik und Strömungstechnik
Lilienthalplatz 7, 38108 Braunschweig
hilal.inac@dlr.de, walid.khier@dlr.de

Introduction

The more precise calculation of the boundary layer in three-dimensional, viscous flow is an old und repeatedly sought after goal in helicopter aerodynamics. The panel method is able to calculate three-dimensional, incompressible, inviscid potential flows quickly and realiably by dividing the surface of the body into several panels. Since viscous drag cannot be predicted with the panel method alone, the panel method is coupled with a boundary layer method. Often, structured panel grids are used to discretize lifting bodies like wings or rotors, while unstructured grids are applied to simulate complex shaped non-lifting bodies, e.g. fuselages. The viscid boundary layer calculation for unstructured surface panels is more demanding than for structured panels, since the boundary layer flow doesn't align with the grid lines as it is often the case for structured panel grids. For unstructured grids the flow data are typically determined along selected stream lines in order to carry out the boundary layer calculation. In DLR's Unsteady Panel Method (UPM) with free-wake modelling the standard stripwise integration of the boundary layer equations is applied for structured grids. In contrast to other methods, for unstructured grids an advancing front algoritm is applied [1]. The advantage of the approach is that no user interaction is required for the extraction of streamlines. In previous works only the streamwise arc length was propagated to compute skin friction using a flat plate analogy. Simple empirical critera are used to predict separation onset. With the aim of improving prediction accuracy, in this paper Truckenbrodt's integral boundary layer is implemented into UPM.

Approach/Method

Truckenbrodt's boundary layer method [2, 3, 4] is an integral boundary layer method. It employs the calculated flow quantities to compute skin friction on each individual panel, and thus, identify flow separation on the components with a higher degree of accuracy.
For the implementation of Truckenbrodt's method, the advancing front algorithm in UPM has been extended to not only propagate the arc length starting from the stagnation point, but to propagate all data needed to solve Truckenbrod's integral boundary layer equations. If flow separation is detected based on a form factor $h_{sep}<0.723$ then the skin friction coefficient c_f is set to zero in the downstream direction. The implementation is validated with wind tunnel data for a helicopter fuselage and related CFD results. The wind tunnel data was obtained in the DLR-internal project FastRescue, where two rescue helicopters, a conventional one and an air taxi, were designed. The wind tunnel experiment for the conventional helicopter fuselage featuring a streamlined body and V-tail were carried out in the DNW-NWB low-speed wind tunnel in Braunschweig. In addition to the wind tunnel data, reference results are available from CFD simulations using CODA, the next generation CFD solver commonly developed by Airbus, DLR and ONERA.
The numerical model features the fuselage and strut fairing based on the original CAD geometry of the wind tunnel model. An unstructured mesh with quadrilateral and triangular panels is used for the fuselage. A structured mesh with quadrilateral panels is used for the V-tails and the strut fairing. In comparison with the CFD analysis, the surface grid for UPM uses significantly less mesh points. The computations cover an angle of attack range between -15° and 15° with 2.5° steps for Mach-number 0.2 and zero yaw angle.
Figure 1 depicts the resulting surface pressure coefficient c_p for UPM (right) and CFD (left) at an angle of attack of 0°. Both figures show similar results. Figure 2 presents the pressure coefficient c_p in the symmetry plane of the fuselage at three different angles of attack. The results show deviations on the engine cowling and at the rear of the tailrotor. The reason behind the difference around the engine cowling is that a finer mesh is taken in account in the CFD calculations.
The drag (c_d), lift (c_l) and pitch moment (c_{my}) coefficients are plotted in Figure 3. The findings indicate that the drag coefficient in UPM between -5° and 15° angle of attack represents better alignment with

the experiments in comparison to CFD results. Lift and pitch moment calculations show a good alignment at the positive angle of attack in UPM. Thus, Truckenbrodt's boundary layer method is shown to be an effective way of calculating the drag coefficient of the fuselage with the fast mid-fidelity simulation method UPM.

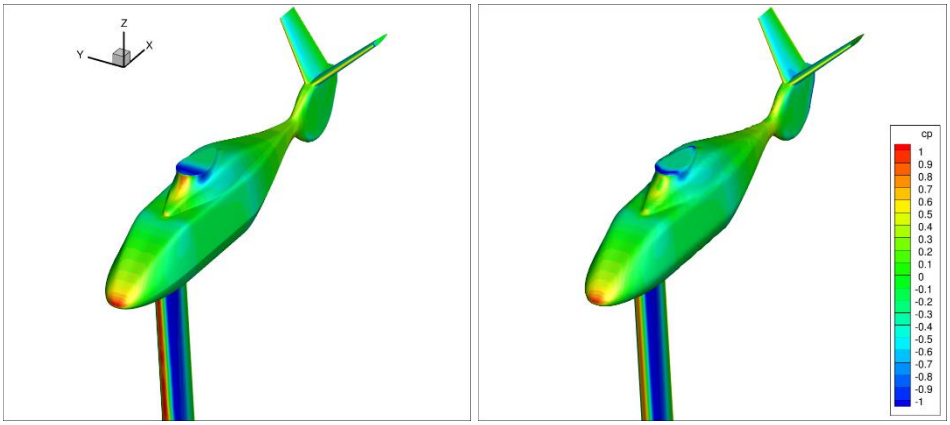

Figure 1 Surface pressure coefficient on CFD (left) and UPM (right)

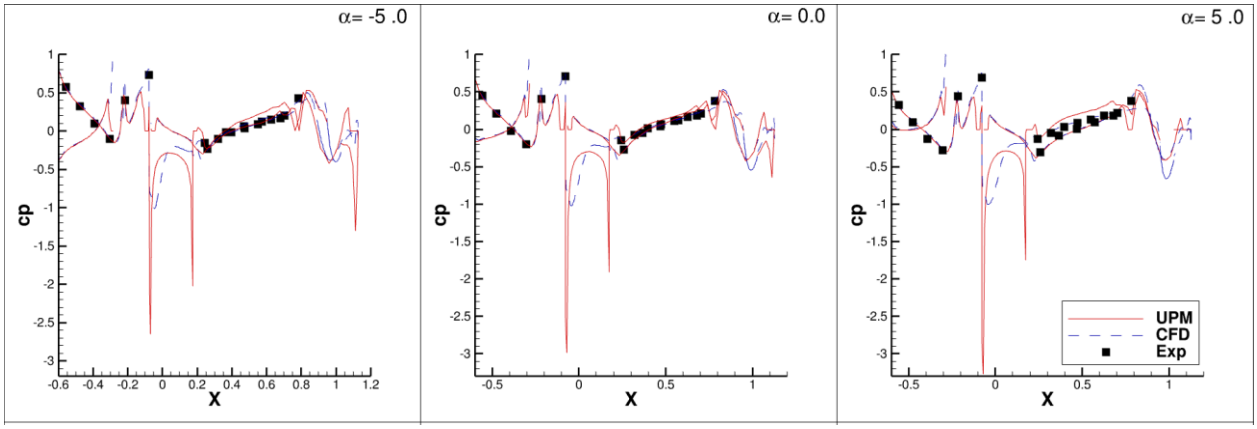

Figure 2 Surface pressure coefficient on UPM, CFD and Experiment in center cross section

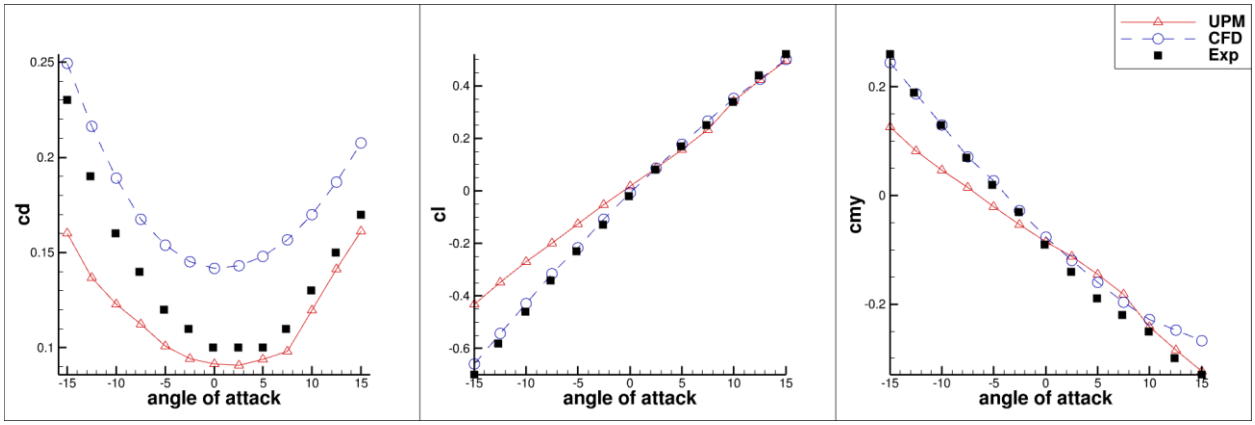

Figure 3 Drag, lift and pitch moment coefficients on UPM, CFD and Experiment

References

[1] P. Kunze, "A panel free-wake code with boundary layer method for helicopter simulations", 45th Europaen Rotorcraft Forum, Warsaw, Poland, 2019, ERF2019-0114
[2] H. Schlichting, "Grenzschicht-Theorie",1982, 8. Auflage, ISBN 376501111, pp. 683-713
[3] E. Truckenbrodt. "Neuere Erkenntnisse über die Berechnung von Strömungsgrenzschichten mittels einfacher Quadraturformeln Teil I", 1973, In: Ingenieur-Archiv 43.1, pp. 9-25.
ISSN : 1432-0681.
[4] E. Truckenbrodt.,"Neuere Erkenntnisse über die Berechnung von Strömungsgrenzschichten mittels einfacher Quadraturformeln Teil II",1974. In: Ingenieur-Archiv 43.2, pp. 136-144. ISSN : 1432-0681

Mitteilung

Fachgruppe: Drehflügler

Hybrid Rotor Noise Optimization

Philipp Mandl, Christian Breitsamter
Chair of Aerodynamics and Fluid Mechanics, Technical University of Munich,
Boltzmannstr. 15, 85748 Garching, philipp.mandl@tum.de

Introduction

The development of future, environmentally friendly and innovative aircraft is facing numerous challenges. In the early stages of the design process, rotor performance and noise reduction are two key variables in assessing the eco-efficiency of VTOL (vertical take-off and landing) configurations, especially in congested areas. Currently developed air taxis e.g. by Airbus, Joby and Volocopter are showing promising drive train concepts. Despite this, comprehensive research studies regarding noise emissions are still missing. The main objective of HyRoNO (Hybrid Rotor Noise Optimization) is to reduce noise emissions of novel multi-rotor-confgurations based on cargo drones.

With the advancement of electric power generation systems (hybrid or all-electric), a new design paradigm emerges through the use of distributed propulsion systems for new aircraft designs. The new type of transport system promises safe, fast, reliable and efficient ways of moving around cities and connecting regions where public acceptance of this type of aircraft is still limited, mainly due to noise. The design of VTOLs requires a fundamental understanding of the predominant aerodynamic influences and effects, and leads to high demands on the engineering perspective for predicting vehicle performance, stability and handling qualities in many different conditions within the flight envelope [1]. The noise emission of a multi-rotor aircraft can be significantly influenced by design and mission specific aspects. In addition to aeroacoustics, the performance of the rotor has to be taken into account when designing noise reduction measures. An appropriate compromise between aerodynamics and aeroacoustics has to be found. In order to meet the various requirements of the eVTOL industry, all aircraft have different rotor concepts. These concepts generate lift and thrust for vertical take-off and cruise flight. Reliable noise prediction is of paramount importance at the design stage.

In the field of rotor/propeller aerodynamics, a fundamental distinction must be made between prediction by means of analytical, efficient procedures and high fidelity numerical flow analyses. Within pre-design analysis, low and mid-fidelity tools are used to investigate the aerodynamics and aeroacoustics behavior, where the industrial and scientifc standard is represented by the blade element theory BEMT [2] [3]. Blade-element models are used for propeller aerodynamics, performance calculations and propeller design, where local induced velocities are used as an input. Thus, the model should be combined with an additional model in order to calculate these induced velocities. The most popular ones are: momentum, simplified-momentum, lifting-line (prescribed or free wake), and vortex (McCormick and Theodorsen) models. The BEMT offers the possibilty of studying various propeller designs in axial flight in a short time range and is therefore a suitable tool for complex shape optimisation and parameter studies [2]. In addition, further aerodynamic and aeroacoustic investigations as well as design considerations for axial and non-axial inflows are carried out on the basis of the

BEMT results using low- and mid-fidelity approaches for studying non-axial inflows. This allows with low computational cost (compared to high-fidelity CFD simulations) the analysis of local and global effects on the aerodynamics and aeroacoustics behaviour. Detailed aerodynamic investigations of rotors are conducted based on numerical flow simulations. State of the art RANS ("Reynolds Averaged Navier-Stokes") numeric methods are widely represented and used in the field of aerodynamics, which are currently used for highly complex confgurations like for detailed propeller aerodynamics analysis for transport aircraft or comprehensive helicopter investigations [4] [5]. In the field of aeroacoustics, scale-resolved flow simulations in combination with the Ffowcs-Williams Hawkings method (FW-H) represent the state of the art. Scale-resolved simulations are used to accurately model the turbulent and highly complex trailing vortex systems. The FW-H method subsequently allows an analysis of the acoustic farfield by taking shading effects, reflection effects and interaction effects into account.

Numerical Approach

Within this work, mission analysis, experimental as well as numerical investigations for single and multi-rotor configurations using low-, mid- and high fidelity approaches are performed. While the numerical part is conducted by the Chair of Aerodynamics and Fluid Mechanis (AER) at Technical University of Munich, the mission specific parameters and the experimental part is accompanied by the Institute of Aerospace Systems (ILR) of RWTH Aachen University at their wind tunnel facility. In cooperation between AER and ILR, extensive numerical and experimental investigations focusing on rotor- on rotor interactions to investigate aerodynamic and aeroacoustic effects in hover and forward flight are conducted. While the focus at AER is on the numerical part by extending an existing tool chain combining low, mid- and high fidelity approaches, experimental studies on the aerodynamic and aeroacoustic behaviour are carried out at ILR. Figure 1 shows an example of a reference cargo drone configuration that will be analyzed in this project.

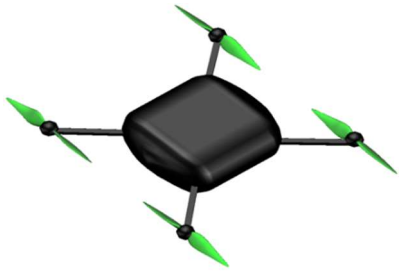

Figure 1: Cargo drone reference configuration

Acknowledgement

The funding of this BayLu-HAMI project HyRoNO (Hybrid Rotor Noise Optimization) HAM-2208-0013 by the Bavarian Ministry of Economic Affairs, Regional Development and Energy is greatfully acknowledged.

References

[1] Davide Montagnani, Matteo Tugnoli, Federico Fonte, Monica Syal, GiovanniDroandi Alex Zanotti.: “Mid-Fidelity Analysis of Unsteady Interactional Aerodynamics of Complex VTOL Configurations“ Department of Aerospace Science and Technology, Politecnico di Milano, Italy; A3 by Airbus LLC, Santa Clara, California, U.S.A.” In: (2019)

[2] Gur O. and Rosen A. “Comparison between blade-element models of propellers”. In: The Aeronautical Journal vol. 112, no. 1138 (2015), pp. 698–704. doi: 10.13140/RG.2.1.3854.5129

[3] Charles N. Adkins and Robert H. Liebeck. “Design Of Optimum Propellers”. In: Journal of Propulsion vol. 10, no.5 (1994), pp. 676–682

[4] You, J. H., Breitsamter, C., and Heger, R. “Numerical investigations of Fenestron™ noise characteristics using a hybrid method”. In: CEAS Aeronautical Journal 7.2 (2016), pp. 185–207. issn: 1869-5582. doi: 10.1007/s13272-015-0180-1

[5] E. R. Busch, M. Keßler, and E. Krämer. “Computational Aeroacoustics of a CounterRotating Open Rotor at different angles of attack”. In: 8. DGLR-FachSymposium der STAB (6.-7. November 2012)

Mitteilung

Fachgruppe: Drehflügler

Simulation of Wake Interaction utilizing a high order finite difference method

Soroush Sohrabi Ataabadi, M.Sc., Prof. Dr.-Ing. Gunther Brenner
TU Clausthal, Institute of Applied Mechanics
Adolph-Roemer Strasser 2A, 38678 Clausthal-Zellerfeld
soroush.sohrabi.ataabadi@tu-clausthal.de

The interaction of wake flow behind propellers of multicopters leads to aerodynamic noise and structural loads. The prediction of such flows requires the appropriate resolution of the turbulent and large-scale fluctuations. The goal of the present study is to asses the performance of a high order finite difference method (Xcompact3D) for the simulation of the wake flow behind rotating propellers. In that, the influence of turbulence modelling based on the implicit Large Eddy Simulations (iLES) and the discretisation details (immersed boundary method IBM, actuator line method ALM) on the prediction of the wake structure is investigated.

Approach
The current study is centered around Xcompact3D, an open-source software designed to solve the incompressible and transient Navier-Stokes equations. Xcompact3D employs a compact finite difference stencil with a high order (up to tenth) accuracy on a Cartesian mesh. In this research, turbulence is simulated using the iLES (implicit large eddy simulation) method in spectral space, combining sixth-order accuracy with a spectral vanishing viscosity (SVV) kernel. Additionally, a unique approach is adopted to connect finite difference and spectral space by utilizing a modified wave number. Instead of using a body-fitted mesh, the boundary conditions for complex (curved) surfaces are formulated using the reconstruction immersed boundary method (IBM). Furthermore, the propeller is modeled using the actuator line model (ALM).

Results
For verification the flow past a simple cylinder in cross flow is investigated. The results show, that the method is able to predict aerodynamic forces up to high Reynolds number quite well in spite of the coarse mesh resolution in the boundary layer which is due to the Cartesian mesh. Apparently, the drag crisis is not resolved due to the missing transition model. The figure shows the visualization of the wake flow around cylinder at Re = 290.

Subsequently, the flow past two rotating propellers is investigated. The propellers operate at a speed of 1000 rpm and have blades with a diameter of 1 meter and a tip speed ratio of 5.23.

Result

Visualization of the wake flow Interaction behind two propeller at Re = 45000.

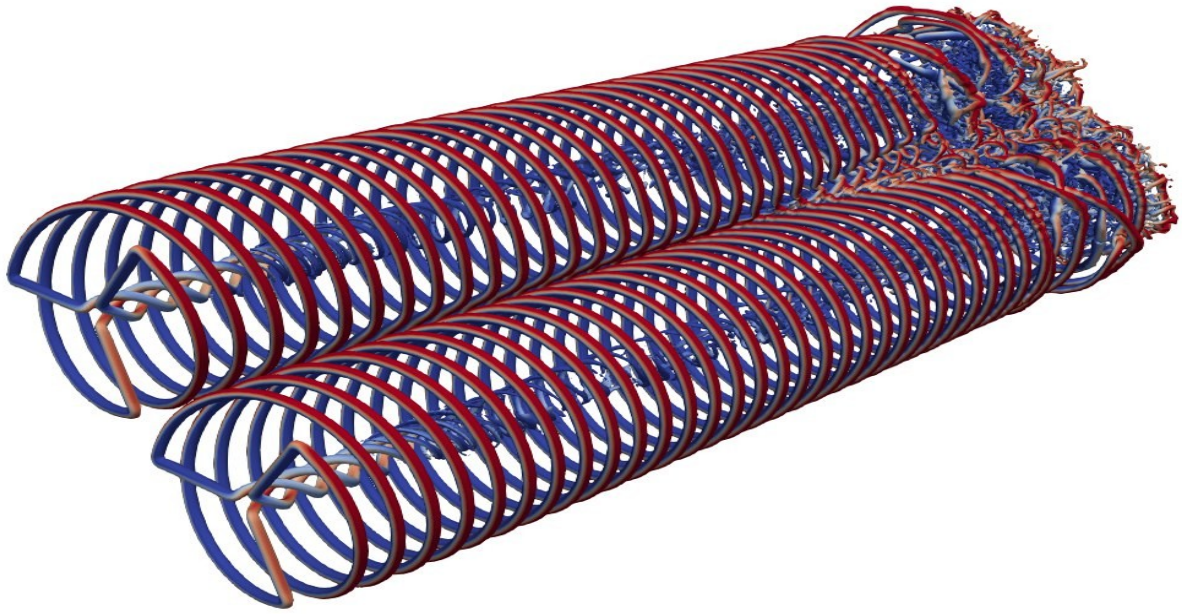

References

Paul Bartholomew, Georgios Deskos, Ricardo AS Frantz, Felipe N Schuch, Eric Lamballais, and Sylvain Laizet. Xcompact3d: An open-source framework for solving turbulence problems on a cartesian mesh. SoftwareX, 12:100550, 2020.

Georgios Deskos, Sylvain Laizet, and Rafael Palacios. Winc3d: A novel framework for turbulence-resolving simulations of wind farm wake interactions. Wind Energy, 23(3):779–794, 2020.

Thibault Dairay, Eric Lamballais, Sylvain Laizet, and John Christos Vassilicos. Numerical dissipation vs. subgrid-scale modelling for large eddy simulation. Journal of Computational Physics, 337:252–274, 2017.

Soroush Sohrabi Ataabadi, Analysis of the Turbulent Wake flow behind a Rotating Propeller using a High-Resolution Numerical Method, Masterthesis,. TU Clausthal, 2023.

Mitteilung

Fachgruppe: Drehflügler

Maximum Thrust of Helicopter Rotors in Hover:
Impact of Comprehensive Code Aerodynamic Modeling

Berend G. van der Wall
German Aerospace Center (DLR) , Lilienthalplatz 7, 38108 Braunschweig, Germany,
berend.vanderwall@dlr.de

Introduction:
Computation of maximum thrust of a helicopter rotor is a challenging task even in hover, because it occurs with a significant amount of stalled region over the rotor blade, which makes a stationary solution using computational fluid dynamics codes impossible. Therefore, a comprehensive rotor code is employed and the impact of aerodynamic modeling on the results is investigated. To isolate the aerodynamic modeling effects from blade design and its elastic response, the blade is assumed rigid, rectangular and linear twisted (Bo105 model rotor geometry and airfoil NACA 23012, 4 blades, radius $R = 2$ m, solidity $\sigma = 0.077$, blade twist -8 deg, tip Mach number $M = 0.641$).

Models affecting maximum airfoil lift:
The airfoil's aerodynamic coefficients are modelled analytially in terms of section normal force, chord force and pitching moments, based on the dynamic pressure of the speed of sound: $C_{n,c,m}M^2$. They include stall angle (α_{SS}) and Mach number (M) effects, yawed flow (yaw angle β) conditions and centrifugal force (CF) effects on the boundary layer, the latter two resulting in a steady stall delay $\Delta\alpha_{SS}$ to larger angles of attack (α). Due to analytic modeling, unsteady aerodynamics result in dynamic lift overshoot and a post-stall vortex shedding model can also be enabled, resulting in unsteady aerodynamic response. Examples are given in **Fig. 1**.

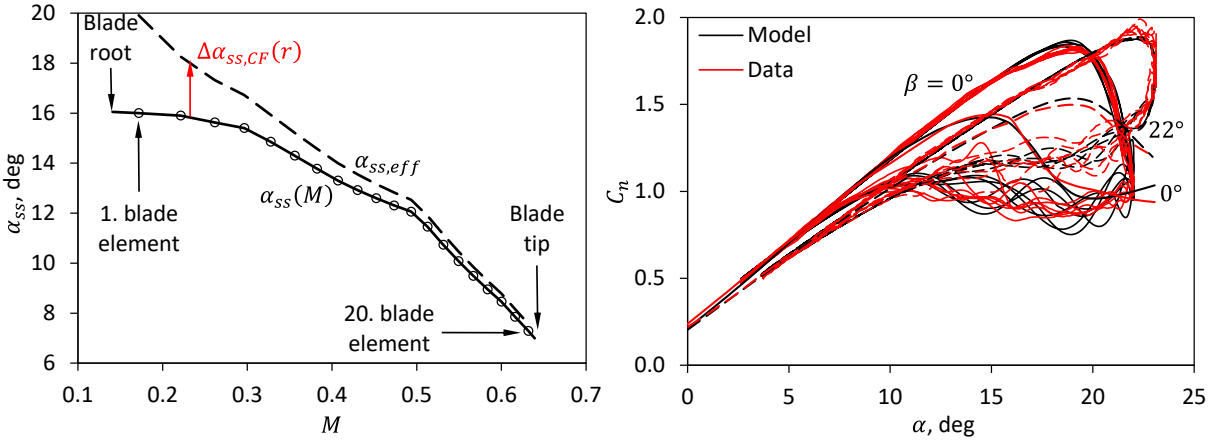

Fig. 1: Impact of modeling features on airfoil aerodynamics. Left: stall delay due to CF model; right: post-stall vortex shedding with and without yaw angle and comparison with data.

The inflow ratio (λ_i) models employed here are no inflow (none), Glauert's constant inflow, Mangler's inflow with non-linear radial distribution, and a prescribed vortex wake (PW) geometry model including blade-vortex interaction. All of them can be combined with a tip loss model, enforcing zero lift at the blade tip and root via additional indcued inflow from a radial position r_{tl} to the tip. Example inflow distributions for the same thrust are given in **Fig. 2** (left) and the impact of the tip loss model on a standard spanwise loading is shown right for a variation of r_{tl}.

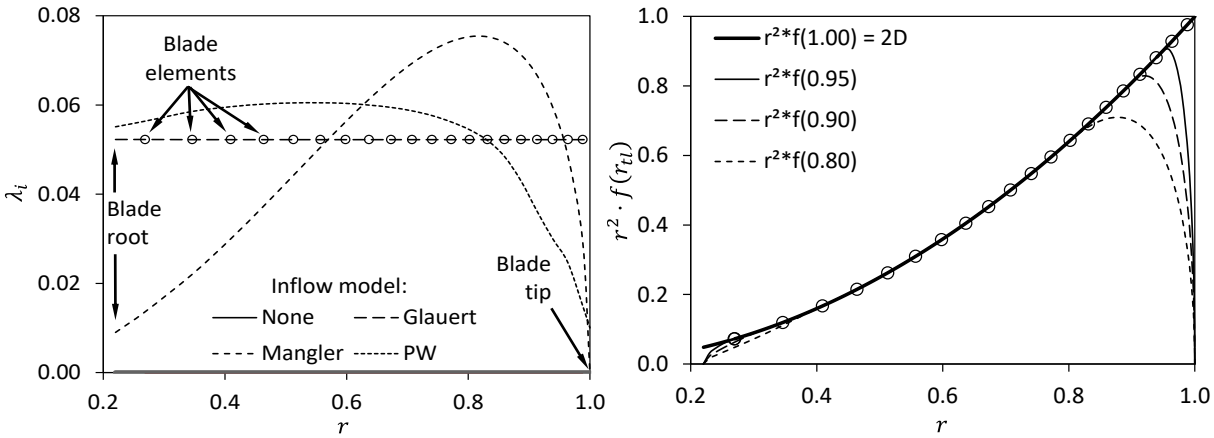

Fig. 2: Inflow distributions (left) and effect of tip loss model (right).

Results:

The rotor blade collective control angle Θ_{75} is increased from moderate lift up to the point of maximum thrust C_T (or, specific blade loading C_T/σ) and beyond, where the thrust due to increasing amount of stall and associated loss of lift is reducing. **Fig. 3** shows results and includes data from wind tunnel test. No inflow is non-physical and achieves the highest thrust, becaue the blade twist resembles the distribution of stall angles and avoids local stall to a large extent. The inflow distributions of Glauert and PW are similar and results as well, stall first occurs at the blade tip. The Mangler model with more inflow in the tip region results in higher lift capability than the PW model. For all inflow models, 2D aerodynamics up to the tip ($r_{tl} = 1$) allow for higher thrust than a large area of tip loss ($r_{tl} = 0.8$). Employing the CF model increases the thrust once the stall angle without it is reached.

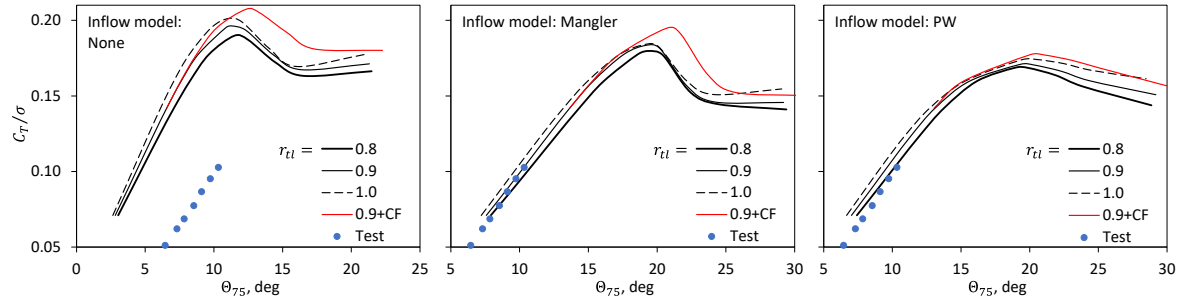

Fig. 3: Impact of inflow model, tip loss and CF on thrust curce and comparison with data

Conclusions:

1. Constant inflow or prescribed wake model have larger inflow ratio in the inner parts of the rotor and less in the outer region than the Mangler model. This leads to smaller angles of attack in the inner regions and larger ones at the blade tip, compared to the Mangler model.

2. The highest possible thrust is obtained by the Mangler model, because of its high inflow in the outer region of the blade, where the stall angle of attack is the lowest due to the high Mach number.

3. Increasing the tip loss region reduces the maximum possible thrust. Realistic values for high thrust range from $r_{tl} = 0.8 - 0.9$.

4. The CF model delays steady stall to higher angles of attack more in the root than in the tip region and has a significant impact on increasing the maximum thrust prediction.

5. All models have a physical background, but data are needed to tune the model parameters, e.g. r_{tl} or $\alpha_{SS,CF}$ to the most realistic values.

Mitteilung

Fachgruppe: Drehflügler

CFD simulations of a rotor within a box:
The STARII rotor within DLR's pre-test facility

Gunther Wilke[AS]
Hideaki Sugawara[JX], Yasudata Tanabe[JX]
Oliver Schneider[FT], and Berend G. van der Wall[FT]
[AS] German Aerospace Center (DLR), Aerodynamics and Flow Technology[DLR]
[JX] Japan Aerospace Exploration Agency (JAXA), Osawa 6-13-1, Mitaka, Tokyo, 181-0015 Japan
[FT] German Aerospace Center (DLR), Flight Systems[DLR]
[DLR] Lilienthalplatz 7, 38108 Braunschweig, Germany

The second Smart Twisting Active Rotor (STAR II) project aims at investigating the beneficts of active twist on a conventional blade design for reduction of required power, noise and vibration in the DNW-LLF wind tunnel. Prior to the wind tunnel test, the rotor is first tested for correct operation in the rotor test hall at the German Aerospace Center (DLR) in Braunschweig, see Figure 1 on the left. However, this test hall is not vented and reduced maximum thrust in combination with strong vibrations have been observed from previous rotor pre-tests. As an extension of the prediction team effort [1], where simulations for the DNW-LLF test matrix have been carried, the two partners, DLR and JAXA, additionally carried simulations of the rotor in the pre-test hall at the DLR in Braunschweig to identify the issues from the runs within the test hall. The in-ground effect has been studied early on [2], and its effect on the rotor is well known [3]. Flight near obstacles has been investigated [4] already as well. However, only JAXA has carried out simulations for a Martian Helicopter within a contained box [5]. Therefore, the novelty of this research is the investigation of a conventional helicopter rotor within a closed test-chamber, here approximated by a box as seen in Figure 1 on the right. Figure 2 visualizes the flow field at 2,000 N thrust. Shown is the vertical velocity, and from this is it is clearly seen that besides the ground effect, recirculation is given. The wake bounces off the ground and moves to the sides, the flow moves up the walls and comes back down into the rotor plane, being the recirculation. In Figure 3, the thrust for a specific collective angle and the Figure of Merit (FM, ideal required rotor power/measured rotor power) are plotted for these simulations in combination with reference 'free air' simulations of the rotor out-of-ground. It is observed that the required collective pitch angles are generally higher in the boxed flow, while the FM is lower. From the ground effect, the opposite is known. Therefore, it could be clearly identified that the recirculation, similar to a climbing state of the rotor, is the dominating physical effect. The effect becomes stronger with higher thrusts. Besides this, the oscillations rapidly increase and for safety reasons only 3,400 N were run in the test hall, while the simulations could still be carried out at the nominal thrust of 3,600 N. The simulatiosn also revealed a high degree of oscillations.

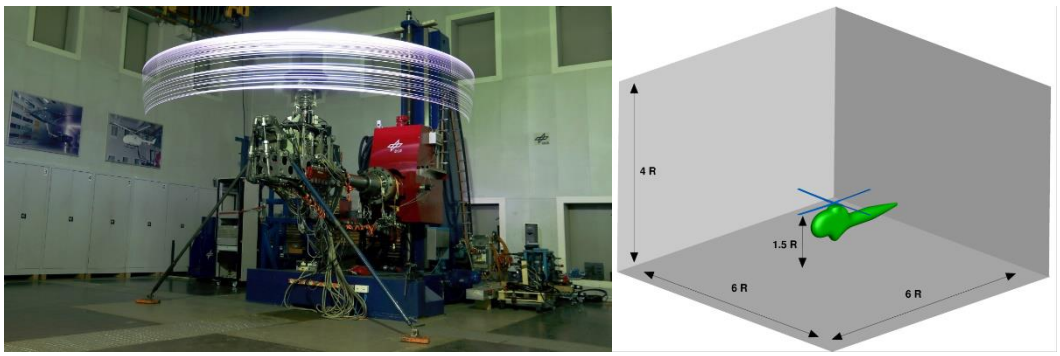

Figure 1: left: Rotor Pre-Test Hall @ DLR Braunschweig. right: simplified model for simulation.

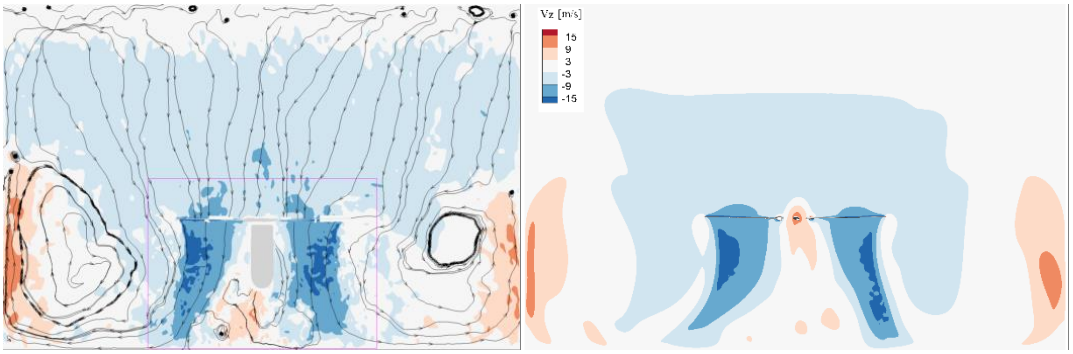

Figure 2: Flow in the box @ 2,000N thrust. Left: DLR's result with DDES, right JAXA's results with U-RANS.

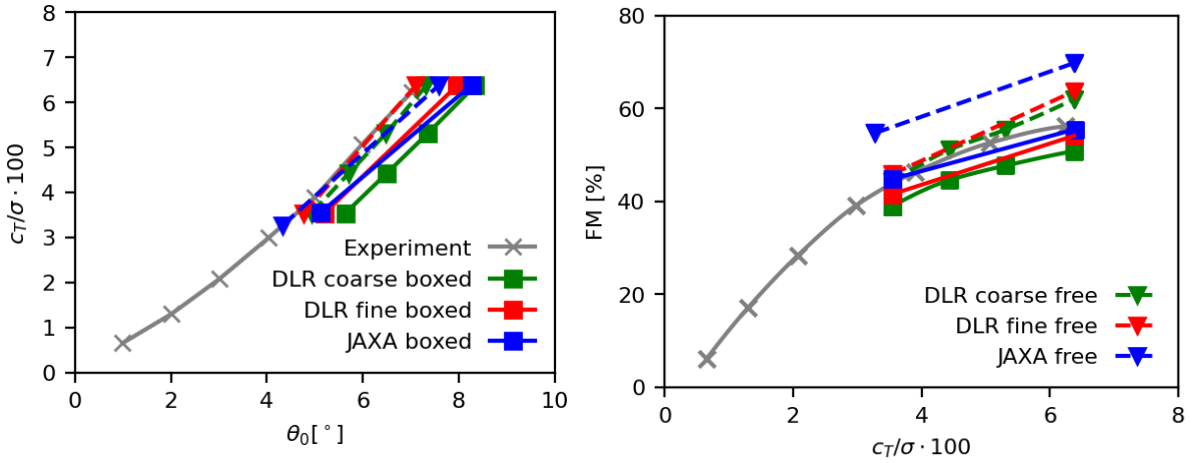

Figure 3: left: Thrust over collective, right: Figure of Merit over thrust.

This also demonstrates the capability to simulate such flow. The application of DDES by DLR allowed to resolve the secondary vortices, yet the impact is little on the final result. Hence, the good agreement with JAXA's U-RANS results. More important is likely the application of a higher order inviscid flux scheme, where both partners utilized a 4th order accurate MUSCL reconstruction in combination with SLAU2 upwinding. However, the runtimes exceeded well over three months for both partners due to the requirement of simulating roughly five seconds in physical time and has not reached a quasi-steady state due to the continuous rise of energy within the box fed from the rotor.

References

[1] B. G. van der Wall, J. W. Lim, J. Riemenschneider, S. Kalow, G. Wilke, and D. D. Boyd, Jr., J. Bailly, Y. Delrieux, I. Cafarelli, Y. Tanabe, H. Sugawara, S. N. Jung, S. H. Hong, D.-H. Kim, H. J. Kang, G. Barakos, and R. Steininger, "Smart Twisting Active Rotor (STAR) - Pre-Test Predictions," in *48th European Rotorcraft Forum*, 2022.

[2] I. C. Cheeseman, and W. E. Bennett, "The effect of the ground on a helicopter rotor in forward flight," *Aeronautical Research Council Reports & Memoranda,* 1955.

[3] A. Graber, A. Rosen, A. and A. Seginer, "An investigation of a hovering rotor in ground effect," *The Aeronautical Journal,* vol. 95, p. 161–169, 1991.

[4] G. Gibertini, D. Grassi, C. Parolini, D. Zagaglia and A. Zanotti, "Experimental investigation on the aerodynamic interaction between a helicopter and ground obstacles," *Proceedings of the Institution of Mechanical Engineers, Part G: Journal of Aerospace Engineering,* vol. 229, p. 1395–1406, 2015.

[5] M. Sugiura, Y. Tanabe, H. Sugawara, K. Kimura, A. Oyama, M. Sato, K. Yoshikawa, Y. Buto, M. Kanazaki, Y. Kishi, D. Kikuchi, and T. Minajima, "Blade Shape Optimization of Mars Helicopter Exploring Pit Craters," in *78th Annual Forum of the Vertical Flight Society*, 2022.

Mitteilung

Fachgruppe: Experimentelle Aerodynamik

Aerodynamischer Einfluss von Lücken im Beladungsschema von Güterzügen
- Teil 1: Parameterstudie zum Strömungswiderstandskoeffizient

Alexander Buhr, James R. Bell, Lars Siegel, Arne Henning
Deutsches Zentrum für Luft- und Raumfahrt e.V., Institut für Aerodynamik und Strömungstechnik (AS-BOA), Göttingen, alexander.buhr@dlr.de

Im Rahmen dieser Arbeit wurde der Einfluss von Lücken im Beladungsschema eines Güterzugs auf den resultierenden Strömungswiderstand in einer Parameterstudie untersucht. Ziel dieses Forschungsprojekts ist die Beschreibung des Potentials zur aerodynamischen Optimierung des Beladungsschemas im Schienengüterverkehr. Eine quantitative Analyse im Sinne der Energieverbrauchsbilanz ermöglicht dann den Betreibern eine Kosten-Nutzen-Analyse unter Berücksichtigung des mit der Optimierung verbundenen logistischen Aufwands. Der Einfluss der Lücken bzw. der Abstände zwischen einer Wechselbrücke und der sich stromauf und stromab befindlichen Ladung auf den aerodynamischen Widerstand wurde in Windkanalexperimenten inkrementell untersucht. Die resultierende Ergebnismatrix ermöglicht eine quantitative Abschätzung des Einflusses einer beliebigen Änderung des Beladungsschemas auf den Gesamtströmungswiderstand des Güterzugs.

Die experimentellen Untersuchungen wurden in der Seitenwindversuchsanlage Göttingen (SWG), einem geschlossenen Windkanal Göttinger Bauart, durchgeführt. Die SWG besitzt eine Teststrecke von 2.4 m Breite, 1.6 m Höhe und 9 m Länge und verfügt über ein 500 kW Gebläse mit dem Strömungsgeschwindigkeiten bis zu 60 m/s in der Teststrecke erzeugt werden können. Abb. 1 zeigt das generische Güterzugmodell im Maßstab 1:15 mit einer Länge von 6.24 m in der Teststrecke der SWG. Für die Untersuchung eines Güterzugmodells dieser Länge wurde der Modellaufbau auf einer speziellen, 8 m langen Splitterplate in einer Höhe von 0.45 m positioniert, um eine freie Anströmung außerhalb der Grenzschicht, die sich nahe des Windkanalbodens ausbildet, zu gewährleisten. Das Modell steht auf einem maßstabsgetreuen, eingleisigen Bahndamm mit Schienen, um eine realistische Strömungsentwicklung in Bodennähe zu simulieren. Vor und hinter dem Testbereich (blau) befinden sich generische Auf- und Abströmkörper (schwarz) mit Radsätzen (orange), um Strömungsbedingungen an einer beliebigen, mittigen Position im Beladungsschema zu repräsentieren. Der Testbereich besteht aus einer generischen Güterwagenplatte mit Drehgestellen (grau), in dem mittig ein Testcontainer (dunkelblau) mit einer Länge L_c von 521 mm und einer Querschnittsfläche von 170 mm x 195 mm auf einer 6-Komponenten DMS-Kraftmesswage montiert ist.

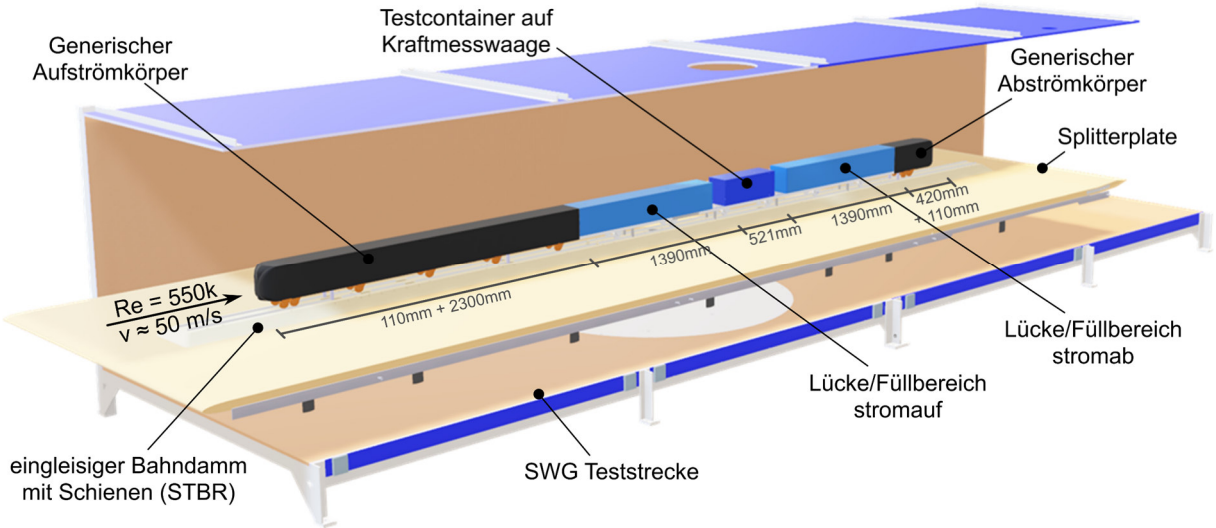

Abb. 1: Messaufbau des Güterzugmodells in der Seitenwindversuchsanlage Göttingen (SWG)

Die Füllbereiche (hellblau) können inkrementell mit Blockelementen aufgefüllt werden, um die Beladungslücken stromauf und stromab zwischen 10.4 mm und 1303.3 mm (entspricht 1/50 L_c bzw. 2.5 L_c) zu variieren. Anhand der Kraftmessdaten wurde der Widerstandbeiwert in Strömungsrichtung $c_{f,x}$ bei einer Reynoldszahl von 5.5 x 10^5 in Bezug auf die Wagenbreite gemessen (entspricht einer Anströmgeschwindigkeit von ca. 50 m/s). Die Parameterstudie wurde bei einem Anströmwinkel von 0° und zusätzlich 5° durchgeführt, um den Effekt von Seitenwind auf die Ergebnismatrix einzubeziehen. Zusätzlich wurden Validierungsmessungen in Bezug auf die Sensitivität der Reynoldszahl sowie der vom Anströmkörper erzeugten Grenzschichtbedingungen durchgeführt. Dazu wurden Messungen mit zusätzlichen Rauigkeiten am Anströmkörper wiederholt, um den Einfluss einer größeren Grenzschicht bzw. der Simulation eines längeren Güterzugabschnitts vor dem Testcontainer zu bestimmen. Des Weiteren wurden bei ausgewählten Konfigurationen die Strömungsstrukturen in der Beladungslücke stromauf, zwischen Anströmkörper und Testcontainer, mit PIV untersucht [1].

Im ersten Schritt wurde der Strömungswiderstand des Testcontainers $c_{f,x}$ für ausgewählte Lückengrößen stromauf und fester Lücke von 52 mm stromab (vice versa) gemessen. Abb. 2 (links) zeigt die resultierende Abhängigkeit für $c_{f,x}$ bei 0° & 5° Anströmwinkel mit Angabe der Beladungslücken in Originalgröße. Die farblich hervorgehobenen Bereiche markieren Beladungslücken, die bei einem typischen Güterwagen, hier: Typ SGMMNS 52' & SGNNSS 80' (CC: Container-Container-Abstand, mit/ohne WW: Wagen-Wagen-Übergang) auftreten können. Zusätzlich ist Abb. 2 (links) in sechs Regime I-VI unterteilt, in denen die Verläufe auf unterschiedliche, charakteristische Strömungsstrukturen hindeuten. Diese Unterteilung kann nicht nur eingesetzt werden um ein bestehendes Beladungsschema, sondern auch zukünftige Güterwagen bereits im Designprozess aerodynamisch zu optimieren. Im zweiten Schritt wurden einzelne Kombinationen gemessen, um die Abhängigkeit zwischen den Lücken stromauf und stromab zu betrachten. Die Abweichung bei unabhängiger Betrachtung der Lücken stromauf/stromab beträgt <3%. Abb. 2 (rechts) zeigt die visualisierte Ergebnismatrix für den quantitativen Zusammenhang zwischen Beladungslücken stromauf/stromab und dem Strömungswiderstand des Testcontainers bei 0°. Die nicht gemessenen Kombinationen wurden linear interpoliert. Diese Ergebnismatrix bildet die Grundlage, um den Einfluss des Beladungsschemas eines Güterzugs im Normalbetrieb auf dessen Energieverbrauchsbilanz zu berechnen.

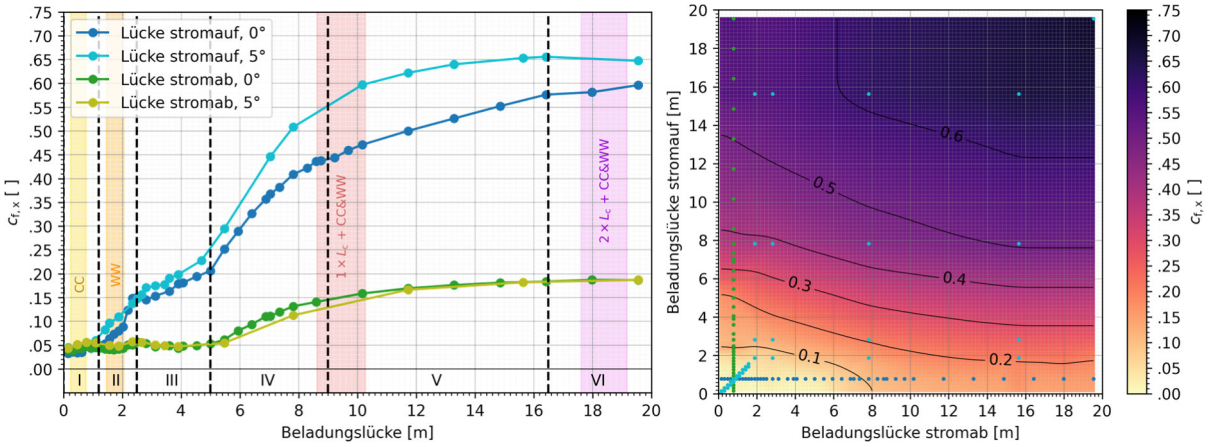

Abb. 2: Abhängigkeit des Strömungswiderstandbeiwerts $c_{f,x}$ von der Größe der Lücken stromauf und stromab bei 0° und 5° Seitenwind (links); Visualisierung der Ergebnismatrix für $c_{f,x}$ bei 0° (rechts)

This work is part of FR8Rail IV project that has received funding from the ER-JU under the European Union's Horizon 2020 research and innovation programme GA 101004051. The article reflects only the authors' views and the Joint Undertaking is not responsible for any use that may be made of the information it contains.

[1] Siegel, Lars et al., „Aerodynamischer Einfluss von Lücken im Beladungsschema von Güterzügen - Teil 2: Analyse der Strömungsstrukturen mittels Particle Image Velocimetry", STAB-Workshop, Göttingen, 2023.

Mitteilung

Fachgruppe**: Experimentelle Aerodynamik**

Standschubmessungen am Biegetorsionsantrieb von BigBird XL

- Versuchsaufbau, Messtechnik und Ergebnisse -

Wolfgang Send[1], Rainer Mugrauer[2], Clemens Gebert[2]
[1]ANIPROP GbR, Sandersbeek 20, 37085 Göttingen
[2]Effekt-Technik GmbH, Robert-Bosch-Straße 21, 72585 Riederich
Ansprechpartner: wsend@aniprop.de

Einführung. BigBird XL ist ein künstlicher Vogel, der seit 2017 nach dem Vorbild von SmartBird[1] entwickelt wird für kommerzielle Zwecke des Transports von leichten Gütern und Aufgaben der bildlichen Inspektion[2]. Das Fluggerät mit einer Spannweite von 5 m ist ausgelegt für ein maximales Abfluggewicht von 25 kg, eine maximale Nutzlast von 10 kg und eine Reichweite von bis zu 50 km (100 km Flugweg). Bei einer Geschwindigkeit im Reiseflug von 15 m/s beträgt der gesamte Leistungsbedarf 750 W. Das entspricht einer spezifischen Leistung von 30 W/kg. Für den Steigflug ist die dreifache Leistung eingeplant. Durch den Einbruch der Arbeiten als Folge der Corona Epidemie ist das Projekt erheblich in Verzug geraten, soll aber weitergeführt werden. Die ersten Messungen des Standschubs, über die hier berichtet wird, sind Anfang 2020 durchgeführt worden. Der Vortrag berichtet auch über die Entwicklungsschritte.

Versuchsaufbau. Für die Entwicklung des Antriebs ist ein Käfig gebaut worden (Bild 1) mit einer Breite von 6 m, einer Höhe von 2 m und der Tiefe von 1.5 m. Das Fluggerät sitzt auf einer 3-Komponentenwaage für translatorische Bewegung bis jeweils 1 kN Last. Im Bild zeigt der Antrieb mit den charakteristischen Zahnrädern nach vorne zum Betrachter. Das Fluggerät hat bei den Versuchen weder Verkleidung noch Fahrwerk. Es würde in Bild 1 dem Betrachter entgegenfliegen. Für die Messungen ist das Fluggerät um 180° gewendet worden, so dass der Luftstrahl aus dem Versuchsstand herausströmt. Die 3-Komponentenwaage sitzt ihrerseits auf einem Schwingtisch, dessen Eigenfrequenz oberhalb der höchsten Schlagfrequenz des Antriebs liegt, die bis 2 Hz reichen kann. Der Schwingtisch ist erforderlich, um die Vertikalbewegung des Antriebs aufzunehmen. Diese Vertikalbewegung entsteht im freien Flug als Gegenbewegung zur Schlagbewegung der Tragflächen. Die beiden virtuellen Drehpunkte der gegenläufigen Bewegung von Antrieb und Tragflächen liegen zwischen beiden Komponenten dicht am Rumpf. In diesen virtuellen Drehpunkten herrscht das Momentengleichgewicht zwischen den Kräften an den Tragflächen und der Gewichtskraft des Antriebs. Werden die Tragflächen durch die Mechanik des Antriebs

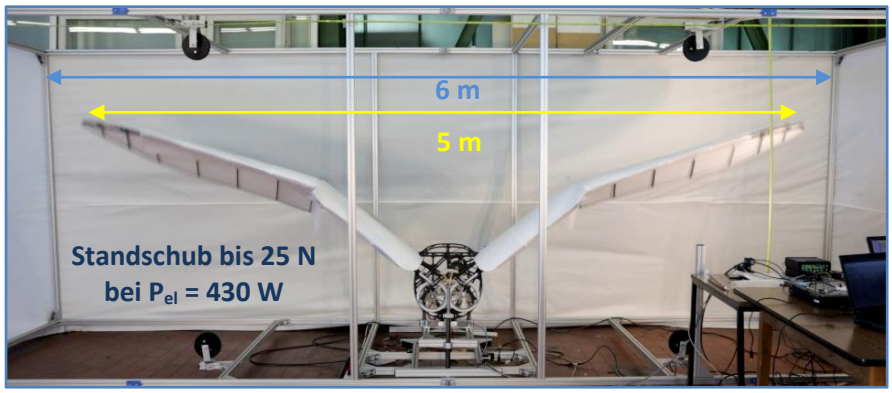

Bild 1. Versuchsstand für BigBird XL mit Kraftmessung und Schwingtisch.

[1] Send W. *Winged artifacts*, ch. 46 in Living machines – A handbook of research in biomimetics and biohybrid systems, Oxford University Press 2018.
[2] W. Send, *Projekt BigBird XL – Kommerzielle Nutzung des Biegetorsionsantriebs*, Deutscher Luft- und Raumfahrtkongress 4. – 6. September 2018, Friedrichshafen. https://www.dglr.de/publikationen/2019/480178.pdf

angehoben, dann senkt sich der Antrieb ab und umgekehrt. Die zusätzlich entstehende Schubkraft geht in diese Überlegung nicht ein, sondern bewegt in Bahnrichtung das gesamte Fluggerät.

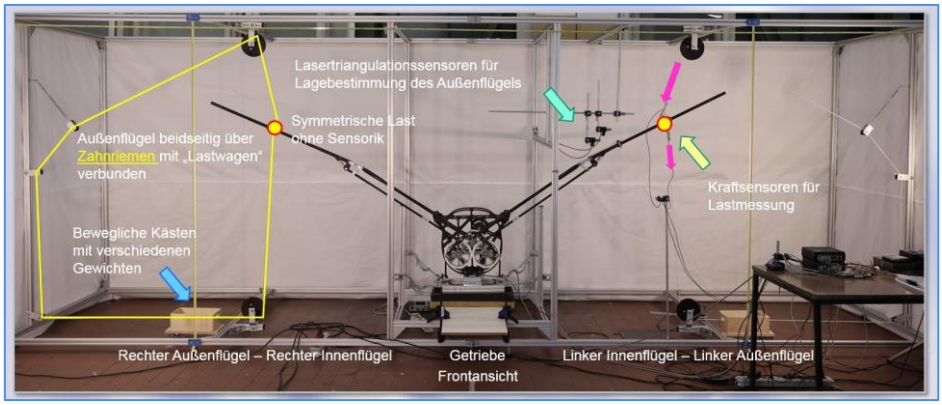

Bild 2. Vermessung der Kinematik und Bestimmung des elektromechanischen Wirkungsgrades.

Messtechnik. Die Entwicklung des Antriebs ist eng verbunden mit der Bestimmung des elektromechanischen Wirkungsgrades. Dieser ist bestimmt durch das Verhältnis von abgegebener mechanischer Leistung an den Tragflächen zur aufgebrachten elektrischen Leistung am Antrieb. Aus der verfügbaren mechanischen Leistung zur Bewegung der Tragflächen kann man über die Annahme eines aerodynamischen Wirkungsgrades auf die erzielbare Schubkraft schließen.

Die entstehenden Luftkräfte an den Tragflächen sind punktförmig mit beschleunigten Massen nachgebildet worden (Holzkästen auf Rädern). Die Kästen sind über Zahnriemen mit den Angriffspunkten an den Flügelholmen verbunden und können mit zusätzlichen Massen belastet werden. Der elektromechanische Wirkungsgrad wird dabei auf zwei Wegen bestimmt: (1) die abgegebene Leistung wird über zwei Kraftsensoren am Flügel (Daten exemplarisch in Bild 3) und die Geschwindigkeit des Angriffspunktes bestimmt; (2) die Beschleunigung der Massen und ihre Geschwindigkeit werden ebenfalls gemessen und hierdurch die aufgebrachte Leistung bestimmt. Dabei wird die Lage des Angriffspunktes am Flügelholm über *zwei* Lasertriangulatoren bestimmt. Die Position der beschleunigten Masse erfasst ein dritter Lasertriangulator.

Ergebnisse aus den beiden unabhängigen Messverfahren lassen sich recht gut zur Deckung bringen und liefern elektromechanische Wirkungsgrade im Bereich zwischen 0.7 und 0.85. Die Mechanik des Antriebs ist im Verlauf der Messungen mehrfach verbessert worden und hat schließlich zu einer maximalen Schlagfrequenz von 2.3 Hz geführt (Bild 4). Für die Messungen sind Kraftsensoren der Firma ME-Meßsysteme verwendet worden zusammen mit zwei Messverstärkern GSV-8DS der gleichen Firma. Alle Versuche sind stets auch optisch aufgezeichnet worden mit einer Canon EOS M50, die komplett ferngesteuert werden kann. Dabei hat der Abstand von 7 m zum Versuchsstand eine recht gute Linearität ergeben, wie der Vergleich zwischen Bild und Konstruktionszeichnung zeigt.

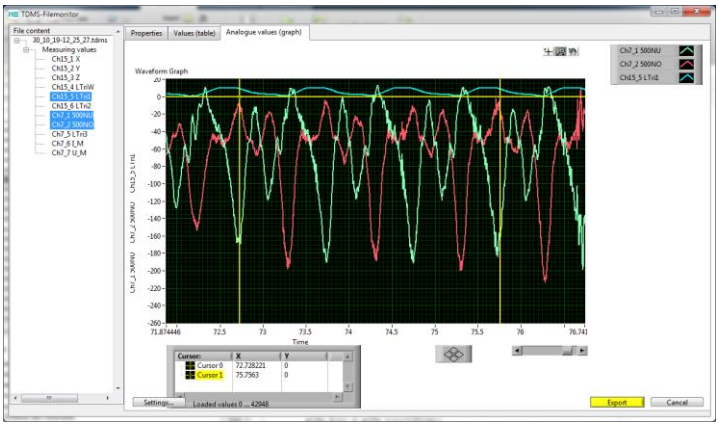

Bild 3. Kraftsensoren am Angriffspunkt bei Auf- und Abschlag.

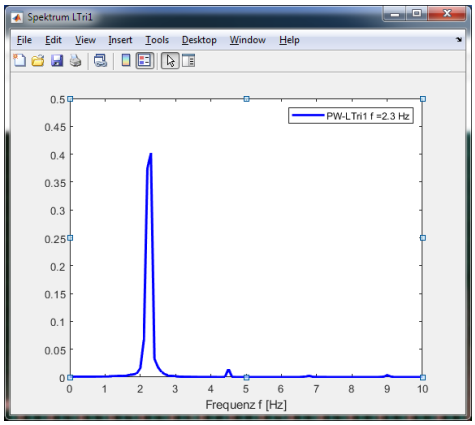

Bild 4. Maximale Schlagfrequenz.

Mitteilung

Fachgruppe: Experimentelle Aerodynamik

Aerodynamischer Einfluss von Lücken im Beladungsschema von Güterzügen
- Teil 2: Analyse der Strömungsstrukturen mittels Particle Image Velocimetry

Lars Siegel, Alexander Buhr, James R. Bell, Arne Henning
Deutsches Zentrum für Luft- und Raumfahrt e.V., Institut für Aerodynamik und Strömungstechnik (AS-BOA), Göttingen, lars.siegel@dlr.de

Im Rahmen der vorliegenden experimentellen Arbeit wurde der Einfluss von Lücken im Beladungsschema eines Güterzugs auf den resultierenden Strömungswiderstand und die auftretenden Strömungsstrukturen untersucht. Das allgemeine Ziel dieses Forschungsprojekts ist die mögliche Berücksichtigung der aerodynamische Optimierung des Beladungsschemas eines Güterzuges in der Energieverbrauchsbilanz. In der vorliegenden Windkanaluntersuchung wurden im Modellmassstab mittels der Particle Image Velocimetry (PIV) die in den Lücken zwischen Wechselbehältern auf einem Güterzug auftretenden Strömungsstrukturen untersucht. Hierbei wurde das Beladungsschema primär stromauf einer fest installierten Wechselbrücke variiert. Synchron zu den PIV-Messungen wurden zudem Kraftmessungen durchgeführt, um den Zusammenhang zwischen den auftreteden Kräften an der Wechselbrücke und den gleichzeitig vorherrschenden Strömungsstrukturen untersuchen zu können.

Die experimentellen Untersuchungen wurden in der Seitenwindversuchsanlage Göttingen (SWG) bei einer Anströmgeschwindigkeit von $U_\infty = 50$ m/s und einer Reynoldszahl von 5,5 x 10^5 in Bezug auf die Wagenbreite $B_c = 170$ mm durchgeführt. Details des allgemeinen experimentellen Aufbaus finden sich in [1]. Für die 2C-2D PIV-Messungen wurde ein Doppelpuls-Laser mit einer maximalen Energie von 350 mJ pro Puls und einer Wiederholrate von 10 Hz verwendet. Der damit erzeugte Laserlichtschnitt wurde seitlich der Windkanalwand durch eine Glasscheibe in den Messbereich eingekoppelt. Der Lichtschnitt befand sich parrallel zum Boden in einer Höhe von 93,3 mm über der Schienenoberkante (siehe Abb. 1), was maßsstabsgetreu einer Höhe von 1,4 m über der Schienenoberkante einer prüfungsrelevanten Messhöhe gemäß Technischer Spezifikationen für Interoperabilitäten entspricht. Die Strömung wurde mit DEHS-Partikeln geimpft, deren Streulicht innerhalb der Lichtschnittebene mittels zweier CMOS Kameras (Typ: PCO edge 5.5) erfasst wurde. Die Kameras befanden sich

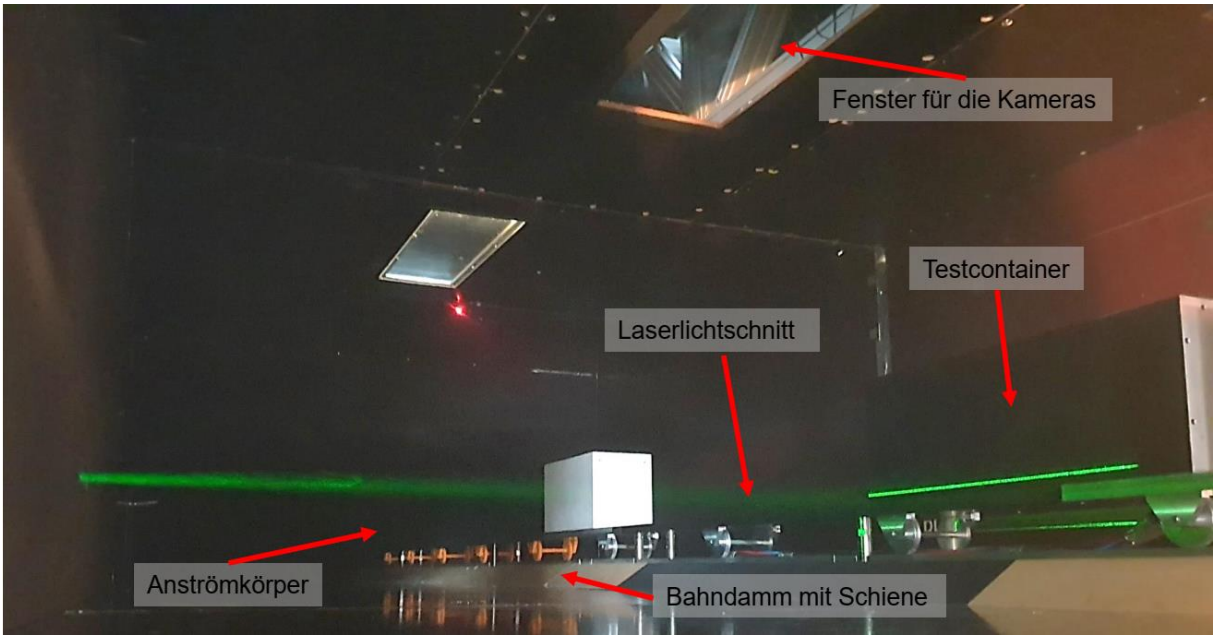

Abb. 1: Foto des Messaufbaus des Güterzugmodells mit Blick in Strömungsrichtung in der Seitenwindversuchsanlage Göttingen (SWG) mit seitlich eingekoppeltem Laserlichschnitt.

dabei vertikal oberhalb des Lichtschnitts hinter einer in der Windkanaldecke eingelassen Glasscheibe. In Kombination mit den genutzen Objektiven ergab sich ein zusammengesetztes Sichtfeld von etwa 750 mm x 320 mm. Die Position der Beobachtungsfenster wurde dabei so gewählt, dass ab dem vorderen Drittel der Wechselbrücke stromauf die Strömungsstrukturen gemessen werden konnten, die sich bei Variation des Beladungsschemas ergeben. Um eine aussagekräftige Statistik zu erhalten, wurden pro Konfiguration 5000 Doppelbilder aufgenommen. Die Auswahl der Konfigurationen erfolgte dabei anhand der Strömungswiderstandbeiwerte, welche im Rahmen einer Paramterstudie ermittelt wurden [1].

Die Ergebnisse der PIV-Aufnahmen sollen dazu genutzt werden, die auftretenden Widerstandskräfte an der Wechselbrücke bei Variation des Beladungsschemas anhand der Topologie der Strömungsfelder und der Verteilung der Strömungsstrukturen nachzuvollziehen und zu erklären. In Abb. 2 ist beispielhaft die Verteilung eines gemittelten Geschwindigkeitsfelds der absoluten Geschwindigkeiten für einen ausgewählten Beladungszustand dargestellt. Die dargestellten Geschwindigkeiten U sind hierbei mit U_∞ und die Achsen mit der Wagenbreite B_c normiert. Zu sehen sind unterschiedliche Geschwindigkeitsbereiche innerhalb der Lücke zwischen der Wechselbrücke und dem stromauf befindlichen Container. Erkennbar sind die Staupunktströmung direkt stromauf der Wechselbrücke, die Beschleunigung an der Vorderkante der Wechselbrücke sowie ein Rezirkulationsbereich stromab des vorderen Containers. Diese Strömungsbereiche sollen darüber hinaus mit CFD-Rechnungen eines vergleichbaren Testfalls verglichen werden [2].

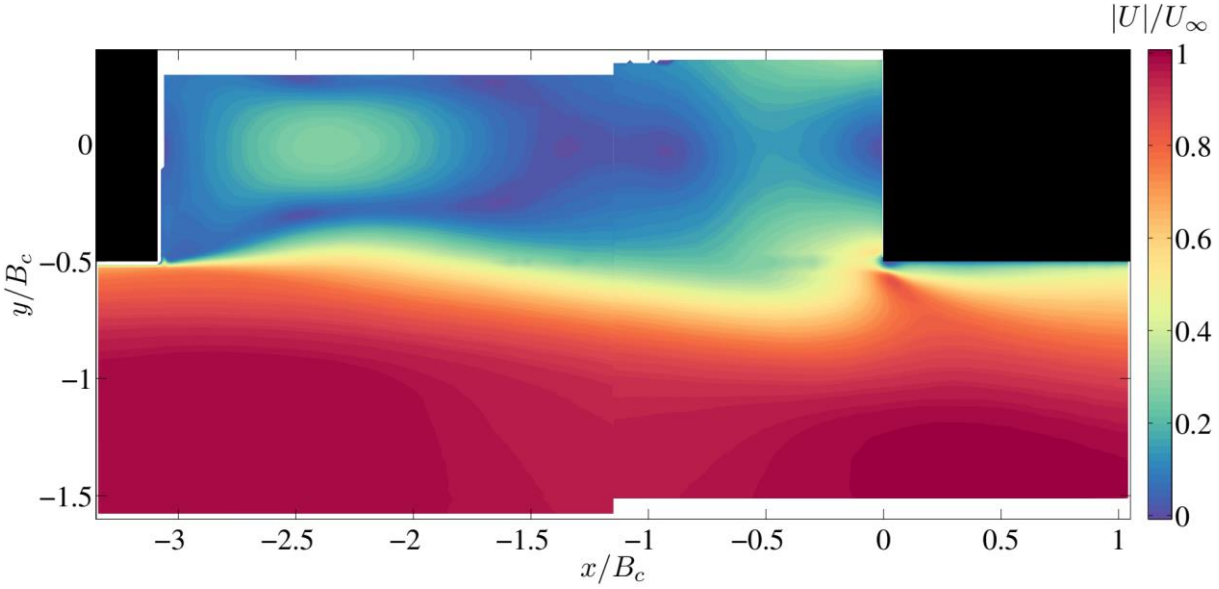

Abb. 2: Gemitteltes absolutes Geschwindigkeitsfeld $|U|$ – normiert mit $U_\infty = 50\ m/s$ – in der Ebene zwischen der Wechselbrücke (rechts oben) und einem ausgewähltem Beladungszustand stromauf.

This work is part of FR8Rail IV project that has received funding from the ER-JU under the European Union's Horizon 2020 research and innovation programme GA 101004051. The article reflects only the authors' views and the Joint Undertaking is not responsible for any use that may be made of the information it contains.

[1] Buhr, Alexander et al., „Aerodynamischer Einfluss von Lücken im Beladungsschema von Güterzügen - Teil 1: Parameterstudie zum Strömungswiderstandkoeffizient", STAB-Workshop, Göttingen, 2023.
[2] Maleki, Siavash et al., „Flow structure between freight train containers with implications for aerodynamic drag", Journal of Wind Engineering & Industrial Aerodynamics, 188 (2019) 194-206.

Mitteilung

Fachgruppe: Hochagile Konfigurationen

Experimental Investigations of Vortex Flow Phenomena on the DLR-F23 Combat Aircraft Configuration at Transonic Speeds

Patrick Hartl[1], Robert Konrath[2], Reinhard Geisler[2], Marc Braune[1], Holger Mai[1]
DLR – Deutsches Zentrum für Luft- und Raumfahrt
[1]Institut für Aeroelastik, Abteilung: Aeroelastische Experimente,
[2]Institut für Aerodynamik und Strömungstechnik, Abteilung: Experimentelle Verfahren,
Bunsenstraße 10, 37073 Göttingen, patrick.hartl@dlr.de

Modern high-agility aircraft are designed to cover a wide range of flight maneuvers, from transonic and supersonic performance to high maneuverability at subsonic speeds. The required flight envelope and mission spectrum of future multi-role combat aircraft lead to the development of new configurations with low aspect-ratio hybrid-delta wing planforms, consisting of multiple swept leading edges (LE). The corresponding flow field is dominated by complex vortex flows even at small angles of attack (AOA), vortex-vortex interactions and vortex-shock interactions, as well as vortex breakdown [1]. These unsteady flow phenomena interact with the aircraft structure. The structural dynamics excitation, which is called buffeting, affects the maneuverability of the aircraft and reduces the lifespan of structural components. The design of the wing planform in terms of different leading edges with different LE sweep angles and additional leading-edge extensions (LEX) has, for this reason, a significant impact on the complexity of the vortex-dominated flow field and the occurring unsteady flow phenomena.

In order to analyze complex flow phenomena, numerical and experimental investigations were conducted at the German Aerospace Center (DLR) as part of the DLR project Diabolo in the framework of Defence Technology [2]. A new high-performance aircraft configuration was developed for the Diabolo project, which resulted in the DLR-F23 geometry [3]. The generic wing-fuselage half-span wind tunnel model consists of a triple-delta wing configuration with an ogival cosine-chined forebody, as shown in Fig. 1. The front wing part, comparable with a leading-edge vortex controller (Levcon), has a medium LE sweep of $\varphi_1 = 45°$, followed by a wing midsection (strake) with a high LE sweep of $\varphi_2 = 75°$ and the main wing section with the similar wing LE sweep as the front section $\varphi_3 = \varphi_1$. The DLR-F23 wind tunnel model consists of elliptic airfoils, that taper into a sharp trailing edge (TE). The LE of each wing section has a constant radius of 0.5 mm.

The experimental investigations are performed in the Transonic Wind Tunnel Göttingen (TWG), operated by the German-Dutch Wind Tunnels (DNW). The Göttingen-type wind tunnel allows continuous inflow in the subsonic, transonic and supersonic speed range. For the investigations presented in this paper, the closed test section with perforated walls with a cross-section of $1.0\,m\,x\,1.0\,m$ and a length of $4.5\,m$ was installed in the plenum chamber. With this wind tunnel setup, a Mach number range of $0.50 < Ma_\infty < 1.20$ was covered in the measurement campaign. Considering the mean aerodynamic chord of $l_\mu = 0.411\,m$ as a reference length, the Reynolds number is in the range of $2.15 \cdot 10^6 < Re_{l_\mu} < 3.30 \cdot 10^6$. The half-span wind tunnel model, installed on a peniche, is actuated by a rotary hydraulic cylinder, as shown in Fig. 2a. A stereoscopic particle image velocimetry (Stereo-PIV) measurement technique was used to analyze the vortex-dominated flow field of the triple-delta wing configuration. Figure 2b shows the stereo-PIV measurement setup with the DLR-F23 wind tunnel model integrated into the test section. The measurement planes are illuminated by a double-pulsed ND: YAG-Laser. Two sCMOS cameras are positioned outside the closed test section on the left and right side in the area of the viewing windows. Figure 3 shows the nondimensional vorticity for the PIV-measurement plane 2, located at $x/c_{r,W} = 0.30$, for an angle of attack of $\alpha = 9°$, a Mach number of $Ma_\infty = 0.85$ and a Reynolds number of $Re_{l_\mu} = 2.93 \cdot 10^6$. The vortex core of the forebody vortex (FBV), which forms from the shear layer on the chined forebody, can be identified in the inner region. In the area of the LE of the strake, the formation of the inboard vortex (IBV) from the vortex shed is observable.

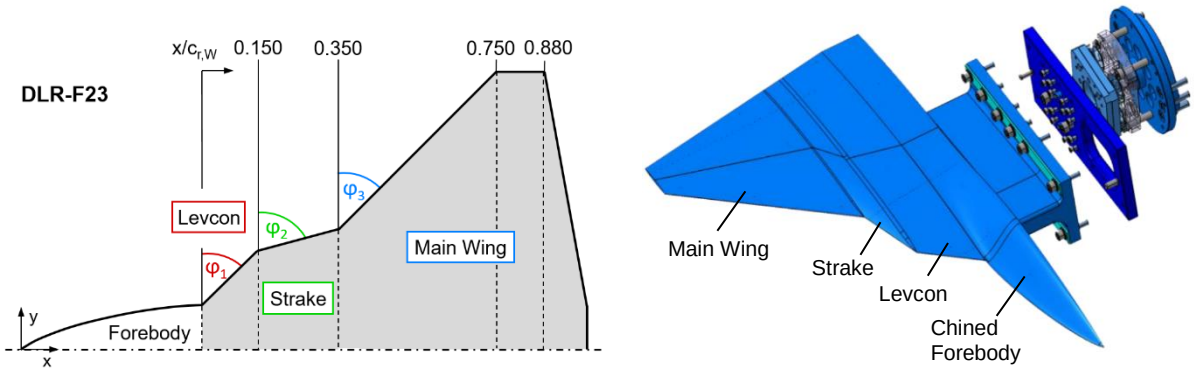

Figure 1: Geometry of the DLR-F23 half-span wind tunnel model

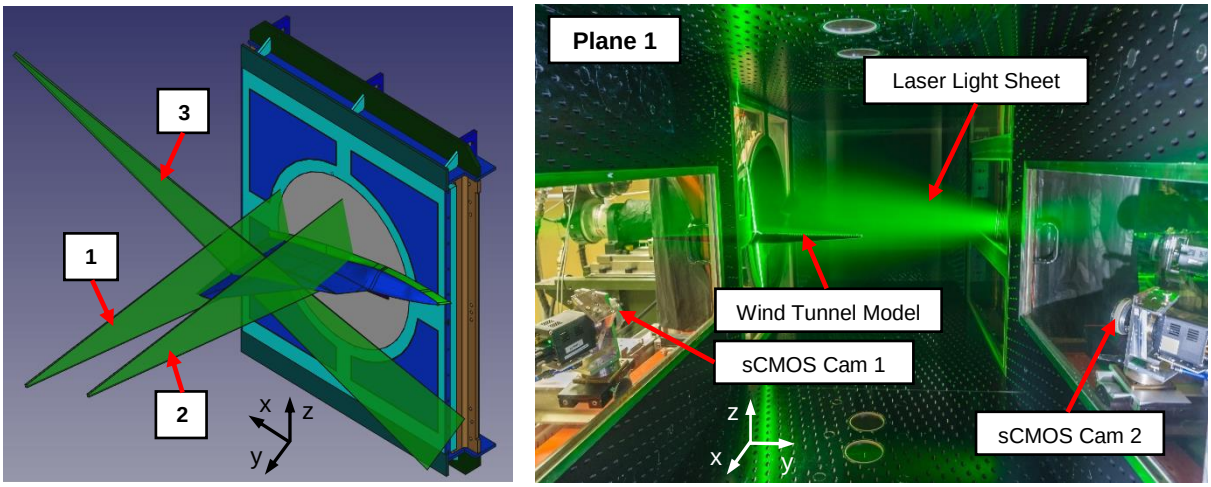

a) PIV measurement planes **b)** Stereo-PIV measurement setup (Photo: J. Agocs)

Figure 2: Stereo-PIV measurement setup of the DLR-F23 in the test section of DNW-TWG

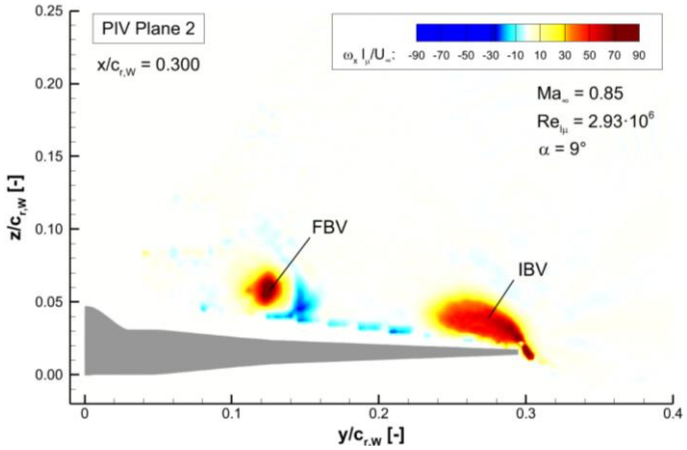

Figure 3: Nondimensional vorticity shown for a PIV-cross flow plane at $x/c_{r,W} = 0.30$ (plane 2); $\alpha = 9°$; $Ma_\infty = 0.85$; $Re_{l_\mu} = 2.93 \cdot 10^6$

References:

[1] J. M. Luckring, N. J. Taylor, S. M. Hitzel. Program Overview: Vortex Interaction Aerodynamics Relevant to Military Air Vehicle Performance. AIAA SCITECH 2022 Forum. January 3-7, 2022, San Diego, CA. DOI: 10.2514/6.2022-0025.

[2] C. M. Liersch, A. Schütte, M. Kalanja. DLR Projekt Diabolo: *Technologien und Entwurf von Kampfflugzeugen der nächsten Generation*. DGLR Netzpublikation. Deutscher Luft- und Raumfahrtkongress 2022. 27.-29. September 2022, Dresden, Deutschland. DOI: 10.25967/570271.

[3] J. Zastrow, F. Oberdieck, U. Henne, C. Klein. *Numerical and Experimental Investigations on the DLR-F23 Combat Aircraft Wind Tunnel Model*. 33rd Congress of the International Council of the Aeronautical Sciences, ICAS 2022, 4.-9. September 2022, Stockholm, Schweden. ISBN 978-171387116-3.

Mitteilung

Fachgruppe: Hyperschallaerothermodynamik

Application of HyperCODA to hypersonic flows around two-dimensional geometries

Chiara Amato*, Stefan Fechter*, Immo Huismann, Tobias Ecker***

German Aerospace Center (DLR)

*Institute of Aerodynamics and Flow Technology, Göttingen

**Institute of Software Methods for Product Virtualization, Dresden

Chiara.Amato@dlr.de, Stefan.Fechter@dlr.de, Immo.Huismann@dlr.de, Tobias.Ecker@dlr.de

Simulating hypersonic flow presents the challenge of describing simultaneous phenomena at different length and time scales. Understanding the relevant physicochemical phenomena within these flows is essential to designing vehicles capable of enduring prolonged survival in environments with high mechanical and thermal loads. The scientific community has developed robust codes that can simulate hypersonic flows using different numerical modeling techniques.

Since 2018, ONERA, DLR, and Airbus have focused their effort on collectively developing a CFD code called CODA (CFD for ONERA, DLR, and Airbus) that is based on the structure and design already employed for the solver Flucs (FLexible Unstructured CFD Software) [1]. This next-generation CFD solver is capable of solving large sparse linear systems derived from the implicit time integration of the RANS (Reynolds-averaged Navier-Stokes) equations with the assumption of a single perfect gas on three-dimensional structured and unstructured grids using either second-order finite-volume or higher-order Discontinuous-Galerkin (DG) discretization.

CODA has been extensively used to solve subsonic and transonic flow regimes because the code has been designed mainly for avionics applications. However, for hypersonic applications, DLR has been internally developing an extension, HyperCODA [2, 3, 4], that expands CODA's physical and numerical modeling capabilities to deal with high enthalpy flows and gas mixtures. This paper aims to explore HyperCODA capabilities and validate its accuracy in solving hypersonic flows around canonical two-dimensional geometries. Making use of the advanced technologies available at DLR, we want to use HyperCODA to solve test cases relevant to the industry and hypersonic research and compare the solutions to DLR CFD solver TAU results and the experiment data from the High Enthalpy Shock Tunnel Göttingen (HEG).

A comparative analysis will be conducted on the solution for a two-dimensional cone-flare and the STORT [5] fin configuration [6]. In particular, the comparison will focus on studying eventual discrepancies in the solutions, comparing computational efficiency and grid requirements in terms of refinement and convergence time, and identifying potential areas of improvement and expansion of HyperCODA capabilities. Figure 1 shows a preliminary comparison of HyperCODA and TAU solutions for a hypersonic flow around a 7/40 degree large cone flare, flying at Mach 5.9 in a single perfect gas. Table 1 summarizes the initial and boundary conditions used for this test case. The free-stream conditions are equivalent to a flight at around 17.75 km of altitude. This preliminary comparison shows good agreement between the solutions. Minor differences are present in the shock interactions and the expansion regions near the outflow. Further investigations are needed to understand the reasons and address them.

References

[1] Leicht, T., Jägersküpper, J., Vollmer, D., Schwöppe, A., Hartmann, R., Fiedler, J., and Schlauch, T., "DLR-Project Digital-X-Next Generation CFD Solver'Flucs'," 2016.

Table 1: Initial and boundary conditions for the 7/40 cone-flare test case

Free-stream Pressure	7808 Pa
Free-stream Temperature	244.38 K
Wall Boundary Condition	Viscous Isothermal Wall
Wall Temperature	300 K

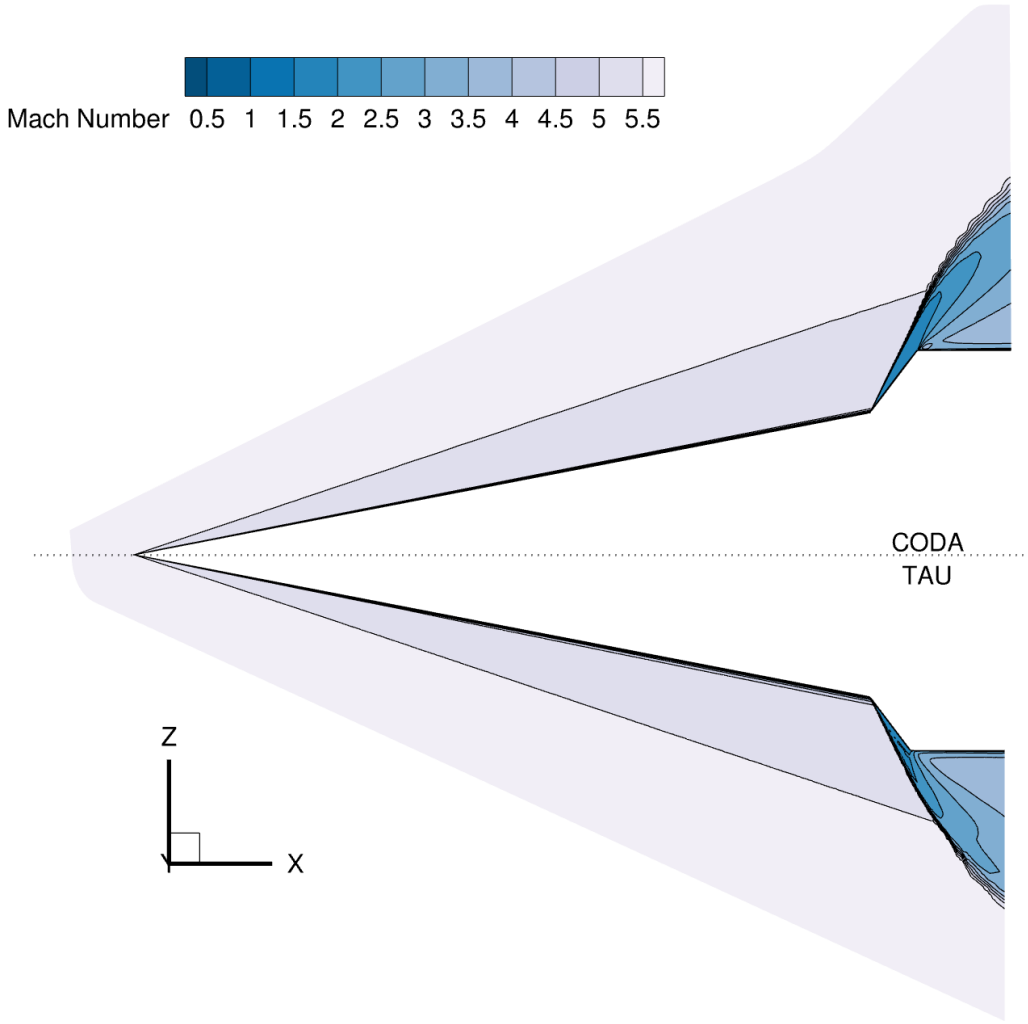

Figure 1: Comparison of HyperCODA and TAU solutions for a perfect gas flow around a cone-flare at Mach 5.9

[2] Huismann, I., Fechter, S., and Leicht, T., "HyperCODA–Extension of Flow Solver CODA to Hypersonic Flows," *HyperCODA–Extension of Flow Solver CODA Towards Hypersonic Flows*, Vol. 13, 2020.

[3] Huismann, I., Fechter, S., and Leicht, T., "HyperCODA–extension of flow solver CODA towards hypersonic flows," *New Results in Numerical and Experimental Fluid Mechanics XIII: Contributions to the 22nd STAB/DGLR Symposium*, Springer, 2021.

[4] Fechter, S. and Huismann, I., "HyperCODA – Extension of Flow Solver CODA Towards Rocket Flows," *2022 9th European Conference for Aerospace Sciences (EUCASS)*, 2022.

[5] Gülhan, A., Willems, S., and Klingenberg, F., "Stort Flight Experiment for High Speed Technology Demonstration," 2021.

[6] Ecker, T., Martinez Schramm, J., Schmidt, L., Surujhlal, D., Wagner, A., and Horchler, T., "Numerical and experimental investigation of the shockwave boundary layer interaction of laminar/transitional flow past a sharp fin," *10th EUCASS–9th CEAS 2023*, 2023.

Mitteilung

Fachgruppe: Hyperschallaerothermodynamik / Turbulenz und Transition

Vorstudien zur DNS einer transitionellen Plattengrenzschicht mit schräg einfallendem Verdichtungsstoß mittels NSMB

Jan Niklas Kuhnlein[1], Alexander Theiß[1], Christian Schnepf[1], Christian Stemmer[2]
[1] DLR Göttingen, Institut für Aerodynamik und Strömungstechnik, Abteilung Hochgeschwindigkeitskonfigurationen, Bunsenstraße 10, 37073 Göttingen
[2] Lehrstuhl für Aerodynamik und Strömungsmechanik, Technische Universität München, Boltzmannstr. 15, 85748 Garching bei München
jan-niklas.kuhnlein@dlr.de

Einleitung: In Einläufen von Staustrahltriebwerken oder an Steuerflächen von Überschallflugkörpern können komplexe Stoß-Grenzschicht-Wechselwirkungen (SGWW) auftreten, welche die weitere Entwicklung der Strömung maßgeblich beeinflussen. Insbesondere bei transitionellen Grenzschichten führen SGWW zu einer deutlichen Intensivierung der transitionsbedingten Wärmelasten gegenüber einer Grenzschichtströmung ohne Verdichtungsstoß. Dieser Effekt ist nicht vernachlässigbar und ist etwa bei der thermischen Auslegung des Fluggeräts zu berücksichtigen. Lunte und Schülein haben zuletzt umfangreiche Windkanalexperimente zu diesem Thema für eine transitionelle Plattengrenzschicht bei Mach 6 durchgeführt [1]. Mittels direkter Numerischer Simulation (DNS) soll das Experiment aus [1] nachgebildet werden. Mithilfe der numerischen Datensätze soll ein besseres physikalisches Verständnis über die Erhöhung der Wandwärmeströme in transitionellen SGWW erlangt werden. Hierzu muss zunächst nachgewiesen werden, dass die Strömung in der DNS mit der des Experiments übereinstimmt. Dies gilt auch für die Referenzströmung ohne Einwirkung des Verdichtungsstoßes. Im Rahmen der vorliegenden Arbeit werden die hierfür notwendigen Schritte erörtert und die beim Aufbau der Simulation aufgetretenen Schwierigkeiten behandelt.

Vorgehensweise und Methodik: Analog zu den Experimenten [1], an denen sich diese Arbeit anlehnt, wird die Strömung über einer ebenen Platte mit einem Vorderkantenradius von 0,1 mm betrachtet. Die Einheitsreynoldszahl der Untersuchung beträgt $8*10^6$ /m bei einer Machzahl von 6. Die Simulationen werden mit dem Finite-Volumen-Strömungslöser Navier-Stokes Multi Block (NSMB) durchgeführt, welcher bereits, unter anderem in [2], erfolgreich zur Untersuchung von SGWW im Hyperschall verwendet wird. Für die räumliche Diskretisierung wurde auf Basis verschiedener Voruntersuchungen ein Zentralschema vierter Ordnung ausgewählt. Die Geometrien der Berechnungsgebiete und die vorliegende Strömungstopologie sind in Abbildung 1 skizziert: Die DNS wird nur auf einem Ausschnitt des Strömungsgebiets durchgeführt. Für dieses Vorgehen werden Strömungsprofile am linken Rand der DNS-Domain benötigt. Da sich an der abgerundeten Plattenvorderkante eine abgelöste Kopfwelle bildet, können hier keine analytisch bestimmten Strömungsprofile vorgegeben werden. Die genutzten Profildaten stammen stattdessen aus einer vorangegangenen 2D-Simulation inklusive Vorderkante. Ein wichtiger Schritt für die DNS einer SGWW ist die Erzeugung einer Grundströmung ohne ungewollte numerische Störungen im Rechengebiet. Die Grundströmung wurde mittels parabolischer Stabilitätsgleichungen (PSE) analysiert und Frequenzen ausgewählt, welche im Gebiet der DNS eine Anfachung erfahren. Nach Erweiterung der vorhandenen instationären

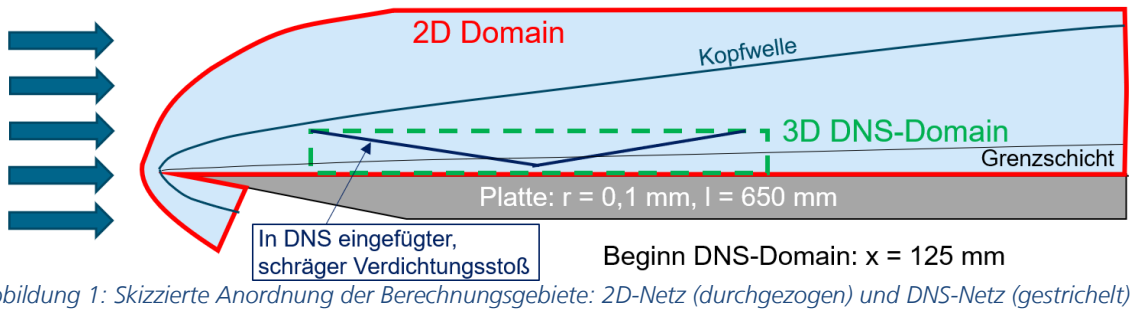

Abbildung 1: Skizzierte Anordnung der Berechnungsgebiete: 2D-Netz (durchgezogen) und DNS-Netz (gestrichelt)

Randbedingung in NSMB um eine ortsabhängige Phasenverschiebung wurden die entsprechenden Moden der PSE als Störung der Grundströmung am Einlaufrand aufgeprägt. Mit Hilfe dieser Störungen soll der, dem Experiment entsprechende, transitionelle Zustand der Plattengrenzschicht erzeugt werden.

Ergebnisse: Die erarbeiteten Rechennetze, Randbedingungen und Einstellungen in NSMB für die Strömung ohne SGWW, sowie die Validierung der ungestörten Grundströmung mittels experimenteller Daten und TAU-Simulationen aus [1] werden im Vortrag vorgestellt. Das Anfachungsverhalten eingebrachter Störungsmoden im gewählten Aufbau der DNS stimmt sehr gut mit den PSE-Ergebnissen überein. In Abbildung 2 ist die Entwicklung der Temperaturfluktuationen in DNS und PSE bei einer Störungsfrequenz von 123 kHz gegenübergestellt. Der in Abbildung 2(a) dargestellte N-Faktorverlauf bestätigt eine gute Übereinstimmung des Dämpfungs- und Anfachungsverhaltens zwischen PSE und DNS. Der Amplitudenverlauf der Temperaturfluktuation in wandnormaler Richtung ist in Abbildung 2(b) für den Einlaufrand gezeigt. Die gute Übereinstimmung zwischen PSE und DNS demonstriert hier das erfolgreiche Einfügen der gewünschten Störung. Ein zweiter Schnitt, 0,1 m weiter stromab, ist in Abbildung 2(c) dargestellt und bestätigt die korrekte Entwicklung der eingekoppelten Mode in der DNS.

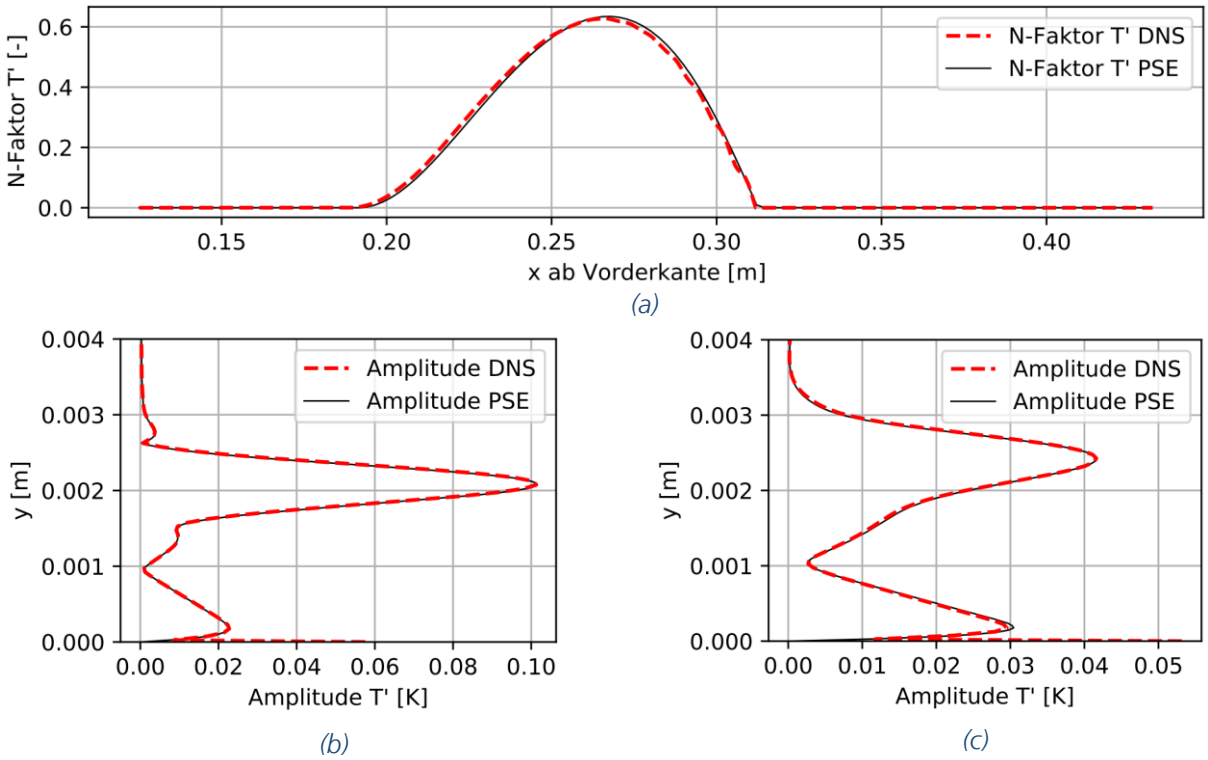

Abbildung 2: Anfachungsverhalten der 123 kHz-Mode anhand der Temperatur. N-Faktor-Verlauf in Strömungsrichtung (a) und Wandnormale Amplitudenverteilung am Einlass (b), sowie 0,1 m stromab des Einlasses der DNS (c)

Weiteres Vorgehen: Es soll eine gute Übereinstimmung mit den Experimenten, hinsichtlich des Transitionsbeginns und der Verteilung der Wärmestromdichte, erreicht werden. Hierzu werden die Störungsfrequenzen und -amplituden variiert und gegebenenfalls mehrere Störungsmoden überlagert. Parallel dazu wird, zur Vorbereitung der anstehenden Untersuchung der SGWW, die Einbringung des schrägen Verdichtungsstoßes über die Randbedingung getestet. Erste Ergebnisse hierzu werden im Vortrag präsentiert.

[1] Lunte, J. und Schülein, E. (2019). *Heat transfer amplifications in transitional shockwave/boundary-layer interactions*, AIAA 2019-3440. AIAA Aviation 2019 Forum. https://doi.org/10.2514/6.2019-3440

[2] Giuseppe Chiapparino, Christian Stemmer, *Numerical investigation of a Mach 6 hypersonic laminar flow on two-dimensional cold-wall compression corners with controlled surface roughness*, International Journal of Heat and Fluid Flow, Volume 94, 2022, 108937, https://doi.org/10.1016/j.ijheatfluidflow.2022.108937

Mitteilung

Fachgruppe: Hyperschallaerothermodynamik

DNS of Transitional Flows at Hypersonic Speeds

Friedrich Ulrich, Giuseppe Chiapparino, Christian Stemmer
Lehrstuhl für Aerodynamik und Strömungsmechanik, Technische Universität München,
Boltzmannstr. 15, 85748 Garching b. München
Christian.Stemmer@tum.de

At TUM, Direct Numerical Simulations (DNS) are used to investigate the laminar-turbulent transition process under re-entry conditions for several geometrical configurations. The simulations are mainly performed with the code NSMB on HPC systems provided by LRZ.

Hypersonic vehicles feature compression-corner geometries such as ramps (in engine intakes or control surfaces of scramjets and re-entry vehicles) and flared geometries (in launchers or missiles) generate strong oblique shock waves close to the surface of the vehicle. As a consequence, Shock-Wave/Boundary-Layer Interaction (SWBLI) creates a complex flow pattern that includes two shock waves at separation and reattachment of the boundary layer and a recirculation bubble at the wall. This flow distribution alters the local pressure and heat loads, impacting the design process of the structure and TPS of the spacecraft. Currently, two SWBLI configurations are being investigated.

Regarding the ramp geometry, the current efforts focus on the effects of discrete roughness elements upstream of the bubble for a Mach 6 flow both in terms of steady modifications to the base flow and as a mean to influence the laminar-turbulent transition process occurring on the ramp downstream of reattachment. In the wake of the roughness patch, counter-rotating vortices form and generate a mushroom-shaped structure on the ramp (figure 1). As shown in [1], roughness parameters, such as position and shape, influence the steady features of the vortical structure downstream of reattachment. The roughness-induced unsteady effects are the object of the currently ongoing simulations. The second configuration under consideration is a Mach 5 flow over a cylinder-flare geometry. The investigation is a part of a larger, multi-national effort that aims at investigating the effect of wind-tunnel background noise and cylinder leading-edge bluntness on the transitional SWBLI observed in two different experiments [2,3] characterized by comparable Reynolds numbers. Specifically, DNS are being performed to evaluate the freestream noise effects at TUM. Preliminary results have confirmed that the background noise has a noticeable impact on the boundary-layer separation position and the Stanton-number distribution at reattachment (figure 2).

A second geometry under investigation is an Apollo-like capsule. In particular, the focus lies on transition due to ablation-induced roughness during re-entry conditions. As shown in Di Giovanni and Stemmer [4], a cross-flow-like vortex can be observed in the wake of a random distributed roughness patch behind the bow shock. This vortex destabilizes the flow, allowing unsteady disturbances to grow in shear-flow regions of the vortex. Recently, a large DNS dataset (over 9000 simulations) containing randomly distributed roughness patches was generated. Each individual patch is created combining multiple sinusoidal base functions. The dataset is used to train machine-learning algorithms to predict the maximum streamwise vorticity and other flow parameters relevant to transition. In Ulrich and Stemmer [5], it was observed that a Convolutional Neural Network (CNN) can predict the streamwise vorticity using only an image of the roughness patch as an input. This approach showed that the mean average error of the CNN was reduced by 30% compared to the mean prediction error of a Deep Neural Network trained on roughness parameters alone.

Further, unsteady simulations are performed by introducing unsteady disturbances with ‘dangerous’ patches selected from our database potentially triggering laminar-turbulent transition more effectively. An isosurface contour of the Q-criterion $Q=5.5 \cdot 10^7$ [-] of the unsteady cross-flow vortex is displayed in figure 3. Finger-like structures emerge at x=0.1 m and break down further downstream. The disturbance evolution in the streamwise direction will be analyzed with a two-dimensional Fourier transformation in time and space.

STAB

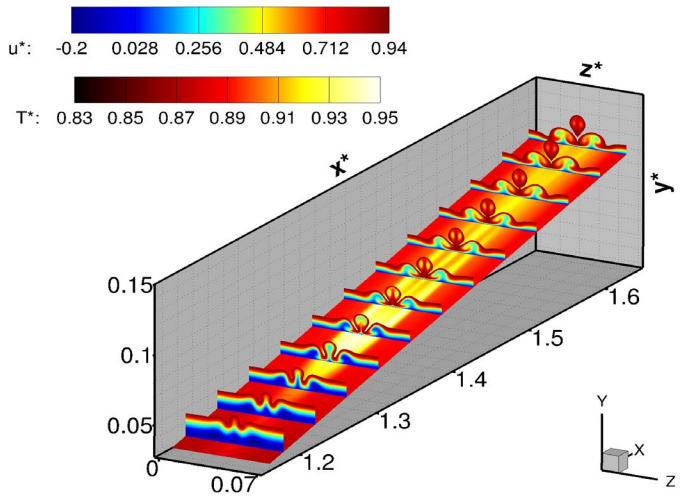

Figure 1: Mach 6 flow over a planar ramp with mushroom-shaped vortices after reattachment

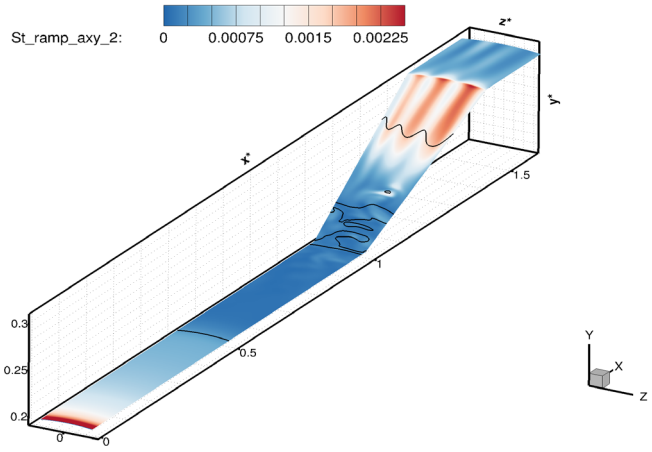

Figure 2: Mach 5 cylinder-flare case [2] for quiet conditions

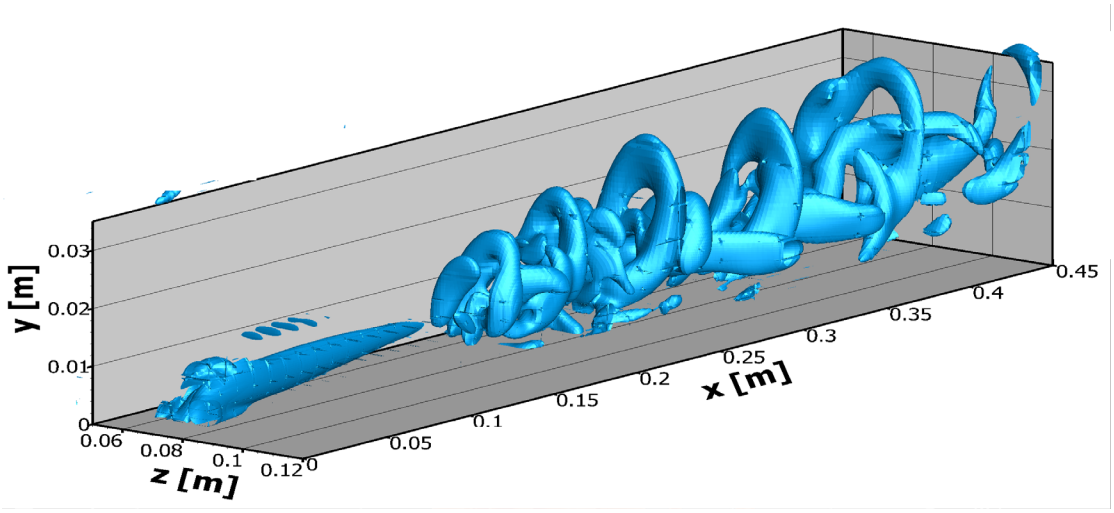

Figure 2: Isosurface contour of the Q-criterium $Q=5.5 \cdot 10^7$ [-] of the unsteady cross-flow vortex (from [5])

References

[1] Chiapparino, G. and Stemmer, C. (2023). "Numerical investigation of a Mach 6 laminar shock-wave/boundary-layer interaction on a two-dimensional ramp with 3D controlled surface roughness." International Journal of Heat and Fluid Flow, Vol. 103, 109193. https://doi.org/10.1016/j.ijheatfluidflow.2023.109193

[2] Lugrin, M., Nicolas, F., Severac, N., Tobeli, J.-P., Beneddine, S., Garnier, E., Esquieu, S. and Bur, R. (2022). "Transitional shockwave/boundary layer interaction experiments in the R2Ch blowdown wind tunnel." Experiments in Fluids, Vol. 63, Art.Nr. 46. https://doi.org/10.1007/s00348-022-03395-9

[3] Threadgill, J., Singh, A., Roskelley Garcia, A. and Little, J. (2023). "Boundary Layer Separation on a Hollow-Cylinder/Flare at Mach 5." AIAA SciTech Forum. https://doi.org/10.2514/6.2023-1246

[4] Di Giovanni, A., and Stemmer, C. (2018). "Cross-flow-type breakdown induced by distributed roughness in the boundary layer of a hypersonic capsule configuration", Journal of Fluid Mechanics, 856, pp. 470–503. doi:10.1017/jfm.2018.706

[5] Ulrich, F., and Stemmer, C. (2023). „Unsteady evolution of distributed roughness-induced vortices under re-entry conditions", CEAS Space Journal 2023, https://doi.org/10.1007/s12567-023-00510-2

Mitteilung

Fachgruppe: Multidisziplinäre Optimierung

Thema: High-fidelity CFD-based Shape Optimization of a Blended-Wing-Body Aircraft for Improved Aerodynamic Performance, Considering Engine Integration Effects

Achyuth Attravanam

German Aerospace Center (DLR), Institute of Aerodynamics and Flow Technology

The technology of an unconventional aircraft such as Blended Wing Body (BWB) has been a holy grail for over two decades in the aircraft industry because of its potential of increasing lift, reducing noise and minimizing drag, thus increasing overall efficiency. The development of such unconventional aircraft requires high-fidelity numerical simulations and shape optimization. This study is an extension to the DLR – SIAM project (Schal-Immisions-Armes Mittlestreck- flugzeug eng: low-noise-emission medium range aircraft) (Fröhler, 2022) which deals with the development of a BWB aircraft model and investigates the feasibility of bringing it into service. This study uses the resulting T-configuration of the SIAM project and aims to improve its aerodynamic efficiency using shape optimization with a focus on engine integration.

To perform the shape optimization of the aircraft, the half model of the BWB aircraft is parameterized by considering multiple sections of airfoil shapes across the body. As the engine is mounted on the top of the body, it is important to consider engine integration effects on the flow over the body. Thus, the area below the engine is also parameterized. To be able to trim the aircraft during cruise, the horizontal tail plane (HTP)-angle is parameterized as well. The parameterization is performed in CATIA (Dassault Systems, 2023), and to streamline the optimization process, a reduced-order model of the parametric changes (CAD-ROM) is built to reconstruct the shape-displacement field which replaces CAD models during optimization. The CAD-ROM is built using the in-house tool DLR-SMARTy (Merle, 2023), from the point-clouds of the CAD model. To train the CAD-ROM, a Design of Experiments (DoE) is conducted on the point-clouds using SOBOL sequence, thus covering the design space evenly. Here two CAD-ROMs are setup, one representing the outer shape changes and the other representing the HTP angle deformation. The CFD mesh is generated using ANSA (Beta Simulation Solutions, 2023) and the flow computation is performed using DLR-TAU (Schwamborn, 1999).

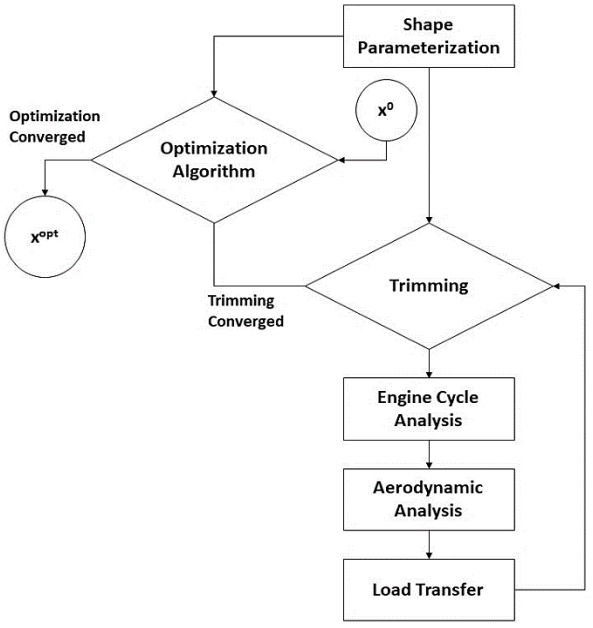

Figure 1: Optimization Process

The design process is driven by an unconstrained gradient-based optimization algorithm, where the trim constraints are implemented implicitly. Due to the lack of the suitable engine model for the trim process, the trimming of the aircraft is not implemented during the optimization. The lower and upper bounds considered during the optimization are:

±3° for wing twists, ±5° for the HTP angle and ±20 mm for remaining design variables that control the parameterized profiles across the BWB. The optimization process is outlined in the Figure 1.

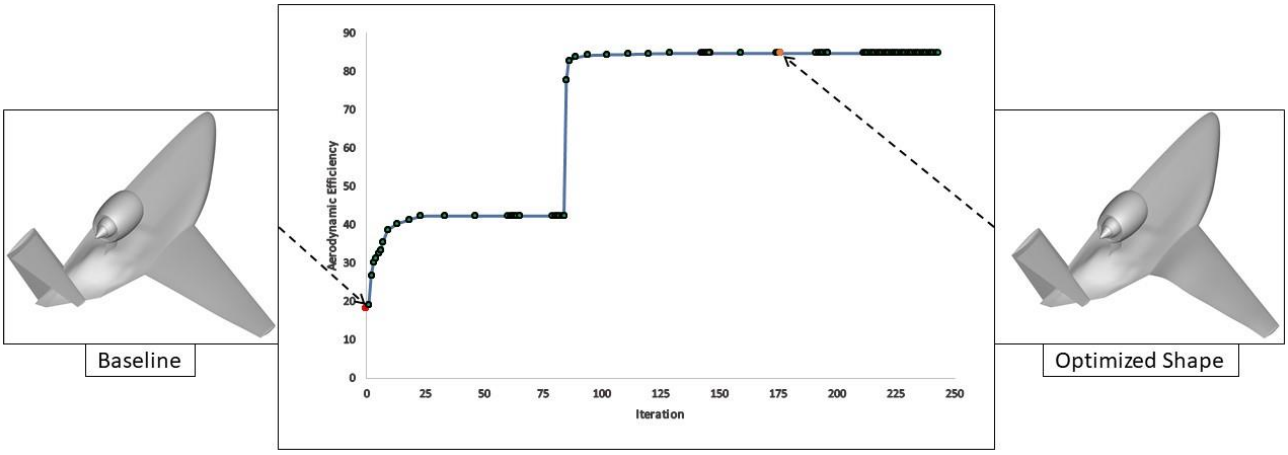

Figure 2: Optimization History with Baseline and Optimized Design

The aerodynamic shape optimization showed a considerable improvement in the aerodynamic efficiency, as shown in Figure 2 and the outputs were eventually validated in a multidisciplinary design analysis (MDA) of fluid-structure coupling at critical design points using Airbus' Lagrange suite for structural MDO. The MDA analysis showed as well considerable improvement in the aerodynamic efficiency.

The study entails geometric changes observed at critical design points of the shape optimization, and their resulting flow characteristics, which are validated using CFD-CSM coupling.

References

Beta Simulation Solutions. (2023, 09 05). *Beta Simulation Solutions ANSA*. Retrieved from Beta CAE Systems: https://www.beta-cae.com/ansa.htm

Dassault Systems. (2023, 09 05). *Dassault Systems CATIA*. Retrieved from Dassault Systems: https://www.3ds.com/de/produkte-und-services/catia/

Fröhler, M. I. (2022). Conceptual Aircraft Design Activities Related to Blended Wing Body Configurations in the Scope of the DLR Project SIAM. *9th European Conference for Aeronautics and Space Sciences*, 15.

Merle, A. a. (2023). Adjoint high-dimensional aircraft shape optimization using a CAD-ROM parameterization. *CEAS Aeronautical Journal*, [729-738].

Schwamborn, D. a. (1999). DLR-TAU Code - an Overview. *1st ONERA/DLR Aerospace Symposium* (pp. S4--2-S4-10). Paris: DLR.

Mitteilung

Projektgruppe/Fachkreis: Multidisziplinäre Optimierung und neue Konfigurationen

Adjoint gradient-based aerodynamic optimization with non-differentiated CAD-in-the-loop and mesh regeneration

Časlav Ilić†, Patrick Wegener

German Aerospace Center (DLR)
Institute of Aerodynamics and Flow Technology, Lilienthalplatz 7, 38108 Braunschweig
†Corresponding author, caslav.ilic@dlr.de

Despite more than two decades of research in aerodynamic optimization for aircraft design, there are still numerous competing approaches and methods. The adjoint gradient-based approach is able to handle efficiently a large number of design parameters (hundreds to thousands), but typically relies on mesh deformation [1, 3], which limits achievable complexity geometry and robustness on large geometry changes. On the other hand, derivative-free and response-surface approaches are often used with mesh regeneration methods and applied to larger geometry changes, but suffer from a limited number of design parameters (a few tens at most) [4, 2].

A further question is how to include commercial, black-box CAD software, which enable highly complex geometry modelling but typically does not provide features important for optimization (such as derivatives). Sometimes an offline ROM-generation is used to this end [3], resulting in a very fast and fully derived geometry representation inside the optimization loop, but requiring a large number of samples (in case of many design parameters) and having up-front unclear accuracy.

In the current work, the classical adjoint gradient-based approach is extended to employ a black-box CAD application (Dassault CATIA) directly in the optimization loop and to perform mesh regeneration on every geometry update. CAD-in-the-loop provides maximum accuracy at every step and reduces to minimum offline processing before the optimization starts. Mesh regeneration can enable extensive geometry changes (such as in wing span or sweep) and robust handling of difficult topological features (such as engine nacelle-pylon-wing area). The drawback of these two elements is a non-straightforward way of computing and employing geometry derivatives.

The demonstration case is based on a short/mid-range transport aircraft with a very high aspect-ratio, the DLR-F25 (Fig. 1), developed within the LuFo VI-2 project VirEnfREI funded by the German Ministry for Economic Affairs and Climate Action (BMWK). The aircraft wing twist and profile parameters are optimized to minimize fuel consumption on an evaluation mission (Mach number 0.78, lift coefficient 0.59, range 1500 km), under constraints of trimmed forces (for balanced horizontal flight), and constant spanwise profile thickness and position of center of lift (for favorable structural properties). The flow solver TAU is used, with RANS flow model and Spallart-Almaras turbulence model.

Specifically, the contributions that will be presented are as follows:

- Topologically constant "point cloud" within the CAD model and its use for finite-difference-regressed estimation of surface mesh-to-geometry derivatives.
- Geometric parametrization with a focus on constraint satisfaction, with specific parameters allotted as controls for specific constraints. (E.g. a hybrid b-spline-thickness profile parametrization as on Fig. 2.)
- A custom gradient optimizer, with a split constraint satisfaction and objective minimization steps, to handle noisy constraint and objetive derivatives due to mesh regeneration.
- Resilient, parallel, many client-server communication between an HPC cluster where the flow solver runs and a workstation where the CAD software runs.

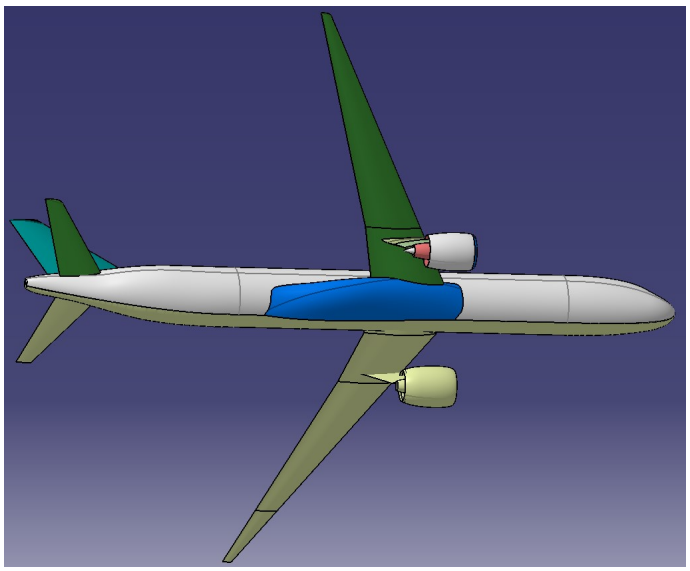

Figure 1: The DLR-F25 configuration modelled in CATIA.

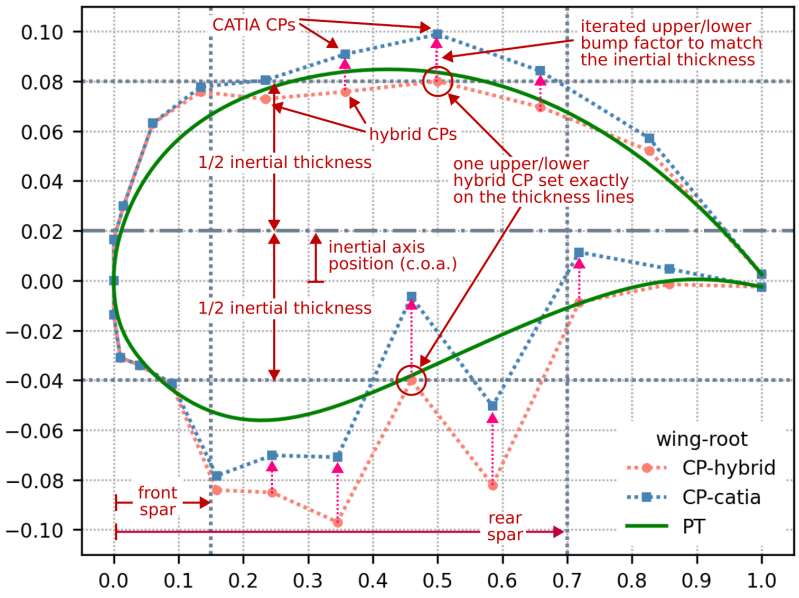

Figure 2: Hybrid b-spline-thickness profile parametrization.

References

[1] J. Brezillon and R. P. Dwight. Applications of a discrete viscous adjoint method for aerodynamic shape optimisation of 3D configurations. *CEAS Aeronautical Journal*, 2011.

[2] D. Haar and J. Brezillon. Engine integration based on multidisciplinary optimisation technique. *CEAS Aeronautical Journal*, 2011.

[3] A. Merle, A. Ronzheimer, P. Bekemeyer, S. Görtz, S. Keye, and L. Reimer. Gradient-based optimization of a flexible long-range transport aircraft using a high-dimensional CAD-ROM parameterization. In *Deutscher Luft- und Raumfahrtkongress 2018*, 2018.

[4] A. Ronzheimer, F. J. Natterer, and J. Brezillon. Aircraft wing optimization using high fidelity closely coupled CFD and CSM methods. In *13th AIAA/ISSMO Multidisciplinary Analysis Optimization Conference*, 2010.

Mitteilung

Projektgruppe/Fachkreis: Multidisziplinäre Optimierung - Neue Konfigurationen

Power Balance Analysis of Wingtip-mounted Propeller and Distributed Propulsion Configurations

Michael Schollenberger, Thorsten Lutz, Ewald Krämer
Institut für Aerodynamik und Gasdynamik (IAG) , Universität Stuttgart
Pfaffenwaldring 21, 70569 Stuttgart
schollenberger@iag.uni-stuttgart.de

Introduction

As part of the LuFo project GNOSIS, the aerodynamic interactions at different novel configurations such as distributed propulsion (DP) and wingtip mounted propellers (WTP) are investigated. Due to the propeller slipstream, the increased velocity in it can be used to increase the wing's lift, and it's swirl can be partially recovered by the wing to reduce the induced drag. Thus the aerodynamic efficiency can be increased and finally the required power of the overall aircraft in cruise flight reduced. A series of paramter studies concerning the interaction effect on the wing and propeller coefficients were already published [1]. Therbye Reynolds-Averaged Navier-Stokes (RANS) simulations, were performed with the second order finite volume flow solver TAU, developed by the German Aerospace Center (DLR). The propellers were modeled using boundary condition based steady state Actuator Discs (ACD) with propeller polars as input data [2].

The already presented results are however now adiitional used for a power balance method (PBM) analysis of the flow field.

Methodology - Power Balance Method (PBM)

The power balance method (PBM) is a relatively new approach introduced by Drela [3] to analyze flow fields based on a balancing of mechanical power and energy flows through a specified control volume. Thereby, the PBM leads to a physical distinction of all power sources and losses present in the flow field including their interactions. With the exergy extension of Arntz [4], it is also possible to distinguish between reusable kinetic energy and already lost anergy in the energy flows. Compared to a classical force and momentum based analysis, the PBM can be used instead of a drag-thrust bookkeeping and also to identify unused energy, which is beneficial in flow cases with aerodynamic interactions such as with DP and WTP.

Results and Discussion

A series of flow cases are analyzed with the PBM: from isolated wings and isolated propellers to different WTP and DP configurations. By comparison of the the TAU force and momentum results as input of the left hand site of the PBM equation, and the PBM integration results as input of the right hand site, the accuracy of the PBM can be demonstrated With the thereby validated PBM an analysis is carried out for WTP and DP configuration. The PBM enables for example to calculate the axial and tangential kinetic energies in the wake of the wing and the slipstream of the propeller. By comparison of the slipstream energies before and after the wing or the

comparison of the isolated and installed flow cases, the efficiency of the configurations to recover the energy inside the propeller slipstream can be assessed. Exemplary PBM results can be found in Figure. 1 and 2.

The PBM was thus found to be a useful tool to understand the interaction effects in more detail and at an energetical level.

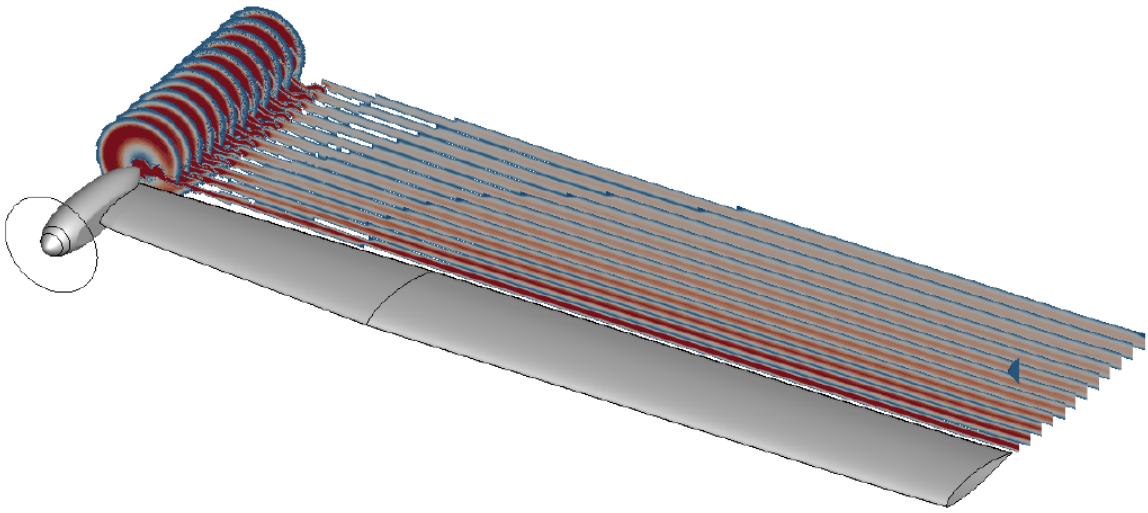

Figure 1: Visualization of the PBM results in the wake of a WTP

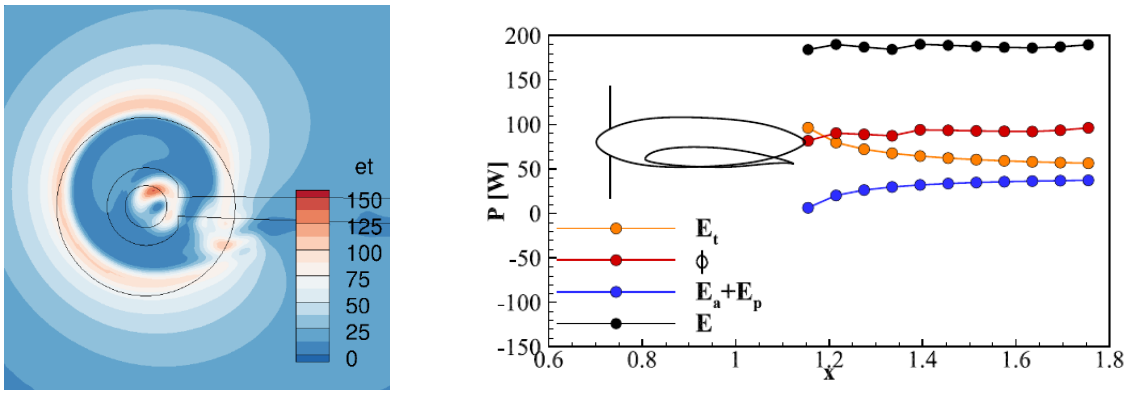

Figure 2: Examples of PBM results

References

[1] **M. Schollenberger, B. Kirsch, T. Lutz, E. Krämer, J. Friedrichs:** Aerodynamic Interactions Between Distributed Propellers and Wings at Electric Commuter Aircraft in Cruise Conditions, DLRK 2022, Dresden

[2] **A. Raichle, S. Melber-Wilkending, J. Himisch**: A new actuator disk model for the TAU code and application to a sailplane with a folding engine, NewResults in Numerical and Experimental Fluid Mechanics VI, 2006

[3] **M. Drela:** Power Balance in Aerodynamic Flows, AIAA journal Vol. 47, No. 7, 2009.

[4] **A. Arntz.:** Exergy-Based Formulation for Aircraft Aeropropulsive Performance Assessment: Theoretical Development, AIAA journal Vol. 53, No. 6, 2015.

Mitteilung

Fachgruppe: Numerische Aerodynamik

Sensitivity Analysis of the Synthetic Turbulence Generator for Vortical Flows

Elrawy Soliman, Tobias Knopp, Philip Ströer, Axel Probst
Institute of Aerodynamics and Flow Technology, DLR
German Aerospace Center, Göttingen, Germany
and
Nils Rathje, Rolf Radespiel
Institute of Fluid Mechanics, TU Braunschweig, Germany

elrawy.soliman@dlr.de

Longitudinal vortices are a common flow phenomenon, emerging downstream of sharp edges and interacting with boundary layers. Accurately predicting the formation and downstream evolution of these vortices is essential for an accurate flow prediction over aircraft. Numerical prediction of longitudinal vortices remains a subject of research, especially due to the unsatisfactory results of RANS modelling [1]. To limit uncertainties associated with complex flow cases, a simplified delta wing test case is investigated (see [1]) using Embedded Wall-Modelled LES (EWMLES).

EWMLES confines the scale-resolving region to the pivotal zones in the domain, with RANS modeling employed across the remaining regions. In contrast to standard non-zonal hybrid RANS-LES methods (HRLM), this strategy demands specific zonal treatment, alongside the introduction of synthetic turbulence at the RANS-(WM)LES interface to accelerate the transition from modelled to resolved turbulence. In such a strategy, the efficacy of RANS-(WM)LES transition is determined by the quality of the injected synthetic turbulence.

The synthetic turbulence generator (STG) of Shur et al. [2] is used in this study. It is based on the superposition of random Fourier modes such that their statistics at the interface are equal to the prescribed Reynolds stress tensor. This study conducts sensitivity analyses on various facets of the STG, with the aim of improving the quality of the synthetic turbulence and thus accelerating the transition to resolved turbulence. Specifically, we investigate the influence of the choice of (i) the length scale and (ii) the energy spectrum when applied to vortical flows.

The length scale in the STG is formulated for boundary layer flows, leaving its applicability to vortical flows uncertain. In the current investigation, we introduce modifications to the length scale in order to evaluate its impact on the development of the longitudinal vortex. To inform our modification, the results of a reference LES simualtion are used to compute the length scale based on the cross-correlation (see Fig. *1*).
Furthermore, the STG formulation adopts a modified Von Kármán spectrum as a target energy spectrum, which reads:

$$E(k) = \frac{(k/k_e)^4}{[1 + 2.4(k/k_e)^2]^{17/6}} f_\eta \, f_{\text{cut}}$$

Where k_e corresponds to the maximum of the spectrum, and f_η and f_{cut} are empirical functions. Although this spectrum is well-suited for 3D turbulence, its applicability to vortical flows, with their effects of rotation on turbulence and quasi-2D behaviour, raises uncertainties. This is assessed by modifying the spectrum to obtain an inertial range with a slope of -3, characteristic of rotating turbulence [3] and indicated by the reference LES results (see *Fig. 1*). Both the standard spectrum and two modified spectra are shown in *Fig. 1*.

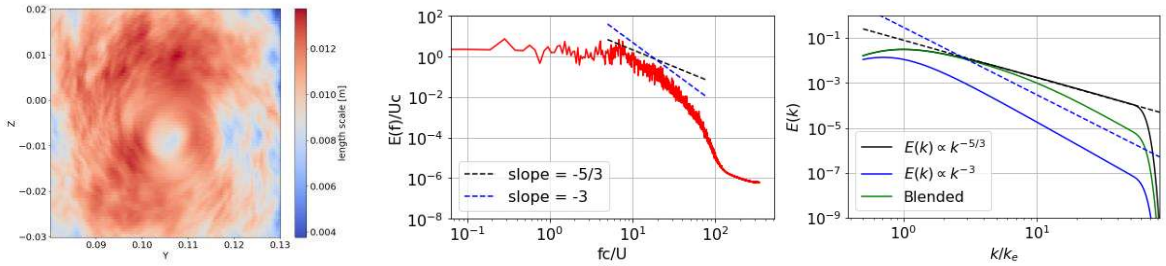

Fig. 1: Turbulent length scale based on the cross-correlation (left). TKE spectrum in the vortex core from the ref LES (middle). Standard Von Kármán spectrum and the proposed modified spectra (right).

The results with the standard STG as well as the modified length scale and energy spectrum are show in Fig. 2. It is observed that the increase of the length scale by a factor two leads to a larger vortex core and larger levels of resolved turbulent kinetic energy. The same is observed for the use of the k^{-3}-spectrum.

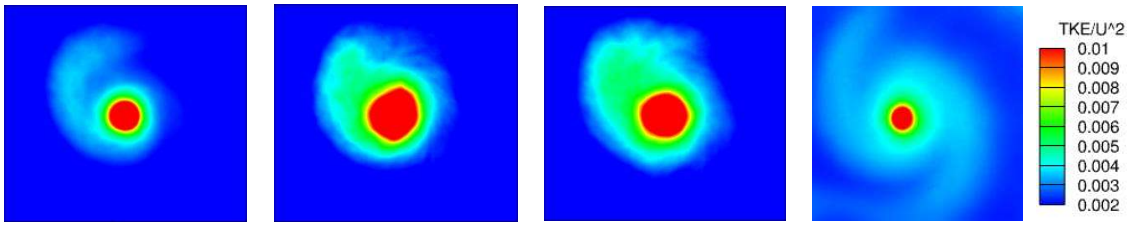

Fig. 2: Normalized TKE of the standard STG (1st column), the modified length scale (2nd column), the modified spectrum of $E(k) \propto k^{-3}$ (3rd column), and the PIV data presented in [1] (4th column).

Through these investigations, this work contributes to the understanding of synthetic turbulence generation and its application to the specific scenario of vortical flows. For the final presentation, results (including the combination of a reduced length scale obtained from the LES reference data and the blended k^{-3}-spectrum) will be shown.

References :

[1] François, D. G., Probst, S., Knopp, T., Grabe, C., Landa, T., & Radespiel, R. (2021). Numerical Simulation of the Streamwise Transport of a Delta Wing Leading-Edge Vortex. *Journal of Aircraft*, *58*(6), 1281-1293.

[2] Shur, M. L., Spalart, P. R., Strelets, M. K., & Travin, A. K. (2014). Synthetic turbulence generators for RANS-LES interfaces in zonal simulations of aerodynamic and aeroacoustic problems. *Flow, turbulence and combustion*, *93*, 63-92.

[3] Yang, X., & Domaradzki, J. A. (2004). Large eddy simulations of decaying rotating turbulence. Physics of Fluids, 16(11), 4088-4104.

Mitteilung

Fachgruppe: Numerische Aerodynamik

Nonlinear Aerodynamic Effects Due To Discrete Gusts on a Transport Aircraft

Johan Feldwisch
Johan.feldwisch@dlr.de
DLR Institute of Aeroelasticity,
Bunsenstrasse 10, 37073 Göttingen

According to certification requirements for transport aircraft, gust loads must be considered for the structural design. The analysis requires unsteady aerodynamic models, which are robust and adequate for the vast range of flight points, mass configura-tions, and gust profiles.

Current industrial methods rely on potential flow based models, which are corrected to match the steady state lift derivatives at multiple sections of the aircraft. However, nonlinear effects such as shock motion and shock induced flow separation are not accounted for in those models. Computational Fluid Dynamic solvers like the DLR-TAU code can solve the Unsteady Reynolds Averaged Navier-Stokes equations, which can predict shock motion and flow separation. While the time-marching methods are too computationally expensive in terms of wall clock time, time linearized methods have been applied for gust loads calculations in academia and industry [1,2,3]. However, those time linearized models seem to underestimate cases whith strong shock motion and attached flow [1,2]. For cases with large regions of detached flow, time linearized models overestimate the aerodynamic loads [1].

This work investigates the gust induced effect of shock motion and flow separation at two different angle of attacks for the XRF1 research aircraft. Furthermore, rigid body motion and structural deformation mitigate the aerodynamic responses. Thus the influence of rigid body motion and structural deformation is studied as well.

Three different gust lengths (short, medium, long) according to the CS-25 regulations are computed for the time-linearized and time-marching methods based on the URANS equations. The time-linearization is achieved with the Linear Frequency Domain (LFD) solver of the DLR-Tau Code. The turbulence is modeld by the negative Spalart-Allmaras model. The gust is realized by the Field Velocity Method and the rigid body motion is imposed via the external motion module.

The results confirm the observation of [1,2], namely that the time-linearized method does not yield lower aerodynamic loads for cases with only mild flow separation but with shock motion (Figure 1). For cases where larger regions of the wing flow are detached, the aerodynamic lift is reduced and hence the aerodynamic loading is lowered compared to the linearized approach (Figure 2). Also, aerodynamic loads are mitigated by including rigid body and elastic motion. The elastic motion can alter the severity of flow separation and therefore lead to cases where the time-linearized method does not over predict the aerody-namic loads anymore.

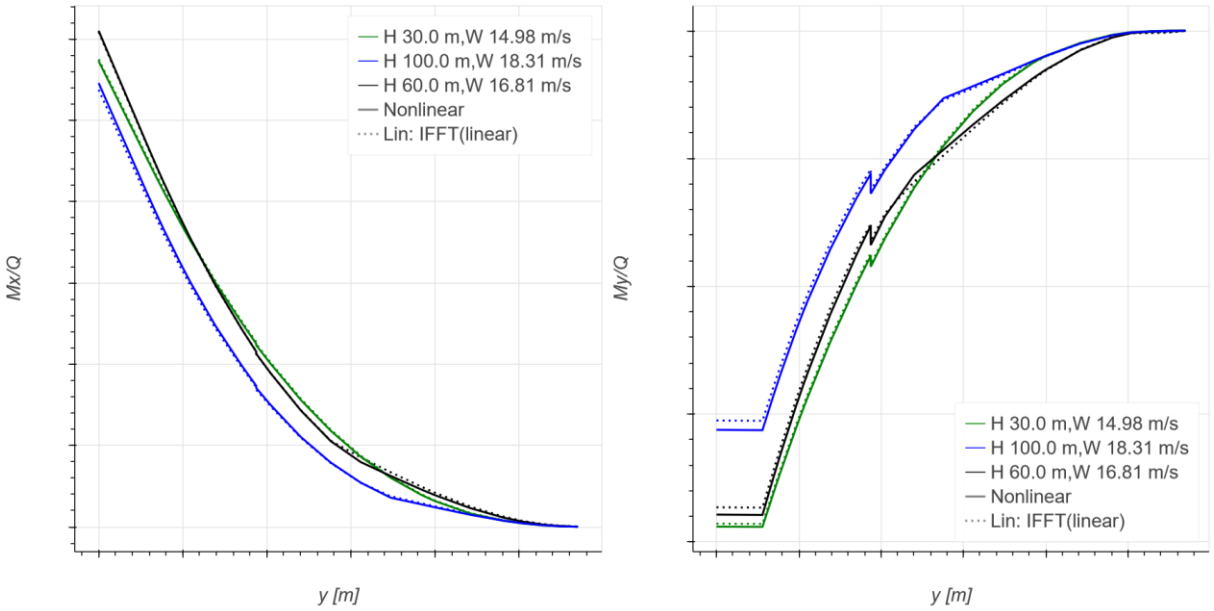

Figure 1 Spanwise distribution of the maximum bending moment and minimum torsion moment for the linear and nonlinear calculation with mostly attached flow.

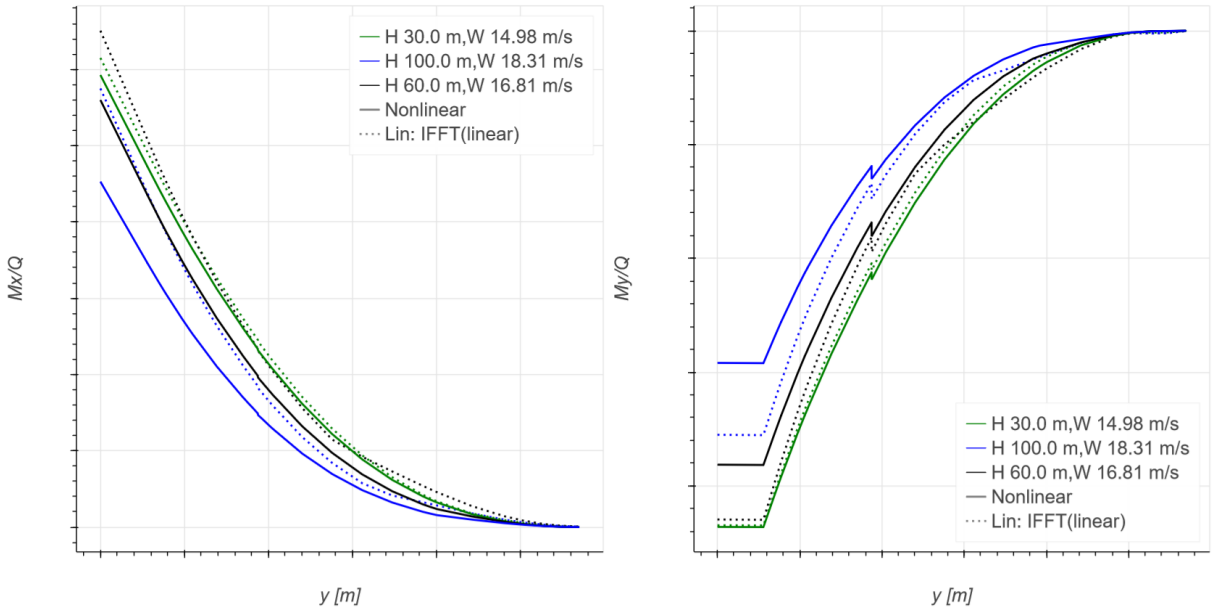

Figure 2 Spanwise distribution of the maximum bending moment and minimum torsion moment for the linear and nonlinear calculation with large regions of detached flow.

Literaturverzeichnis

1. **Friedewald, Diliana.** Large-Amplitude Gusts on the NASA Common Research Model. *Journal of Aircraft.* 2023.

2. *Quantification of nonlinear effects in gust load prediction.* **Kaiser, Christoph and Quero, David and Nitzsche, Jens.** Savannah, GA (USA) : AIAA, 2019. IFASD 2019 - International Forum on Aeroelasticity and Structural Dynamics.

3. *Linearized Unsteady CFD for Gust Loads with TAU .* **Weigold, Wolfgang und Stickan, Bernd und Travieso-Alvarez, Inocencio und Kaiser, Christoph und Teufel, Patrick.** Milano : s.n., 2017. IFASD 2017 - International Forum on Aeroelasticity and Structural Dynamics.

Mitteilung

Fachgruppe: Numerische Aerodynamik

Identification of Buffet Onset by means of Global Stability Analysis

Alberto Franco, Michael Werner, Stefan Hein
DLR, Bunsenstrasse 10, 37073 Goettingen
Juan.franco@dlr.de

Motivation:
The transonic buffet phenomenon can limit the flight envelope of commercial aircraft for certain cruise conditions in terms of angle of attack for a given Mach number and Reynolds number. It consists of the oscillation of the shock on the suction side of the wing, coupled with variations in size of the flow separation. These oscillations change the pressure distribution around the wing, inducing lift and drag variations. Usually, the structural motion of the wing is completely neglected [1]. In this sense, the buffet phenomenon is *purely* a fluid instability problem [2]. Numerically, unsteady Reynolds-Averaged Navier-Stokes (URANS) simulations are used to determine at which parameter combination (usually Mach number, angle of attack, Reynolds number) the onset of buffet phenomenon appears. Alternatively to the computationally expensive URANS simulations, steady RANS computations combined with Global Stability Analysis (GSA) are able to link the appearance of an unstable global mode with the transonic buffet onset [2].

Objective:
The present work aims for validating the capabilities of the GSA approach developed at DLR for studying the buffet phenomenon. On a first stage, purely two-dimensional computations are performed, with the purpose of direct comparison with URANS simulations [1] in order the check the feasibility of the GSA for the prediction of buffet onset for several parameter combinations. After that, the numerical investigations are directed to infinite swept wings. In order to limit the increased parametric space of the second part of the research, a particular combination of angle of attack, Mach number and Reynolds number is considered. Several sweep angles and different three-dimensional instability modes will be considered. Main findings found in literature ([3], [4]) will be reproduced in order to verify that our GSA is a valid tool for the study and analysis of the transonic buffet phenomenon on airfoils at swept / unswept conditions.

Methods:
All computations of the steady base flows have been carried out with the DLR TAU code, a three-dimensional finite volume code for the solution of the Navier-Stokes equations on unstructured meshes. Detailed description of the GSA method can be found in the work of Werner and Hein [5]. The OAT15A airfoil is used for all cases. For convenience, the Reynolds number is fixed at $Re = 3 \cdot 10^6$. Flow conditions normal to the leading edge are kept constant when a sweep angle is introduced. Finally, the Spalart-Allmaras turbulence model is employed.

Results:
A very good agreement between URANS [1] and RANS + GSA results was found for 2D cases not only for prediction of the buffet onset (equivalent to the appearance of a complex eigenvalue with negative real part of the linearized Jacobian matrix) for a given Mach number and angle of attack, but also in terms of frequency of the oscillations (temporal evolution of the lift coefficient in URANS simulations vs. imaginary part

of the corresponding complex eigenvalues from GSA). A particular example is shown in **Figure 1**, where buffet onset is determined by varying the angle of attack while the Mach number remains fixed to a value of 0.71. Moreover, on-going activities for infinite swept conditions indicate that the current status of the GSA approach is able to reproduce the main outcomes found in literature ([3],[4]) for three-dimensional buffet modes (aka “buffet cells”). Trends and conclusions for these cases are planned to be shown and discussed.

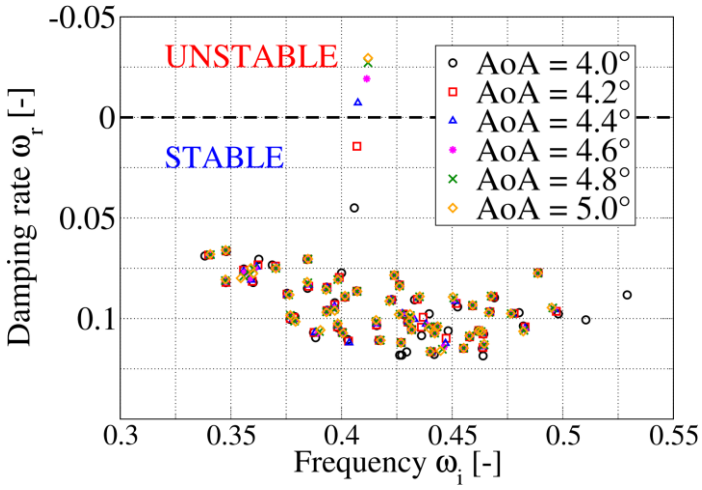

Figure 1. Frequency spectrum obtained from GSA for cases with Mach number 0.71 and varying the angle of attack.

Next steps:
A natural step forward in the validation process of our GSA tool will be to extend the range of studies to fully three-dimensional wings. Moreover, extended parametric studies for infinite swept conditions are planned and will be discussed.

Acknowledgement:
The authors thank J. Nitzsche and C. Kaiser of the Institute of Aeroelasticity (DLR) for the provision of the computational grids. The funding of the presented investigations within the LuFo VI project INTELWI (Intelligent Wing, FKZ: 20A1903L) by the German Federal Ministry for Economic Affairs and Energy (BMWi) is gratefully acknowledged.

References:
[1] Nitzsche, J., Otte, J., Kaiser, C., and Hennings, H.: *The effect of shock control bumps on the transonic flutter and buffeting characteristics of a typical wing section*. In: 19th International Forum on Aeroelasticity and Structural Dynamics, IFASD 2022, 13.-17. June 2022, Madrid, Spain. ISBN 978-840942353-8.

[2] Crouch, J., Garbaruk, A., Magidov, D., and Travin, A.*: Origin of transonic buffet on aerofoils*. Journal of Fluid Mechanics, 628, pp. 357-369. 2009. Doi:10.1017/S0022112009006673.

[3] Paladini, E., Beneddine, S., Dandois, J., Sipp, D., and Robinet, J.-C.: *Transonic buffet instability: From two-dimensional airfoils to three-dimensional swept wings.* Phys. Rev. Fluids, 4, 103906, 2019. Doi:10.1103/PhysRevFluids.4.103906.

[4] Plante, F., and Laurendeau, E.: *Matrix-free global stability analysis framework for 2D and 3D applications*. AIAA AVIATION 2022 Forum, 2022-3227, June 2022.

[5] Werner, M. and Hein, S.: *Global stability analysis of the interaction between a longitudinal vortex and an oblique shock wave*. Proc. Appl. Math. Mech., 23, 2023. Doi: 10.1002/pamm.202200237.

Mitteilung

Projektgruppe/Fachkreis: Numerical Aerodynamics

Experimental and numerical investigation of vortex decay in a rotating system

Filippo Gajo
Institut für Aerodynamik und Gasdynamik der Universität Stuttgart
70569 Stuttgart, filippo.gajo@iag.uni-stuttgart.de

The analysis of the wake decay of the rotorcraft is an important topic to address the physical effects of a rotating system far from the system itself. The rotor flow is strongly affected by the formation and the propagation of the rotor wake, especially by the blade tip vortices. The blade-vortex interactions, which cause strong pressure fluctuations, are mainly related to the excitation of mechanical vibrations on other structures, separation on the flow and eventually impact the acoustics signature of the system. These interaction can have a strong effect on the safety of the rotocraft in peculiar flight conditions such as in ground flight.
The DLR-IAG joint project on the vortex decay aims at comparing the numerical simulations with experimental results in order to validate the capabilities of numerical solvers. A substantial focus lies in examining how the numerical configuration influences the forecast of vortex decay. Within the wake, two distinct phenomena demand consideration: foremost, the macro-instabilities inherent to the principal helical vortex; and secondly, the emergence of secondary vortical structures, significantly amplifying the dissipation rate of the primary tip vortex (see Fig. 1).

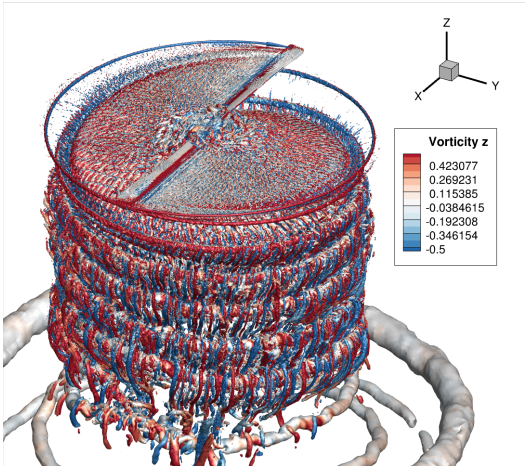

Figure 1: λ_2 isosurface of a 2 blade rotor highlighted by vorticity in the z direction.

Regarding the main helical vortex, a number of qualitative investigations have been presented ([1], [2], [3]) but quantitative measurements of the vortex properties are still a major challenge, especially regarding vortex pairing. Vortex dynamics in a rotating system is complicated by the strong curvature of the vortices themselves and by the small spacing between consecutive blade vortices. Helical instabilities have been studied on a single filament ([4]), so as with various number of helical filaments ([2],[5]).
The macro-instabilities observed within the primary vortex constitute just a portion of the wake's decay mechanism; this process also encompasses the existence of smaller vortical secondary structures. Initially identified in highly refined numerical simulations as artificially generated phenomena, these secondary vortices have recently been validated through experiments conducted at DLR-Göttingen via PIV measurements ([6]). Primarily characterized by the elongation and curling of

the shear layer resulting from the presence of the principal tip vortices, these secondary structures significantly intensify the dissipation of the wake.
Currently, the first simulations have been carried and the main effort has been paid towards the postprocessing of the results. In this context, a pivotal concern has been the formulation of a technique to accurately characterize and track vortices located at great distances from the rotor plane (see Fig. 2). Employing a geometric setup involving a hovering rotor with a variable number of blades (1, 2, or 4) and with a mesh refinement of 3 % of the blade chord (approximately 300 million cells), the effects of the background mesh has revealed to be very impacting.

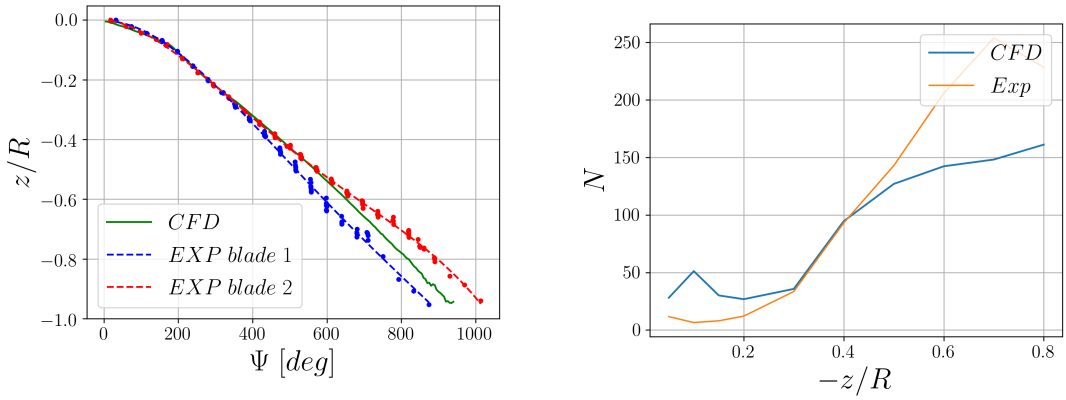

Figure 2: Left: axial position of the main tip vortex. Right: number of secondary structures in the axial direction.

In conclusion, the high-fidelity simulations conducted so far have successfully captured physically meaningful secondary structures. However, their precise extent still requires validation through experimental results. The primary objective of the project is to investigate the effects of various numerical setups, such as grid resolution and turbulence model, on the nature of these secondary structures. This research endeavor aims to gain a comprehensive understanding of the factors influencing the appearance and behavior of these vortical elements in the wake, ultimately enhancing the accuracy and reliability of the simulations.

References

[1] Felli, M., Camussi, R., Di Felice, F. Mechanisms of evolution of the propeller wake in the transition and far fields. *Journal of Fluid Mechanics*, 682, 5-53, 2011, doi:10.1017/jfm.2011.150.

[2] Okulov, V. L. On the stability of multiple helical vortices. *Journal of Fluid Mechanics*, 521, 319-342, 2004.

[3] Leishman, J.G. and Bagai, A. Challenges in Understanding the Vortex Dynamics of Helicopter Rotor Wakes. *AIAA Journal*, Vol. 36, No. 7 (1998), pp. 1130-1140. doi:10.2514/2.510.

[4] Widnall, S. E. The Stability of a Helical Vortex Filament *Journal of Fluid Mechanics*, Vol. 54, No. 4, 1972.

[5] Wood, D. H., Boersma, J. On the motion of multiple helical vortices. *Journal of Fluid Mechanics*, vol. 447, 149-171, 2001.

[6] Schwarz, C., Bodling, A., Wolf, C.C., Michaelis, D., Kaufmann, K., Gardner, A., Bosbach J., Schanz, D., Schröder, A. Experimental study of secondary structures in a rotor wake. *45th Rotorcraft Forum*, 2019.

Mitteilung

Fachgruppe: Numerische Aerodynamik

Investigation of the order of the discontinuous Galerkin method in combination with an immersed boundary condition

Miquel Herrera
DLR, Institut für Aerodynamik und Strömungstechnik,
Lilienthalplatz 7, 38108 Braunschweig, miquel.herrera@dlr.de

The aerospace industry is interested in scale-resolving simulations (SRS) with shortened time-to-solution. Work is underway at the DLR to develop a rapid SRS process chain, which combines: 1) automatic mesh generation, 2) immersed imposition of boundary conditions, 3) use of wall models, and 4) the discontinuous Galerkin spectral element method (DGSEM). This fourth ingredient caters to the requirements of large eddy simulation (LES), as it is capable of resolving a wide range of wavenumbers with minimal numerical dispersion and dissipation, while being both robust and efficient [2]. The present work represents a first attempt at combining a high-order discontinuous Galerkin (DG) discretization with automatically generated meshes by means of an immersed boundary method (IBM), in the context of the CFD software by ONERA, DLR, Airbus (CODA)[1] [3]. Efforts towards extending the split-form DGSEM in CODA to support h/p-nonconforming setups are ongoing.

The meshing software Cassiopée [1] is used to generate a block-uniform Cartesian grid around a closed shape (the solid), which employs iterative octree refinement towards the boundary of the solid such that the smallest cell size ends up being (approximately) equal to a user-specified value. Here, no attempt is made to have the mesh boundary conform to the solid boundary; see Figure 1. This mesh is converted to single-block unstructured before being imported into CODA. Cassiopée is also responsible for generating a donor and a wall point for each immersed face integration point.

The imposition of an immersed slip boundary condition (the Euler equations are the initial focus of this work) is closely related to the approach in [4] and consists of two steps. The first step is a (high order) reconstruction of the state vector at the donor point. The second step is the interpolation of each of the state quantities, between a donor point and its associated wall point, to the location of their corresponding immersed face integration point. For the normal component of momentum, which is zero at the wall, a linear interpolation is used for simplicity. Density, tangential momentum and total energy, whose gradients in normal direction should be zero at the wall, are obtained via constant interpolation (i.e. each takes the same value at all three points).

The spatial discretization is a modal DG scheme with orthonormal polynomial basis functions of up to a specified total degree in 3D physical space. The numerical flux at faces is computed using the Riemann solver of Roe without entropy fix. The discrete equations are solved with a linearized implicit Euler scheme. The linear problem in each nonlinear solver iteration is solved using the GMRES method with a lines-implicit Jacobi preconditioner. All solutions are converged in the sense of each equation's residual being reduced by a factor of 10^{-10}.

A subsonic, inviscid flow around a circular cylinder of unit diameter has been computed on a family of meshes like the one shown in Figure 1, for DG polynomial degrees from 0 to 3. Figure 2 summarizes the obtained results. There are two main findings: first, the combination of IBM and DG does achieve the design order of (approximately) 2 in the linear basis function

[1] *CODA is the computational fluid dynamics (CFD) software being developed as part of a collaboration between the French Aerospace Lab ONERA, the German Aerospace Center (DLR), Airbus, and their European research partners. CODA is jointly owned by ONERA, DLR and Airbus.*

case; second, the design order is not retained as the degree of the discretization increases (accuracy remains bound to 2nd order), even under the ideal circumstances represented by this model problem.

The use of linear interpolation in the normal momentum component is hypothesized to be the cause of this loss of order, as this process introduces a 2nd order error independent of the reconstruction order – precisely what the data seems to suggest. In order to test this hypothesis, the linear interpolation will be replaced with a quadratic one for the case of degree 2. Measuring 3rd order of accuracy would then confirm the hypothesis. Future work would, in that case, consist on generalizing the higher-order interpolation to any discretization degree. Should this not be the case, an alternative explanation of these observations would need to be found.

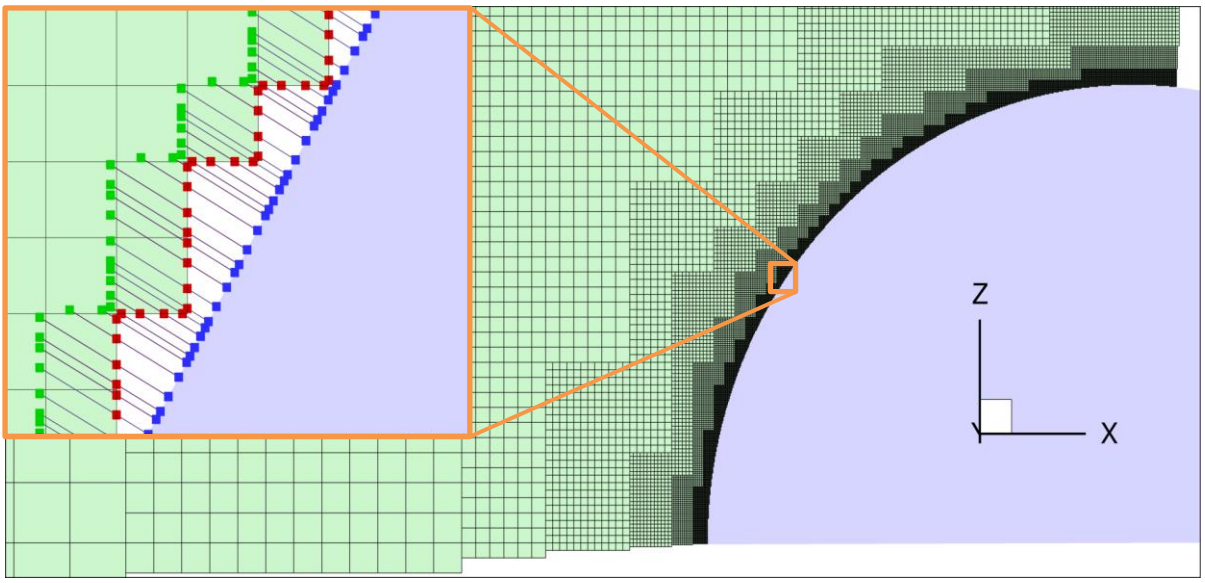

Figure 1: Example of a mesh for the circular cylinder and close-up of the immersed boundary with wall, integration and donor points, as well as wall-normal lines shown, for the case of DG of degree 3.

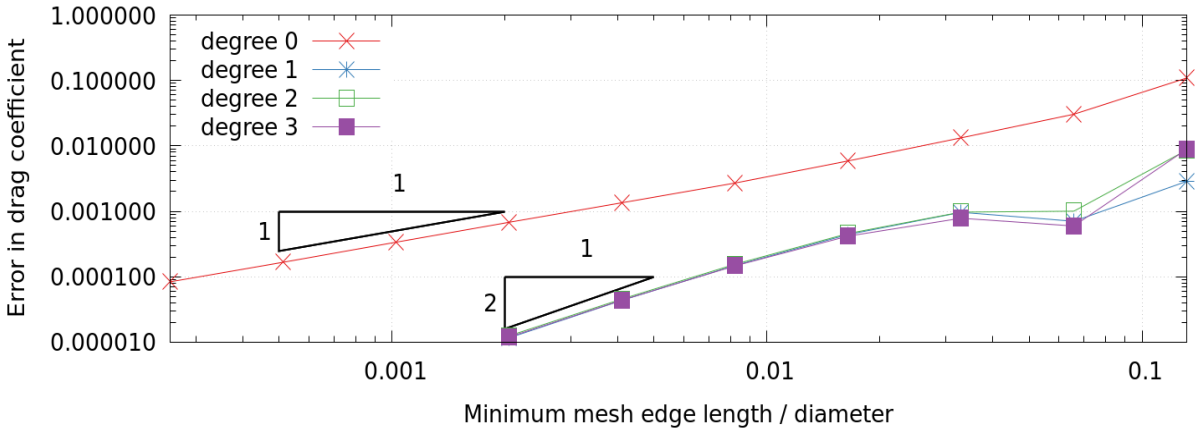

Figure 2: Rate of convergence of the error in drag coefficient as the minimum cell size is reduced, for DG of given degree in combination with an immersed slip-wall boundary condition that uses linear interpolation.

References

[1] C. Benoit, S. Péron, and S. Landier, "Cassiopee: A CFD pre- and post-processing tool," *Aerospace Science and Technology*, vol. 45, pp. 272–283, Sep. 2015, doi: 10.1016/j.ast.2015.05.023.

[2] D. Flad and G. Gassner, "On the use of kinetic energy preserving DG-schemes for large eddy simulation," *Journal of Computational Physics*, vol. 350, pp. 782–795, Dec. 2017, doi: 10.1016/j.jcp.2017.09.004.

[3] T. Leicht *et al.*, "DLR-Project Digital-X - Next Generation CFD Solver 'Flucs,'" in *Deutscher Luft- und Raumfahrtkongress 2016*, Feb. 2016. [Online]. Available: https://elib.dlr.de/111205/

[4] S. Péron, C. Benoit, T. Renaud, and I. Mary, "An immersed boundary method on Cartesian adaptive grids for the simulation of compressible flows around arbitrary geometries," *Engineering with Computers*, vol. 37, no. 3, pp. 2419–2437, Jul. 2021, doi: 10.1007/s00366-020-00950-y.

Mitteilung

Fachgruppe: Numerische Simulation

Modeling the Pressure-Strain-Correlation in Differential Reynolds Stress Models using Feature Engineering and a Genetic Evolution Algorithm

Vincent Peterhans
DLR, Institut für Aerodynamik und Strömungstechnik, Abteilung $C^2A^2S^2E$,
Bunsenstraße 10, 37073 Göttingen
vincent.peterhans@dlr.de

Simulating turbulent flows using Reynolds-Averaged-Navier-Stokes-Equations (RANS) models is a very efficient approach for most practical applications, as they aim to produce accurate results, while being more performant than scale-resolving methods. However all RANS approaches require the modeling of unknown terms, one of them being the pressure-strain-correlation (PSC) in the differential Reynolds Stress Model.
A state-of-the-art model for this is the Speziale-Sarkar-Gatski (SSG) model [1], which tries to represent the PSC term using a set of basis tensors and (in its simplest form) five coefficients that need to be calibrated to achieve the desired behavior.
These coefficients are usually assumed to be constant, however, theoretical considerations suggest they should be functions of the current flow-state [2], considerably increasing the models complexity and capabilites.

In order to determine such functional dependencies, a machine learning approach referred to as Genetic Evolution Programming (GEP) [3] has successfully been employed by Alaya et al. [4]. This method uses evolutionary principles to evolve a set of possible equation-candidates for the coefficients over multiple iterations. For that, each candidate is evaluated via a predefined fitness-criterion and multiple techniques such as mutation, cross-combination or overwrites are applied to the less successfull candidates to explore the search-space of possible functions in a directed manner [3].
The method has advantages over traditional black-box-style neural networks, as it produces interpretable and easily implemented equations and allows the usage of complex fitness-criteria that would otherwise be very difficult to optimize via classical gradient-descent.
On the other hand, the convergence of this method is less predictable and controllable than other machine learning techniques and shows a high sensitivity to its initialization, inputs and training parameters.

To improve on these issues, a multi-step feature engineering process has been designed to select the most promising input features to be considered for the functional dependencies, effectively reducing the search-space the GEP has to explore.
In the first step data from a Large Eddy Simulation (LES) simulation, in this case the curved-backward-facing step of Bentaleb et al. [5], is used to reconstruct reference fields for each of the coefficients of the SSG term as a basis for further statistical analysis. Afterwards, five input variables identified as relevant for characterizing the flowfield are selected:

$$II_b, \quad III_b, \quad II_S, \quad Re_t, \; L = k^{3/2}/\epsilon, \quad r = \sqrt{S_{ij}S_{ji}/\Omega_{ij}\Omega_{ij}}$$

The variables are the second and third invariants of the Reynolds stress anisotropy tensor, the second invariant of the strain-rate tensor, the turbulent Reynolds number, turbulent length scale and strainrate- to vorticity-magnitude-ratio.

Their predictive capability for the previously reconstructed reference coefficient fields is determined by two different methods: A random forest approach and gradient boosting. Both methods estimate the predictive power each of the input variables has on the coefficient fields and form an importance-ranking based on this. To increase the procedures robustness, the rankings of both methods are averaged.
Next, the space of considered inputs can be expanded further by applying a multitude of transformations such as trigonometric, exponential and polynomial functions to the previously selected features. Then for each feature individually the most useful transformation is ranked using the Spearman-correlation between the transformed feature and the reference coefficient field as a criterion.
Finally, this feature engineering- and ranking method yields a set of 3-4 features and their most favourable transformation per coefficient that can be used as inputs for building functions with GEP.

In alignment with the work of Alaya et al. [4], the method is evaluated on the curved-backward-facing step test case [5], which was already used for the feature engineering, and the skin friction- and pressure-coefficients at the surface are identified as target-variables, that the optimization should try to match. Preliminary results for this procedure are shown in Figure 1, displaying the reference LES data, the predictions made by the original SSG model with constant coefficients and the improved SSG model utilizing the feature engineering and genetic evolution process (SSG GEP).

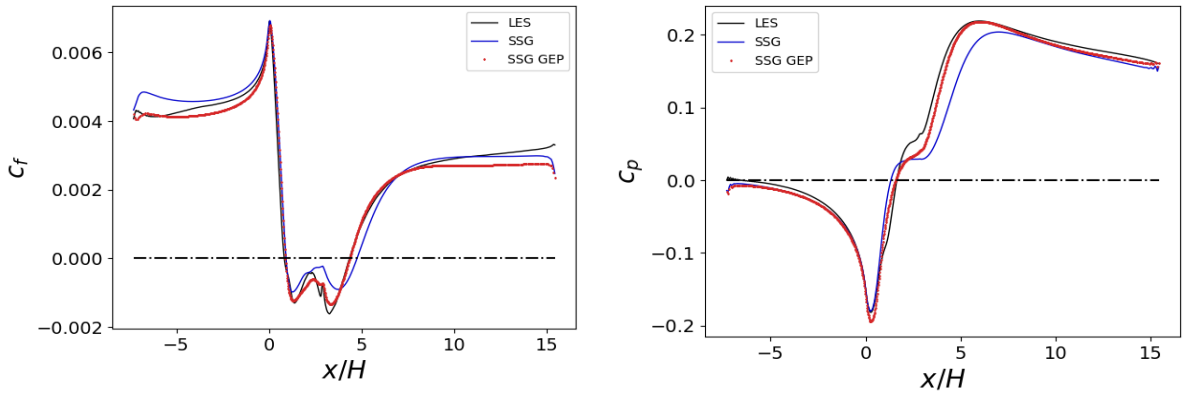

Figure 1: Preliminary Results of the GEP with Feature Engineering

Future work will focus on determining the limits and capabilities of the designed process by evaluating the GEP-trained models on other test-cases that were not used during training.

[1] Speziale, C. G., Sarkar, S., and Gatski, T. B., “Modelling the pressure–strain correlation of turbulence: an invariant dynamical systems approach,” Journal of Fluid Mechanics, Vol. 227, 1991, pp. 245–272

[2] Wilcox, D., Turbulence modeling for CFD, DCW Industries, Inc, La Canada, CA, 1993

[3] Ferreira, C., “Gene Expression Programming: A New Adaptive Algorithm for Solving Problems,” Complex Systems, Vol. 13, No. 2, 2001, pp. 87, 129

[4] Alaya, E., Grabe C. and Eisfeld, B.: “Evolutionary Algorithm applied to Differential Reynolds Stress Model for Turbulent Boundary Layer subjected to an Adverse Pressure Gradient”, AIAA Aviation Forum, June 2022, Chicago, USA. doi: 10.2514/6.2022-3337.

[5] Bentaleb, Y., Lardeau, S., and Leschziner, M. A.: “Large-eddy simulation of turbulent boundary layer separation from a rounded step,” Journal of Turbulence, Vol. 13, 2012, p. N4, URL https://doi.org/10.1080/14685248.2011.637923

Mitteilung

Fachgruppe: Numerische Aerodynamik

Learning the Viscous Flow Field of a Shockwave Boundary Layer Interaction from Limited Data using Physics-Informed Neural Networks

Lennart Rohlfs and Julien Weiss
Institut für Luft- und Raumfahrt, Technische Universität Berlin,
Marchstraße 12, 10587 Berlin
l.rohlfs@tu-berlin.de

Advancements in the field of machine learning are constantly opening up new possibilities for enhancing data with computational methods to improve our understanding of complex flow phenomena. One notable example are Physics-Informed Neural Networks (PINNs) that incorporate a set differential equations, such as the Navier Stokes equations, into the loss function of the NN to supplement the data loss [1]. They can be used to extract latent variables such as pressure or velocity fields from limited, noisy, or even purely qualitative data. [2]

Our current research efforts aim to apply PINNs to an oblique turbulent shockwave-boundary layer interaction (SBLI) that represents a complex, compressible flow configuration with the goal of assimilating all physical variables using only density gradient data as input. In a previous study the compressible Euler equations were implemented into a PINN and the inviscid velocity field of the SBLI was successfully reconstructed from Background Oriented Schlieren (BOS) measurements in a supersonic wind tunnel. [3]

The present contribution extends this work by replacing the Euler equations with the Reynolds-Averaged Navier Stokes (RANS) equations and the full viscous flow field is reconstructed. To enable a thorough validation of the method before moving on to the experimental BOS input, the density gradient data is extracted from high-fidelity DNS simulations of a similar flow configuration with a freestream Mach number of 2.28 [4]. Additionally the numerical dataset enables an easy variation of additional boundary conditions for the PINN such as wall pressure- or shear stress distributions.

The basic network architecture is shown in Figure 1. The left side is a fully-connected neural network with a number of hidden layers that takes spatial coordinates as input and outputs physical variables. The right part shows the physics-informed part of the network. Using automatic differentiation, the partial derivatives of all outputs are obtained with respect to the inputs and evaluated using a set of PDEs.

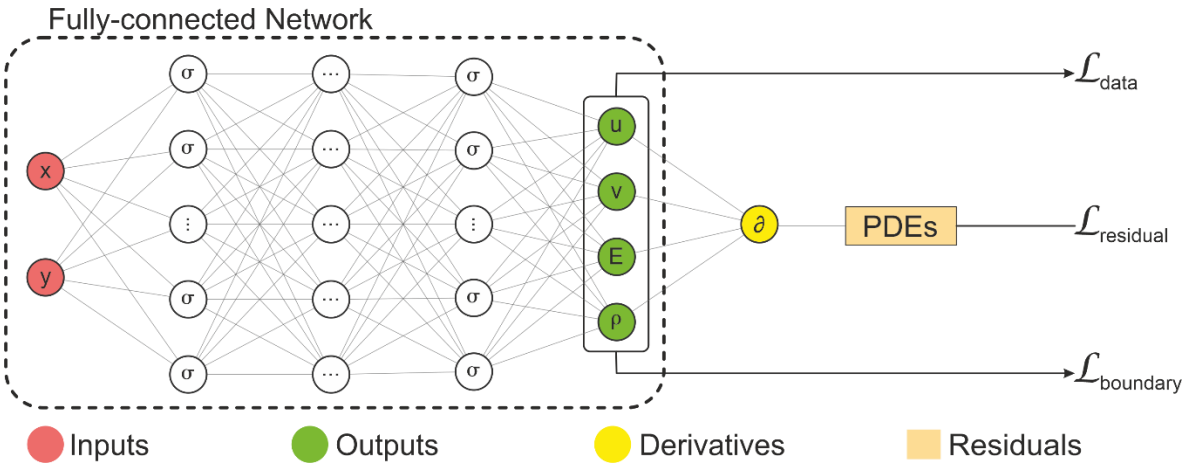

Figure 1: Schematic diagram of the Physics-Informed Neural Network architecture for a fluid mechanics problem

Each equation generates a non-zero residual that is summed up to form a residual loss term. The total loss function is the sum of this residual loss as well as a data loss term that compares predicted values to the supplied training data and a boundary loss that enforces the freestream-or wall conditions. During the training, the total loss is minimized using a combination of the Adam optimizer and the L-BFGS algorithm.

Figure 2 shows an example of the predicted velocity fields and the respective prediction errors that were obtained after training a PINN with density gradient data as well as enforcing inlet and wall boundary conditions. The predicted velocity fields show a very good agreement with the DNS simulations with errors below 0.05 throughout the entire flow field. The highest deviations are found in the incoming boundary layer where the predicted velocity profile is less full than the reference. In contrast to a traditional CFD simulations where the upstream boundary layer profile is crucial for accurate results, these differences to not appear to influence the predictions of the SBLI and the developing shear layer. The pressure and density fields are not shown here, but their accuracy is about an order of magnitude higher than the velocity predictions which is as expected since the training data includes the density gradient field.

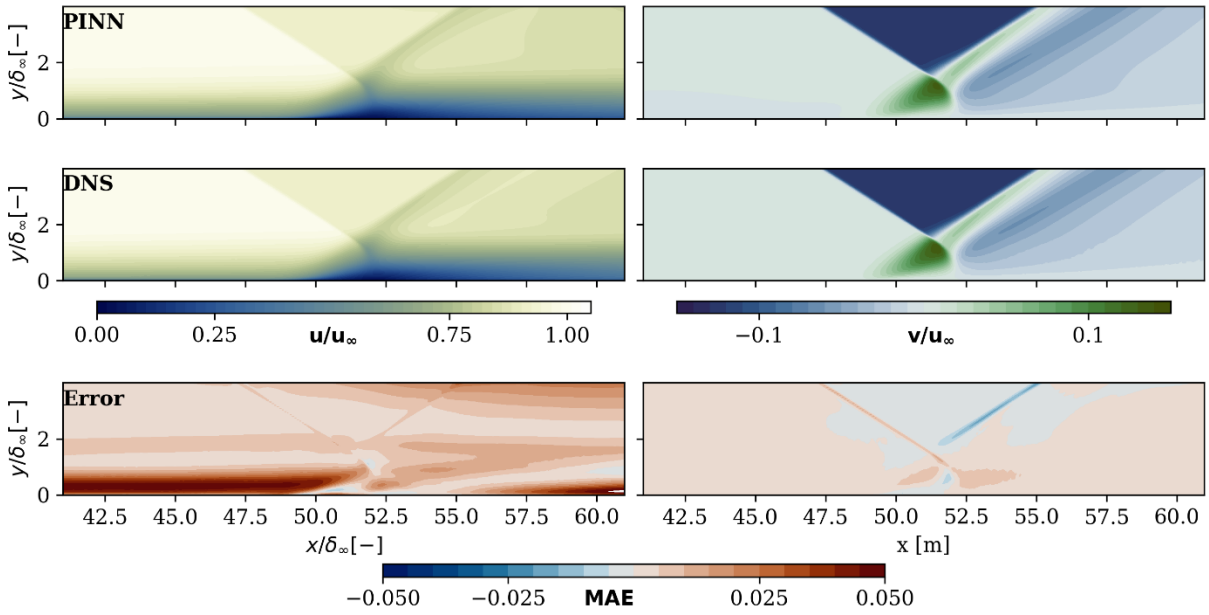

Figure 2: Comparison of the normalized predicted- and measured streamwise (left) and wall- normal (right) velocity fields Top: PINN prediction, Center: DNS Results, Bottom: Reconstruction Error (DNS - PINN)

References:

[1] Raissi, M., Perdikaris P., Karniadakis, G.E. (2019). Physics-informed neural networks: A deep learning frame- work for solving forward and inverse problems involving nonlinear partial differential equations. Journal of Computational Physics, 378(10), 686-707.

[2] Cai, S., Mao, Z., Wang, Z., Yin, M., Karniadakis, G.E. (2021). Physics-informed neural networks (PINNs) for fluid mechanics: a review. Acta Mechanica Sinica, 37, 1727-1738.

[3] Rohlfs, L., Weiss, J. (2023). Assimilating Velocity Fields from BOS Measurements in Supersonic Flows Using Physics Informed Neural Networks. AIAA Aviation Forum 2023.

[4] Pirozzoli, S., Bernardini, M. (2011). Direct Numerical Simulation Database for Impinging Shock Wave/Turbulent Boundary-Layer Interaction. AIAA Journal, 49(6), 1307-1312.

Mitteilung

Fachgruppe: Numerische Aerodynamik

Towards „Rapid CFD“ via an Immersed Boundary Method in the CFD software by ONERA, DLR, Airbus (CODA)

Roberto Sanchez-Ortiz, Jesús Miguel Sánchez-Gil
DLR, Institut für Aerodynamik und Strömungstechnik
Bunsenstraße 10, 37073 Göttingen, Roberto.SanchezOrtiz@dlr.de
Lilienthalpl. 7, 38108 Braunschweig, Jesus.SanchezGil@dlr.de

In recent years, the industry has been looking for methods to simulate external aerodynamics at low overall turnaround times, such as Lattice-Boltzmann and Cartesian solvers. This paper proposes a “Rapid CFD” capability based on the Immersed Boundary Method (IBM) [1] in the unstructured CFD software by ONERA, DLR, Airbus (CODA). The main advantage of this method is a fully automatic mesh generation, which addresses this well-known bottleneck in industrial CFD applications.
The mesh generation consists of an octree algorithm where the mesh is automatically refined in the vicinity of the geometry, as shown in Figure 1. The generation is based on a near-wall size ($\Delta y_{\min}$) and a growth parameter. The software used is Cassiopée [2], which generates a series of Cartesian blocks that are treated together as a single unstructured mesh with pseudo elements connecting the hanging faces between the different refinement levels. The boundary of this mesh does not conform to the geometry, leaving a gap between the computational boundary and the physical wall.
The IBM method in CODA follows the work of ONERA [3], [4], who impose the boundary condition directly without requiring any modification of the solver as those in [5], [6]. This is achieved by a hole-cutting algorithm [2] and a proper placement of the donor points [4]. Cells close to the wall are removed until the face centers of the immersed boundary, known as integration points, are immediately above a specified distance. This distance is specified by estimating a y^+ of 100, using the flat plate analogy. The donor points are located within the next cell. This location of the donor points provided the best results compared to other locations (such as constant distance to the wall). A full view of an octree mesh and a schematic view of the immersed points (donor, integration and wall) can be seen in Figure 1.

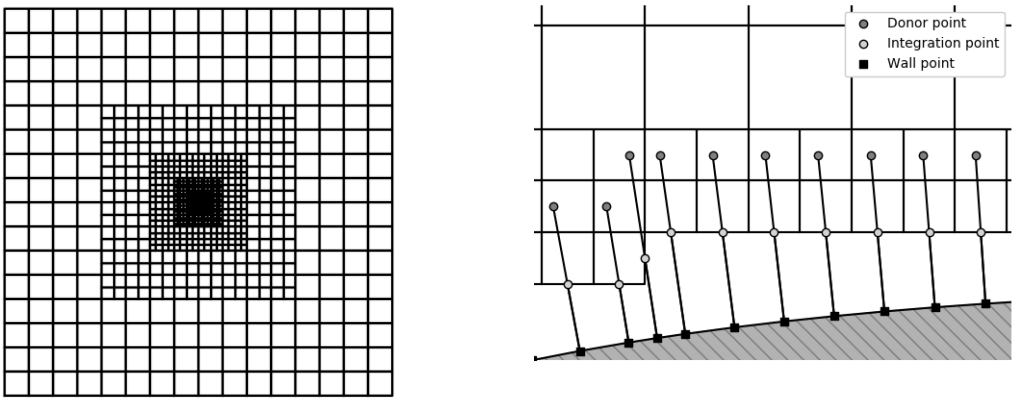

Figure 1. Octree mesh of NACA 0012 (left) and a close-up (right) showing donor, integration and wall points

The boundary conditions are imposed as follows, using the RANS equations and the negative Spalart-Allmaras (SAneg) turbulence model [7]. The fluid state at the donor point is recovered using a linear reconstruction in the cell in which the donor point is located. A wall function is then solved using the fluid state and distance of the donor point, and evaluated at the integration point, giving the velocity at the mesh boundary. This velocity is used as the parallel component with respect to the wall, while the normal component is interpolated linearly as the product of the normal component at the donor point and the ratio of distances from the wall of the integration point over the donor point. Density and pressure are assumed to be constant

from the donor point, and the energy is computed accordingly using the equation of state for perfect gas. Finally, the SAneg variable is computed considering constant eddy viscosity as:

$$\tilde{\nu} = f_{vq}^{-1} \kappa y^{+}$$

The wall function used is the algebraic wall function of Musker [8], which includes the viscous sublayer, buffer, and logarithmic regions.
IBM was tested with a NACA 0012 airfoil subsonic case at a Mach number of 0.15 and Reynolds number of 6 million at zero angle of attack. The solution was compared against two references: a body-fitted (BF) simulation with fully resolved boundary layer ($y^{+} = 0.2$), and a coarser one using the Musker's wall function (BFWF) with a first cell height of $y^{+} = 100$. Figure 2 shows preliminary results of the present IBM, which gives good agreement with the fully resolved body-fitted case, in the leading-edge region even better than the body-fitted case with wall functions.

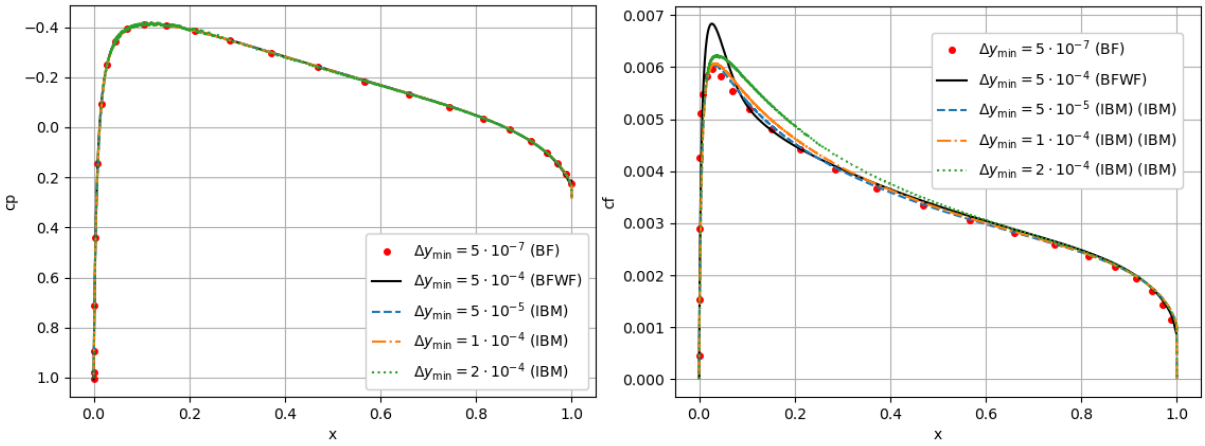

Figure 2. Pressure and friction distribution of NACA 0012, M=0.15, Re=6E6, AOA=0° for body-fitted (BF: circles), body-fitted with wall function (BFWF: solid), and IBM with three sizes (dashed, dashdot, and dotted).

Future applications will include 3D cases with complex geometries that pose significant challenges to mesh, as well as an extension to wall-modeled LES (WMLES) and Hybrid RANS-LES to enable scale-resolving simulations.

Acknowledgment CODA is the computational fluid dynamics (CFD) software being developed as part of a collaboration between the French Aerospace Lab ONERA, the German Aerospace Center (DLR), Airbus, and their European research partners. CODA is jointly owned by ONERA, DLR and Airbus.

Bibliography

[1] R. Mittal and G. Iaccarino, "Immersed Boundary Methods," *Annu. Rev. Fluid Mech.*, vol. 37, no. 1, pp. 239–261, 2005, doi: 10.1146/annurev.fluid.37.061903.175743.

[2] C. Benoit, S. Péron, and S. Landier, "Cassiopee: A CFD pre- and post-processing tool," *Aerosp. Sci. Technol.*, vol. 45, pp. 272–283, Sep. 2015, doi: 10.1016/j.ast.2015.05.023.

[3] S. Péron, C. Benoit, T. Renaud, and I. Mary, "An immersed boundary method on Cartesian adaptive grids for the simulation of compressible flows around arbitrary geometries," *Eng. Comput.*, vol. 37, Jul. 2021, doi: 10.1007/s00366-020-00950-y.

[4] B. Constant, S. Péron, H. Beaugendre, and C. Benoit, "An improved immersed boundary method for turbulent flow simulations on Cartesian grids," *J. Comput. Phys.*, vol. 435, p. 110240, Jun. 2021, doi: 10.1016/j.jcp.2021.110240.

[5] F. Capizzano, "Turbulent Wall Model for Immersed Boundary Methods," *AIAA J.*, vol. 49, no. 11, pp. 2367–2381, Nov. 2011, doi: 10.2514/1.J050466.

[6] Y. Tamaki, M. Harada, and T. Imamura, "Near-Wall Modification of Spalart–Allmaras Turbulence Model for Immersed Boundary Method," *AIAA J.*, vol. 55, no. 9, pp. 3027–3039, 2017, doi: 10.2514/1.J055824.

[7] S. Allmaras, F. Johnson, and P. Spalart, "Modifications and clarifications for the implementation of the Spalart-Allmaras turbulence model," *Seventh Int. Conf. Comput. Fluid Dyn. ICCFD7*, pp. 1–11, Jan. 2012.

[8] A. J. Musker, "Explicit Expression for the Smooth Wall Velocity Distribution in a Turbulent Boundary Layer," *AIAA J.*, vol. 17, no. 6, pp. 655–657, Jun. 1979, doi: 10.2514/3.61193.

Mitteilung

Fachgruppe: Numerische Aerodynamik

Implementation and assessment of the DLR γ Transition transport model in the CFD software by ONERA, DLR and Airbus (CODA)

V. Togiti[1], C. Grabe[2], D. François[2]
DLR, Institute of Aerodymiacs and Flow Technology, Dept. : $C^2A^2S^2E$
[1]Lilienthalplatz 7, 38108 Braunschweig / [2]Bunsenstrasse 10, 37073 Göttingen
vamshi.togiti@dlr.de

Introduction

Reducing aerodynamic drag while improving performance of modern civil aircraft has become crucial to lower energy consumption, thereby reduce environmental pollution. Towards this goal, one of the promising approaches is to employ laminar flow technologies, in which laminar-turbulent transition is delayed. In aircraft design optimization, modern computational fluid dynamics (CFD) flow solvers capable of predicting accurately the turbulent onset plays a key role. For this, transition transport models are often favored due to their simplicity and integrability in a CFD flow solver. Therefore, a new γ-based model was developed at DLR [1]. In this model, one transport equations is solved for the intermittency γ, which models laminar-turbulent transition, and a local formulation for the pressure gradient parameter is employed which allows assessing the transition criterion inside the boundary layer. In [1], the new model shown to be delivering more accurate predictions compared to other two-equation transition transport model predictions.
Currently, a new CFD flow solver is being developed jointly by Airbus, ONERA and DLR with the aim to provide a flow solver with high flexibility and high degree of innovation for a wide range of multidisciplinary applications using modern software techniques and utilizing latest HPC architectures. The new flow solver CODA (CFD by ONERA, DLR and Airbus) [2] operates on unstructured grids employing cell centered schemes. It combines second-order finite volume and higher-order Discontinuous-Galerkin (DG) methods. The new generation flow solver addresses efficient utilization of current and upcoming high-performance computing cluster.
In the current work, the aforementioned transition transport model is implemented in the CODA flow solver and the model is coupled with the SST k-ln(ω) turbulence model. The present work focuses on examining the correctness of the model implementation in CODA.

Results

To assess the model implementation, numerical investigations are conducted for the flow over a DSA-9A [3] airfoil and NLF416 [4] airfoil using the CODA and the predictions are compared to experimental data and the DLR-TAU code predictions. For the DSA-9A airfoil, the investigation is carried out at a Reynolds number based on chord length of 1.8 million and Mach of 0.3 with a freestream turbulent intensity of 0.1% and the incidence angle of 7.9^o on a fully structured grid with 250,000 grid points. While for the NLF-416 airfoil, investigations are conducted at a Reynolds number based on chord length of 4 million and Mach number of 0.1 and turbulence intensity of 0.03% for the incidence angles ranging from -6^o to 12^o. For both configurations, at the aforementioned flow conditions, transition occurs due to Tollmein-Schlichting instabilities on the upper side of the airfoil and on the lower side transition is caused by laminar separation.
Comparison of c_p distribution for the DSA-9A airfoil in Fig 1(a) shows that the CODA pressure distribution matches the TAU predictions. However, the comparison of c_f distribution in Fig. 1(b) unveils differences in skin friction near the transition region due to differences in predicted transition locations. The solid black in the figure indicate the experimental transition location, which is located at about x/c of 0.06. In CODA predictions, the transition location is observed slightly downstream of the experiments while in the TAU predictions it is predicted slightly upstream of experimental data. Overall, the predicted locations agree with the experimental data.
Transition locations delivered by the CODA for the NLF-416 airfoil at different incidence angles are shown in Fig 2(a) and compared with experimental data and TAU predictions. In the experimental data, Exp.laminar indicates the location up to which a laminar region is observed, while Exp.turbulent displays the turbulent region. The comparison with the experiments unveils that the transition locations delivered

by CODA are within the experimental transitional range, showing agreement with experiments. However, the comparison of CODA predictions to TAU shows minor differences in the predicted transition locations. The comparison of skin-friction distribution at the incidence angle of 0° shown in Fig. 2(b) displays CODA delivering cf almost identical to TAU except in the transition region due to difference in predicted transition location.

Overall, the assessment of the DLR γ transition transport model in CODA shows the correctness of model implementation by showing good agreement with experiments and TAU predictions. However, minor differences in predicted transition locations compared to TAU are possibly due to different discretization and different length scale variable employed in CODA investigations. The presentation at the workshop will focus on discussing the performance of CODA and the reasons for differences between different flow solvers.

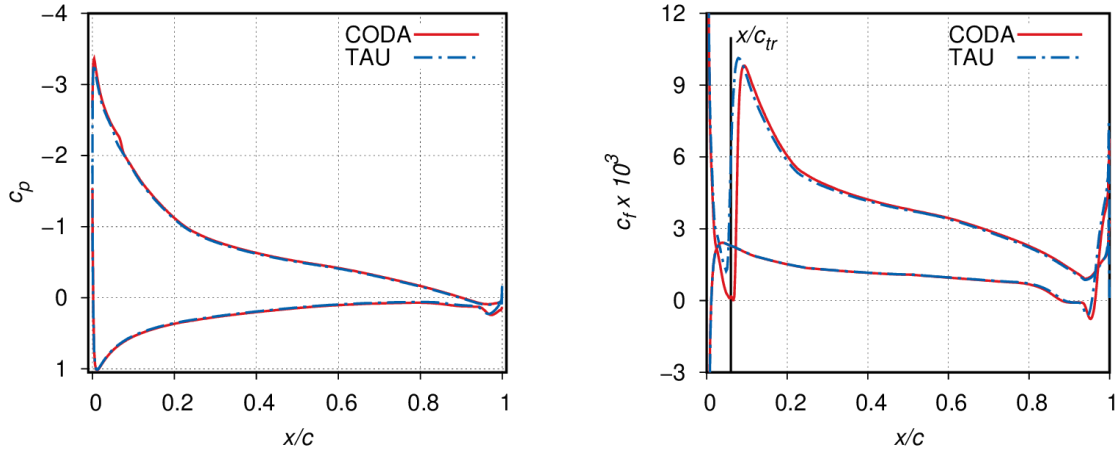

(a) Pressure coefficient (b) Skin-friction coefficient

Figure 1 DAS-9A Airfoil

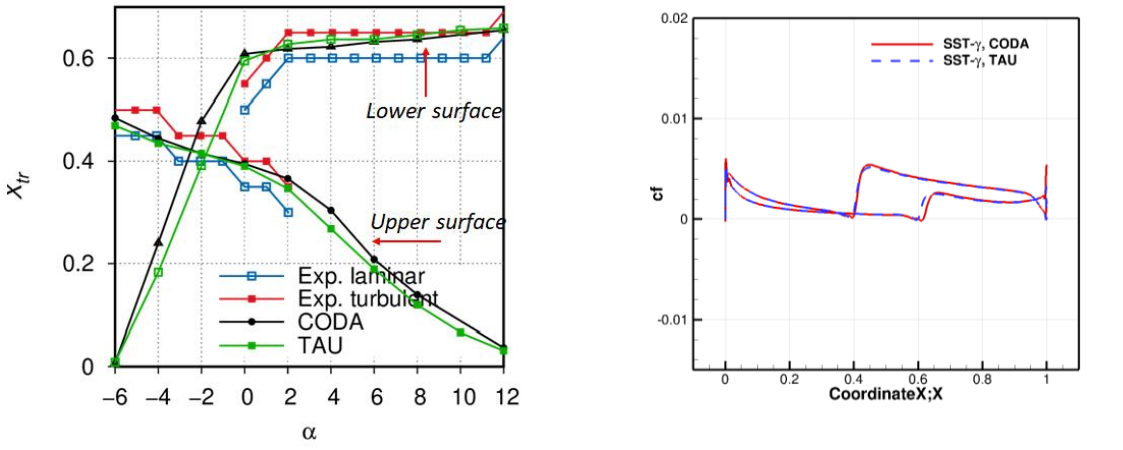

(a) Transition locations (b) Skin-friction coefficient at α = 0°

Figure 2 NLF(1)-416 airfoil

Acknowlegements: CODA is the computational fluid dynamics (CFD) software being developed as part of a collaboration between the French Aerospace Lab ONERA, the German Aerospace Center (DLR), Airbus, and their European research partners. CODA is jointly owned by ONERA, DLR and Airbus.

References:

[1] François D., Krumbein, A., Krimmelbein, N., Grabe, C., "Simplified Stability-Based Transition Transport Modeling for Unstructured Computational Fluid Dynamics", AIAA SciTech Forum,2022, DOI: 10.2514/6.2022-1543.

[2] Leicht, T., Vollmer, D., Jägersküpper J., Schwöppe, A., Hartmann, R, Fiedler, J., Schlauch T. "DLR-PROJECT DIGITAL-X NEXT GENERATION CFD SOLVER 'FLUCS' ", DLRK-2016, DocumentID: 420027.

[3] Gardner, A. D., and Richter, K., "Transition Determination on a Periodic Pitching Airfoil Using Phase Averaging of Pressure Data," *New Results in Numerical and Experimental Fluid Mechanics X*, edited by A. Dillmann, G. Heller, E. Krämer, C. Wagner, and C. Breitsamter, Springer International Publishing, Cham, 2016, pp. 291–301. doi:10.1007/978-3-319-27279-5_26.

[4] Somers, D. M., "Design and Experimental Results for a Natural-Laminar-Flow Airfoil for General Aviation Applications," Tech. Rep. NASA-TP-1861, NASA Langley Research Center Hampton, VA, United States, 1981.

Mitteilung

Fachgruppe: Numerische Aerodynamik

Anisotropic p-adaptive Discontinuous Galerkin methods

Malte Wegener
Institut für Aerodynamik und Strömungstechnik, Lilienthalplatz 7,
38108 Braunschweig, malte.wegener@dlr.de

Introduction:
Solving numerical flow problems using higher order Discontinuous Galerkin methods is computationally very expensive due to the high number of degrees of freedoms and the resulting highly coupled systems. In order to reduce the cost of these methods adaptive algorithms can be employed to increase the order of the discretization only in regions where the discretization error is high. Furthermore, as high Reynolds number flows feature anisotropic phenomena, the polynomial degree can be increased selectively in directions where the additional resolution is needed.

Methods:
For the spatial discretization a hierarchical modal basis is used, which is defined in physical space. For the anisotropy indicator two different methods were examined. The first indicator is the non-conformity anisotropy indicator (NCF) introduced in [1] by Leicht and Hartmann and here generalized to general mesh elements. The anisotropy is defined as the jump of the flow state over the element interfaces in the coordinate axis directions.
The second indicator considered is a novel competitive indicator based on a least-squares reconstruction first used in [2], [3] by Dumbser et al. in the context of reconstructed Discontinuous Galerkin (rDG) methods. The reconstruction is however not used to elevate the order of the method but to estimate the effect of unrepresented modes. The reconstruction operator is defined such that the reconstructed solution is weakly indistinguishable over the reconstruction stencil under the basis functions of the discretization.
During the refinement, only modes with sufficient energy according to the reconstruction are used. The anisotropy indicators are combined with a residual based error indicator [4].

Results:
The first test case considered is the zero-pressure gradient flat plate from the NASA turbulence modelling resource[1]. This case is chosen, as it features a boundary layer, which is inherently anisotropic. The meshes used are provided by the turbulence modelling resource and feature between 816 and 52224 quadrilateral elements. The flow over the plate is at Mach number 0.2 and at a Reynolds number of 5×10^6.

The convergence of drag coefficients for various different refinement strategies can be seen in Figure 1(a) for three different hexahedral meshes. It can be seen that the competitive indicator based anisotropic p-adaptation performs better than the isotropic p-adaptation and better than the anisotropic p-adaptation based on the NCF indicator. Furthermore, the NCF indicator seems to struggle to identify good candidates for anisotropic refinement as can be seen by the inferior accuracy per degree of freedom compared to the isotropic refinement. This might be caused by the highly anisotropic cells which are present in the mesh.

[1] Turbulence Modeling Resource (nasa.gov)

The second test case is the Joukowski airfoil, which is part of the HiFiCFD workshop 2024[2]. The case features an airfoil which is created via a conformal mapping of a circle. The meshes used are generated by applying the same conformal mapping to the mesh of a cylinder. The three considered meshes feature 768, 3072 and 12288 quadrilateral elements, respectively. A flow around this airfoil is considered at a Mach number of 0.2, zero angle of attack and a Reynolds number of 6×10^6. The results can be seen in Figure 1(b). For this test case it can be seen, that the competitive refinement yields better results than both the isotropic refinement and the anisotropic refinement based on the NCF indicator, similar to the previous test case. Furthermore, it can be seen that all adaptive methods struggle to provide significant improvements on the coarsest of the three meshes.

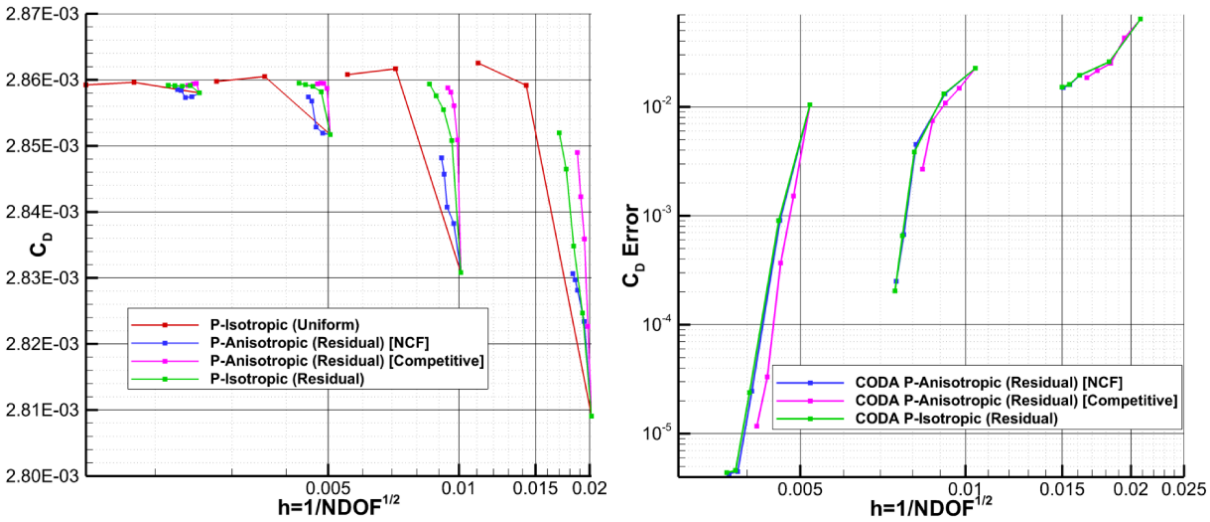

Figure 1(a) Drag Coefficient convergence for different refinement techniques for the zero-pressure gradient flat plate. (Red) Isotropic p-refinement for all elements. (Blue) Anisotropic p-refinement based on the residual based indicator and the non-conformity indicator. (Pink) Anisotropic p-refinement based on the residual based indicator and the competitive refinement. (Green) Isotropic p-refinement based on the residual-based indicator. (b) Drag Coefficient Error convergence for different refinement techniques for the Joukowski airfoil. The colours are the same as for Figure 1(a).

Conclusion and Outlook:

For two-dimensional flow problems, the newly developed competitive indicator was shown to provide better anisotropy information than the generalized non-conformity indicator. It was also shown that anisotropic p-refinement can provide a lower error per degree of freedom than isotropic p-refinement. It remains to be seen, how the competitive indicator performs for three-dimensional test cases.

[1] T. Leicht and R. Hartmann, “Anisotropic mesh refinement for discontinuous Galerkin methods in two-dimensional aerodynamic flow simulations,” *Int. J. Numer. Methods Fluids*, vol. 56, no. 11, pp. 2111–2138, 2008, doi: https://doi.org/10.1002/fld.1608.

[2] M. Dumbser, D. S. Balsara, E. F. Toro, and C.-D. Munz, “A Unified Framework for the Construction of One-Step Finite Volume and Discontinuous Galerkin Schemes on Unstructured Meshes,” *J. Comput. Phys.*, vol. 227, no. 18, pp. 8209–8253, Sep. 2008, doi: 10.1016/j.jcp.2008.05.025.

[3] M. Dumbser and O. Zanotti, “Very High Order PNM Schemes on Unstructured Meshes for the Resistive Relativistic MHD Equations,” *J. Comput. Phys.*, vol. 228, no. 18, pp. 6991–7006, Oct. 2009, doi: 10.1016/j.jcp.2009.06.009.

[4] T. Leicht and R. Hartmann, “Error Estimation and Anisotropic Mesh Refinement for 3d Laminar Aerodynamic Flow Simulations,” *J Comput Phys*, vol. 229, no. 19, pp. 7344–7360, Sep. 2010, doi: 10.1016/j.jcp.2010.06.019.

[2] High Fidelity CFD Workshop 2022 (nasa.gov)

Mitteilung

Fachgruppe: Strömungsakustik

Vorstellung und erste strömungsmechanische Ergebnisse des Braunschweig Tip-Gap-Noise Experimentes zu kopfspaltströmungsinduzierter Geräuschentstehung

Lev Liberson, Fabian Reuschling, Stephan-Michael Pott-Pollenske, Roland Ewert und Jan W. Delfs
Deutsches Zentrum für Luft- und Raumfahrt e.V. (DLR), Institut für Aerodynamik und Strömungstechnik
Lilienthalplatz 7, 38108 Braunschweig
Lev.Liberson@dlr.de

Zur effektiven Lösung ingenieurwissenschaftlicher Fragestellungen ist das Verständnis der physikalischen Zusammenhänge innerhalb des betrachteten Problems von entscheidendem Vorteil. Ein solches in ausreichendem Detailgrad zu erlangen ist häufig nicht ohne Weiteres möglich, beziehungsweise verlangt nach einem, aus Wirtschaftsaspekten nicht mehr zu rechtfertigenden, Forschungsaufwand. Einen möglichen Ausweg bietet hier ein zielgerichtetes, naturwissenschaftliches Experiment, welches bei sorgfältig durchdachter Konzeptionierung erlaubt, die Komplexität des eigentlichen Problems bis hin zu einem erfassbaren Ausmaß zu reduzieren, gleichzeitig jedoch ausreichende Rückschlüsse auf die relevanten Aspekte zu ermöglichen.

Die Entstehung und Ausbreitung von aerodynamisch erzeugtem Schall an einem modernen Axialventilator, vornehmlich jedoch die daraus abgeleitete Ingenieursaufgabe der Minderung desselben, stellt in deren Komplexität zweifelsohne eine nicht triviale Aufgabe an die entsprechenden Hersteller. Umso mehr, da günstige akustische Eigenschaften ein relevantes Alleinstellungsmerkmal darstellen und folglich einen Marktvorteil verschaffen können. In diesem Zusammenhang verfolgt der Ventilatorhersteller ebm-papst in einer fortlaufenden Kooperation mit der Abteilung Technische Akustik (TEA) des DLR Braunschweig das gemeinsame Ziel, ein effizientes Computational Aeroacoustics (CAA) Vorhersageverfahren für Ventilatorschall zu entwickeln. Besonderer Fokus liegt dabei auf der Vorhersage der sogenannten Kopfspaltschallquelle, deren Entstehungsmechanismus auf die druckdifferenzgetriebene Ausgleichsströmung zwischen der Druck- und Saugseite der Ventilatorblätter im Spaltbereich zwischen Blattspitzen und Ummantelung zurückzuführen ist. Die lokale Geometrie übt hierbei einen starken Einfluss auf diese sogenannte Sekundärströmung aus, welche unter Anderem durch Strömungsablösung, daraus resultierender Wirbelbildung sowie der Interaktion derselben mit der Hauptströmung geprägt ist. Neben der offensichtlichen Komplexität der Strömungsvorgänge, in Verbindung mit der starken, räumlichen Beschränkung des relevanten Einflussbereiches, stellt die Rotation des Ventilators zusätzlich eine besondere Schwierigkeit dar. Daraus folgt für die Untersuchung der kopfspaltströmungsbedingten Schallentstehung für numerische, wie auch experimentelle Ansätze ein gleichermaßen erheblichen Aufwand.

Dem zu Beginn erwähnten Prinzip entsprechend, soll ein gemeinsam von ebm-papst und TEA geplanter, aeroakustischer Versuch mit der Bezeichnung „Braunschweig Tip-Gap-Noise Experiment“ (BTGNX) eine systematische, parametrisierte Untersuchung der Kopfspaltschallentstehung ermöglichen. Der grundlegende Aufbau orientiert sich hierbei an einem, in der Vergangenheit ausgiebig untersuchten, aeroakustischen Experiment der Ecole Centrale de Lyon [1], wobei dessen Fokus vornehmlich auf strömungsmechanische Aspekte ausgerichtet war. Auf ähnliche Art wird auch bei BTGNX die komplexe geometrische Situation am Kopfspalt eines rotierenden Ventilatorblattes mittels eines stationär zwischen zwei Platten befindlichen Flügels in einem Windkanal simplifiziert nachgebildet. Da das BTGNX hingegen vornehmlich auf die akustische Fragestellung der Kopfspaltschallquelle ausgerichtet ist, findet die Durchführung des Experimentes in dem lärmarmen, Akustischen Windkanal Braunschweig (AWB) [2] statt. Die experimentelle Datenerfassung erfolgt sowohl hinsichtlich der

Schallquellenlokalisation mittels eines akustischen Mikrofonarrays, als auch die durch Aufzeichnung instationärer Druckfluktuation mithilfe eines eigens dafür gefertigten Micro-Electro-Mechanical Systems (MEMS) Arrays. Weitere Details zum geometrischen Aufbau sowie den experimentellen Variationsparametern finden sich in [3].

Neben der experimentellen Betrachtung erfolgt parallel eine ausgiebige, numerische Untersuchungen am vorgestellten Aufbau. Dabei soll das reelle Experiment möglichst exakt sowohl strömungstechnisch als auch nachfolgend durch aeroakustische Rechnungen nachgebildet werden. Das zuvor erwähnte CAA Vorhersageverfahren der TEA kann somit in Gänze, sowie in dessen jeweiligen Teilschritten validiert werden. Dem Ablauf eines hybriden CAA Verfahrens entsprechend, erfordert der erste Schritt eine Computational Fluid Dynamics (CFD) Lösung zur untersuchten Problemstellung, welche im Anschluss als Eingangsgröße der akustischen Simulationen dient. Dies wird durch Lösung der Reynolds-Averaged Navier-Stokes (RANS) Gleichungen anhand des DLR-TAU Codes erreicht. Besonderer Wert liegt dabei auf einem möglichst niedrig-dissipativen Vorgehen, welches durch eine angepasste Vernetzungsstrategie sowie entsprechende Parameter innerhalb des CFD Lösers angestrebt wird. Nähere Details hierzu, die Simulationsstrategie wie auch erste Simulationsergebnisse am BTGNX, dargestellt in Abbildung 1, werden in diesem Beitrag erstmalig vorgestellt und diskutiert.

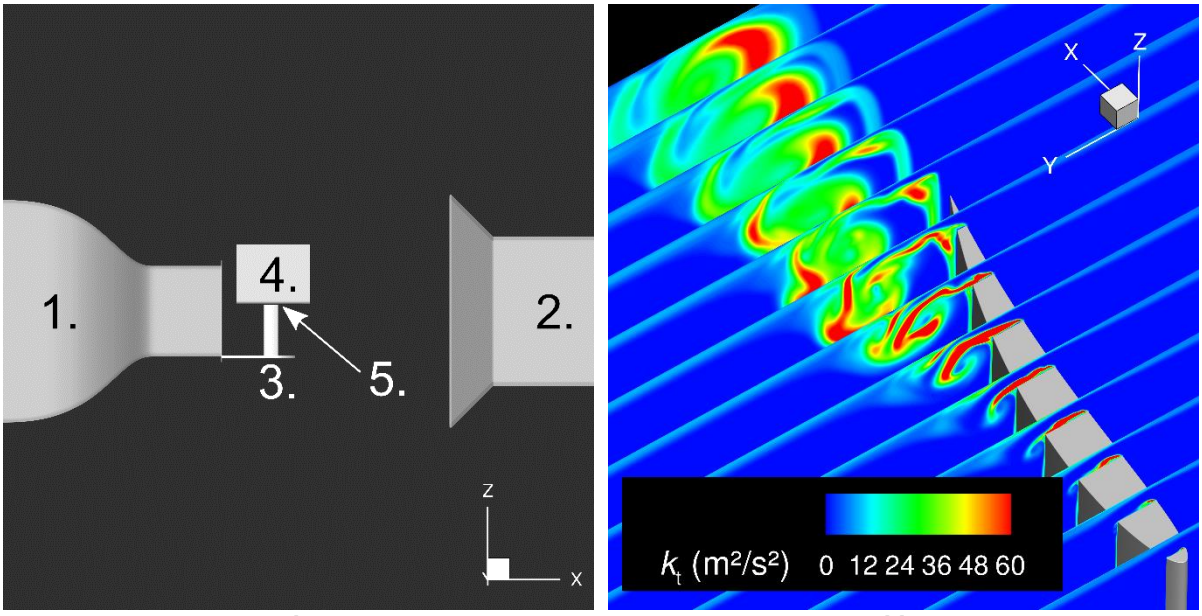

a) **b)**

Abb. 1: a) Seitenansicht der für numerische Simulationen verwendeten, detailreduzierten Geometrie bestehend aus Windkanal-Düse (1), Kollektor (2), Basisplatte (3), Abscheideblech (4) sowie Flügel mit variablem Kopfspalt (5). **b)** Detaildarstellung der Wirbelformation im Splatbereich als Konturplot der Turbulenten Kinetischen Energie auf Schnittebenen (Abscheideblech ausgeblendet). Saugseitiges Aufrollen der abgelösten Strömung resultiert im deutlich sichtbaren Kopfspaltwirbel.

Literatur:

[1] Grilliat, J., Jacob, M. C., Camussi, R. and CaputiGennaro, G.: Tip leakage experiment - Part one: Aerodynamic and acoustic measurements. 13th AIAA/CEAS Aeroacoustics Conference (28th AIAA Aeroacoustics Conference) (2007)
[2] Pott-Pollenske, M., Delfs, J. W.: Enhanced capabilities of the Aeroacoustic Wind Tunnel Braunschweig. 14th AIAA/CEAS Aeroacoustics Conference (29th AIAA Aeroacoustics Conference) (2008)
[3] Liberson, L., Anderson, J. L., Reuschling, F., Pott-Pollenske, M., Ewert, R. und Delfs, J. W.: Simulationsgestützte Konzeptionierung eines aeroakustischen Experimentes zur Untersuchung von kopfspaltströmungsinduzierter Geräuschentstehung. Fortschritte der Akustik - DAGA 2023 (49. Jahrestagung für Akustik) (2023)

Mitteilung

Fachgruppe: Strömungsakustik

Numerical Simulation of Propeller-Airfoil Interaction Noise

Zhe Yang*, Matthias Meinke, Wolfgang Schröder

Institute of Aerodynamics, RWTH Aachen University
Wüllnerstr. 5a, 52062 Aachen, Germany
*z.yang@aia.rwth-aachen.de

Distributed propulsion systems [1] are one of the promising approaches that could achieve less emission, higher efficiency, and maneuverability for future Urban Air Mobility (UAM) aircraft. The tight integration of the propulsion system with the airframe increases the airfoil lift-to-drag ratio as well as the propeller propulsive efficiency. However, along with the aerodynamic benefits, the configuration also brings challenges to the acoustic design. On the positive side, installing the propulsion system closer to the airframe should provide interesting acoustic shielding effects [2], reducing the far-field noise level of the aircraft in certain directions. On the adverse side, the integrated design may reinforce acoustic sources due to the unsteady loads caused by potential distortion or wake/boundary layer viscous effects, increasing the overall noise emission. Some research efforts have been made to seek a balance between the aero-dynamic benefits and the noise generation [3-5].

The object of this work is to improve the analysis of the noise generation mechanisms of propeller-airfoil interactions. Large eddy simulations (LES) of a distributed propulsion system are performed based on the multiphysics flow solver m-AIA [6] of RWTH. The unstructured hierarchical Cartesian mesh is generated according to predefined mesh parameters for the target geometry. The Navier-Stokes equations are solved by a finite volume (FV) solver at second-order accuracy in time and space to perform wall-resolved LES of the turbulent flow field. To track the rotating geometry of the propeller blades, a level-set solver based on the kinematic motion level-set approach is employed and coupled with the FV solver, providing solution adaptive mesh refinement (AMR) during the simulation run. A postprocessing module is integrated into the simulation workflow to conduct time averaging or time-series data sampling. For the far-field noise, the Ffowcs-Williams and Hawkings (FW-H) method formulated in the frequency domain is used to predict the pressure signals at far-field observers. During the simulation run, dynamic load balancing (DLB) is performed to alleviate the load imbalances from the AMR and to allow high parallel computing efficiency on high-performance computing systems of HAWK at HLRS from the University of Stuttgart.

The test geometry is the ENODISE-B1 configuration provided by TUDelft [7]. It has a tractor setup with three XPROP-S propellers which are installed upstream of a wing with an airfoil shape of NLFMod22(B). The incoming flow velocity is 30 m/s and the propeller advance ratio is 0.8. The propeller has an installation shaft incidence angle of -5 deg and the incoming flow has a +2 deg angle of attack (AoA) with respect to the wing chord. To reduce the computational cost, the simulation only includes the middle propeller. Periodic boundary conditions are used to mimic the effects of the two surrounding propellers. The Reynolds number based on the airfoil chord length is set to approximately 600,000 in accordance with the experimental setup. To resolve the turbulent boundary layer near the solid surfaces, the minimum spatial resolution near solid boundaries is chosen to be 7*10^-5 m, resulting in about 200 cells

along the propeller chord length and 4,000 cells along the wing chord length. Adaptive mesh refinement is applied to the fluid-solid interface with the minimum spatial resolution and coarsening to the far field until a maximum spatial step of 2*10^-3 m is reached. Overall, this leads to O(10^9) grid cells. The rotating propeller and the high-frequency turbulent scales are resolved with a timestep of 1*10^-7 s, which is determined by the stability limit of the numerical method.

The analysis of this work focuses on the interaction of the propeller slipstream with the downstream wing and its impact on noise generation. Preliminary results are shown in Figure 1. Figure 1(a) uses the Q-Criterion to visualize the propeller wake and tip vortex structures. The tip vortexes impinge on the leading edge of the wing and break down while traveling around the wing. Time series of pressure and velocity around the wing surfaces are recorded to investigate the wing turbulent flow field and to further identify potential noise sources. The contour of the instantaneous perturbed pressure field is plotted in Figure 1(b). It reveals the sound waves radiated from the propeller blades and also scattered from the leading edge of the wing. The noise level at the far-field observer 1.5 m away from the center is predicted by the Ffowcs-Williams and Hawkings method, shown in Figure 1(c). It is found that the noise radiation is concentrated in the forward and side directions, while the backward noise is reduced due to the acoustic shielding of the wing. The directivity of far-field noise at different frequencies will be further analyzed in the final paper.

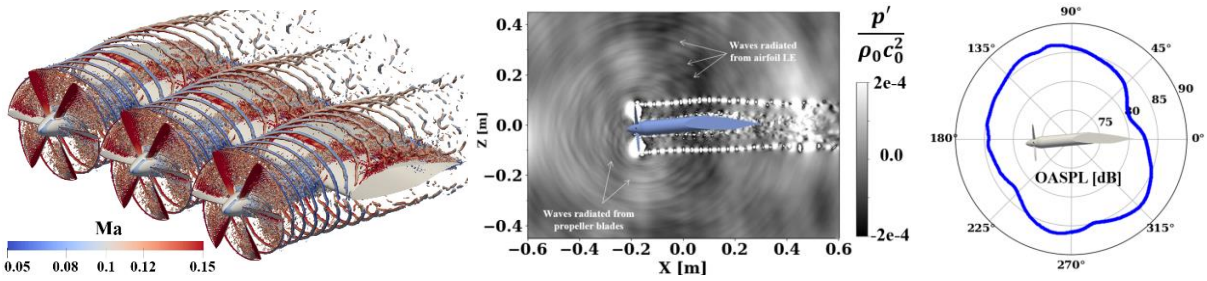

(a) (b) (c)

Figure 1: Exemplary results of the propeller-airfoil interaction. (a) The propeller wake and tip vortex structures denoted by Q-Criterion which is color coded by the local Mach number. (b) Instantaneous perturbed pressure field *p'* around the propeller and wing. (c) The overall sound pressure level at far-field observer predicted by the Ffowcs-Williams and Hawkings method.

References

[1] Gohardani, A.S., Doulgeris, G. and Singh, R., 2011. Challenges of future aircraft propulsion: A review of distributed propulsion technology and its potential application for the all electric commercial aircraft. Progress in Aerospace Sciences, 47(5), pp.369-391.

[2] Agarwal, A. and Dowling, A.P., 2007. Low-frequency acoustic shielding by the silent aircraft airframe. AIAA journal, 45(2), pp.358-365.

[3] Akkermans, R.A., Pott-Pollenske, M., Buchholz, H., Delfs, J. and Almoneit, D., 2014. Installation effects of a propeller mounted on a high-lift wing with a Coanda flap. Part I: aeroacoustic experiments. In 20th AIAA/CEAS aeroacoustics conference (p. 3191).

[4] Avallone, F., Casalino, D. and Ragni, D., 2018. Impingement of a propeller-slipstream on a leading edge with a flow-permeable insert: A computational aeroacoustic study. International Journal of Aeroacoustics, 17(6-8), pp.687-711.

[5] Acevedo Giraldo, D., Roger, M. and Jacob, M.C., 2023. Experimental Study of the Aerodynamic Noise of a Pair of Pusher-Propellers Installed Over a Wing. In AIAA AVIATION 2023 Forum (p. 3359).

[6] Lintermann, A., Meinke, M. and Schröder, W., 2020. Zonal Flow Solver (ZFS): a highly efficient multi-physics simulation framework. International journal of computational fluid dynamics, 34(7-8), pp.458-485.

[7] Duivenvoorden, R., Suard, N., Sinnige, T. and Veldhuis, L.L., 2022. Experimental Investigation of Aerodynamic Interactions of a Wing with Deployed Fowler Flap under Influence of a Propeller Slipstream. In AIAA AVIATION 2022 Forum (p. 3216).

Mitteilung

Fachgruppe: Strömungsbeeinflussung

Numerische Untersuchungen zur selektiven Detektion charakteristischer Strömungsfeldmuster in einer turbulenten Grenzschichtströmung

L. Bagdenand, M. Kurz, A. Beck, C. Wenzel, U. Rist
Institut für Aerodynamik und Gasdynamik der Universität Stuttgart
70569 Stuttgart, lisa.bagdenand@iag.uni-stuttgart.de

Bei genauerer Betrachtung von einigen Insekten, wie Fliegen oder Grillen und Spinnentieren fällt ein teils stark behaarter Körper dieser Lebewesen ins Auge. Sie nutzen diese Haare an Körper und Beinen als Sensoren, um Änderungen in der umgebenden Strömung zu detektieren. So können sie den genauen Standort von Beute oder Feinden ausmachen und entsprechend reagieren [1].
Fortschritte bei der Herstellung mikro-mechanischer Strukturen erlauben es heute, neue Sensoroberflächen herzustellen, die der dichten Anordnung von Haarsensoren bei Insekten und Spinnentieren ähnlich sind. Dadurch werden neue Formen der räumlichen und zeitlichen Signalerfassung möglich.
Hierzu gehören mikro-mechanische Sensoren, wie z.B. die von Brücker und Rist [2] vorgestellten flexiblen Micropillars zur Vermessung der Wandschubspannung. Nach dem biologischen Vorbild soll eine Anordnung von Fasersensoren in einer turbulenten Grenzschicht dazu genutzt werden, charakteristische Muster in der Strömung zu erkennen. Ähnlich einem Räuber, der seine Beute frisst, soll dann mittels eines Aktuators auf die detektierten Ereignisse in der Grenzschicht reagiert werden. Die nachfolgende Abbildung zeigt die detektierten Muster in einer turbulenten Grenzschicht, einen nachgeschalteten Aktuator und die ideale Wirkweise des Mechanismus schematisch.

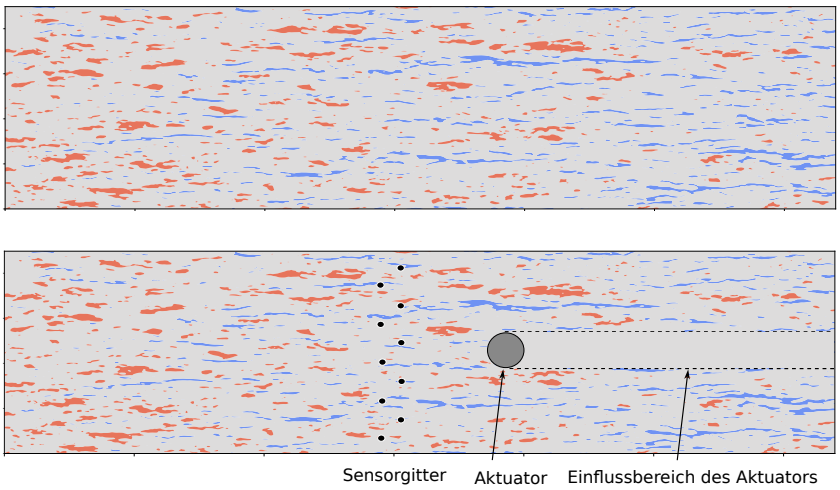

Abbildung 0: Wandparallele Ebene mit High- und Lowspeed Streaks. *Oben*: ohne Kontrollmechanismus. *Unten*: mit schematischem Kontrollmechanismus

Die Fasersensoren werden als steife Biegebalken betrachtet, auf die die ankommende Strömung als Kraft auf den Balken wirkt. Durch die verursachte Auslenkung des Sensors kann das Biegemoment der Sensorwurzel berechnet und als Messsignal verarbeitet werden. Anschließend wird dieses Messsignal mit dem momentanen Geschwindigkeitsfeld korreliert. So kann gezeigt werden, dass die maximale Korrelation von Geschwindigkeitsfeld und Biegemomentenfeld im Maximum der Geschwindigkeitsfluktuationen in Strömungsrichtung liegt und so die geeignete Messebene ermittelt werden.

Für die aktive Strömungskontrolle mittels Aktuator wird ein Kontrollmechanismus gesucht, um spezifisch auf die ankommenden Ereignisse zu reagieren. Da hier auf detektierte Messsignale der Fasersensoren in Echtzeit reagiert werden soll, ist ein Feedback control Mechanismus notwendig. Eine etablierte Methode ist die opposition control [3], die hier als Mechanismus genutzt werden soll. Diese Methode wird verwendet, wandnahe Strukturen zu beeinflussen mit dem Ziel, den Widerstand zu reduzieren. Es werden Geschwindigkeitssignale in wandnormalen Richtung ermittelt und entgegengesetzt mit Ausblasen oder Absaugen darauf reagiert. Ziel ist es, die wandnahen turbulenten Strukturen zu unterdrücken und so den Widerstand zu reduzieren. Das ist allerdings abhängig von der Sensorhöhe, die idealerweise dort liegt, wo die maximalen Geschwindigkeitsfluktuationen in Strömungsrichtung auftreten.

Nachteilig an diesem Ansatz ist, dass nur die Geschwindigkeitsfluktuationen in wandnormaler Richtung für den Kontrollmechanismus genutzt werden. Die Sensoruntersuchungen zeigen jedoch vor allem einen Einfluss der Fluktuationen in Strömungsrichtung, sodass auch dieser Einfluss für einen gesuchten Mechanismus berücksichtigt werden sollte. Zur Ermittlung einer Gewichtung im Kontrollschema kann Deep Reinforcement Learning genutzt werden. Dieser Ansatz findet immer mehr Anwendung in der aktiven Strömungskontrolle [4]. Durch ein neuronales Netz können sehr viele Daten gesammelt werden, um eine bessere Kontrollstrategie zu finden. So können komplexe Zusammenhänge basierend auf instantanen Geschwindigkeitsfluktuationen gesucht werden [5], die später mit den Fasersensoren kombiniert werden sollen.

Literatur

[1] Klopsch, C., Kuhlmann, H. C., Barth, F. G. Airflow elicits a spider's jump towards airborne prey. I. Airflow around a flying blowfly. *Journal of the Royal Society Interface*, 9(75), 2591-2602 2012.

[2] Brücker C., Rist U. Complex flow detection by fast processing of sensory hair arrays *in: H. Bleckmann et al. (eds.), Flow Sensing in Air and Water Springer-Verlag Berlin Heidelberg 2014*, 489-498, 2014.

[3] H. Choi, P. Moin and J. Kim. Active turbulence control for drag reduction in wall-bounded flows *Journal of Fluid Mechanics*, 262(4), 75-110., 1994.

[4] Rabault, J., Kuchta, M., Jensen, A., Réglade, U., Cerardi, N. Artificial neural networks trained through deep reinforcement learning discover control strategies for active flow control. *Journal of Fluid Mechanics*, 865(March), 281-302, 2019.

[5] Sonoda, T., Liu, Z., Itoh, T., Hasegawa, Y. Reinforcement Learning for Reduction of Skin Friction Drag in a Fully Developed Turbulent Channel Flow. *Journal of Fluid Mechanics*, 960, A30, 2022.

Mitteilung

Projektgruppe/Fachkreis: Strömungsbeeinflussung

Numerical Design Study on Active Flow Control on Inlets of UHBR Engine Nacelles

Stefan Hayböck, Christian Breitsamter
Chair of Aerodynamics and Fluid Mechanics, Technical University of Munich
Boltzmannstr. 15, 85748 Garching b. München, stefan.hayboeck@tum.de

Introduction

Turbofan engines are moving towards higher bypass ratios and larger fan diameters to increase propulsive efficiency. Shorter inlets are required to reduce drag and weight penalties of ultra-high bypass ratio (UHBR) engine nacelles. Aerodynamic limitations for short inlets are the fan rotor interaction with over-speed regions at the inlet lip and reduced flow straightening. Inlet separation and non-uniform pressure distribution in climb and crosswind conditions alter the fan operating conditions, and eventually, the fan could experience rotating stall.

In the framework of the Lufo VI-2 project AKTIVER, active flow control (AFC) is being investigated experimentally and numerically on an inlet of an UHBR engine nacelle. AFC can prevent stall and engine surge at off-design conditions by ensuring inflow quality specified by engine manufacturers. Local air injection at the inlet lip can help to energize and stabilize the boundary layer, increasing the aerodynamic load capacity of engine inlets far beyond current levels. AFC technology has been extensively investigated on engine intakes, showing great potential [1], [2].

In the present work, a numerical design study for an AFC system on a future wind tunnel model is conducted. The study on a generic, axisymmetric nacelle geometry representative of a modern short inlet engine nacelle is performed by unsteady RANS simulations. This initial design phase neglects possible interactions between a fan and the inlet flow. Thus, the nacelle is modeled as a flow-through nacelle. Starting from a clean configuration without AFC, predefined design parameters of the system are varied, and effects on the quality of the inlet flow are evaluated. Quantities for the evaluation of the AFC system are the pressure recovery coefficient η_σ, the distortion coefficient DC_{60}, and the swirl coefficient SC_{60}.

Model Design and Numerical Setup

A custom parameterization tool was developed for the design of the inlet and outer hull of the generic nacelle. A set of 14 parameters fully describes the smooth profile curve of the dimensionless, axisymmetric nacelle geometry. The inlet length over fan diameter ratio L/D of the inlet is 0.34, which is significantly lower than typical L/D ratios of current long-range aircraft engines.

A set of nine parameters characterizes the AFC system. The angles, θ_1 and θ_2 define the circumferential distribution of the circular blowing ports, d_{jet} sets the jet diameter, x_{jet}/l_{int} specifies the location of the blowing ports in x-direction relative to the inlet length, and the pitch angle α_{jet} and skew angle β_{jet} dictate the spatial orientation of the jets. Further, N_{jet} determines the number of blowing ports, U_{jet}/U_∞ controls the velocity of the jet relative to the freestream velocity, and rot_β determines whether the rotation of blowing port pairs around β_{jet} is done in a co-rotating or counter-rotating manner. Figure 1 gives a possible AFC configuration with its parameters θ_1, θ_2, α_{jet}, β_{jet} and x_{jet}.

The AFC use case of the design study is the wing $C_{L,max}$ condition since it is crucial in the certification process, and high levels of turbulence and flow separation are expected. The corresponding angle of attack of the engine inlet is $\alpha = 29°$. The freestream Mach number is fixed

at $Ma_\infty = 0.15$. This value is governed by the highest achievable speeds in future wind tunnel tests at the wind tunnel A of the Chair of Aerodynamics and Fluid Mechanics at the Technical University of Munich (TUM).

All computations are conducted with the pressure-based flow solver ANSYS Fluent. A steady-state solution is used to initialize unsteady RANS simulations. The numerical setup is validated against experimental data of a flow-through nacelle provided by Schulze and Kähler [3]. The k-ω GEKO-1.0 turbulence model accurately predicts separation behavior and reproduces the suction peak at the bottom inlet lip in agreement with the experiment. A Poly-Hexcore grid, created in ANSYS Fluent Meshing, combines high-quality octree hexahedron cells in the bulk region with isotropic poly-prisms in the boundary layer. The final computational grid consists of approximately 14 million cells, with minor variations resulting from changes in the parameters of the AFC system.

Results

First, a sensitivity analysis is performed on all parameters of the AFC system, changing each parameter within lower and upper bounds. A pre-defined baseline configuration of the system serves as a starting point for the optimization. Preliminary results of the sensitivity analysis show that the x-position of the blowing ports x_{jet}, the number of jets N_{jet}, and the pitch angle of the jets α_{jet} have the strongest influence on the system's overall efficiency and are therefore prioritized. The optimization strategy includes freezing prioritized parameters one at a time and sequentially adjusting the remaining parameters. Figure 2 illustrates the typical separation pattern at the inlet lip and the dynamic pressure loss at the aerodynamic interface plane (AIP).

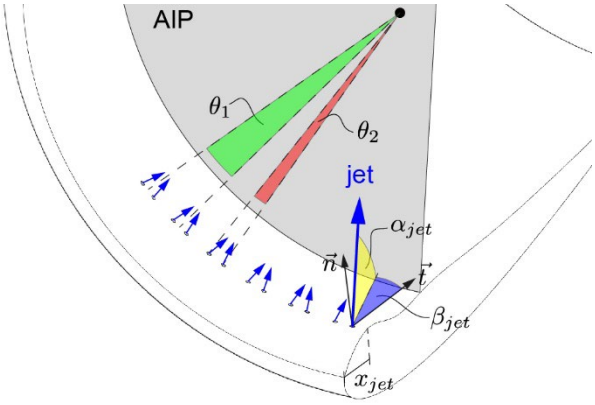

Figure 1: Example of a jet configuration, along with its design parameters θ_1, θ_2, α_{jet}, β_{jet} and x_{jet}.

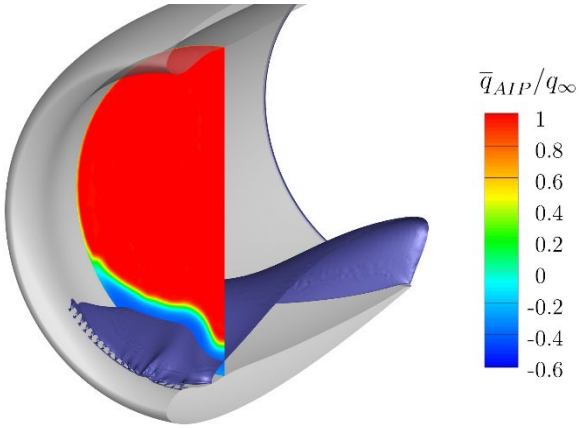

Figure 2: Visualization of the zero axial flow isosurface and the dynamic pressure loss at the AIP

Acknowledgments

The funding of this work by the BMWK within the LuFo VI-2 project AKTIVER (Aktive Strömungsbeeinflussung in Verdichterkomponenten künftiger Flugantriebe, FKZ: 20E2113A) is gratefully acknowledged.

References

[1] E. Garnier, “Flow Control by Pulsed Jet in a Curved S-Duct: A Spectral Analysis,” *AIAA Journal*, vol. 53, no. 10, pp. 2813–2827, 2015, doi: 10.2514/1.J053422.

[2] V. R. Nambiar and V. Pachidis, “Nacelle intake flow separation reduction at cruise condition using active flow control,” *Propulsion and Power Research*, vol. 11, no. 3, pp. 337–352, 2022, doi: 10.1016/j.jppr.2022.07.005.

[3] S. Schulze and C. J. Kaehler, “Analysis of the Flow in Stalling Engine Inlet Models with Different Visualization and Measurement Techniques,” in *Second Symposium ”Simulation of Wing and Nacelle Stall”*, Braunschweig, 2010.

Mitteilung

Fachgruppe: Strömungsbeeinflussung

On the influence of a wavy leading edge on the aerodynamic drag of a wing: A numerical parameter study

Marten Klein Robert W. Kessler Heiko Schmidt

Lehrstuhl Numerische Strömungs- und Gasdynamik, Brandenburgische Technische Universität (BTU) Cottbus-Senftenberg, Siemens-Halske-Ring 15A, 03046 Cottbus
marten.klein@b-tu.de

Wings are found in many technical flows. While most applications are associated with dynamic lift generation (e.g., airfoils, blades of propellers and turbines), wings also provide means to guide the flow around an obstacle in a controlled way. In the latter case, the goal is to minimize aerodynamic drag for some targeted operation conditions under additional geometric constraints. Optimization problems of this kind arise in aviation and automotive engineering, but perhaps even more so in high-performance sports due to rather frequently changing regulations. A number of studies has reported drag reduction effects by wavy leading edge (WLE) wings. These are inspired by whale fins and due to the previous interest in aviation, the lift-to-drag ratio [1,2] has been in the focus. No study so far, to the best of our knowledge, has addressed drag alone, which is important for applications to sports.

In the present study, some fundamental aspects of aerodynamic drag due to wing shape modifications are addressed specifically from the perspective of high-performance track cycling. The attention is here limited to the fork of the bike in order to focus the discussion on a canonical set-up. That is, the basic configuration investigated consists of a single wing in a cross flow that represents a section of only one arm of the fork of a track bike. Several numerical simulations were conducted with the open-source CFD software *OpenFOAM* [3] (version 8), where *simpleFoam* was used for Reynolds-averaged Navier–Stokes simulation (RANS) and *pisoFoam* for large-eddy simulation (LES).

Figure 1(a) shows a sketch of the WLE wing configuration investigated and Figure 1(b) a flow visualization based on a preliminary LES. The WLE wing is defined by a modification of a straight leading edge (SLE) symmetric base profile. The geometry perturbation is parameterized by the wavelength w, the wave amplitude a, and the edge radius k. The remaining circular wave radius is governed by the other parameters and obtained by a tangential matching condition. The flow domain extends $4w$ in spanwise, $25c$ in streamwise, $12.5c$ in cross-stream direction, where $c=80\,mm$ is the chord length of the SLE base profile. The SLE base profile is $d=11\,mm$ thick. These dimensions are motivated by the regulations of the Union Cycliste Internationale (UCI) [4]. The wing is centered in the flow domain and placed $8c$ behind the inflow plane. The angle of attack is 0°. The Reynolds number is $Re=88{,}000$ based on the inflow velocity, the chord length of the underlying SLE base profile, and the density and viscosity of air at standard conditions.

For RANS, the so-called *k-ω* SST turbulence model [5] was selected based on pre-simulations for the flow around a NACA 0021 wing profile. This model requires to initialize the unresolved turbulent kinetic energy (TKE). For open roads the turbulence intensity varies between 2–15% [6,7], but for tracks the ambient flow almost vanishes so that a turbulence intensity I of 1% is used. The so-called *nutLowReWallFunction* was prescribed for the wall-resolved simulations, assuring $y_1^+<1$ for the first layer of meshes all around the wing. Three-dimensional body-fitting meshes with mostly linear hexahedra and a few prisms and tetrahedra were generated by *snappyHexMesh* that is shipped with *OpenFOAM*. Here, 20 inflation layers were used for the near-wall region.

Figure 2 summarizes all RANS results in terms of the aerodynamic drag coefficient C_d using the actual frontal area of the wing for normalization. For convenience, the relative modification $\Delta C_d=(C_d^{WLE}-C_d^{SLE})/C_d^{SLE}$ is shown, where the SLE base profile acts as reference.

The RANS-based reference value is $C_d^{SLE} = 0.128$. Each data point is a RANS result for a specific geometry. Labels follow a common convention, for instance, “w40a175k05” implies that $w = 40\,mm$, $a = 17.5\,mm$, $k = 0.5\,mm$ is used. Figure 2 (left) shows that the drag saturates for a dimensionless wave amplitude of $a/c \approx 0.2$ under track-bike conditions. However, the effect is weak and partly nonmonotonic as highlighted by the interpolating splines. The edge radius has demonstrably a minor influence on drag characteristics as it manifests itself only by a small offset between the triangles ($k/c = 0.025$) and the bullets ($k/c = 0.00625$). Figure 2 (right) demonstrates that the drag reduces with increasing wave amplitude, but only up to $w/c \leq 0.2$ for the present set-tup. The modeled drag reduction is becomes almost independent of the wavelength once the wing is long enough. This suggests that the ratio of the wave amplitude and the profile thickness, a/d, is the limiting geometry parameter.

Forthcoming research aims to utilize high-fidelity LES to consolidate the RANS results. A modification of the wall-boundary condition in the wall-modeled LES (WM-LES) may be needed as the default *OpenFOAM* implementation as shown limitations over spanwise curvature [8]. In the contribution, the emphasize will be on the systematic analysis of the RANS results, supplemented by field experiments (as available) and LES.

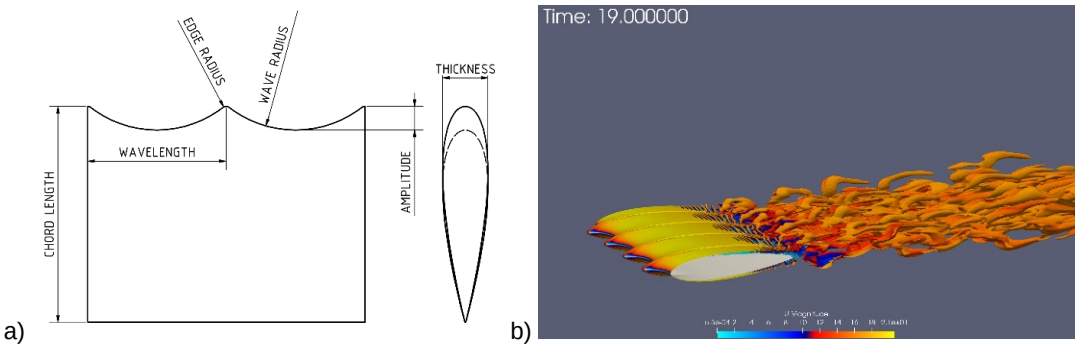

Figure 1: a) Wing geometry and geometry parameters for the wavy leading edge (WLE) case. Top view (left) and side view (right). b) Momentary flow solution visualized by the *Q*-criterion in a preliminary WM-LES of the wing labeled “w25a10k05”.

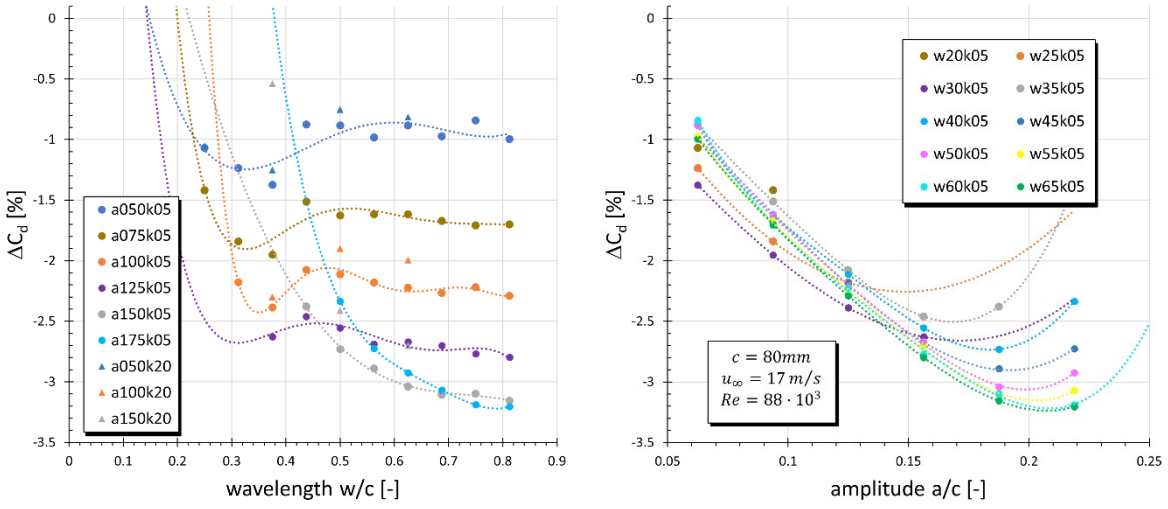

Figure 2: Relative drag reduction predicted by RANS for WLE wings relative to the SLE base profile. (left) Drag reduction as function of dimensionless wavelength. (right) Drag reduction as function of the dimensionless amplitude. Spline interpolations (dotted lines) are shown to guide the eye but have no physical implication.

References

[1] D. T. H. New, B. F. Ng, *Flow control through bio-inspired leading-edge tubercles: morphology, aerodynamics, hydrodynamics and applications*, Springer, 2020. ISBN 978-3030237936.
[2] W. Chen, W. Qiao, Z. Wie, *Aerospace Science and Technology* **106**:106216, 2020
[3] H. G. Weller, G. Tabor, H. Jasak, C. Fureby, *Comput. Phys.* **12**(6):620, 1998.
[4] Union Cycliste Internationale, *Clarification Guide of the UCI Technical Regulation.* Version 2021-10-05.
[5] Menter, F. R., NASA Technical Memorandum, TM 103975, 1992.
[6] J. W. Saunders, R. B. Mansour, *SAE Trans.* **109**:477–496, 2000
[7] S. Watkins, J. W. Saunders, SAE Technical Paper, Technical Report No. 950997, 1995.
[8] M. Klein, P.-Y. Tsai, H. Schmidt, *New Results in Numerical and Experimental Fluid Mechanics XIV - Contributions to the 23rd STAB/DGLR Symposium,* 2023, in press.

Mitteilung

Fachgruppe: Strömungsbeeinflussung

SCDP- A Suction Chamber Design Program

Geza Schrauf
Bremen, contact@schrauf.de

Drag reduction with the help of boundary-layer suction has been an ongoing topic of interest in the drive to reduce CO_2-emissions on aircraft. State-of-the art suction systems [1-4] are based on a microperforated titanium skin which is supported by a metallic or CFRP substructure. A major improvement compared to earlier designs [5] was the ALTTA double-skin structure [6], which satisfies both aerodynamic and structural requirements, resulting in much lighter systems.

Moreover, previously, the design process was complicated and time-consuming, because we needed a combination of several tools from different departments, or even institutions, for each design cycle. To speed up the design process of an ALTTA-type double-skin system, we have proposed a new modelling method and developed a new program. An example calculation is shown in Fig. 1.

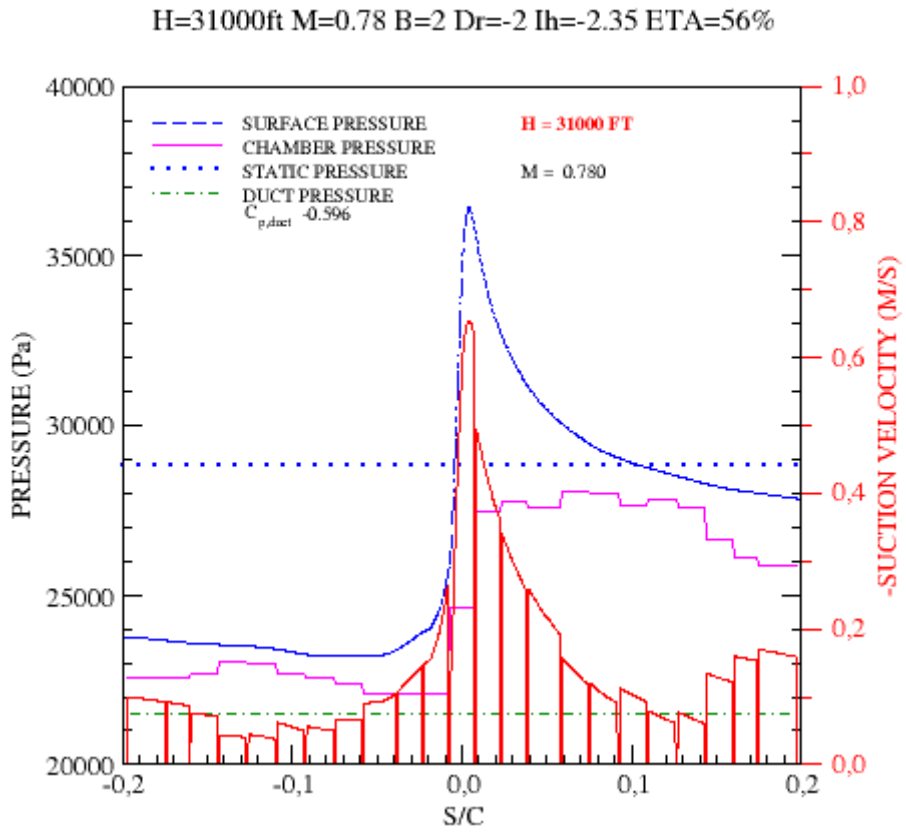

Fig. 1: Example of SCDP output for an ALTTA-type system [Fig. 8a of 3].

Meanwhile, the program has been updated [7] to be applied to the latest designs with very few or only one suction chamber and variable micro-perforation [8,9].

Furthermore, the program estimates the power needed to drive the air through the microperforation, the throttle holes, and, for an active system, to drive the compressor that pushes the air back into the atmosphere.

The aerodynamic design of a wing profile is based on non-dimensional quantities, such as the pressure coefficient C_p. However, for the design of a suction system, we need dimensional pressures, as can be seen from Fig. 1. The conversion between non-dimensional and dimensional quantities is theoretically straightforward. However, inconsistencies often occur. In the presentation, we describe how we handle these inconsistencies.

We will also show the underlying flow models, the numerical procedure based on a Newton iteration exploiting the special structure of the matrix, as well as two important design concepts:

- The allowable range of pressure-loss characteristic for the microperforation.
- The throttle hole design parameter.

These concepts allow a separation of the aerodynamic, system, and structure design from the manufacturing of the laser-drilled microperforation. With this separation, manufacturing of the microperforation can start early in the project and we can accommodate for deviations in the manufactured hardware. This makes the production of a suction system very robust.

Literature:

[1] G. Schrauf, H. von Geyr: “Simplified Hybrid Laminar Flow Control for Transport Aircraft”. ECCOMAS 2012, Vienna, Austria.

[2] G. Schrauf, H. von Geyr: “Validation of Simplified Hybrid Laminar Flow for Transport Aircraft”. ECFD VI, 2014, Barcelona, Spain.

[3] G. Schrauf, H. von Geyr: “Hybrid Laminar Flow Control on A320 Fin: Retrofit Design and Sample Results”. AIAA Journal of Aircraft (2021), Vol. 58, No. 6, November-December 2021, pp. 1272-1280. https://arc.aiaa.org/doi/10.2514/1.C036179.

[4] T. Dubois: “Does Airbus A350 Laminar Flow Test Signal Production Possibilities?” Aviation Week Network, April 30, 2019. https://aviationweek.com/air-transport/does-airbus-a350-laminar-flow-test-signal-production-possibilities.

[5] R. Henke: “First Results from the "A320 HLF Fin" Programme”. Notes on Numerical Fluid Mechanics (NNFM), vol. 72, 1999 (STAB Symposium Berlin 1998).

[6} K.H. Horstmann, W. Schröder: “A Simplified Suction System for a HLFC L/E Box of an A320 Fin”. ALTTA Technical Report 23, 10.09.2001, revised version 25.10.2009.

[7] G. Schrauf: “SCDP - A Suction Chamber Design Program. Version 2.1”. GSSC TR 8.7, 11.08.2023.

[8] T. Streit, M. Kruse, T. Kilian, J. von Geyr, I. Petropoulos: “Aerodynamic Design and Analysis of HLFC Wings within the European Project HLFC-WIN." 33. ICAS Congress, 2022, Stockholm, Sweden.

[9] G. Schrauf, T. Kilian: “Some Specific Challenges of HLFC Design on a Long-range Wing”. To appear in NNFMMD 154, 2023. https://elib.dlr.de/193840.

Mitteilung

Fachgruppe: Transportflugzeugkonfigurationen

Aerodynamische Nichtlinearitäten in instationärer, transsonischer Strömung am Beispiel des NASA Common Research Models

Diliana Friedewald
Deutsches Zentrum für Luft- und Raumfahrt e.V., Institut für Aeroelastik, Göttingen
Diliana.Friedewald@dlr.de

Für die Auslegung eines Flugzeuges muss eine Vielzahl von Lastenrechnungen durchgeführt werden. Von den Zulassungsvorschriften gefordert sind beispielsweise Böensimulationen mit verschiedenen Böenamplituden und -längen. Gerade für Anregungen mit großen Amplituden ist die Lösung der instationär nichtlinearen RANS-Gleichungen im Zeitbereich sinnvoll, etwa um eine beginnende Ablösung und damit verbundene aerodynamische Nichtlinearitäten zu identifizieren. Im Folgenden soll am Beispiel einer Transportflugzeugkonfiguration untersucht werden, welche nichtlinearen Effekte bei monofrequenter Böenanregung in transsonischer Strömung auftreten können und wie diese sich auf den Verlauf des Auftriebsbeiwertes auswirken.

Im Fokus der Arbeiten steht das NASA Common Research Model (CRM) in der Highspeed-Konfiguration [1], dessen Designpunkt bei Mach 0.85, einer Reynoldszahl von 40 Millionen (Referenzlänge 7m) und einem Auftriebsbeiwert von C_L=0.5 liegt. Die Geometrie des Modells wird als starr angenommen und entspricht der Designform. Gerechnet wird mit dem Ein-Gleichungs-Modell von Spalart und Allmaras in der Originalversion [2]. Das CFD-Netz ist mit dem Netzgenerator CENTAUR® erstellt. Es umfasst ca. 11 Millionen Knoten bei knapp 112000 Oberflächenpunkten, siehe Abb. 1. Zur Untersuchung der Amplitudeneffekte werden monofrequente Böensimulationen an drei stationären Punkten durchgeführt, siehe Abb. 2. Böenamplituden und -längen variieren dabei in einem breiten Bereich.

Für die betrachtete Konfiguration werden zwei Arten von Nichtlinearitäten identifiziert:

a) Instationär nichtlineare Effekte, die aufgrund von signifikanter, stoß-induzierter Strömungsablösung zu einem vorzeitigen Auftriebseinbruch und damit zu einem geringeren maximalen Auftriebsbeiwert (im Vergleich zur linearisierten Lösung) führen
b) Instationär nichtlineare Effekte, die aufgrund einer signifikanten, topologischen Änderung des Strömungsfeldes (*ohne* signifikante Strömungsablösung) zu einer Erhöhung des maximalen Auftriebsbeiwertes führen

Die Kombination beider Effekte kann, je nach Anregungsamplitude, zu einem konstanten oder kleineren maximalen Auftriebsbeiwert im Vergleich zur linearisierten Lösung führen.

Die identifizierten Effekte werden exemplarisch an der NASA CRM-Konfiguration bei Mach 0.83 und einem Anstellwinkel von 2.02° gezeigt. Unter diesen Anströmbedingungen stellt sich ein Doppelstoß im Bereich des mittleren Flügels ein, siehe Abb. 3. Für kleine Frequenzen mit großen Amplituden treten kleinere maximale Auftriebsbeiwerte auf, als mit der linearisierten Lösung berechnet, siehe Abb. 4. Für mittlere Amplituden und/oder mittlere Frequenzen kommt es zu einer Überschätzung der linearisiert vorhergesagten Maximalwerte, die vermutlich auf die topologische Änderung des mittleren Strömungsfeldes zurückzuführen ist: der stationär vorhandene Doppelstoß geht zeitweise in einen einfachen Stoß über, siehe Abb. 5. Es erhöht sich sowohl der Betrag des zeitlich gemittelten Auftriebsbeiwertes als auch der Betrag der ersten Antwort-Harmonischen.

[1] VASSBERG, J. C.; DEHAAN, M. A.; RIVERS, M. S. & WAHLS, R. A.: Retrospective on the Common Research Model for Computational Fluid Dynamics Validation Studies. In: *Journal of Aircraft* 55 (2018), Nr. 4, S. 1325-1337

[2] SPALART, P. & ALLMARAS, S.: A One-Equation Turbulence Model for Aerodynamic Flows. In: *30th Aerospace Sciences Meeting and Exhibit*., 1992

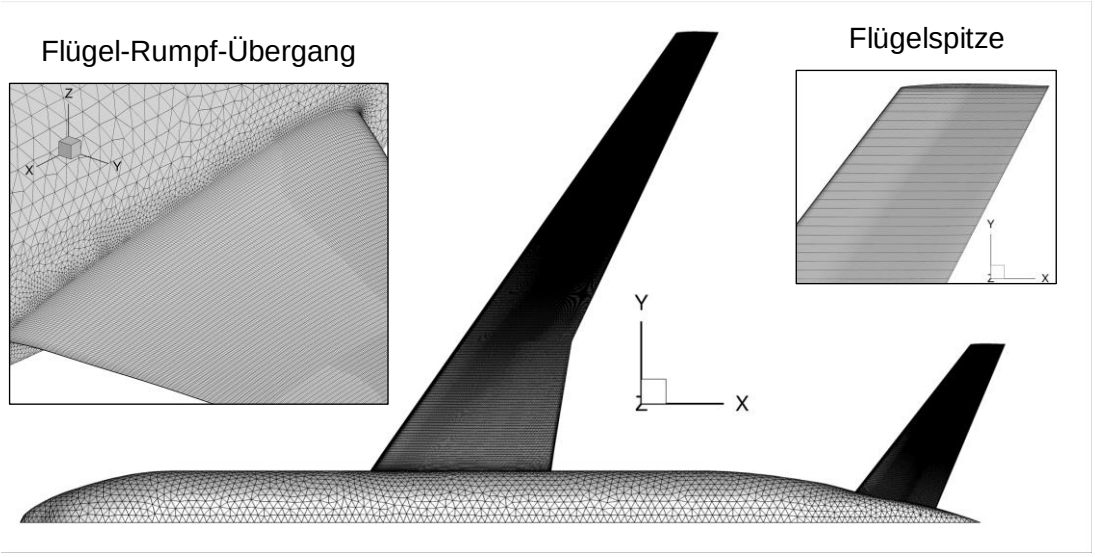

Abb. 1 CFD-Netz für das Halbmodell des NASA Common Research Models

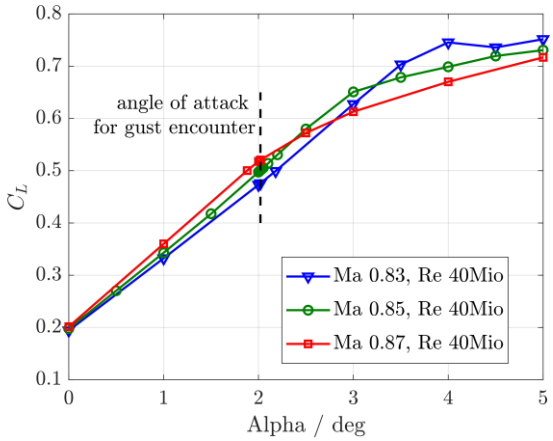

Abb. 2 Stationäre Polaren; zusätzlich gekennzeichnet ist der stationäre Anstellwinkel von 2.02° für die Böentreffer

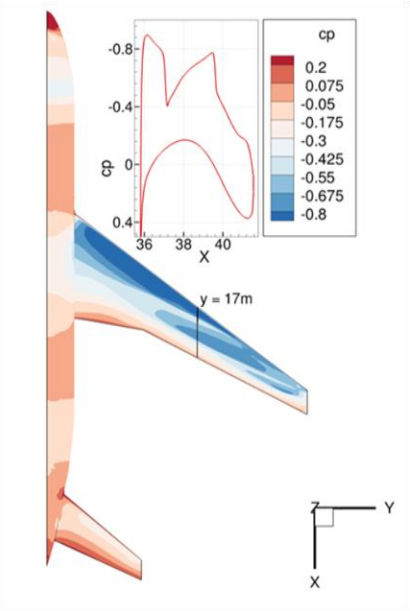

Abb. 3 Stationäre Druckverteilung bei Mach 0.83, einem Anstellwinkel von 2.02° und einer Reynoldszahl von 40 Mio

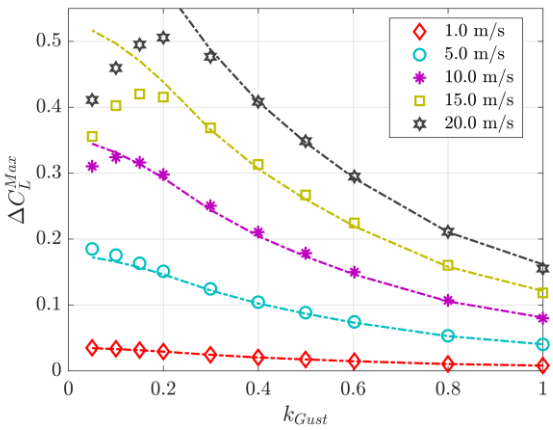

Abb. 4 Maximale Auftriebsinkremente für alle Böen bei Mach 0.83
(Linien: linearisiert, Symbole: nichtlinear)

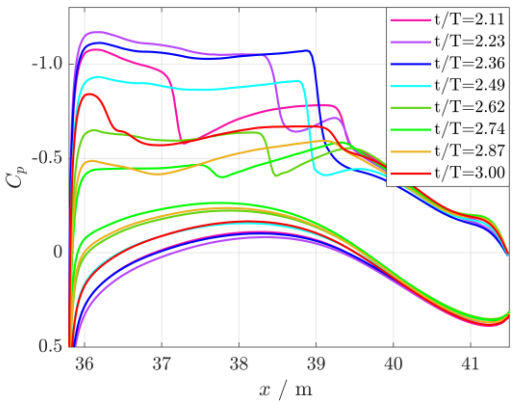

Abb. 5 Druckbeiwerte über eine Antwortperiode für den Flügelschnitt bei y=17m, Mach 0.83, $k_{Gust} = 0.4$, $\widehat{W}_G = 10\ m/s$

Mitteilung

Projektgruppe/Fachkreis: Transportflugzeugkonfigurationen

Aerodynamic Analysis of a Foldable Outer Wing Segment on a Transonic Transport Aircraft

Andreas Molz, Jonathan Pflüger, Christian Breitsamter
Chair of Aerodynamics and Fluid Mechanics, Technical University of Munich
Boltzmannstr. 15, 85748 Garching b. München, andreas.molz@tum.de

Introduction

Within the scope of environmental and economic sustainable flight operations, increasing the efficiency of modern transonic transport aircraft can be seen as a key requirement. Considered from an aerodynamic point of view, an innovative approach of high span wings combined with folding outer segments offers many advantages.

The higher aspect ratio by the folding wing yields a reduction of induced drag and, thus, an increase in aerodynamic efficiency. In atmospheric turbulent conditions, the folding outer wing segment can help to reduce loads and improve stability. [1,2]

Based on the great potential of both technologies, the LuFo VI-2 project GUSTAFO (Gust Load Alleviation by Folding non-linear Wing Tip) has been started in cooperation between the Institute of Aerospace Systems (ILR) of RWTH Aachen University, the Institute of Flight Mechanics, Flight Control and Aeroelasticity (FRMA) of TU Berlin and the Chair of Aerodynamics and Fluid Mechanics (AER) of the Technical University of Munich. The main goals of the project are dedicated to the evaluation of the potential efficiency increase and capabilities of gust load alleviation when applying a nonlinear folding outer wing segment to a transport aircraft wing. The assessment of synergetic interaction effects between both coupled technologies is of major interest [3,4].

The flexible wing segment resulting effects are assessed on various fidelity levels on the one hand employing the overall aircraft design (OAD) toolbox MICADO at ILR and supplementary performing on the other hand computational fluid dynamics (CFD:URANS) simulations at AER. The multi-fidelity approach allows an overall mission level, as well as the consideration of complex three dimensional aerodynamic effects on a detailed CFD level. Additionally, the project comprises a coupling of multi-fidelity analyses through reduced order modeling (ROM) of the CFD calculations.

In the following section a brief overview of the numerical setup and the selected CFD results for the reference configuration are described. Subsequently, an outline of future simulations is given.

Reference Configuration and Numerical Setup

CFD Simulations are carried out with Ansys Fluent, solving the Reynolds-Averaged Navier-Stokes (RANS) equations. The computational gird is generated by Ansys Fluent Meshing. A grid independence study results in a final grid for the semi span model of $24 \cdot 10^6$ elements. Turbulence modelling is performed with the $k-\omega$ SST Shear Stress Transport model. The reference wing features a wing span of b = 35,8 m with a corresponding aspect ratio of AR = 10,08. The wing tip rotational axis is defined at a spanwise position of $\eta = \frac{y}{s} = 0{,}9$ and limited to a rotation of the longitudinal axis (hinge line).

Results

The simulations are conducted at cruise Mach number of Ma = 0.78 and a Reynolds number of Re = $26{,}9 \cdot 10^6$, corresponding to the initial cruise altitude of h = 33000 ft. Figure 1 shows the pressure distribution Cp on the suction side of the wing with a static deflection of the wing segment of δ = 20°. Considering the folding wing tip segment, preliminary simulations reveal a reduction in total lift of the wing, due to a lower AR of wing by wing tip deflection. Hence, the lift vector on the outer segment is tilted inboard, consequently an alleviation of the wing root bending moment occurs. Further investigations will concentrate on the gust response of the wing equipped with a dynamic, spring loaded tip segment. A reduction of the wing root bending moment under gust load, allows a lighter airframe design, resulting in a more efficient configuration.

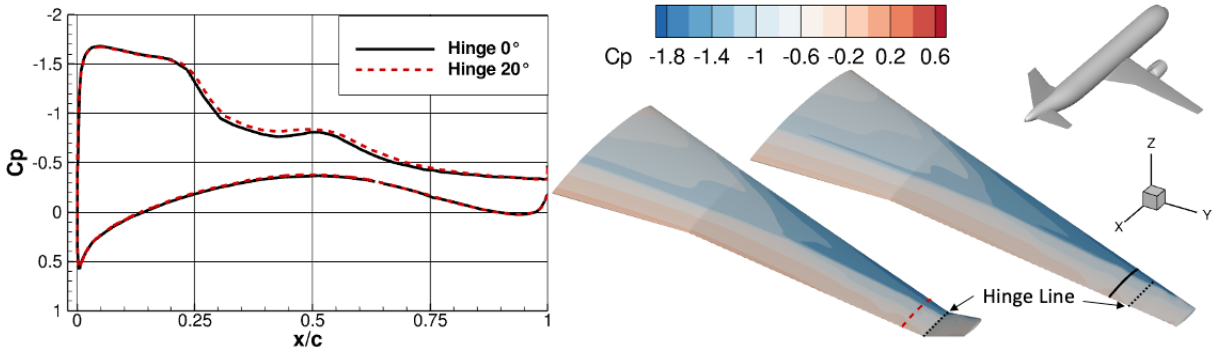

Figure 1: Pressure distribution for folding reference wing tip, left 20°/ right 0°deflection.

Acknowledgments

The funding of these investigations within the LuFo VI-2 project GUSTAFO (Gust Load Alleviation by Folding non-linear Wing Tip, FKZ: 20E2104C) by the Federal Ministry for Economic Affairs and Climate Action (BMWK) is gratefully acknowledged. The authors want to thank ANSYS for providing the flow simulation software used for the numerical investigations and the Gauss Centre for Supercomputing e.V. (www.gausscentre.eu) for funding this project by providing computing time on the Linux Cluster at Leibniz Supercomputing Center (LRZ, www.lrz.de).

References

[1] Smith, M.H. and Renzelmann, M.E. and Marx, A.D.: The Boeing Company, 1995. Folding wing-tip system. U.S. Patent 5,381,986.

[2] Healy, F. and Cheung, R. C. and Neofet, T. and Lowenberg, M.H. and Rezgui, D. and Cooper J.E. and Castrichini, A. and Wilson, T.: Folding Wingtips for Improved Roll Performance. AIAA Scitech Forum, 2021.

[3] Castrichini, A. and Wilson, T. and Saltari, F. and Mastroddi, F. and Viceconti, N. and Cooper, J. E.: Aeroelastics Flight Dynamics Coupling Effects of the Semi-Aeroelastic Hinge Device. Journal of Aircraft, Vol. 57, No. 2, pp. 333-341, 2019.

[4] Castrichini, A. and Hodigere Siddaramaiah, V. and Calderon, D.E. and Cooper, J.E. and Wilson, T. and Lemmens, Y.: Nonlinear Folding Wing Tips for Gust Loads Alleviation. Journal of Aircraft, Vol. 17, 2016.

[5] F. Schültke, B. Aigner, T. Effing, P. Strathoff and E. Stumpf, “MICADO: Overview of Recent Developments within the Conceptual Aircraft Design and Optimization Environement,” in Deutscher Luft- und Raumfahrtkongress, Aachen, 2020.

Mitteilung

Fachgruppe: Transportflugzeugkonfigurationen

Master Thesis: Numerical Investigation of the Swirl Recovery Potential using Wing Shape Adaptation for Distributed Propulsion Systems

Richard Straube (B.Sc.)
Institut für Aerodynamik und Gasdynamik der Universität Stuttgart (IAG),
Pfaffenwaldring 21 in 70569 Stuttgart, Richard.c.Straube@googlemail.com

Distributed propulsion (DP) has gained much interest in recent years due to its potential for improving aircraft aerodynamic and propulsive efficiency. Unlike conventional propulsion systems that use centralized engines, distributed propulsion involves the integration of multiple smaller propulsion units distributed across the aircraft's airframe. Primarily this involves the utilization of electric propulsion units, also known as distributed electric propulsion (DEP). Here, the propulsion units are distributed along the entire wingspan. This arrangement offers several advantages, such as enhanced aerodynamic performance, increased control authority, and improved safety margins.

In DEP systems, the interactions between the propeller and the wing play a crucial role. The propeller generates both axial and tangential acceleration within the flow, where the latter leads to swirl in the slipstream, which does not contribute to the system's thrust and can also be seen as a loss of the system's energy. Moreover, the swirl of the propeller slipstream induces a spanwise highly variable flow approaching the wing. In the case of an unadapted wing, this results in suboptimal flow conditions over a significant spanwise extent, which consequently leads to non-optimal flow conditions across a large portion of the wing's surface and therefore inefficient recovery of swirl energy.

One potential solution to improve swirl recovery is to adapt the wing shape to the local flow conditions. This work aims to explore the potential of swirl recovery through the modification of the local wing geometry for distributed propulsion systems. Various forms of wing shape modification are investigated in a parameter study, e.g. the influence of geometric twist, aerodynamic twist, and leading edge adaption on the swirl recovery potential (see Figure 1). The study employs a simplified baseline NACA0012 wing model, which is deformed using different methods, including modifications to the 2D airfoil and spanwise variations. To facilitate the investigation, a 2.5D approach is adopted, focusing on an idealized, infinitely extended wing equipped with distributed propulsion units. Additionally, the six-bladed propeller is represented using a BEM-based actuator disk model (ACD). Within this work, a toolchain is developed for automated wing geometry modification and mesh generation, followed by high-fidelity CFD RANS simulations using the DLR TAU code [1]. In this context, the geometric modifications are achieved by altering wing sections in the spanwise direction and using a cubic B-spline surface interpolation technique across the control sections.

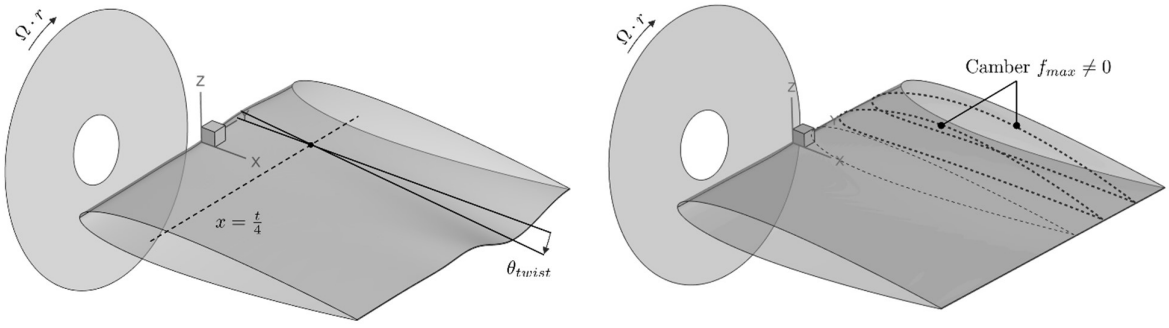

Figure 1 : *Geometric twist modification (left) and aerodynamic twist modification (right) of the trailing wing in the slipstream region of the ACD*

Preliminary investigations of a High-Speed Case (HSC), representing realistic cruise flight conditions of an ATR-72 equivalent aircraft, reveal that the propeller-induced swirl and consequently spanwise effects on the trailing wing are significantly less pronounced than for a Low-Speed Case (LSC). This strongly limits the potential design space for wing shape adjustments in the HSC scenario. Consequently, the LSC (corresponding to take-off conditions) is chosen as the primary test case to enhance the sensitivity of the study. Special attention is directed toward the investigation of co-rotating propellers by employing periodic boundary conditions at the lateral domains of the 2.5D setup. Within the parameter study, the lift coefficient of the trailing wing is set to a constant value, corresponding to the baseline model's (ACD + unmodified NACA0012 wing) maximum aerodynamic efficiency.

Based on the baseline model, the wing sections located on the upwash side (UWS) and the downwash side (DWS) of the ACD slipstream are modified independently. Among the variable parameters considered, including the geometric twist angle, the airfoil camber, and the droop nose deflection angle, it appears that the geometric twist modification has the weakest impact on the overall propulsive efficiency improvement of the system. Interestingly and somewhat counterintuitively, the simulation results indicate a slight reduction in wing drag when pitching the leading edge (LE) upward on the UWS or pitching the LE downward on the DWS within a certain range.

In contrast, the camber modification emerges as the most influential parameter among the investigated geometric shape parameters. In order to gain a deeper understanding of the underlying flow physics, the exergy analysis method by Arntz [2] is used to quantify the actual reduction in transverse (swirl) energy at different axial positions in the slipstream of the ACD. As shown in Figure 2a, the camber increase on the DWS leads to a significant enhancement of the transverse energy rate downstream of the configuration, while the camber increase on the UWS reveals even a slight reduction in the transverse energy rate compared to the baseline model. In Figure 2b, the aerodynamic efficiency of the wing is plotted against the maximum camber for independent camber adjustments on the UWS and DWS. In general, this parameter study suggests that a higher camber on the UWS and lower camber on the DWS can be advantageous up to a certain point in reducing the swirl and enhancing the system's overall propulsive efficiency.
Finally, the work reveals that a droop nose modification has a similar but compared to the camber modification weaker influence on the potential for wing drag and swirl reduction.

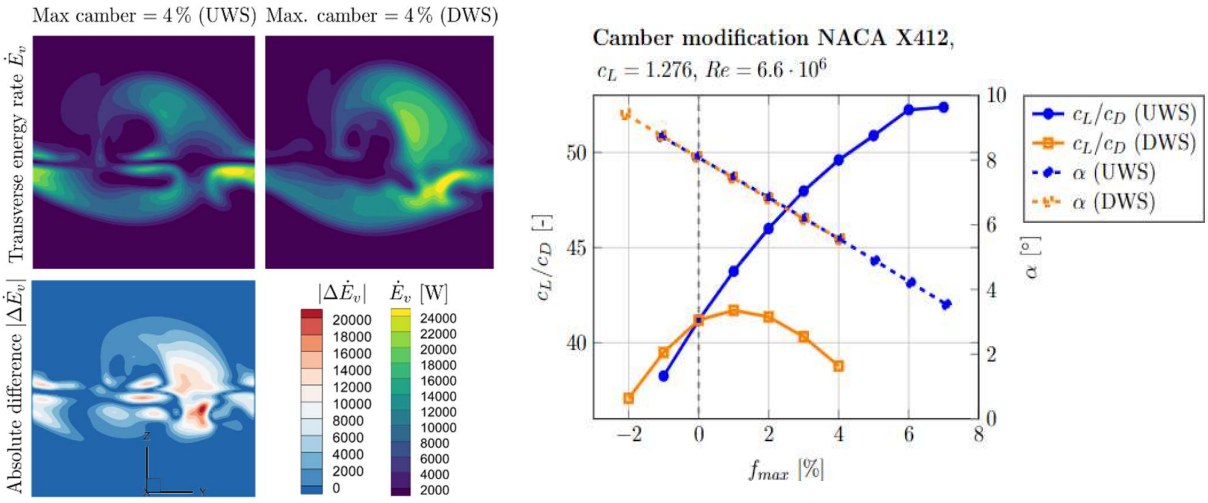

(a) *(b)*

Figure 2: (a) *Visualization of the transverse (swirl) energy rates in the survey plane downstream of the aerodynamic configuration for a camber increase of 4% on the UWS and DWS and the absolute difference between both cases.* ***(b)*** *Aerodynamic efficiency and far-field angle of attack plotted against the maximum camber for a camber modification on the UWS and DWS.*

[1] Technical report: Technical documentation of the DLR Tau-code release 2018.1.0. Deutsches Zentrum für Luft- und Raumfahrt e.V. (DLR), Institute of Aerodynamics and Flow Technology Braunschweig/ Göttingen.

[2] Aurélien Arntz. Civil aircraft aero-thermo-propulsive performance assessment by an exergy analysis of high-fidelity CFD-RANS Flow Solutions. PhD thesis, Université de Lille 1, 2014.

Mitteilung

Projektgruppe/Fachkreis: Transportflugzeugkonfigurationen

Numerical investigation of transonic buffet at a transport aircraft at forced wing oscillations

Vinzenz Völkl, Christian Breitsamter
Chair of Aerodynamics and Fluid Mechanics, Technical University of Munich
Boltzmannstr. 15, 85748 Garching b. München, vinzenz.voelkl@tum.de

Introduction

One of the main tasks in the analysis and certification process of aircraft including the aerodynamic and structural optimization is the determination of the flight envelope limits as accurate as possible. Here, mostly dynamic aeroelastic phenomena limit the flight envelope apart from the quasi-steady stall limit. The most dominant phenomenon at higher subsonic Mach number and increased angle of attack being Buffet/Buffeting. Transonic buffeting is a structural shaking phenomenon occurring as a result of prevailing shock fluctuations in chord and span direction on the wing, combined with shock-induced, locally separated flow, cf. Raveh [1]. The aerodynamic excitation forces are classified under the terms transonic or high-speed buffet, Iovnovich [2].

In order to better understand the unsteady flow and interaction phenomena at High Speed Stall conditions the research unit FOR2895 with seven subprojects and the European Transonic Windtunnel (ETW) facility has been established [3]. At the ETW experiments with the Airbus XRF-1 model have been made, providing input and validation data for all other subprojects, see figure 1, left side.

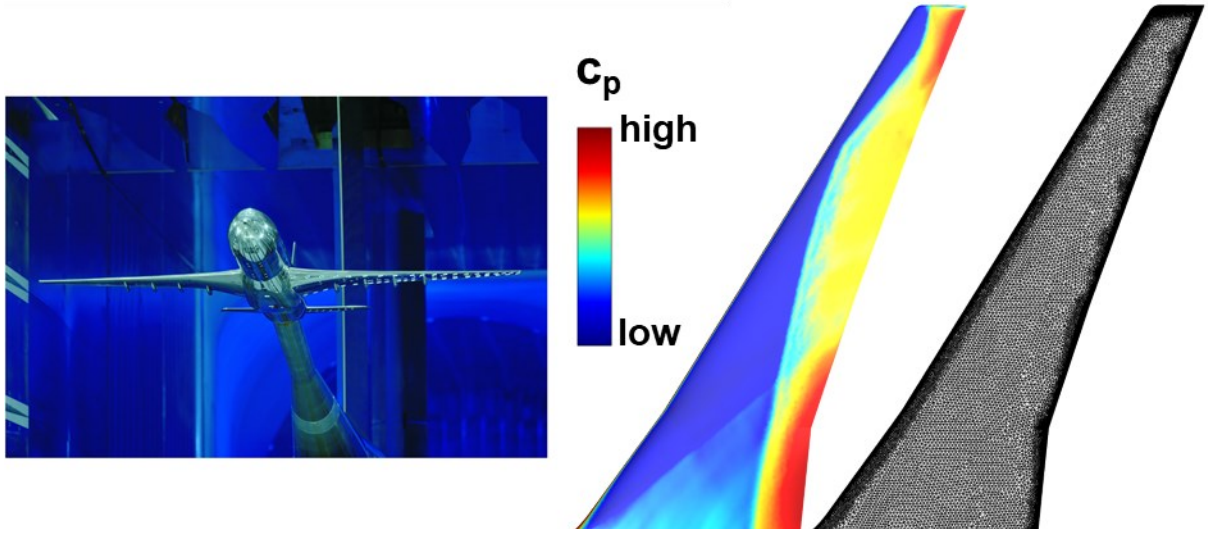

Figure 1: left side: Front view of the Airbus XRF-1 wind tunnel model [4], right side: Instantaneous c_p from CFD simulation using TAU on upper side of the wing at Ma = 0.84, Re=25•10^6 and α =4.5

Reference Configuration and Numerical Setup

Based on the results of various numerical and experimental studies, 3D buffet/buffeting is caused by the interaction of various physical mechanisms. An established way to separate those is to use Dynamic Mode Decomposition (DMD). One mode is associated with the shock movement in chord direction (Sr ≈ 0.05 – 0.1; Strouhal number based on mean chord), other so-called “buffet cells” move in spanwise direction (Sr ≈ 0.2 – 0.6) from wing root to tip. At low frequencies pressure waves run inboard along the shock front (Sr ≈ 0.05 – 0.15) [5]. Right now, only the inboard running buffet cells cannot be found by numerical simulations.

A simplified structural model representing one structural Eigenmode of the wind tunnel model is used here. The Eigenmodes of the wind tunnel model where derived from Ground Vibration Tests (GVT) of the XRF-1 wind tunnel model.

The numerical investigations are carried out using the DLR TAU code, solving the Unsteady-Reynolds-Averaged Navier-Stokes (URANS) equations. The unstructured computational grid is created using the grid generator CENTAUR. Turbulence modelling is performed with the $SSG/LRR\ \ln\omega$ Reynolds Stress Model (RSM). The structure is externally excited in a selected Eigenmode. The resulting wing deformation is then transferred onto the mesh using radial basis functions by the TAU mesh deformation tool.

Results

The buffet conditions are set at a Mach number of Ma=0.84, a Reynolds number of Re=25•10^6 and an angle of attack of α =4.5°, corresponding to the flow conditions in the ETW [3]. In figure 1 on the right side a preliminary mesh and instantaneous c_p distribution for no excitation is displayed. As the aircraft model is proprietary only qualitative results are shown.

The effect of different Eigenmodes in the vicinity of the measured buffet range is investigated. Preliminary investigations regarding the deformation were carried out with the NASA Common Research Model (CRM) and showed promising DMD results.

Acknowledgments

The authors gratefully acknowledge the Deutsche Forschungsgemeinschaft (DFG) for funding this work in the framework of the research unit FOR2895, subproject TP7, Grant number BR1511/14-1 and the Helmholtz Gemeinschaft HGF (Helmholtz Association), Deutsches Zentrum für Luft - und Raumfahrt DLR (German Aerospace Center) and Airbus for providing the wind tunnel model and financing the wind tunnel measurements. Further, the authors would like to thank the Gauss Centre for Supercomputing e.V. (www.gauss-centre.eu) for funding this project by providing computing time on the GCS Supercomputer SuperMUC at Leibniz Supercomputing Centre (www.lrz.de), as well as the DLR for providing the TAU source code.

References

[1] Raveh, D. E. and Dowell, E. H. „Aeroelastic Responses of Elastically Suspended Airfoil Systems in Transonic Buffeting Flows“. In: AIAA Journal 52.5 (2014), S. 926–934.

[2] Iovnovich, M. and Raveh, D. E. „Numerical Study of Shock Buffet on Three-Dimensional Wings“. In:AIAA Journal 53.2 (2015), S. 449–463.

[3] Waldmann, A., Ehrle, M. C., Kleinert, J., Yorita, D. and Lutz, T. „Mach and Reynolds Number Effects on Transonic Buffet on the XRF-1 Transport Aircraft Wing at Flight Reynolds number“. In: Experiments in Fluids 64.5 (2023), S. 1–25.

[4] Lutz, T., Kleinert, J., Waldmann, A., Koop, L., Yorita, D., Dietz, G. and Schulz, M. „Research Initiative for Numerical and Experimental Studies on High-Speed Stall of Civil Aircraft“. In: Journal of Aircraft (2022), S. 1–14.

[5] Masini, L., Timme, S. and Peace, A. J. „Scale-Resolving Simulations of a Civil Aircraft Wing Transonic Shock-Buffet Experiment“. In: AIAA Journal 58.10 (2020), S. 4322–4338.

Mitteilung

Projektgruppe/Fachkreis: Turbulence and Transition

Secondary instabilities of stationary crossflow vortices:
Comparison of LST-2D and PSE-3D with DNS.

B. Ambrosino, F. Tocci, A. Theiß, S. Hein
DLR – Institut für Aerodynamik und Strömungstechnik (AS)
Abteilung Hochgeschwindigkeitskonfigurationen
Bunsenstr. 10, 37073 Göttingen
biagio.ambrosino@dlr.de

Introduction

A significant reduction of aircraft drag could be attained by achieving laminar flow on wings. The need to control the laminar-turbulent transition process in swept-wing flows motivates the research on three-dimensional boundary layers. Laminar-turbulent transition in swept wing boundary layers is often initiated by stationary or travelling crossflow instabilities. At low levels of free stream turbulence such as those in free-flight conditions, the transition process of three-dimensional flows is known to be dominated by stationary crossflow vortices. Those vortices redistribute momentum across the boundary layer and result in a distortion of the otherwise spanwise invariant boundary layer. The distorted boundary layer is characterized by strong shear layers and is prone to the growth of secondary instabilies that finally trigger the laminar breakdown.
The secondary instability problem of crossflow vortices can be studied with different approaches. Koch et al. [1] used secondary instability theory and modelled the saturated crossflow vortices by nonlinear equilibrium solutions. Groot et al. [2] employed two-dimensional linear stability theory (LST-2D) to study an experimentally measured baseflow. Then, Casacuberta et al. [3] compared the secondary instability modes computed with LST-2D with the ones extracted from an unsteady direct numerical simulation (DNS). The LST-2D equations were derived in a non-orthogonal coordinate system following the approach of Li and Choudari [4]. In this work, we go beyond established approaches by employing both LST-2D and plane-marching parabolized stability equations (PSE-3D) in a non-orthogonal coordinate system, validating these methodologies through a comparative study with DNS results.

Numerical approach

A DNS computation of a swept-wing configuration was carried out with Nek5000 in a separate study, providing both the distorted base flow and the data for the secondary instability analyses. The NOLOT/LST-2D and NOLOT/PSE-3D codes have been employed to analyse the distorted baseflow. The former is a *local* approach, which solves a generalized eigenvalue problem, the latter is a *nonlocal* approach which is solved by a marching procedure in streamwise direction taking into account the upstream flow information to march downstream.
To overcome the well known dilemma of the extraction procedure for the baseflow to use for the stability analysis [5] the LST-2D/PSE-3D approach has been formulated in a non-orthogonal coordinate system. This formulation simultaneously allows for the fulfillment of the periodicity in the spanwise direction and accommodates the slow variation of the baseflow in the out-of-plane direction required by the PSE-3D. In this study the aforementioned direction is taken to be the one along which the derivative in the streamwise direction is the lowest, which closely resembles the crossflow vortex axis direction.

Results

The instability results (LST-2D and PSE-3D) are compared against the DNS data in Figures 1 and 2 for a type III secondary instability for a frequency of 900 Hz. This type of secondary instability is dominant in the near-wall region and can be interpreted as low-frequency travelling crossflow instabilities which are modulated by the presence of the stationary crossflow vortices. The integrated amplification rate versus the dimensionless surface arc length is shown in Figure 1. It can be noted that the LST-2D computation underpredicts the values attained in the DNS, while switching to a marching procedure (PSE-3D) allows for a more accurate match until station x/δ_0

≈ 650, where transition to turbulence starts to take place. In Figure 2 the normalized magnitude of the streamwise velocity amplitude function ($|\hat{u}|/|\hat{u}_{max}|$) is shown for LST-2D (left) and PSE-3D (right) at a station $x/\delta_0 \approx 450$. Also, the PSE-3D approach yields improvements in the resulting amplitude function compared to the LST-2D solution, demonstrating a generally good match with the DNS data. Further analysis will be presented during the workshop.

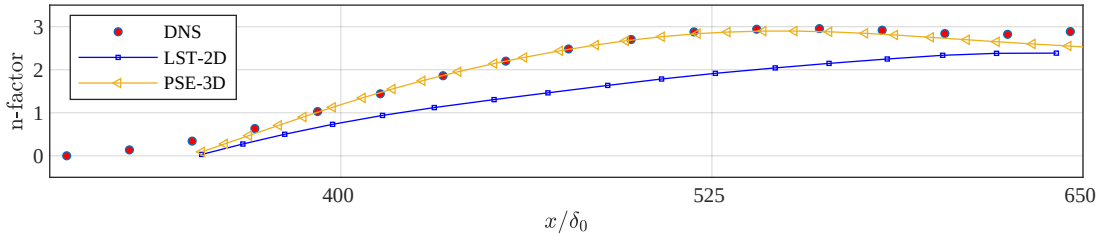

Figure 1: n-factor curves versus x/δ_0 for a type III secondary instability for a frequency of 900 Hz for: DNS (red dots), LST-2D (blue squares) and PSE-3D (yellow triangles). δ_0 is the displacement thickness at the first station of the instability computation.

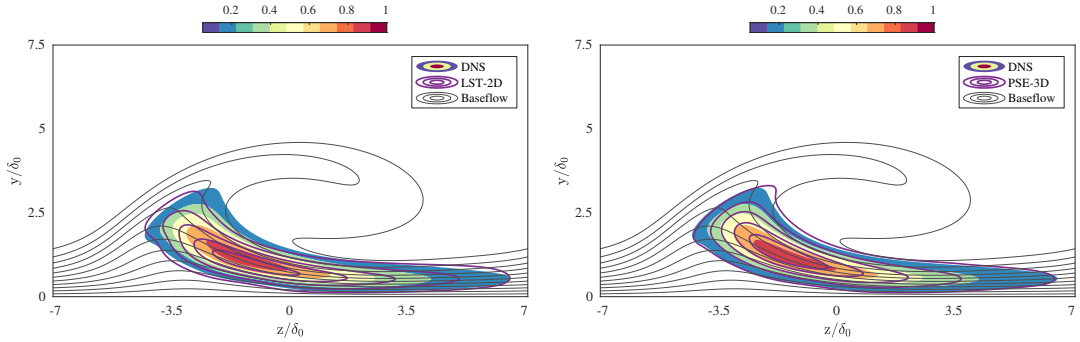

Figure 2: Normalized magnitude of the streamwise velocity component amplitude function ($|\hat{u}|/|\hat{u}_{max}|$) for a type III secondary instability for a frequency of 900 Hz at $x/\delta_0 \approx 700$. DNS (filled contour) compared with LST-2D (left) and PSE 3D (right) both represented in solid purple lines. Isolines of streamwise velocity component of the distorted baseflow (solid black).

Acknowledgement

This project has received funding from the European Union's Horizon 2020 research and innovation programme under the Marie Skłodowska-Curie grant agreement No. 955923.

Literature

[1] Koch W., Bertolotti F.P., Stolte A., Hein S.: Nonlinear equilibrium solutions in a three–dimensional boundary layer and their secondary instability. *J Fluid Mech.* **406**:131-174, 2000.

[2] Groot K., Serpieri J., Pinna F. and Kotsonis M.: Secondary crossflow instability through global analysis of measured base flows. *J. Fluid Mech.* **846**:605-653, 2018.

[3] Casacuberta J., Groot K., Hickel S. and Kotsonis M.: Secondary instabilities in swept-wing boundary layers: Direct Numerical Simulations and BiGlobal stability analysis. *AIAA Paper* **2022-2330**, 2022.

[4] Li F. and Choudhari M.: Spatially developing secondary instabilities in compressible swept airfoil boundary layers. *Theor. Comput. Fluid Dyn.* **25**:65-84, 2011.

[5] Bonfigli G. and Kloker M.: Secondary instability of crossflow vortices: Validation of the stability theory by direct numerical simulation. *J. Fluid Mech.* **583**:229-272, 2007.

Mitteilung

Fachgruppe: Turbulenz und Transition

Numerical investigation of the influence of streamline curvature on a turbulent boundary layer

Jason Appelbaum, Leonie Kling & Christoph Wenzel
appelbaum@iag.uni-stuttgart.de , wenzel@iag.uni-stuttgart.de
Institut für Aerodynamik und Gasdynamik (IAG)
Universität Stuttgart
Pfaffenwaldring 21
70569 Stuttgart

Direct numerical simulations (DNS) have been performed to investigate the effect of concave wall curvature on a subsonic turbulent boundary layer (TBL).

Several real-world applications involve turbulent flows over curved surfaces, for example turbomachinery or airfoil leading edges. Such wall curvature induces pressure gradients in the flow field in both the wall-tangential and wall-normal directions as required to achieve a momentum equilibrium with the centrifugal forces present in the turning flow. Boundary layers developing over curved surfaces, which are often fully turbulent in practical applications, have significantly different mean and statistical properties with respect to boundary layers on geometrically flat surfaces.

Such is at least in part due to differences in the stability properties of the dynamic system. Locally accelerated fluid regions tend to get transported radially outward (+r) and decelerated fluid regions tend to get transported radially inward (-r). If the radial direction is aligned with the local wall-normal direction, as in the case of concave curvature, then decelerated flow is transported back to the wall whereas accelerated flow is transported towards the faster outer flow, representing a stabilizing tendency. In the case of concave curvature however, the local wall-normal direction is aligned opposite the local radial direction. As such, accelerated flow is swept toward the slower near-wall region where it ejects slower flow. Concave curvature therefore brings about a destabilizing tendency in terms of TBL dynamics.

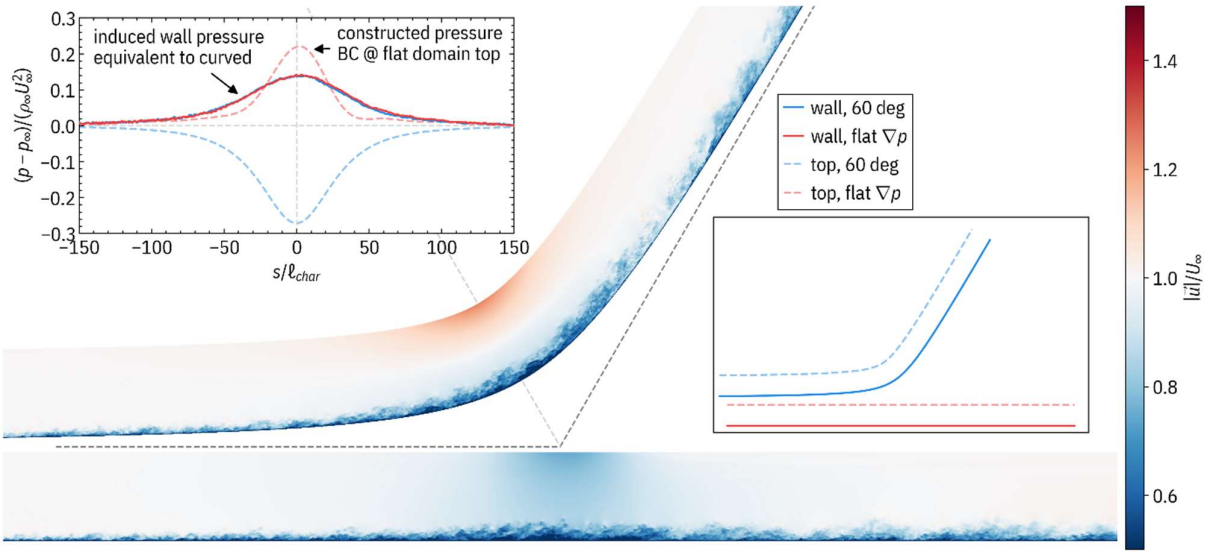

While the study of wall curvature effects on TBLs is not in itself a novel topic of research, one confounding aspect that has been present in studies to date is the presence of wall-tangential pressure gradients for generalized, non-axisymmetric geometries. Such wall-tangential pressure gradients also affect the mean and statistical properties of the boundary layer.

A novel DNS setup has been developed which seeks to control for wall-tangential pressure gradient effects. First, a DNS of a TBL in a geometrically curved channel setup (with a zero-stress top boundary) is run. A second DNS is then run using a flat wall setup and a pressure boundary condition at the top boundary which induces the same mean pressure profile at the lower wall boundary as in the curved case, however without any significant mean streamline curvature. The boundary condition is derived iteratively using a coarse setup. The flat DNS therefore achieves the same wall pressure gradient, thus by comparing results from the two DNS, one can begin to make conclusions about the isolated influence of mean streamline curvature, which is associated with the presence of a wall-normal pressure gradient and corresponding non-zero centrifugal momentum term. Results from the curved channel DNS and the flat, wall pressure matched counterpart DNS will be presented, along with a description of the DNS setup used to obtain the complementary datasets.

The investigatory setup is planned to be used as a basis for more thorough future studies of streamline curvature effects, including history and compressibility effects.

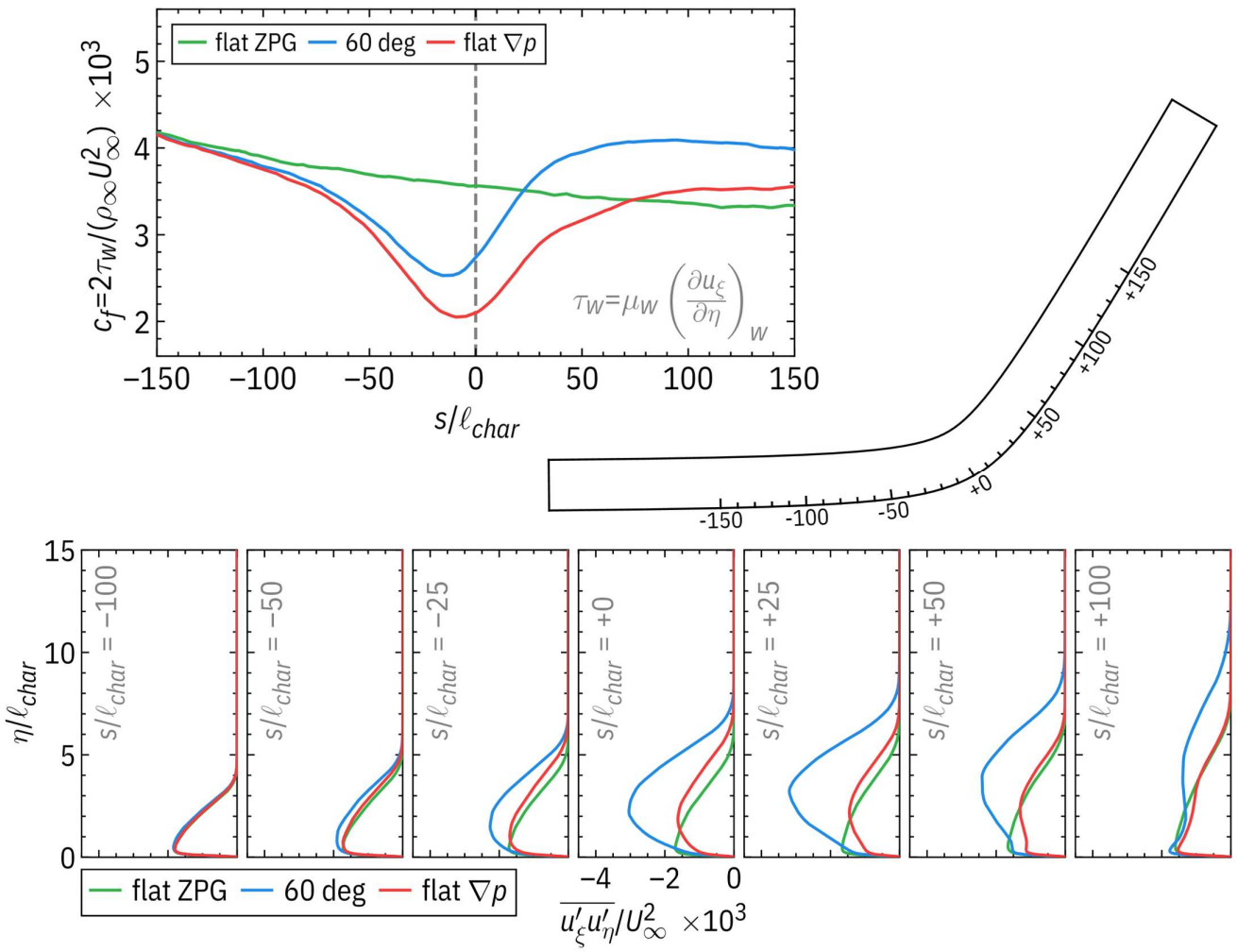

Mitteilung

Fachgruppe: Turbulenz und Transition

Direct numerical simulation of H-type transition
in a flat-plate boundary layer with supercritical fluids

Pietro Carlo Boldini, Benjamin Bugeat, Pedro Costa, Jurriaan Peeters, Rene Pecnik
Process & Energy Department, Delft University of Technology
Leeghwaterstraat 39, 2628 CB Delft, The Netherlands, p.c.boldini@tudelft.nl

Introduction

In recent years, supercritical fluids have gained interest in industrial applications to increase their efficiency; for example, in supercritical CO_2 (hereafter, sCO_2) power cycles [1]. Here, the complex, non-ideal thermodynamic mechanisms above the critical pressure and the strong property variations across the Widom line (i.e. $\max(C_p)$, see figure 1) play a key role in the flow instability and transition mechanisms.

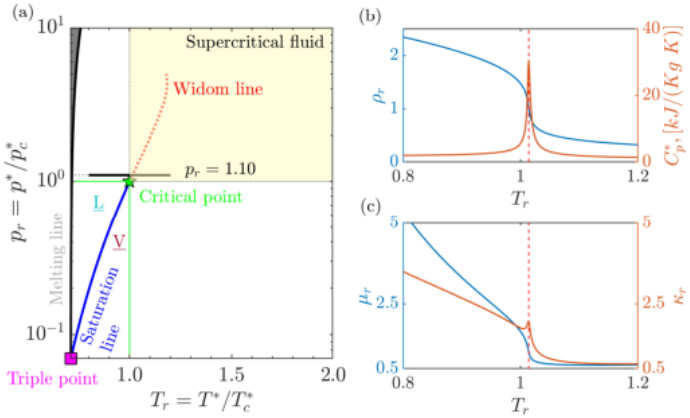

Figure 1: (a) Pressure-temperature (p-T) diagram of CO_2. At a reduced pressure of $p_r = 1.10$ as a function of reduced temperature T_r: (b) reduced density ρ_r and dimensional specific heat C_p^*, (c) reduced viscosity μ_r and reduced thermal conductivity μ_r. The Widom line (in red) is at T_{pc}^*, or $T_{r,pc} = 1.024$.

Yet, only the linear stability of non-ideal gases in boundary layers has been recently studied. A review can be found in [2]. For instance, Ren et al. [3] found that, in transcritical boundary layers, the flow is highly destabilised by a new inviscid mode (Mode II), which is not related to Mack's second mode. Following Ren et al. but ruling out any acoustic effect (low-Mach-number approximation), Bugeat et al. [4] carried out an inviscid stability analysis of Mode II. While these studies focused on linear instabilities, the subsequent non-linear interactions towards transition to turbulence remain unexplored for supercritical fluids. On the contrary, in ideal gases, numerous "controlled" experiments [5] and Direct Numerical Simulations (DNS) [6] of the H-type breakdown mechanism were performed. Hence, the present study aims to gain insight into the H-type breakdown in supercritical fluids.

Methodology

We consider a single-phase flat-plate boundary-layer flow of a supercritical fluid governed by the fully compressible Navier-Stokes (NS) equations for a Cartesian coordinate system (x, y, z). The system of equations is closed by a cubic equation of state (EoS), namely the reduced Van der Waals (VdW) EoS. In addition, the models proposed by Jossi et al. and Stiel and Thodos are used for the transport properties (see [4]). In the context of DNS, the NS equations are numerically integrated with a newly developed GPU-accelerated in-house finite-difference solver, SCRINS (SuperCRItical Navier-Stokes).

Results

All simulations are conducted at the same supercritical pressure of $p_r = 1.10$, free-stream temperature of $T_{r,\infty} = 0.90$ (liquid-like region), a finite Mach number of $M_\infty = 0.2$, $Pr_\infty = 1.0$ and $C_{v,r} = C_v^*/R^* = 9/2$. Three different reduced wall temperatures are used (two in the liquid-like region and one in the gas-like region). The latter, defined hereafter as transcritical case, with $T_{r,w} = 1.10$ ($T_w^*/T_\infty^* = 1.222$) exhibits, in the laminar region, a large density stratification ($\rho_w^*/\rho_\infty^* = 0.328$), and an extremum in the kinematic-viscosity profile. After performing a linear stability analysis of the laminar profiles, the DNS cases have been set up such that a modal instability is triggered at the same primary frequency F_{2-D} of the ideal-gas case in [6]. Therefore in a disturbance strip at $Re_{\delta,mid} = 415$, a two-dimensional wave (1,0) with $F_{2-D} = 124 \times 10^{-6}$, $A_{2-D} = 1.75 \times 10^{-3}$ and oblique subharmonic waves $(1, \pm 1)$ with $F_{2-D} = 0.5F_{3-D}$, $A_{3-D} = 2.5 \times 10^{-5}$ are introduced. A snapshot of the streamwise velocity inside the boundary layer at a constant wall-normal height of $y/\delta_0 = 0.35$ is presented for the transcritical case in figure 2(a). In figure 2(b), skin friction coefficient C_f and Stanton number St are displayed.

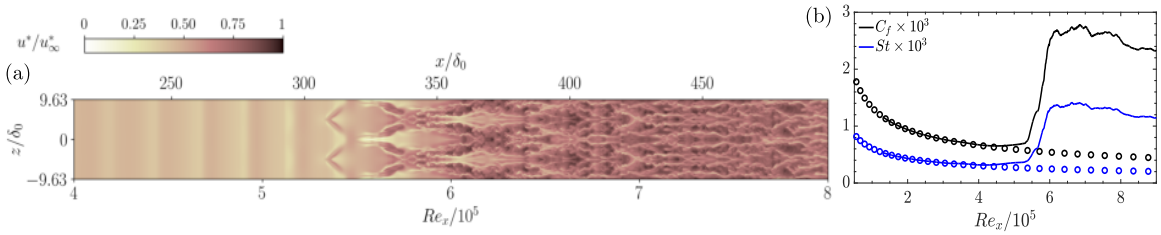

Figure 2: (a) contours of instantaneous streamwise velocity (xz-plane at $y/\delta_0 = 0.35$); (b) skin friction coefficient C_f and Stanton number St (DNS results: solid lines, self-similar laminar profile: symbols).

A clear staggered pattern of the Λ-structures is not present. Instead, a combination of strong vortical structures, resembling Λ-vortices, and high-low-speed streaks with high-low-density fluid was found. Moreover, no clear overshoot in C_f and St is found, which is typical of by-pass transition. Instantaneous flow structures are displayed in figure 3 by isocontours of the Q-criterion. In the turbulent regime, thermophysical-property fluctuations are found to be two orders of magnitude larger than in ideal-gas simulations at the same Mach number.

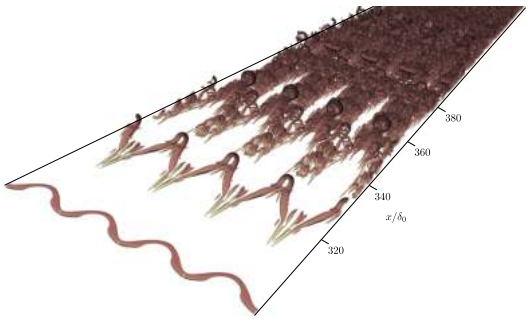

Figure 3: Instantaneous flow structures using the Q-criterion ($Q = 0.025$) coloured by the streamwise velocity.

References

[1] Liu, Y., Wang, Y. and Huang, D. (2019), Supercritical CO2 Brayton cycle: A state-of-the-art review, *Energy*, Vol. 189, 115900.

[2] Robinet, J.-C. and Gloerfelt, X. (2019), Instabilities in non-ideal fluids. *J. Fluid Mech.*, Vol. 880, pp. 1-4.

[3] Ren, J., Marxen, O. and Pecnik, R. (2019b), Boundary-layer stability of supercritical fluids in the vicinity of the Widom line. *J. Fluid Mech.*, Vol. 871, pp. 831–864.

[4] Bugeat, B., Boldini, P. C. and Pecnik, R. (2022), On the new unstable mode in the boundary layer flow of supercritical fluids, *In Proceedings of TSFP12, Osaka, Japan (Online), July 19-22.*

[5] Kachanov, Y. S., Kozlov, V. V. and Levchenko, V. Y. (1977), Nonlinear development of a wave in a boundary layer, *Fluid Dyn.* 12, 383–390.

[6] Sayadi, T., Hamman, C. and Moin, P. (2013), Direct numerical simulation of complete H-type and K-type transitions with implications for the dynamics of turbulent boundary layers, *J. Fluid Mech.*, Vol. 724, pp. 480–509.

Mitteilung

Fachgruppe: Turbulenz und Transition

Low-frequency Receptivity of a Pressure-Induced Turbulent Separation Bubble

Carolina Cura, Ardeshir Hanifi, André Cavalieri and Julien Weiss
Technische Universität Berlin, Institut für Luft- und Raumfahrt, Marchstraße 12-14, 10587 Berlin, c.cura@tu-berlin.de

The dynamic phenomena that manifest when a turbulent boundary layer separates from a solid surface and reattaches further downstream have been extensively reported in the literature. Such flows, which exhibit turbulent separation bubbles (TSBs), feature unsteadiness at distinct frequency ranges, including a low-frequency oscillation characterized by the expansion and contraction of the separated region. This phenomenon is usually referred to as the "breathing" or "flapping" mode of the TSB. Notably, the breathing mode has so far primarily been detected through experimental investigations, where a Strouhal number based on the bubble length L_{B} and the reference velocity U_{ref} of $St = 0.01$ has been suggested to characterize the breathing motion (e.g. [1-2]).
Although the existence of the breathing mode is widely established in the literature, its underlying mechanism remains poorly understood. Consequently, multiple conjectures regarding the origin of the low-frequency breathing mode are vying for recognition within the existing body of literature. Within the framework of stability theory, two main hypotheses are particularly interesting. The first hypothesis assumes a self-sustained oscillation of the TSB, where a temporal imbalance between the entrainment of the shear layer bounding the recirculation region and the reinjection of fluid near the reattachment line leads to a downstream mechanism reminiscent of a global/absolute instability. In the second assumption, the selective amplification of large-scale coherent structures in the incoming turbulent boundary layer (streaks) is hypothesized to cause the low-frequency breathing (upstream mechanism).

In this work we employ an array of stability and data analysis techniques to investigate the mechanism causing the low-frequency breathing. Specifically, Global Linear Stability Analysis (GLSA), using the DNS base flow from [3], is employed in order to analyze whether or not a global/absolute instability may trigger the breathing motion (downstream mechanism), while Resolvent Analysis (RA) is employed to study the forced dynamics of the bubble (upstream mechanism). To verify the findings, Spectral Proper Orthogonal Decomposition (SPOD) is performed based on high-speed PIV data and compared to the results of the stability analysis.

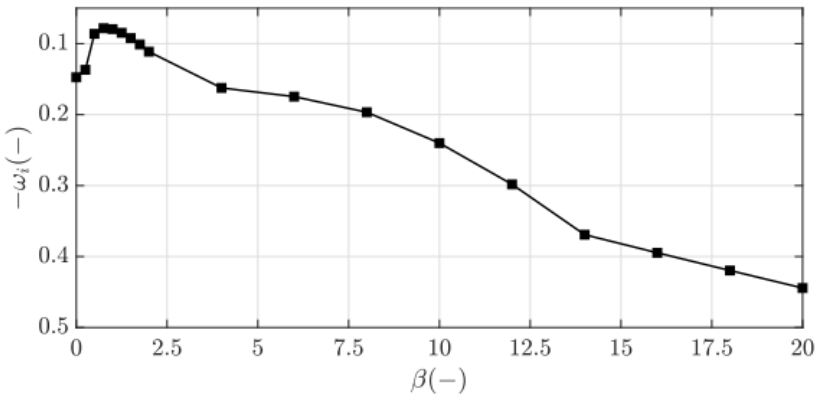

Figure 1:Growth rate −ωi from GLSA over non-dimensional spanwise wavenumber β. The most unstable mode of the respective spectrum is depicted.

Figure 1 displays the growth rate $-\omega_i$ of the GLSA for different non-dimensional spanwise wavenumbers β. The most unstable mode of each calculation is depicted. Regardless of the spanwise wavenumber, no eigenvalue exhibits positive values. This implies that the investigated TSB flow is globally stable in the asymptotic time limit. However, a region of low non-zero β values can be identified, where the growth rate exhibits values closer to the stability threshold.
In Figure 2 the streamwise component of the optimal forcing and response of the Resolvent Analysis are shown at low-frequency $St = 0.01$ and at low non-zero spanwise wavenumber $\beta = 0.75$. The optimal forcing consist of a large elongated structure primarily located in the region upstream of the TSB, resulting in an optimal response that bounds the recirculation region. These structures closely resemble the most amplified mode of the GLSA at low non-zero β, suggesting that the low-frequency breathing mode might be caused by a modal mechanism. We then introduce the alignment metric φ, which consist of the projection of the RA modes on the SPOD modes. Here, a value of $\varphi = 1$ indicates perfect alignment, whereas a value of $\varphi = 0$ indicates orthogonality. At low frequency $St = 0.01$, we achieve the maximum alignment with $\varphi = 0.95$ for a spanwise wavenumber $\beta = 0.25$. This result implies that the receptivity observed at low frequency in the RA closely matches the dynamic processes observed in experiments (SPOD).

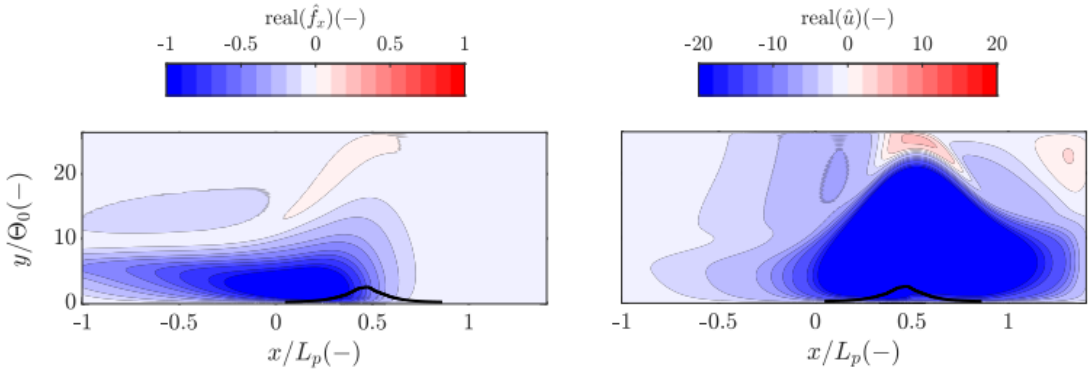

Figure 2: Optimal forcing (left) and response (right) for non-dimensional spanwise wavenumber $\beta = 0.75$.

In conclusion, this work investigates the low-frequency characteristics of turbulent separation bubbles by means of stability and data analysis methods. Through GLSA, we demonstrate that the present flow does not exhibit a global/absolute instability of the oscillator type, as the eigenvalues of the GLSA remain stable for all investigated spanwise wavenumbers β. Moreover, by means of RA, we show that the optimal response of RA closely resembles the GLSA modes. This result suggests that the receptivity at low frequency most likely occurs due to a modal mechanism.

Literature

[1] Mohammed-Taifour, A. and Weiss, J., “Unsteadiness in a large turbulent separation bubble,” *Journal of Fluid Mechanics*, Vol. 799, 2016, p. 383–412.
[2] Weiss, J., Steinfurth, B., Chamard, L., Giani, A., & Combette, P., “Spectral proper orthogonal decomposition of unsteady wall shear stress under a turbulent separation bubble”. *AIAA Journal*, 60(4), 2022, 2150-2159.
[3] Coleman, G. N., Rumsey, C. L. and Spalart, P. R., "Numerical study of turbulent separation bubbles with varying pressure gradient and Reynolds number." *Journal of Fluid Mechanics* 847 (2018): 28-70.

Mitteilung

Fachgruppe: Turbulenz und Transition

Untersuchung von Sekundärströmungen in differenziell beheizten Rohrströmungen mittels Direkter Numerischer Simulationen

André Dachwitz, Christian Bauer, Claus Wagner,
DLR, Institut für Aerodynamik und Strömungstechnik, Bunsenstr. 10, 37073 Göttingen
andre.dachwitz@dlr.de

Turbulente Mischkonvektion in vertikalen Rohrströmungen spielt bei der Wärmeübertragung in vielen technischen Anwendungen eine wesentliche Rolle, z. B. in den Wärmeempfängern eines Solarturms (B. Norton (2013)). Nach R. Narasimha und K.R. Sreenivasan (1979) kann die Erwärmung der Strömung in vertikalen Rohren auch zu einer Relaminarisierung und damit zu einer Verringerung des Widerstandskoeffizienten führen.
Um die Turbulenzstruktur der Grenzschichtströmung gezielt zu beeinflussen und damit ggf. den Widerstandsbeiwert der Strömung zu reduzieren, wurden im Rahmen dieser Arbeit direkte numerische Simulationen (DNS) der vertikalen Rohrströmung mit variabler sinusförmiger Erwärmung und Kühlung der Wand durchgeführt. Dabei werden die dimensionslosen inkompressiblen Navier-Stokes-Gleichungen mit einer Boussinesq-Approximation zusammen mit der Energiegleichung mit einer Finite-Volumen-Methode mit zentralen Differenzen vierter Ordnung diskretisiert (Feldmann und Wagner, 2012) und zeitlich mit

$$\frac{\partial \vec{u}}{\partial t}+\vec{u}\cdot\nabla\vec{u}+\nabla p=\frac{\mathbf{1}}{Re_b}\nabla^2\vec{u}+\frac{Gr}{Re_b^2}\theta\,\delta_{ij} \qquad (1)$$

$$\nabla\cdot\vec{u}=\mathbf{0} \qquad (2)$$

$$\frac{\partial \theta}{\partial t}+\vec{u}\nabla\theta=\frac{\mathbf{1}}{Pr\,Re_b}\nabla^2\theta \qquad (3)$$

einem semi-impliziten Euler-Leapfrog-Verfahren zweiter Ordnung (Shishkina und Wagner, 2004) integriert. Die Transportgleichungen (1)-(3) werden mit der Volumenstromgeschwindigkeit u_b und dem Durchmesser D des glatten Rohrsegments der Länge $\mathbf{21}\,D$ normiert, woraus sich mit der kinematischen Viskosität ν von Luft die Reynolds-Zahl $Re_b=u_b D/\nu=\mathbf{4328}$ ergibt. Entsprechend werden die Prandtl-Zahl $Pr=\nu/k=\mathbf{0.71}$, mit der Wärmeleitfähigkeit k der Luft und die Grashof-Zahl $Gr=g\beta\Delta T\,u_b^3/\nu^2=\mathbf{9.5\cdot10^6}$, mit der Temperaturdifferenz ΔT zwischen dem Maximum des wärmeren und dem Minimum des kälteren Bereichs, der Schwerebeschleunigung g und dem Wärmeausdehnungskoeffizienten β definiert. Die Wandtemperatur wurde in Umfangsrichtung φ gemäß

$$\theta_w=\sin(\varphi) \qquad (4)$$

variiert. Die Temperatur wird mit ΔT und dem arithmetischen Mittel der Wandtemperaturen $T_\mathbf{0}$ normiert, woraus sich $\theta=(T-T_\mathbf{0})/\Delta T$ ergibt. Die auftriebsbedingte Beschleunigung bzw. Abbremsung der warmen bzw. kalten Strömungsbereiche führt zur Ausbildung von Sekundärströmungen ähnlich zu denen in einem gekrümmten Rohr (A. Noorani et al. (2013)). Solche Sekundärströmungen wurden auch für den Fall temperaturabhängiger Flüssigkeitseigenschaften beobachtet (A. Antoranz et al. (2020)). Abbildung 1 zeigt die Felder der mittleren Temperatur und der mittleren axiale Strömungsgeschwindigkeit im Rohrquerschnitt. In Abbildung 1a sind im oberen Teil des Querschnitts niedrigere Temperaturen als im unteren Teil zu erkennen, was auf die differentielle Beheizung zurückzuführen ist. Dies führt aufgrund der Auftriebskraft zu einer Verlangsamung der mittleren axialen Strömungsgeschwindigkeit im kühleren Teil und zu einer Beschleunigung im wärmeren Teil, wodurch sich ihr Maximum in Richtung der erwärmten Wand verschiebt (Abbildung 1b). Dadurch ist das Geschwindigkeitsfeld nicht achsensymmetrisch und es bildet sich eine Sekundärströmung aus. Letztere ist in Abbildung 2 als
Vektordarstellung der mittleren Geschwindigkeitskomponenten $\langle u_r\rangle$ und $\langle u_\varphi\rangle$, sowie der Betrag dieser mittleren Geschwindigkeiten $\langle u_b\rangle=\sqrt{\langle u_r\rangle^2+\langle u_\varphi\rangle^2}$, im Rohrquerschnitt visualisiert. Abbildung 2a zeigt zwei gleichgerichtete Strömungswirbel, von denen der linke das kühlere Fluid entlang der linken Rohrwand vom oberen zum unteren Teil des Querschnitts transportiert, während

der rechte das wärmere Fluid entlang der rechten Rohrwand vom unteren zum oberen Teil des Querschnitts transportiert. Die Zentren der Strömungswirbel sind an den Minima der Absolutbeträge der Geschwindigkeitskomponenten normal zur Hauptströmungs-richtung in Abbildung 2b zu erkennen. Weiterhin ist zu erkennen, dass die Sekundärströmung in Wandnähe am stärksten ist und an den Stellen der Temperaturmaxima schwächer wird (vgl. Abbildung 1a). Diese auftriebsinduzierte Sekundärströmung wird im Rahmen des Workshops turbulenzstatistisch erklärt und mit der Sekundärströmung in gekrümmten Rohren verglichen.

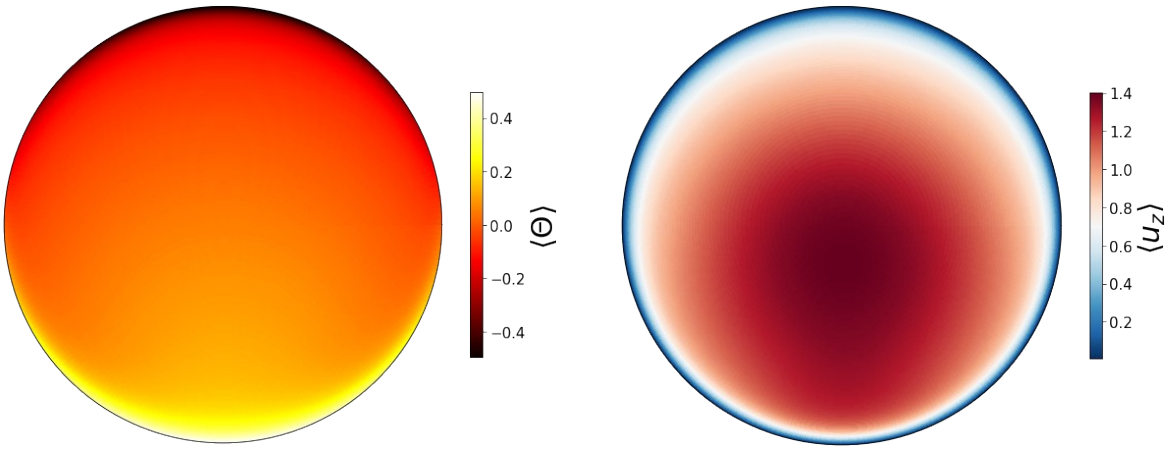

(a) (b)

Abbildung 1: (a) Mittlere Temperatur $<\theta>$, (b) und mittlere axiale Strömungsgeschwindigkeit $<u_z>$ in einem Rohrquerschnitt.

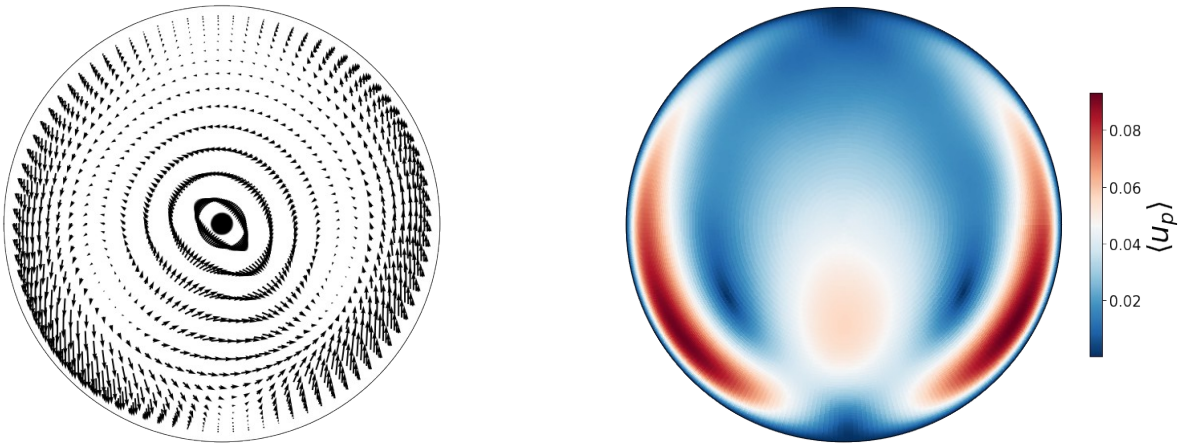

(a) (b)

Abbildung 2: (a) Vektordarstellung der mittleren Geschwindigkeitskomponenten $<u_r>$ und $<u_\varphi>$, (b) Betrag der mittleren Geschwindigkeiten $<u_p>=\sqrt{<u_r>^2+<u_\varphi>^2}$ in einem Rohrquerschnitt.

B. Norton (2013). Harnessing Solar Heat Vol. 18. *Springer Science & Business Media. ISBN: 978-94-007-7275-5.*

R. Narasimha und K.R. Sreenivasan (1979). Relaminarization of Fluid Flows. *Advances in Applied Mechanics, vol. 19, pp. 221-309.*

A. Antoranz, O. Flores und M. García-Villalba (2020). DNS of Turbulent Pipe Flow With Temperature-Dependent Fluid Properties Subject to Non-Uniform External Heating. *Direct and Large Eddy Simulation XII, pp. 233-238.*

A. Noorani, G. K. El Khoury und P. Schlatter (2013). Evolution of Turbulence Characteristics from Straight to Curved Pipes. *International Journal of Heat and Fluid Flow, vol. 41 pp. 16-26.*

D. Feldmann und C. Wagner (2012). Direct Numerical Simulation of Fully Developed Turbulent and Oscillatory Pipe Flows at Re τ = 1440. *Journal of Turbulence, vol. 13, N32.*

O. Shishkina und C. Wagner (2004). Stability Conditions for the Leapfrog-Euler Scheme with Central Spatial Discretization of any Order. *Applied Numerical Analysis & Computational Mathematics, vol. 1, pp. 315-326.*

Mitteilung

Fachgruppe: Turbulenz und Transition

Heißfilmmessungen zur Transition im Freiflug bei thermisch aktiver Konvektion

U. Deck und W. Würz,
Institut für Aerodynamik und Gasdynamik (IAG), Universität Stuttgart, 70569 Stuttgart, Pfaffenwaldring 21, ulrich.deck@iag.uni-stuttgart.de, wuerz@iag.uni-stuttgart.de

1. EINLEITUNG

Erst in der jüngeren Zeit hat sich gezeigt, dass der Turbulenzgrad beim Flug in thermisch aktiver Luftmasse signifikant über dem Turbulenzniveau moderner Laminarwindkanäle liegt [1, 2]. Während die Entwicklung moderner Laminarprofile auf Messungen in ebensolchen turbulenzarmen Windkanälen basiert werden Flugzeuge der allgemeinen Luftfahrt, Segelflugzeuge, Windkraftanlagen und nicht zuletzt unbemannte Fluggeräte fast ausschließlich in der durch Konvektion und Windscherung deutlich turbulenteren unteren Atmosphäre betrieben. Dieses offensichtliche Dilemma ist Gegenstand aktueller Forschungsarbeiten am Institut für Aerodynamik und Gasdynamik (IAG) der Universität Stuttgart.

2. KURZFASSUNG

Aufgrund von dominanten niederfrequenten Anstellwinkelfluktuation, die physikalisch bedingt nicht im Windkanal nachgebildet werden können [3], aber beim Flug in turbulenter Atmosphäre eine zentrale Rolle spielen [4], sind Freiflugmessungen zur Untersuchung der Profileigenschaften bei erhöhter Anströmturbulenz unumgänglich. Im Rahmen des LuFo-Projektes HPIA wurde daher eine autarke Flugmessanlage entwickelt und in mehreren umfangreichen Messkampagnen am Tragflügel eines Segelflugzeuges zur Vermessung der Profileigenschaften unter dem Einfluss erhöhter Anströmturbulenz eingesetzt. Neben Nachlaufmessungen zur Bestimmung der Profilpolare werden Heißfilmsensoren eingesetzt. Mit diesen ist es möglich die instationären Wandschubspannungen an den Sensorpositionen zu erfassen und daraus die Transitionslage abzuleiten. Hierfür müssen die Heißfilmsensoren kalibriert werden, was aufgrund der zahlreichen Einflussgrößen nur mit einem in-situ Verfahren praktikabel ist. Anstatt einer Referenzmessung der Wandschubspannung, z.B. mit einem Prestonrohr, wird die berechnete (XFoil [5]) Wandschubspannung im laminaren Teil der Grenzschichtströmung als Referenzwert angesetzt [6]. Die eigentlich Kalibrierung erfolgt mit einem klassischen King's Law Ansatz [7] zur Bestimmung der sensorspezifischen Konstanten A, B und n:

$$E^2 * \left(\frac{T_{film} - T_{mean}}{T_{film} - T_\infty}\right) \approx I^2 * R * \left(\frac{T_{film} - T_{mean}}{T_{film} - T_\infty}\right) = A + B * \left(\frac{\tau_{eff.} * \rho_\infty}{\mu_\infty}\right)^n$$

$$\tau_{eff.} = \frac{\rho_\infty}{2} * {U_\infty}^2 * C_{f,XFoil} \qquad (4)$$

Aufgrund der umfangreichen Messdatensätze (ca. 50 Flüge à 1h-4h Flugzeit resultierend in 100h Gesamtmesszeit) ist es möglich die ausgewerteten Wandschubspannungswerte entsprechend der simultan aufgezeichneten Anströmturbulenz zu kategorisieren und über dem lokalen Auftriebsbeiwert aufzutragen. Dies wird in Abb.1 exemplarisch für eine Sensorposition auf der Profiloberseite bei 60% *x/t* und für eine Sensorposition auf der Profilunterseite bei 90% *x/t* dargestellt. Deutlich sichtbar zeigt sich dabei der Einfluss erhöhter Anströmturbulenz, durch einen weiteren Bereich transitioneller Grenzschichtströmung am Ort des Sensors:

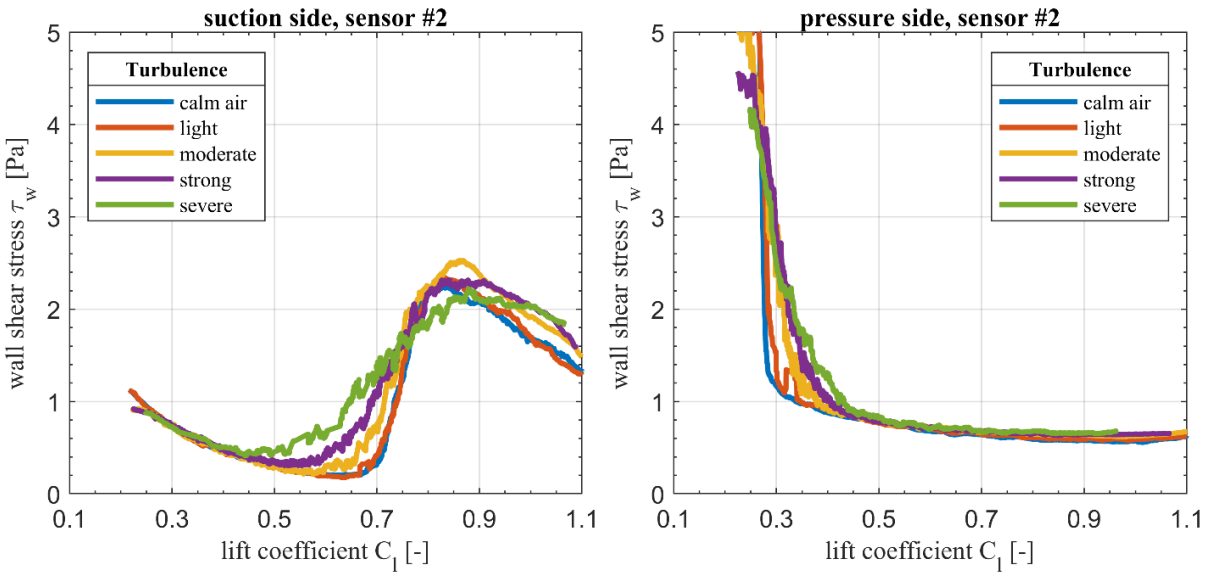

Abb 1: Wandschubspannung über dem lokalen Auftriebsbeiwert für die Profiloberseite (linkes Diagramm) und die Profilunterseite (rechtes Diagramm)

Für einen lokalen Auftriebsbeiwert von C_a = 0,5 wird in Abb.2 die spektrale Auswertung der Heißfilmsignale gezeigt. Bei diesem Auftriebsbeiwert liegt an der Sensorposition auf beiden Profilseiten eine laminare Grenzschichtströmung vor. Auf der Profiloberseite erkennt man deutlich eine Amplitudenüberhöhung im angefachten Frequenzbereich (1-2kHz) für TS-Wellen:

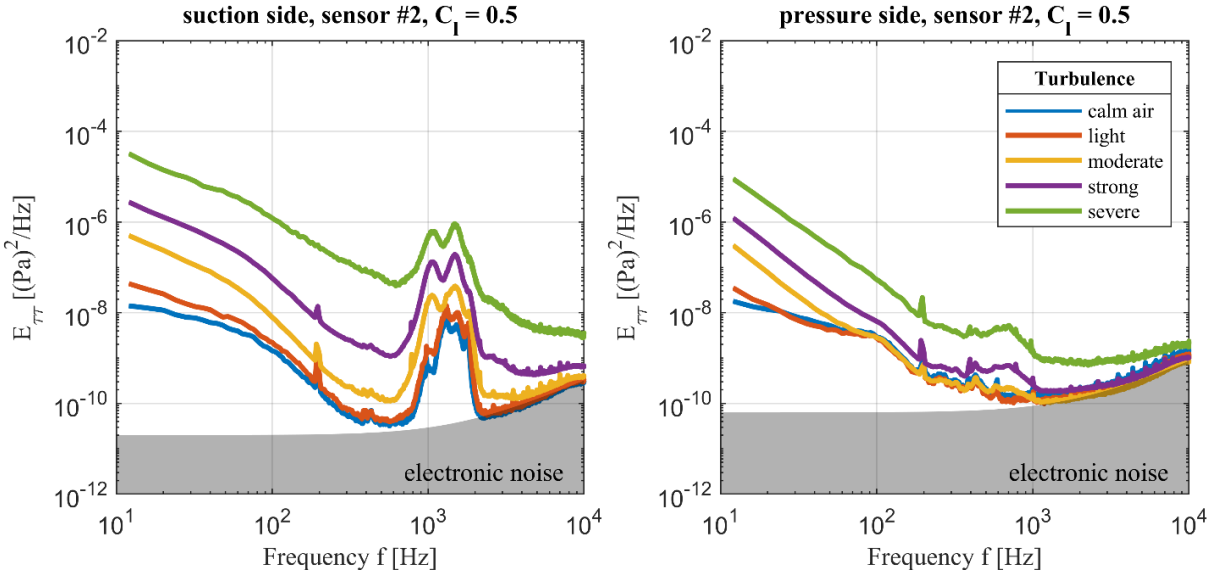

Abb. 2: Wandschubspannungsspektren für die Profiloberseite (linkes Diagramm) und die Profilunterseite (rechtes Diagramm) bei einem lokalen Auftriebsbeiwert von C_a = 0,5

Detailiertere Ergebnisse für verschiedene Anströmturbulenzen werden im Vortrag nach einem kurzen Überblick über das Messsystem präsentiert und diskutiert.

[1] Guissart A., Romblad J., Nemitz T., Tropea C. (2021) "Small-scale atmospheric turbulence and its impact on laminar-to-turbulent transition". AIAA Journal 59(9) pp. 3611–3621.

[2] Greiner M., Würz W., (2022) "In-flight measurement of free-stream turbulence in the convective boundary layer", Experiments in Fluids, pp. 63:162

[3] Romblad J., Greiner M., Guissart A., Würz W. (2022): "Characterization of low levels of turbulence generated by grids in the settling chamber of a laminar wind tunnel" Experiments in Fluids, 2022, pp. 63-65

[4] Reeh A.D. (2014) "Natural laminar flow airfoil behavior in cruise flight through atmospheric turbulence". Dissertation, Technische Universität Darmstadt.

[5] Drela M. (1989) "XFOIL: an analysis and design system for low Reynolds number airfoils." Mueller TJ (ed) Low Reynolds number aerodynamics. Springer, Berlin Heidelberg. https://doi.org/10.1007/ 978-3- 642- 84010-4_1

[6] Seitz A. (2007), „Freiflug-Experimente zum Übergang laminar-turbulent in einer Tragflügelgrenzschicht", Institut für Aerodynamik und Strömungstechnik, Deutsches Zentrum für Luft- und Raumfahrt, Braunschweig, DLR-FB—2007-01

[7] Bruun H.H. (1995) "Hot-Wire Anemometry, Principles and Signal Analysis" Oxford University Press, Oxford, New York, Tokyo

Mitteilung

Fachgruppe: Turbulenz und Transition

The influence of turbulence on the development of a laminar separation bubble

Wolfgang Dierl, Timothy Lawrenz, Rainer Hain and Christian J. Kähler
Institut für Strömungsmechanik und Aerodynamik
Universität der Bundeswehr München, wolfgang.dierl@unibw.de

1. Introduction

Due to the influence of laminar separation bubbles (LSB) on the pressure distribution on the suction side of airfoils, they can negatively affect the generated lift, drag and pitching moment of an airfoil [1]. Depending on the used airfoil and inflow conditions, LSBs form mainly at low chord Reynolds numbers ($Re_c \leq 500{,}000$) which corresponds to the operational range of micro aerial vehicles and wind turbines.
Investigations of the influence on the topology of LSBs at various turbulence intensity levels Tu and length scales Λ revealed a decreasing length of the LSB at increasing Tu [2] and Λ [3]. In contrast to the study of Herbst et al. [3] in which experiments at Tu = 10 % were conducted, the aim of this work is to examine the influence of artificially grid generated turbulences at Tu = 1-2 % with various Λ on the development of LSBs.

2. Experimental Setup

All experiments were performed in a water towing tank at the University of the Bundeswehr Munich. The test facility is 8 m long, with a cross-section of 0.9 m × 0.9 m. The water height during the experiments was 0.75 m. An SD7003 airfoil model with a chord length of c = 250 mm and a span of 750 mm was employed. The model was mounted at an angle of attack α = 4°, 6° and 8° and was accelerated from rest to a constant chord Reynolds number of Re_c = 60,000 and Re_c = 45,000. Three stainless steel grids, with different grid parameters (wire diameter, mesh width) attached via a device to the carriage of the water towing tank were used to artificially generate various turbulences during the measurement runs. A hot film probe was used to characterize the turbulences with respect to the used grids and distance between grid and hot film probe (later the model position). Quantitative flow field measurements were performed using two-component time-resolved Particle Image Velocimetry (PIV) in a setup illustrated in Figure 1. The flow was illuminated by a Photonics DM150-532 DH Nd:YAG double pulse laser. The laser sheet was formed within a submerged device connected to the carriage of the towing tank, containing a combination of spherical and cylindrical lenses. Recordings were acquired by two sCMOS cameras at 55 Hz in double-frame mode.

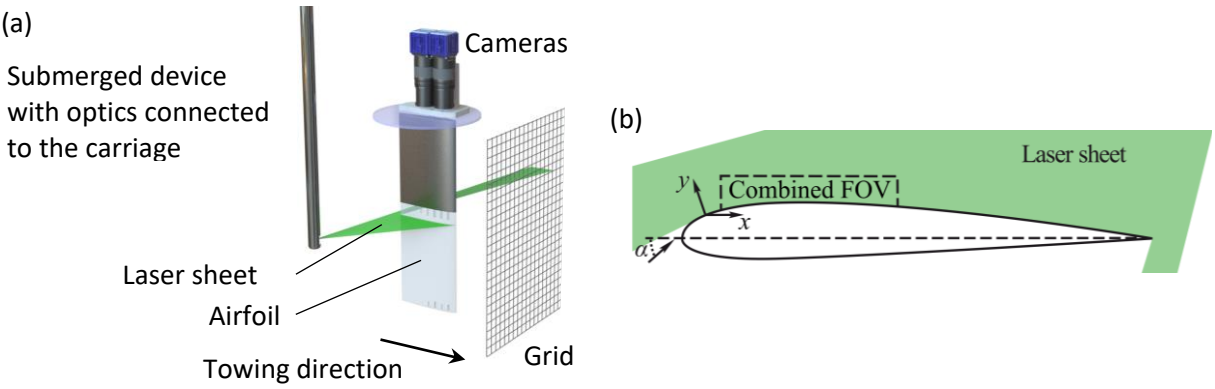

Figure 1 Experimental setup (a) Airfoil model and PIV setup. (b) Field of View (FOV) and coordinate system.

Results and Discussion

Figure 3a presents the results of the hot film probe measurements for the three used turbulence grids at various distances x between the hot film probe and the turbulence grids. Compared to the values based on the equations to calculate the turbulence characteristic generated by turbulence grids [4, 5], the resulting Tu in this study is higher than calculated by the equations.

However, the results follow the expected exponential progression and show that the chosen turbulence grid geometry complies with the requirements so that the artificially generated turbulence levels are independent of Re_c [4].

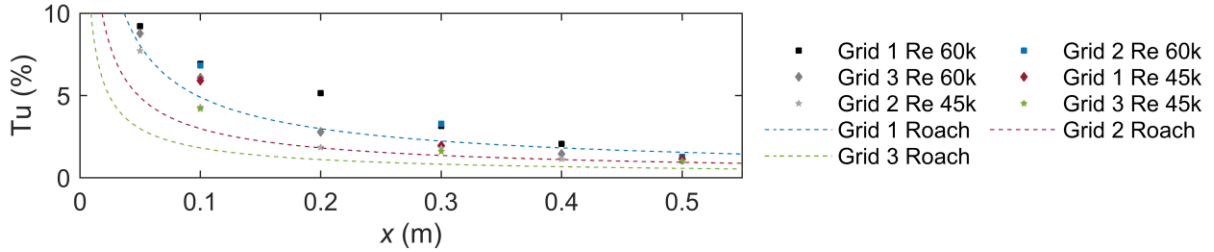

Figure 2 Characterization of the generated turbulences: (a) turbulence intensity levels based on the distance x between hot film probe and turbulence grid for all grids at Re_c = 60,000 and Re_c = 45,000. Dashed curves indicates Tu based on the equations provided by Roach [4] and Kurian and Fransson [5].

Figure 3 presents the contours for the mean flow field for α = 8° and Re_c = 60,000. A LSB forms between $0.13 \leq x/c \leq 0.22$ and the transition point is located at $x/c \approx 0.17$ for both configuration whereby there is a difference in Tu (left: 1.42 %; right: 1.13 %) and Λ (left:0.013c; right: 0.02c). The change in size of the LSB compared to the baseline configuration (downstream shift of separation point and upstream shift of transition and reattachment point) corresponds to results of previous studies [2, 3]

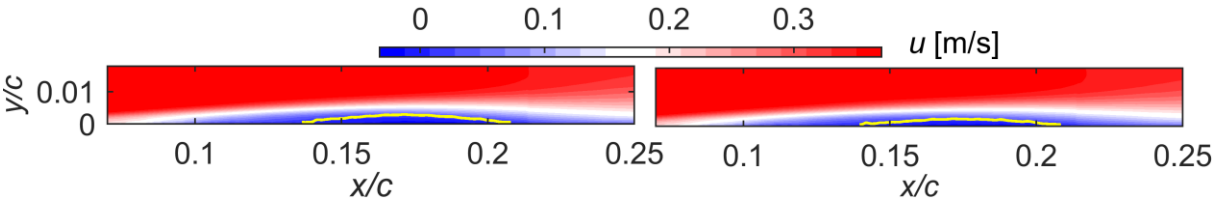

Figure 3 Mean flow field for α = 8° and Re_c = 60,000 for (left) for Tu = 1.42 %, generated by grid 2 at x = 40 cm and (right) for Tu = 1.13 % generated by grid 1 at x = 60 cm. The solid yellow line indicates the dividing streamline.

3. Conclusion

The presented study examined the influence of low level turbulences on the LSB over an SD7003 airfoil model. Hot film anemometry was used to characterize the turbulence induced by the grids and time-resolved PIV was used to measure the flow field. The conducted experiments at various α, Re_c, Tu and Λ revealed that the development of a laminar separation bubble can be partially or completely suppressed by the utilized grids in the mean flow field. The influence of Λ on the development of the LSB is inversely proportional whereby with increasing Λ the LSB becomes smaller in size.

Acknowledgements

The authors gratefully acknowledge the financial support of the German Research Foundation for this project (Analysis of the transition process around laminar separation bubbles (LSB‘s) in a towing tank using time-resolved 3D particle tracking techniques, Project number 422177304). We also acknowledge Serhiy Yarusevych from the University of Waterloo and his research group for providing Matlab-codes for data analysis.

References

[1] Lissaman PBS. Low-Reynolds-Number Airfoils, Annu. Rev. Fluid Mech.,1983, Vol. 15: 223–239

[2] Ol M, McCauliffe B, Hanff E, Scholz U, Kähler CJ. Comparison of Laminar Separation Bubble Measurements on a Low Reynolds Number Airfoil in Three Facilities, 35th AIAA Fluid Dynamics Conference and Exhibit, 6-9 June 2005, Toronto, Canada, 483

[3] Herbst SL, Kähler CJ, Hain R. Influence of large-scale free-stream turbulence on an SD7003 airfoil at low Reynolds numbers, Applied Aerodynamics Conference, 25-29 June 2018, Atlanta, Georgia, USA

[4] Kurian T, Fransson JHM. Grid-generated turbulence revisited, Fluid Dyn. Res., 2009, Vol. 41

[5] Roach PE. The generation of nearly isotropic turbulence by means of grids,” International Journal of Heat and Fluid Flow, 1987, Vol. 8: 82–92

Mitteilung

Fachgruppe: Turbulenz und Transition

Expeditious Evaluation of the Dynamic Response of Natural Laminar Flow Configurations to Small Pitching Oscillations

Daniela Gisele François[1], Andreas Krumbein[2], Markus Widhalm[3]
[1,2,3]DLR, Institut für Aerodynamik und Strömungstechnik, C²A²S²E
[1,2]Bunsenstraße 10, 37073 Göttingen
[3]Lilienthalplatz 7, Braunschweig
[1]daniela.francois@dlr.de

Introduction:
Modern aircraft designs tend towards attaining higher cruise velocities combined with lighter and more flexible structures. This intensifies the fluid-structure interactions raising the risks of flutter. Therefore, determining the aeroelastic stability boundaries for the whole range of flight conditions at an early stage of the design process is crucial to save unnecessary costs on later modifications. Nevertheless, time-accurately solving the dynamic response to structural perturbations is prohibited in terms of computational effort, mainly due to the wide range of flight conditions that needs to be considered (e.g. Mach amplitude, altitude, load, deformation mode shape and frequency). An efficient alternative to accomplish this task is by assuming small harmonic perturbations and applying the Linear Frequency Domain (LFD) [1] method to linearly evaluate the dynamic response of the flow. The small perturbation assumption is justified on the interest of capturing the flutter onset, which will occur at infinitesimal displacements, rather than solving the flutter effect. The LFD approach was extensively verified with the DLR TAU code for fully turbulent configurations with the Spalart-Allmaras (SA) turbulence model [1,2]. However, the increased demand for cost-efficient aircraft designs and the growing awareness for global warming effects have shifted the attention back towards natural laminar aircraft designs [3]. To adapt the design capabilities of the DLR TAU code to the current demands, the LFD solver was extended to account for free transition effects when transition is predicted by the DLR γ transition transport model which was successfully integrated to the negative SA turbulence model in [4]. This work is part of the multi-disciplinary project LamTA (Laminar Tailored Aircraft) which aims to investigate the maximum potential of laminar technologies to reduce the energy consumption in flight.

Numerical Method:
The LFD method is based on the concept that under small amplitude perturbations, the RANS equations can be linearized about the steady state by using a Taylor series expansion up to its first order term. Then, the residual can be written as

$$R(W,x,\dot{x}) \approx R(\overline{W},\bar{x},\dot{\bar{x}}) + \frac{\partial R}{\partial W}\Big|_{\overline{W},\bar{x},\dot{\bar{x}}} \widetilde{W} + \frac{\partial R}{\partial x}\Big|_{\overline{W},\bar{x},\dot{\bar{x}}} \tilde{x} + \frac{\partial R}{\partial \dot{x}}\Big|_{\overline{W},\bar{x},\dot{\bar{x}}} \dot{\tilde{x}}.$$

Expressing the perturbations $\widetilde{W}$, $\tilde{x}$, and $\dot{\tilde{x}}$ in terms of the first harmonic of a Fourier series, $\tilde{\varphi}(t) = \hat{\varphi}e^{i\omega t}$, the governing equations get reduced to a complex linear system that reads

$$\left[i\omega + \frac{\partial R}{\partial W}\right]\widehat{W} = -\left[\frac{\partial R}{\partial x} + i\omega\frac{\partial R}{\partial \dot{x}}\right]\hat{x}.$$

Then, splitting the amplitude of the fluctuations into their real and imaginary parts, $\widehat{W} = \mathrm{Re}\widehat{W} + i\mathrm{Im}\widehat{W}$ and $\hat{x} = \mathrm{Re}\hat{x} + i\mathrm{Im}\hat{x}$, the complex linear systems is turned in to two coupled linear systems,

$$\begin{bmatrix} \frac{\partial \mathrm{R}}{\partial W} & -\omega n\mathrm{I} \\ \omega n\mathrm{I} & \frac{\partial \mathrm{R}}{\partial W} \end{bmatrix} \widehat{W}^* = \begin{bmatrix} \frac{\partial \mathrm{R}}{\partial x} & -\omega n\frac{\partial \mathrm{R}}{\partial \dot{x}} \\ \omega n\frac{\partial \mathrm{R}}{\partial \dot{x}} & \frac{\partial \mathrm{R}}{\partial x} \end{bmatrix} \hat{x}^*,$$

where $\widehat{W}^* = [\mathrm{Re}\widehat{W} \quad \mathrm{Im}\widehat{W}]^T$ and $\hat{x}^* = [\mathrm{Re}\hat{x} \quad \mathrm{Im}\hat{x}]^T$. Given the linearization of the model, it is only valid for small perturbations of the flight and aircraft parameters, and thus non-linear effects such as shifts in frequency or harmonic modes are neglected. For the coupled γ – SAneg transition transport model $W = [\rho\ u\ v\ w\ p\ \tilde{\nu}\ \gamma]^T$ and $R = \left[R^\rho\ R^u\ R^v\ R^w\ R^p\ R^{\tilde{\nu}}\ R^\gamma\right]^T$. For further details on the implementation of the LFD method and the DLR γ transition transport model the authors refer to [1,2,4].

Results:

Figure 1 shows the first validation results for the implementation of the DLR γ model into the LFD solver of the DLR TAU code. For this purpose, a harmonic perturbation is generated on the NLF(1)-0416 airfoil at a chord-based Reynolds number of $Re_\infty = 4 \cdot 10^6$ and an incidence angle of α = -4° through a pitching oscillation around x/c = 0.25 of amplitude $\hat{\alpha}$ = 0.1° and a wide range of reduced frequencies ranging from *k* = 0.001 to *k* = 500. The left side of figure compares the lift coefficient amplitude and phase of the dynamic response obtained with the LFD solver with its time-accurate RANS counterpart for the whole range of assessed reduced frequencies, *k*, whereas the right side depicts the distributions of the real and imaginary parts of the fluctuation amplitude of the pressure coefficient for the reduced frequency of *k* = 0.2. The results show an overall nice agreement between the linearly and non-linearly resolved dynamic response of the flow.

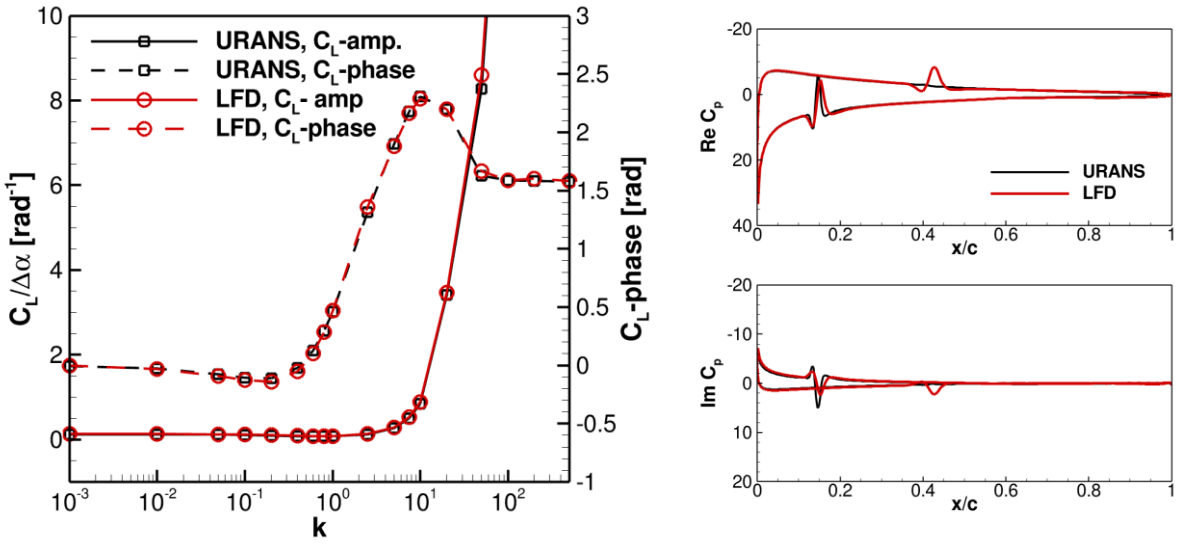

Figure 1: First harmonic lift coefficient on the NLF(1)-0416 airfoil for a pitching motion of amplitude $\hat{\alpha} = 0.1°$ as a function of the reduced frequency, $k = 2\pi f \cdot c/U_\infty$, (left), and first harmonic of the pressure coefficient distribution for the reduced frequency of $k = 0.2$ (right).

Reference:

[1] Thormann, R., Widhalm M., "Linear-Frequency-Domain Predictions of Dynamic-Response Data for Viscous Transonic Flows" AIAA Journal, Vol 51, No 11, pp:2540-2557, 2013. https://doi.org/10.2514/1.J051896

[2] Widhalm, M., Thormann, R., "Efficient Evaluation of Dynamic Response Data with a Linearized Frequency Domain Solver at Transonic Separated Flow Condition", AIAA Paper 2017-3905. 35th AIAA Applied Aerodynamics Conference, 2017. https://doi.org/10.2514/6.2017-3905

[3] Green, J. E., "Laminar Flow Control - Back to the Future?", 38th Fluid Dynamics Conference and Exhibit, AIAA Paper 2008-3738, 2008. https://doi.org/10.2514/6.2008-3738

[4] François, D. G., Krumbein, A., "On the Coupling of a γ-based Transition Transport Model to the Negative Spalart-Allmaras Turbulence Model", 56th 3AF International Conference on Applied Aerodynamics, FP36-AERO2022-francois, 2022.

Mitteilung

Fachgruppe: Turbulenz und Transition

Compressible turbulent boundary layers with the combined effect of heat transfer and pressure gradients

T. Gibis, & C. Wenzel
Institut für Aerodynamik und Gasdynamik der Universität Stuttgart
70569 Stuttgart, gibis@iag.uni-stuttgart.de

In contrast to incompressible boundary layers, compressible turbulent boundary layers can exhibit large temperature gradients in the wall normal direction even under adiabatic wall conditions, and the turbulent field also includes temperature, density, and total temperature fluctuations. Although considerable progress has been made in the description of compressible turbulent boundary layer flows in the last decades, their description is not nearly as complete as in the case of their incompressible counterpart. Open issues in compressible flows include fundamental principles such as the strong Reynolds analogy and the influence of compressibility on the quantities of the averaged flow field. For example, the Reynolds analogy is derived under the assumption of zero pressure gradient, so it is not readily apparent to what extent the results of the analogy hold for cases with pressure gradients.

This study aims to gain a deeper understanding of compressible turbulent boundary layers under the combined influence of pressure gradients and strong wall heat transfer. The essential problem of this case is the large number of influencing and interacting factors that have a significant impact on the resulting flow (such as the additional wall temperature condition), making their clear understanding inevitable. For example, in compressible flows with pressure gradients, the displacement effect observed in incompressible adverse pressure gradients is counteracted by compression due to the pressure gradient in the flow direction, depending on the Mach number and heat transfer conditions. Furthermore, when more than one parameter is changed simultaneously, it is often not possible to easily assign the resulting boundary layer behavior to the individual influences. Although the parameter space is more complex, the main research idea in understanding compressible boundary layers has been to transfer and apply incompressible knowledge using semi-empirical transformations that need to be transferred and improved to better handle these complex cases. However, some critical assumptions made in their derivation always depend on their verification by real flow data, and the lack of universal and sufficiently accurate data is a major bottleneck in their further development. From the current state of the literature, it can be concluded that the isolated influences of Mach number, heat transfer and partly pressure gradient on the momentum and energy transfer in TBLs are reasonably well described, which serves as a starting point.

Given the complexity of the parameter space, this study aims to perform a well-designed direct numerical simulation study of cases using a representative pressure gradient with strong heat transfer. To reduce the potential influence of Reynolds number effects, all cases of the study are designed to be self-similar in the flow direction, which controls the flow history and allows the most general conclusions; it also allows direct comparison with the adiabatic cases presented in [3, 1].

All cases considered are designed at a supersonic Mach number of $M_e \approx 2$ with a kinematic Rotta-Clauser parameter of $\beta_K \approx 0.65$ and wall temperature conditions that are heated, adiabatic and cooled. Solely for a reference zero pressure gradient a case with very strong

cooling is considered. If classified in terms of the Eckert number, the heating strength with regard to the given Mach number has to be denoted to be very strong up to extreme, [2]. Further design criteria are that a Reynolds number range has to be ensured that includes regions of identical Re_τ to allow for a meaningful comparison between the different cases and a domain length sufficiently long to proof self-similarity.
In the talk, a characterization of the flow will be given that evaluates the state of self-similarity for the pressure gradient cases simulated and the heat flux and shear stress distribution within the boundary layer will be discussed; lastly some commonly used results from the strong Reynolds analogy are shown. As an example, figure 1 shows the shear stress and heat flux, where the effect of both heat transfer and pressure gradient is clearly visible.

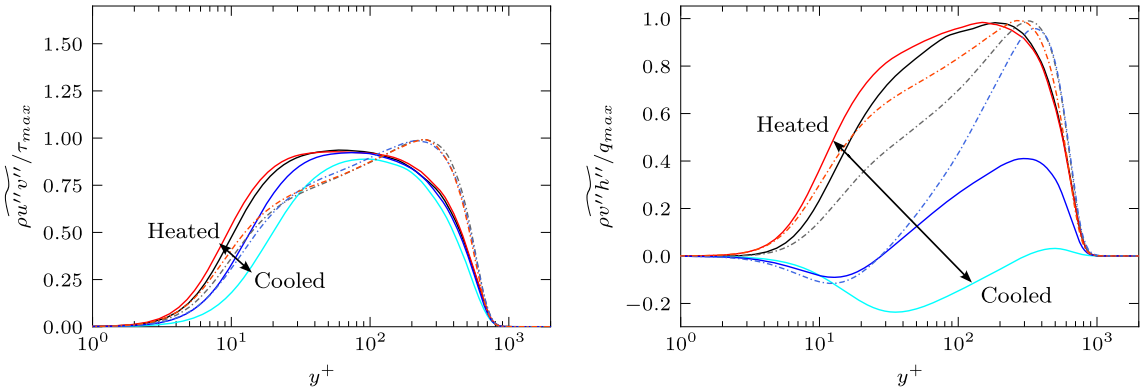

Figure 1: Left: Turbulent shear stress normalized by the maximum shear stress within the boundary layer profile for cases with different heating conditions and pressure gradients. Right: Turbulent heat flux normalized by the maximum heat flux within the boundary layer profile for cases with different heating conditions and pressure gradients. Red lines denote heated cases, black/gray lines mark adiabatic cases and blue/cyan denote cooled/strongly cooled cases. The solid lines show cases with zero pressure gradient, the dash-dotted lines show cases with an adverse pressure gradient at $\beta_K \approx 0.65$.

References

[1] T. Gibis, C. Wenzel, M. Kloker, and U. Rist. Self-similar compressible turbulent boundary layers with pressure gradients. Part 2. Self-similarity analysis of the outer layer. *Journal of Fluid Mechanics*, 880:284–325, December 2019.

[2] C. Wenzel, T. Gibis, and M. Kloker. About the influences of compressibility, heat transfer and pressure gradients in compressible turbulent boundary layers. *Journal of Fluid Mechanics*, 930:A1, January 2022.

[3] C. Wenzel, T. Gibis, M. Kloker, and U. Rist. Self-similar compressible turbulent boundary layers with pressure gradients. Part 1. Direct numerical simulation and assessment of Morkovin's hypothesis. *Journal of Fluid Mechanics*, 880:239–283, December 2019.

Mitteilung

Fachgruppe: Turbulenz und Transition

Enhancement of Wall Modelled LES for the Prediction of Laminar-Turbulent Transition

E. Guseva[1], F.R. Menter[1]
A. Stabnikov[2], A. Matyushenko[2], A. Garbaruk[2]
[1]Ansys Germany GmbH, Staudenfeldweg 20, 83624 Otterfing
[2]SPbPU, Polytechnicheskaya 29, 195251 St.Petersburg
katia.guseva@ansys.com

Motivation: Wall-Resolved LES (WRLES) of aerodynamic devices is in most cases not feasible due to the severe grid resolution requirements. LES of boundary layers requires therefore modeling assumptions to bridge the resolution gap. One such approach is Wall-Function LES (WFLES), where the near wall portion of the boundary layer is not resolved in wall-normal direction and the first cell center is placed in the logarithmic layer. The missing wall shear-stress is then computed from a wall function closure. An alternative is the use of Wall-Modelled LES (WMLES) where the inner layer is resolved in wall-normal direction, but where the missing resolution in the wall-parallel directions is covered by a RANS model. The current group has recently published [1] an algebraic WMLES framework, where any algebraic LES model can be combined with Prandtl's algebraic near wall mixing length model. The generic name of the model family is aWM-LES and the specific name when combined with a LES model (say the σ model) is aWM-σ. It has been shown (see [1]) that this model family can be calibrated to correctly reproduce the logarithmic layer without any noticeable Log-Layer Mismatch (LLM) as had been observed in other formulations.

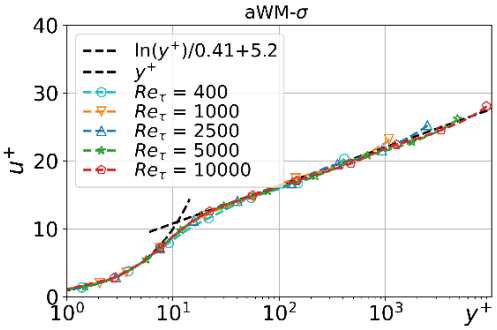

Figure 1. Velocity profiles in log-scale for the aWM-σ model for different Re numbers

One of the open questions concerns the application of this model to transitional flows, where the RANS layer can be activated upstream of transition and can thereby destroy the laminar boundary layer development. The current work will explore methods to optimize and/or augment the model to avoid this effect.

Methods: The aWM-LES formulation uses a blend of the RANS and the LES model $\nu_t = f_{sw}\nu_{t,RANS} + (1 - f_{sw})\nu_{t,LES}$, where $\nu_{t,LES}$ can be any algebraic LES model. The RANS model is given by $\nu_{t,RANS} = f_{wd}(0.41d_w)^2 S$, where d_w is the wall distance and S is the strain rate. The two functions involved are the switching function f_{sw} and the sublayer damping function f_{wd}. The switching function $f_{sw} = e^{-\left(\frac{C_{w1}d_w}{h_{max}}\right)^{C_{w2}}}$ (h_{max} is the generalized maximum edge length of the cell) has two parameters $C_{w1} = 2.45$ and $C_{w2} = 2.0$, which have been optimized to reproduce the correct logarithmic layer (Fig.1).

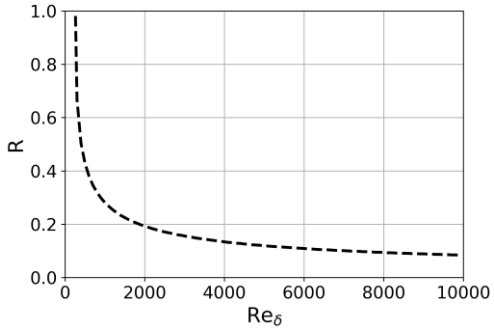

Figure 2. Resolution criterion as a function of Re_δ

To prevent activating of the RANS layer in the laminar part of transitional flows, one can ensure using in those regions a mesh, that is fine enough to push the RANS model into the sublayer. As shown in [1] the mesh requirement to absorb the RANS model into the sublayer is $h_{max} < \frac{C}{\sqrt{Re_\delta}}\delta$, where δ is the boundary layer thickness and C is a coefficient which depends on the model coefficients. Fig. 2 shows the value of the resolution parameter $R = h_{max}/\delta$, which

ensures $\nu_{t,RANS}/\nu < 0.01$ generated by aWM-LES, as a function of Reynolds number Re_δ.

Fig. 3 shows the effect of the mesh refinement for the Volino test case [2] which features a separation-induced transition. To ensure $\nu_{t,RANS}/\nu < 0.01$ in the laminar part, mesh should satisfy a requirement $R = h_{max}/\delta_{inlet} < 0.25$ (at the inlet, $Re_\delta \approx 1500$). On the coarsest mesh (R_{Mesh1} = 0.8), the upstream boundary layer is disturbed, and the transition process is negatively affected. The finest mesh (R_{Mesh3} = 0.2) satisfies the resolution requirement for this Reynolds number, and, as a result, transition laminar to turbulent transition is predicted well.

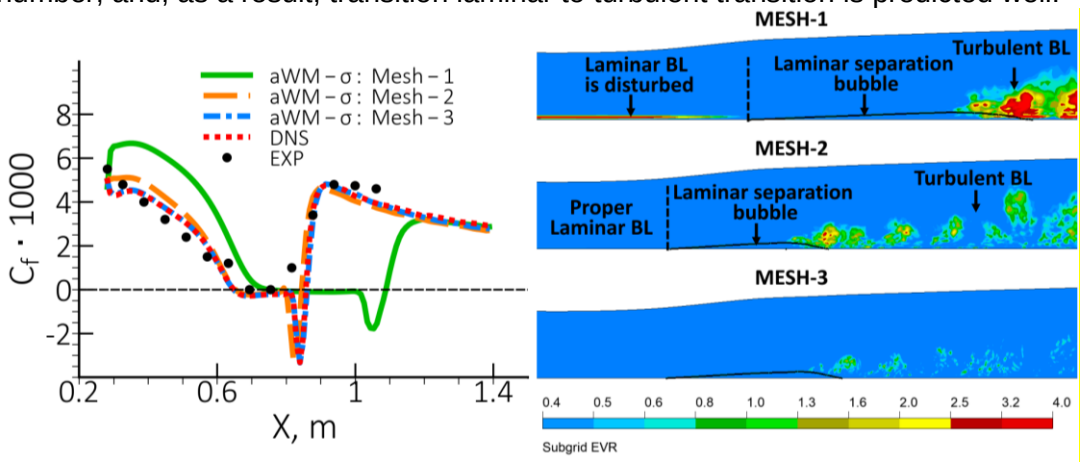

Figure 3: Skin friction coefficient (left) and eddy viscosity ratio contours (right) for the aWM-σ model on different meshes

It is desirable to provide methods which allow to switch off the RANS part in the entire laminar region without excessive mesh refinement. For this purpose, a transport equation for an indicator variable is introduced which detects three-dimensional disturbances in the outer part of the boundary layer and transports that information into the near wall 'RANS'-region. If the indicator detects laminar flow (Figure 4) in the outer part, the RANS model is turned off.

Activating the indicator equation, results in the proper prediction of the laminar flow and significantly improves transition behavior in the Volino case on the coarsest mesh Mesh-1 (Figure 5).

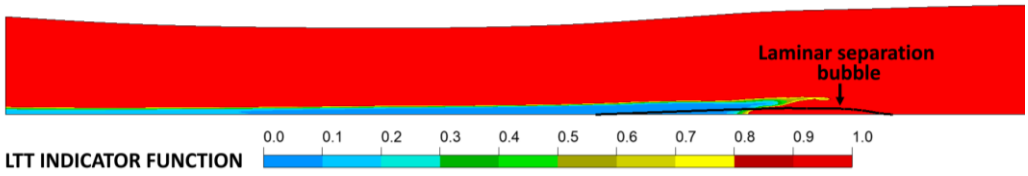

Figure 4: LTT indicator function

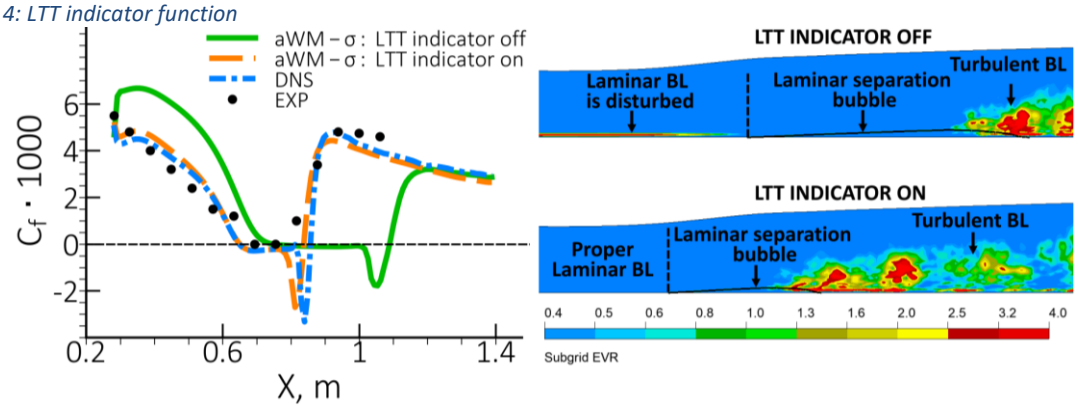

Figure 5: Skin friction coefficient (left) and eddy viscosity ratio contours (right) for the aWM-σ model with activated and deactivated laminar turbulent transition indicator

References

[1] Menter F. et al. A Family of Wall-Modeled Large Eddy Simulation Formulations // 14th International ERCOFTAC Symposium on Engineering Turbulence Modelling and Measurements. 2023, Barcelona, Spain

[2] Volino R.J., Hultgren L.S. Measurements in Separated and Transitional Boundary Layers Under Low-Pressure Turbine Airfoil Conditions // Journal of Turbomachinery, Vol. 123, 2001. pp. 189–197. https://doi.org/10.1115/1.1350408

Mitteilung

Fachgruppe: Turbulenz und Transition

Validation of CFD-based transition transport models to predict laminar-turbulent transition of swept transport aircraft wings

S. Helm[1,2], D. G. François[2], A. Krumbein[2]
[1] Cluster of Excellence SE²A – Sustainable and Energy-Efficient Aviation, TU Braunschweig, Deutschland
[2] Deutsches Zentrum für Luft- und Raumfahrt (DLR), Institut für Aerodynamik und Strömungstechnik, C²A²S²E, Bunsenstraße 10, 37073 Göttingen, sebastian.helm@dlr.de

Background

Reducing the viscous drag of future commercial aircraft by means of laminar flow plays a key role in the transformation to climate-neutral aviation. To mitigate financial risks and to accelerate the design process of laminar aircraft, increasing use is being made of numerical methods, such as CFD. The applicability of CFD methods for the design process depends on a high degree of automation of the individual components and on the accuracy and reliability of the simulation results. In this respect, the design of laminar aircraft is particularly demanding for the CFD process.
Streamline-based methods, based on linear local stability theory (LST) and the e^N method [1] or, more rarely, based on the non-local Parabolized Stability Equations (PSE) [2] offer a high degree of maturity and are therefore considered state-of-the-art. Although, these models have shown to be accurate and reliable, they require expert knowledge and automation is limited.
At the same time, a new class of models for predicting laminar-turbulent transition is gaining attention. Transport equation transition models are based on information available locally (at the CFD node level), making them particularly well suited for automation and parallelization of 3D simulations with modern unstructured CFD codes. Despite the advantages these correlation-based transition models, the accuracy, robustness, and reliability of the models need to be ensured and demonstrated more extensively.

Objective

This work contributed to the continuous development and validation of transition transport models, in particular the DLR γ-CAS model. The presentation will demonstrate the capabilities of the model to predict three-dimensional and transonic cases at high Reynolds number, compared to wind tunnel data. Furthermore, the inclusion of the effect of surface roughness into the model is discussed.

Approach

The DLR TAU-Code is used for RANS simulations. On the one hand, transition prediction is based on the linear stability code LILO and the e^N method [1], as a reference. On the other hand, the DLR γ-CAS model [3] is used. The latter consists of a transport equation for the intermittency-like variable γ, an auxiliary field variable taking values between 0 (laminar) and 1 (turbulent) and acting as a switch for the turbulence model. The model has similarities with the γ-$Re_{\Theta t}$ model and includes advancements for the application of transport aircraft, e.g. the improved accounting of pressure gradient and compressibility on transition. This is achieved by means of a simplified version of the AHD transition criterion. In addition, the model offers extensions to account for crossflow transition [4], one based-on the helicity criterion and the other using the C1 criterion.
The NLF-ECOWING-FSW [5] and the CRM-NLF [6] are swept wing configurations designed for natural laminar flow (NLF). The former exploits the advantages of a forward swept wing to alleviate crossflow, whereas the latter is based on the CATNLF (Crossflow Attenuated NLF) concept, restricting flow acceleration to the vicinity of the leading edge. Both test cases are considered for validation in this work.

Results

Near the design condition of the NLF-ECOWING-FSW model both approaches for transition prediction yield good agreement with the experimental transition detection by means of temperature sensitive paint (TSP). A validation including the more challenging off-design conditions will be presented at the workshop. The baseline version of the DLR γ-CAS model was successfully applied to the CRM-NLF configuration before [7]. The present work extends the validation of the crossflow extension to this test case.

The effect of compressibility on Tollmien-Schlichting transition as well as the effect of surface roughness of crossflow transition is investigated based on both test cases.

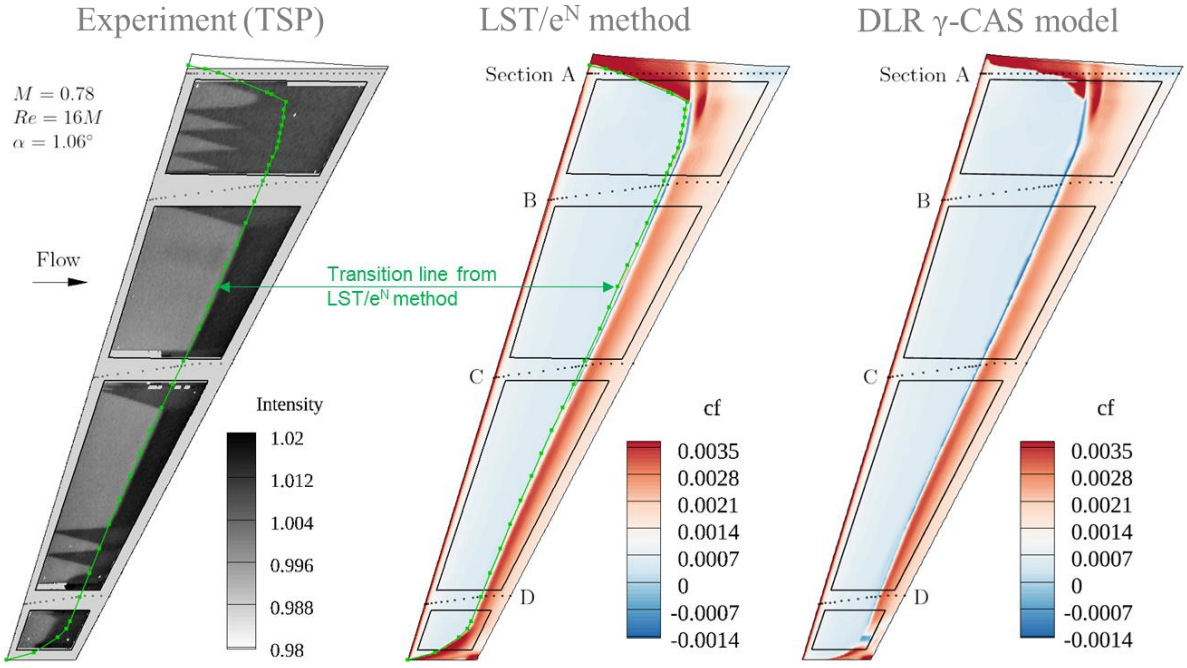

Fig. 1 : Experimental and numerical surface characteristics of the NLF-ECOWING-FSW model near the design condition. Laminar flow manifests itself as lighter area of low heat transfer in the TSP image (left) and light blue area of low skin friction c_f in the numerical solution (middle, right).

Literature

[1] Krumbein, A., Krimmelbein, N., Schrauf, G.: Automatic transition prediction in hybrid flow solver, part 1: Methodology and sensitivities. Journal of Aircraft, 46, pp. 1176-1190 (2009)

[2] Hein, S., "Nonlinear Nonlocal Transition Analysis - Code Development and Results" Recent Results in Laminar-Turbulent Transition, p. 123–134 (2004)

[3] François, D. G., Krumbein, A., Krimmelbein, N., Grabe, C.: Simplified stability-based transition transport modeling for unstructured computational fluid dynamics. J. of Aircraft (2023)

[4] François, D. G., Krumbein, A., Krimmelbein, N., „Crossflow Extension of a Simplified Transition Transport Model for Three-Dimensional Aerodynamic Configurations", AIAA AVIATION Forum (2022)

[5] Seitz, A., Hübner, A., Risse, K.: The DLR TuLam project: design of a short and medium range transport aircraft with forward swept NLF wing. CEAS Aeronautical Journal (2019)

[6] Lynde, M. N., Campbell, R. L.: Computational Design and Analysis of a Transonic Natural Laminar Flow Wing for a Wind Tunnel Model. 35th AIAA Applied Aerodynamics Conference. (2017)

[7] Krumbein, A., François, D. G., Krimmelbein, N.: Transport-based Transition Prediction for the Common Research Model Natural Laminar Flow Configuration. Journal of Aircraft, Vol. 59, No. 6, p. 1562-1573 (2022)

Mitteilung

Fachgruppe: Turbulenz und Transition

Artificial neural networks as a surrogate model for linear stability analysis of compressible, three-dimensional boundary layers

Paul Hoffmann, Alexander Theiß, Stefan Hein
DLR – Institut für Aerodynamik und Strömungstechnik (AS)
Abteilung Hochgeschwindigkeitskonfigurationen
Bunsenstr. 10, 37073 Göttingen
paul.hoffmann@dlr.de

Motivation

One impactful factor for the reduction of carbon emissions in aviation is the reduction of viscous drag, which in turn is heavily influenced by the boundary-layer state. Due to this dependency, a crucial design parameter in this context is the position of laminar-turbulent transition. In order to estimate the transition location, the semi-empirical e^N-method is commonly used, which relies on stability characteristics of the laminar boundary layer computed based on the linear stability theory (LST). Transition is predicted, where the integrated growth rate of disturbances modes, the N-factor, reaches an experimentally derived critical limit. How-ever, the transition prediction based on LST is so far mostly used by expert users only. In order to make this method accessible to a wider range of potential users and to profit from improved performance, various strategies to construct an according surrogate model, such as lookup tables [1], have been proposed in the past. After having proven their strong potential in different branches and fields of application, artificial neural networks (ANN) have lately gained attention as a suitable candidate for surrogate models for boundary-layer stability predictions again [2]. In the present work, an ANN-based approach for surrogate modelling of LST-based stability computation is presented for three-dimensional compressible boundary layers. Within the scope of this work, two different instability mechanisms, two-dimensional (2D) Tollmien-Schlichting waves (TS) and stationary cross-flow instabilities (CFI), are covered.

Methodology

The regression tasks posed to the ANNs investigated is the prediction of the stability characteristics of 2D Tollmien-Schlichting instabilities (TSI) and stationary CFI. The models are trained using supervised learning, i.e. the model is shown both the model inputs and the expected outputs during the training phase. For the training data, an existing data base was used that served Theiß and Hein [3] as supporting points for a radial basis function interpolation method in their approach to build a surrogate model for LST. This dataset is based on stability computations with the NOLOT code of boundary-layer profiles generated from local self-similar solutions of compressible Falkner-Skan-Cooke (FSC) flow [4] and covers a broad Mach number range from fully incompressible to slightly supersonic flow conditions.
Different network architectures and input information are investigated. On the one hand, classical multilayer perceptron (MLP) networks are studied, i.e. networks consisting only of several fully connected hidden layers. For the presented task, such networks rely on only a few scalar quantities describing the analysed boundary-layer flow plus specific instability information. When properly trained for the dataset, the ANN can be seen as a function $(\alpha_r, \sigma) = f(Ma_e, H_{12,ic}, Re_{\delta_1}, \omega)$ for the TSI case, where α_r represents the streamwise wavenumber, σ the amplification rate, Ma_e the boundary-layer edge Mach number, $H_{12,ic}$ is the shape factor in incompressible form, Re_{δ_1} the displacement thickness based Reynolds number and ω the non-dimensional circular frequency. For the CFI case the ANN is an approximator in the form of $(\alpha_r, \sigma) = f(Ma_e, \Lambda, V^*_{Max}, Re_{CF}, \beta)$, where Λ is the local sweep angle, V^*_{max} the maximum cross-flow velocity in relation to the boundary-layer edge velocity, Re_{CF} the cross-flow Reynolds number and β the transverse wavenumber. On the other hand, neural networks that rely on complete boundary-layer profiles, i.e. the streamwise and cross-flow velocity components U and

V, respectively, are also investigated. Their network architectures comprise 1D convolutional layers to process the profile data and extract the information contained therein and relevant to the stability problem.

Results

For both instability types, the performance of different network architectures is first evaluated on a test set consisting of further samples of FSC flow that were excluded in the training process. For validation, Fig. 1 shows a comparison of the exact amplification rates σ computed with LST and the ones predicted by a neural network for one of the FSC test cases from the CFI scenario. The agreement between ground truth and the model predictions is excellent, as can be seen.

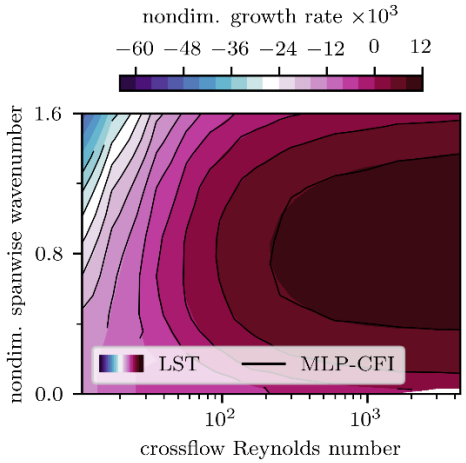

Figure 1: Comparison of LST- and ANN-computed CFI amplification rate for a 3D locally self-similar FSC boundary-layer flow at $Ma_e = 1.4$, $\Lambda = 55°$, $V^*_{max} = 3.55\%$

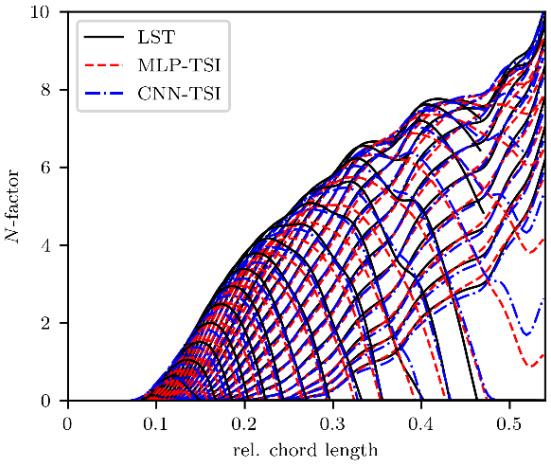

Figure 2: Comparison of LST- and ANN-computed N-factors for TSI on ATTAS flight test data ($Ma_\infty = 0.58$, $Re_\infty = 23.1 \times 10^6$)

A direct comparison of actual LST results and network predictions is made for real, non-self-similar 3D compressible boundary-layer flow data stemming from an ATTAS flight experiment [5]. Thus, this test case evaluates in particular the learned abstract representation of the relevant training data features in terms of good generalisation of the problem and thus transfer capabilities from the locally self-similar training dataset to representative application-related data. The surrogate models are evaluated in terms of the error in the stability quantities with respect to the ground truth LST results as well as the resulting deviation of the integrated N-factors. As can be seen exemplarily for a TSI case in Fig. 2, satisfactory results were achieved for the N-factor envelope, shown here for two different network architectures, an MLP and a convolutional neural network (CNN).

References

[1] M. Drela: Implicit implementation of the full e^n transition criterion. 21st Applied Aerodynamics Conference, AIAA 2003-4066, 2016.

[2] M.I. Zafar, H. Xiao, M.M. Choudhari, F. Lei, C.-L. Chang, P. Paredes and B. Venkatachari: Convolutional neural network for transition modelling based on linear stability theory. Physical Review Fluids 5,11, 113903, 2022.

[3] A. Theiß and S. Hein: A surrogate-based e^N transition prediction method for three-dimensional compressible boundary layers. New Results in Numerical and Experimental Fluid Mechanics XIV: Contributions to the 23rd STAB/DGLR Symposium Braunschweig, Springer, in press.

[4] Z. Liu. Compressible Falkner-Skan-Cooke boundary layer on a flat plate. Physics of Fluids, 33 126109, 2021.

[5] K. Horstmann, G. Redeker, A. Quast, U. Dressler and H. Bieler: Flight tests with a natural laminar flow glove on a transport aircraft. Flight Simulation Technologies Conference and Exhibit, 385-392, 1990.

Mitteilung

Projektgruppe/Fachkreis: Flow control, Laminar-Turbulent Transition,Turbulence

Ansprechpartner: Prof. Dr.-Ing.habil. J. Jovanović[1], Su Ja Lee, M.Sc.[2], Marleen Krysl[1], Prof. Dr. P. Schlatter[1]

Institution: [1]Institute of Fluid Mechanics, University of Erlangen-Nuremberg
[2]German Engineering and Development Center, LSTME Busan

Adresse:

[1]Cauerstraße 4
91058 Erlangen
Telefon: (09131) 85-29507
Telefax: (09131) 85-29503
e-mail: jovan.jovanovic@fau.de

[2]1276 Jisa Dong
Gargseo-Gu, Busan
Telefon: (+82) 51-899-8075
Telefax: (+82) 51-899-8077
e-mail: suja.lee@lstme.org

Topic:

Further experiments on drag reduction in a groove-modified channel flow

Introduction:

In attemt to further clarify the drag reduction effects induced by surface embedded grooves and support the fundamental deduction stating that origin of the drag reduction phenomena is associated with the axisymmetric structure of the Reynolds stresses further measurments in in groove-modified channel flow were performed.

Objectives:

The aim of the experiments is to demonstrate that early stabilization of the laminar boundary layer with a grooved surface promote drag reduction furter downstream in a flow developeding over flat surface.

Methodology:

The promicing pattern was sought in the form of square grooves with flat interspacing region between them arranged periodically along the spanwise direction. The period between neighbouring grooves was fixed to three groove depths assuming that such arrangement will induce favourable interaction between the grooves and enforce axisymmertry over the entire wetted surface. The two-dimensional channel and the related equipment that were used in the present experiments are similar to the ones employed in the previous investigations of flow control in fully developed turbulence.

Results:

The resultes of previous measurments have been confirmed qualitatively and exteneded quantintiatively. Comparisons of the pressure differentials measured along flat and groove-modified channels for indentical flow conditions and the volume flow rates confirms appearence of skin friction reduction in the range of flow velocities corresponding to groove dimensions that correlate with viscous length scale. For smooth inlet conditions large drag reduction up to DR≈30% was mesured owing to extended persistence of the laminar flow when compared to flow development in a flat channel.

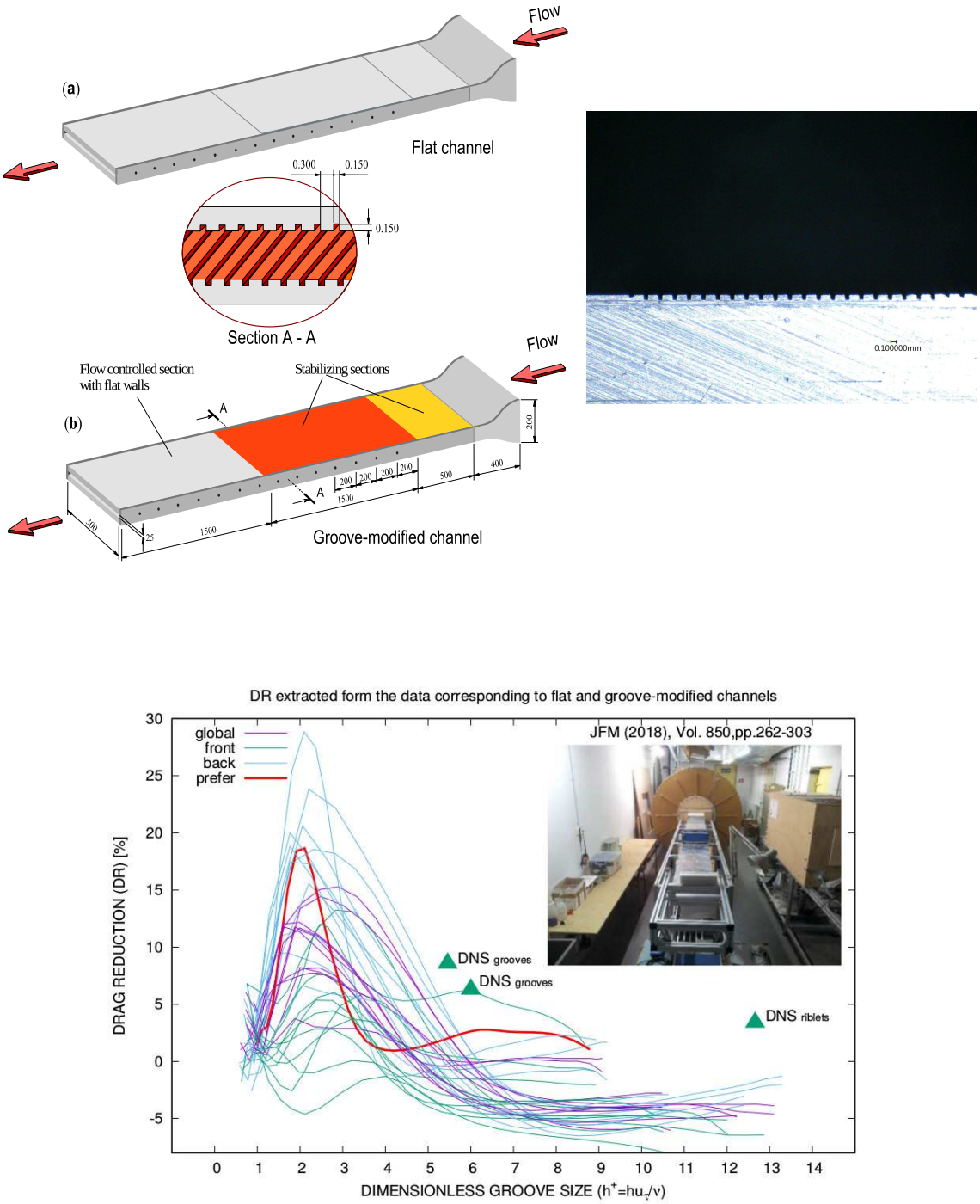

Figure 1: Two-dimensional channel flow with flat and groove-modified test section arrangements. (a) Reference test section configuration. (b) Configuration of the test section for laminar flow control (left). (bottom) Drag reduction versus non-dimensional groove height.

References:

[1] Kriger, V., Perić, R., Jovanović, J., Lienhart, H. and Delgado, A. 2018 Towards design of the antiturbulence surface exhibiting maximum drag reduction effect. *J. Fluid Mech.* **850**, 262–303.

Mitteilung

Projektgruppe/Fachkreis: Turbulenz und Transition

Towards Local Application of Data-Driven Turbulence Modeling based on Field Inversion and Machine Learning

Yasunari Nishi[1], Tobias Knopp[1], Axel Probst[1], Cornelia Grabe[1], Andreas Krumbein[1]
[1] DLR-AS C²A²S²E , Bunsenstraße 10, 37073 Göttingen
Yasunari.Nishi@dlr.de

Introduction:

Recent advancement in data-driven turbulence modeling has shown the potential of the usage of machine learning techniques to enhance classical Reynolds-averaged Navier-Stokes (RANS) turbulence models. However, one of the main limitations of the current data-driven approaches includes their limited applicability to flows that are very similar to the training cases. Moreover, when data-augmented model is applied to out-of-training flow scenarios, the predictive accuracy is often harmed, i.e., the data-driven turbulence model provides worse prediction than the baseline model.

While efforts have recently been made to address such robustness and generalizability issues of data-driven methods by improving the training strategy (e.g., [1,2]), we present a sensor-based approach towards more general data-driven models here, namely the local activation or deactivation of (different) model augmentations depending on the local flow state. For this, physics-based classical sensors and also machine learning classifiers could potentially be used.

Numerical methodology:

We consider a data-augmented negative Spalart-Allmaras model based on the field inversion and machine learning (FIML) framework presented in [3]. The fundamental idea of FIML is to introduce a spatially-varying model correction coefficient β into an existing turbulence model and to find a machine learning model that predicts β based on the local flow state. The modified SA model reads

$$\frac{D\tilde{\nu}}{Dt} = \beta P - D + \frac{1}{\sigma}[\nabla \cdot \left((\nu + \tilde{\nu})\nabla\tilde{\nu}\right) + c_{b2}(\nabla\tilde{\nu})^2],$$

where β denotes the correction coefficient, $\tilde{\nu}$ the SA variable, P the production term, and D the destruction term. To localize the model augmentation, the production term of the original FIML implementation is reformulated such that $(1-f)P + f\beta P$ where f is a blending factor which takes the value between 0 and 1. Therein, the value of the blending factor f is given by a suitable sensor or a machine learning classifier. The numerical simulations are conducted using the DLR-TAU code coupled with the SMARTy toolbox [4], which provides various optimization methods and capabilities from deep learning libraries.

Results:

The idea of localized model augmentation has been tested on the NASA wall-mounted hump case [5]. Figure 1 shows the results using analytically derived sensor functions presented in [6], which detect the attached boundary layer at adverse pressure gradient. As can be seen from Figure 1 (a), the globally augmented model (in red) shows worse prediction of the reattachment point than the original SA model (in blue). This is due to the undesired model corrections in the region of zero pressure gradient and favorable pressure gradient, see Figure 1 (b). With the use of the sensor functions, those model corrections have been excluded (Figure 1 (c)), and therefore the predictive accuracy of the reattachment point has almost been reverted back to the original model (in green), see Figure 1 (a).

The final talk includes results on airfoil flow cases and an exemplary usage of the machine learning classifier.

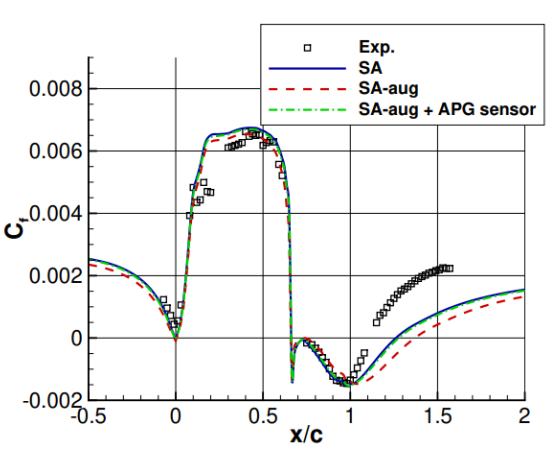

(a) Skin friction coefficient

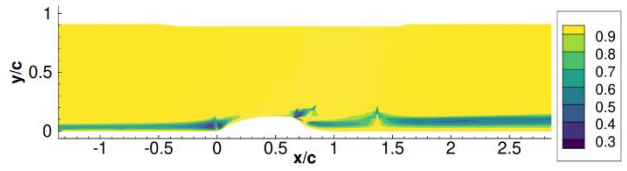

(b) Field of β with global model augmentation

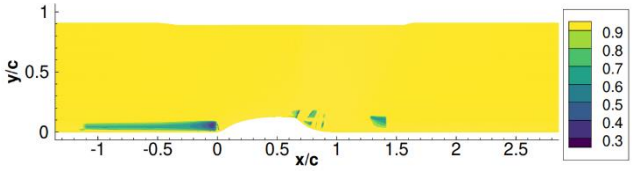

(c) Field of β with local model augmentation controlled by the APG sensor

Figure 1: Results on the NASA hump case [5]

References:

[1] Rumsey, C. N., Coleman, G. N. and Wang., L. (2022), In search of data-driven improvements to RANS models applied to separated flows. AIAA SCITECH 2022 Forum

[2] Srivastava, V. and Duraisamy, K. (2021), Generalizable physics-constrained modeling using learning and inference assisted by feature-space engineering. *Physical Review Fluids*, Vol. 6, p. 124602

[3] Jäckel, F. (2022), A closed-form correction for the Spalart-Allmaras turbulence model for separated flows. AIAA SCITECH 2022 Forum.

[4] Bekemeyer, P., Bertram, A., Hines Chaves, D. A. et al. (2022), Data-Driven Aerodynamic Modeling Using the DLR SMARTy Toolbox. AIAA Aviation 2022 Forum.

[5] Greenblatt, D., Paschal, K. B., Yao, C. S., Harris, J., Schaeffler, N. W., and Washburn, A. E. (2006). Experimental investigation of separation control part 1: Baseline and steady suction. *AIAA Journal*, 44(12), 2820–2830.

[6] Knopp, T., Reuther, N., Novara, M., Schanz, D., Schülein, E., Schröder, A., and Kähler, C. (2023), Modification of the SSG/LRR-ω model for turbulent boundary layer flows in an adverse pressure gradient. *Flow Turbulence Combust*, Vol. 111, pp. 409438.

Mitteilung

Fachgruppe: Turbulenz und Transition

Charakterisierung der Wechselwirkung zwischen Aufnahme und der turbulenten/nicht-turbulenten Grenzfläche (TNTI) in einer turbulenten Grenzschicht

Agastya Parikh[1], Prof. Dr. rer. nat. habil. Christian J. Kähler

Institut für Aerodynamik und Strömungsmechanik,
Universität der Bundeswehr München,
Werner-Heisenberg-Weg 39, 85577 Neubiberg

[1]agastya.parikh@unibw.de

Eine Vielfalt von natürlichen und technischen Prozessen sind entweder von turbulenten Strömungen getrieben oder beeinflusst. Seit dem Beginn der strömungsmechanischen Forschung bilden turbulente Grenzschichten eine Modellströmung, um die hochkomplexe Mechanik von turbulenter Advektion aufzuklären und zu verstehen. Ein Forschungsschwerpunkt in diesem Bereich umgibt die Charakterisierung und Dynamik der turbulenten/nicht-turbulenten Grenzfläche (TNTI). Die Aufnahme von Teilen der Außenströmung in der Grenzschicht ist ein Effekt, der das TNTI formt und für die Übertragung von Impuls zwischen der Außenströmung und der Grenzschicht sorgt.

Die experimentelle Charakterisierung des TNTI ist mit verschiedenen Methoden grundsätzlich möglich, allerdings sind alle diese Methoden mit Unsicherheiten verbunden. Die Detektion von Teilen der Außenströmung, die Teil der Grenzschicht durch Aufnahme geworden sind, und im umgekehrten Fall, Teilen der Grenzschicht, die Teil der Außenströmung durch Ausstoß geworden sind, ist schwierig eindeutig auszuführen. Um dieser Problematik zu begegnen, ist die Entwicklung einer neuen Variante von PIV-Messtechnik mit fluoreszierenden PIV-Partikeln vielversprechend. Hierbei werden fluoreszierende DEHS-Partikel (P567 Partikel) für die lokale Markierung der Grenzschicht gleichzeitig mit den herkömmlichen DEHS-Partikeln, die nur Mie-Streuung erzeugen, genutzt, wobei letztere nur für das globale Seeding eingesetzt werden. Bei synchronisierten Aufnahmen mit zwei Kameras, die auf dem gleichen Sichtfeld gerichtet sind und einer davon mit einem Sperrfilter (Wellenlänge 532nm) ausgerüstet ist, ist es möglich, die Strömung der Grenzschicht von dem gesamten Strömungsfeld zu trennen. Dieses Ergebnis ist in der Abbildung 1. dargestellt.

Mit der Trennung der zwei Strömungszonen ist es nun möglich, jene Regionen zu

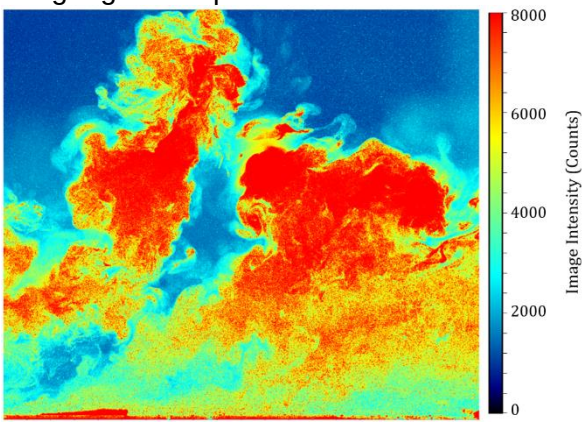

1a. Aufnahme mit Mie-Streuung

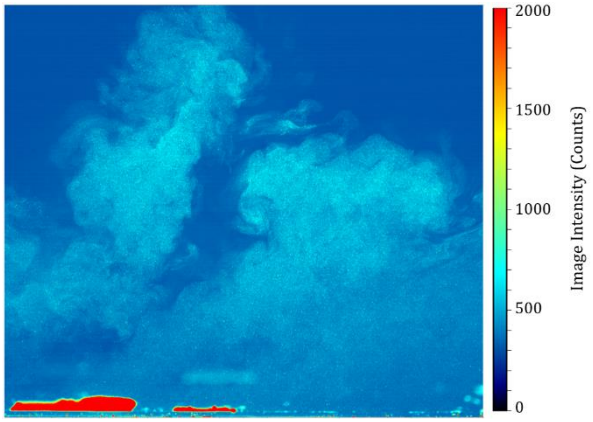

1b. Aufnahme mit fluoreszierenden Partikeln

1. PIV-Bilder des gleichen Sichtfeldes, mit 2 Kameras aufgenommen. Eine Kamera (1a.) ist für Aufnahmen mit Mie-Streuung benutzt und die andere (1b.) ist für Aufnahmen mit P567 Partikeln benutzt.

2. Binarisiertes Bild mit aufgenommenen (rot) und ausgestoßenen (b) Regionen

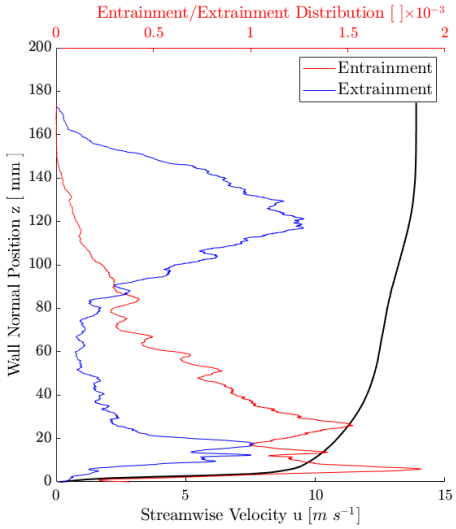

3. Die Verteilung der Aufnahme (rot) und Ausstoßes (blau) als Funktion von der Wandentfernung; das Geschwindigkeitsprofil ist in schwarz gezeigt.

identifizieren, die irgendwann Teil der Grenzschicht geworden sind. Der Ansatz beruht auf der Idee, dass die fluoreszierenden Partikeln, die als lokale Seeding in die Grenzschicht eingebracht wurden, nur aus der Grenzschicht stammen können. Daraus folgt, dass umschlossenen Regionen, die keine P567-Partikeln enthalten, von der Strömung außerhalb der Grenzschicht stammen müssen. Entsprechend folgt, dass Regionen mit P567-Partikeln, die von der Grenzschicht komplett abgelöst sind und sich in der Außenströmung befinden, aus der Grenzschicht stammen müssen. Zur Verarbeitung der Daten für diesem Zweck werden die Bilder mit fluoreszierenden Partikeln benutzt. Um die Partikeln in einer benutzbaren Maske zu wandeln ist die Verwendung eines Erosionsfilters und eines Gauss-Filters erforderlich. Danach können aufgenommene und ausgestoßene Regionen wie in der Abbildung 2. identifiziert werden. Mit dieser Verarbeitungsmethode kann z.B. die Verteilung der Aufnahme-Events und Ausstoß-Events in der Grenzschicht berechnet werden, siehe Abbildung 3.

Die beschriebene Verarbeitung kann auch in Verbindung mit den PIV-Ergebnissen der Mie-Streuung Aufnahmen kombiniert werden. Auf diese Weise kann z.B. das turbulente Verhalten der aufgenommenen und ausgestoßene Regionen der Strömung, z.B. turbulente Bewegungsenergie und Schubspannung, isoliert betrachtet werden, um weiteren Einblicke in die Physik der Grenzschichtströmung zu ermöglichen.

Referenzen

[1] Chauhan, K., Philip, J., de Silva, C. M., Hutchins, N., & Marusic, I. (2014). The turbulent/non-turbulent interface and entrainment in a boundary layer. Journal of Fluid Mechanics, 742, 119–151. https://doi.org/10.1017/jfm.2013.641

[2] Dahm, W. J. A., & Dimotakis, P. E. (1987). Measurements of entrainment and mixing in turbulent jets. AIAA Journal, 25(9), 1216–1223. https://doi.org/10.2514/3.9770

[3] McKeon, B. J., et al. (2007, July). Velocity, Vorticity, and Mach Number. In C. Tropea (Ed.). A. Yarin (Ed.). J. F. Foss (Ed.), Springer Handbook of Experimental Fluid Mechanics (pp. 215–472). Springer.

[4] Okada, M., Pinho, J., & Lavagnoli, S. (2022). Fluorescent Tracer Particles for PIV Measurement in Gas Flows. Proceedings of the 20th International Symposium on Application of Laser and Imaging Techniques to Fluid Mechanics, 20.

[5] Pedocchi, F., Martin, J. E., & García, M. H. (2008). Inexpensive fluorescent particles for large-scale experiments using particle image velocimetry. Experiments in Fluids, 45(1). https://doi.org/10.1007/s00348-008-0516-2

[6] Raffel, M., Willert, C. E., Scarano, F., Kähler, C. J., Werely, S. T., & Kompenhans, J. (2018). Particle Image Velocimetry: A Practical Guide (3rd ed.). Springer. https://doi.org/10.1007/978-3-319-68852-7

[7] Reuther,N., & Kähler, C. J. (2018). Evaluation of large-scale turbulent/non-turbulent interface detection methods forwall-bounded flows. Experiments in Fluids, 59. https://doi.org/10.1007/s00348-018-2576-2

[8] Scharnowski, S., & Kähler, C. J. (2020). Particle image velocimetry - Classical operating rules from today's perspective. Optics and Lasers in Engineering, 135, 106185. https://doi.org/10.1016/j.optlaseng.2020.106185

[9] Towers, D. P., Towers, C. E., Buckberry, C. H.,& Reeves, M. (1999). A colour PIV system employing fluorescent particles for twophase flow measurements. Measurement Science and Technology, 10(9). https://doi.org/10.1088/0957-0233/10/9/309

Mitteilung

Fachgruppe: Turbulenz und Transition

Linear Instability Analyses of Supersonic and Hypersonic Flows over Rotating Cones

J. Penning, A. Theiß, S. Hein
DLR – Institut fur Aerodynamik und Strömungstechnik (AS)
Abteilung Hochgeschwindigkeitskonfigurationen
Bunsenstr. 10, 37073 Göttingen
jonas.penning@stud.uni-goettingen.de

Introduction

Rotating objects are present in numerous real-world applications. The state of the boundary layer significantly effects the skin friction drag and thermal load of aeronautical objects in high-speed flow. To understand and predict the laminar-to-turbulent boundary-layer transition on rotating configurations, the prevailing boundary-layer instabilities involved in the transition process need to be known depending on the rotation speed and inflow velocity. Basic research on the influence of rotation on boundary-layer instabilities has focused mainly on simple geometries such as rotating disks and cones. However, even for such simple geometries, the effect of rotation on boundary-layer instabilities is not yet fully understood, especially for compressible inflow. Recently, Song & Dong [1] numerically studied the impact of rotation on the instability characteristics of the 1st-Mode, the crossflow-, and centrifugal instability for the boundary layer on a 7° half-opening angle cone subjected to supersonic axial flow. This work extends the study to more half-opening angles, rotation speeds, and to hypersonic axial inflow velocity. The aim is to investigate whether rotation has a stabilizing or destabilizing effect on the primary instability mechanisms as a function of half-opening angle and inflow velocity using local linear stability theory. Furthermore, the influence of the Coriolis and centrifugal force terms (in combination: rotation terms) appearing in the linearized disturbance equations on the instability characteristics is of particular interest as well as the metric terms, which represent effects of surface curature and conical divergence.

Numerical Approach

The laminar basic flows for the rotating cone geometries with super- and hypersonic axial inflow at zero degree angle of attack are computed with the DLR TAU code on a structured grid. Grid converegence was checked and the final grid consists of 550 points along the centerline, 484 points in the wall normal direction, and 3 points in the circumferential direction. The simulations were performed with a moving wall boundary condition and rotational periodicity. The rotational velocities in the simulation were adjusted to have fixed ratios of boundary-layer edge velocity to the circumferential wall velocity (i.e., $\bar{\Omega}$) at $x = 0.4$ m, where x is the streamwise coordinate along the cone's surface. The freestream conditions for the supersonic case match the values as used by Song & Dong [1] (Ma_∞= 3.214), whereas Ma_∞= 6.1 was set for the hypersonic case. Linear local stability theory is used to analyze the instability properties of the primary instability mechanisms at $x = 0.4$ m, using the DLR in-house instability code NOLOT, which has been extended for rotating reference frames [2]. In this work, n describes the number of wave fronts in circumferential direction (i.e., the wavefront count) and ω is the angular frequency.

Results

Figures 1 & 2 show the unstable domain in the frequency-wavefront-count space of the 1st- and the 2nd-Mode for the 7°-cone with hypersonic axial flow. In Figure 1, the cone is not rotating, while Figure 2 visualizes the influence of rotation on both modes: The symmetrical characters of the 1st- and the 2nd-Mode break, as the 2nd-Mode shifts towards negative wavefront counts (waves travelling against the cone's rotation) and higher frequencies and the 1st-Mode

towards positive wavefront counts and lower frequencies. Further, rotation has a general destabilising effect on both the 1st- and the 2nd-Mode, as the maximal growth rates of both modes increase with increasing rotation intensity. Figures 3 & 4 show growth-rate curves as functions of the wavefront count *n* to visualize the effects of the metric and rotational terms, as well as the Coriolis and centrifugal terms. Figure 3 shows the growth rate curves of the 2nd-Mode, while Figure 4 is based on the linear stability results for the 7° cone with supersonic axial flow and therefore shows the growth-rate curves of the 1st-Mode. For both modes, the metric terms have a stabilizing effect, because their exclusion from the stability equations leads to increased growth rates. The opposite holds for the rotation terms, which therefore have a destabilizing effect on the 1st- and the 2nd-Mode. Furthermore, Figure 4 visualizes that the centrifugal terms also have a stabilizing effect on the 1st-Mode, while the Coriolis terms represent a destabilizing mechanism. Note that the instability results for the 1st-Mode are consistent with the literature [1] when both the metric and rotational terms are included in the stability analysis. In Figure 2, the extension to negative frequencies is identified as a crossflow mode. Its destabilization is caused by the onset of a cross-flow velocity component in the base flow.
Furthermore, with the inclusion of both the metric and rotational terms, the centrifugal instability (cf. [1]) is destabilized.
Each of these modes is analyzed in terms of the influence of rotation and the dependence on the metric, rotational, Coriolis, and centrifugal terms. In addition, the effects of the half-opening angle and the two different inflow velocities on the instability characteristics are studied.

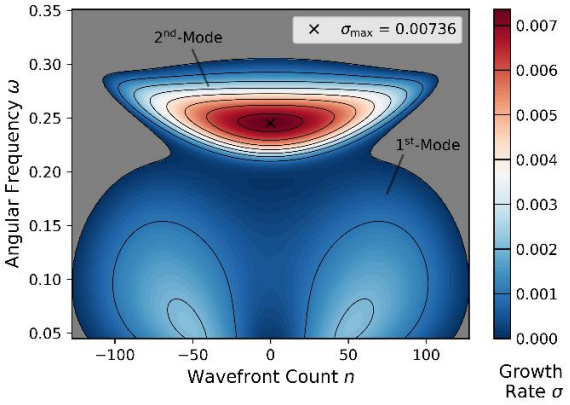

Figure 1: Isosurfaces and contour-lines of the 1st- and the 2nd-Mode in the frequency-wavefront-count domain for the non-rotating 7°-cone with hypersonic axial flow ($\bar{\Omega} = 0$).

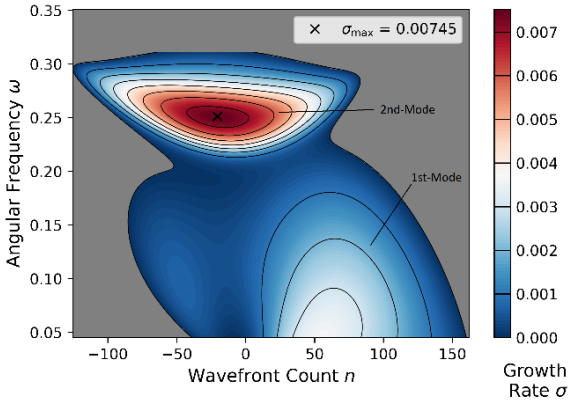

Figure 2: Isosurfaces and contour-lines of the 1st- and the 2nd-Mode in the frequency-wavefront-count domain for the rotating 7°-cone with hypersonic axial flow ($\bar{\Omega} = 0.3$).

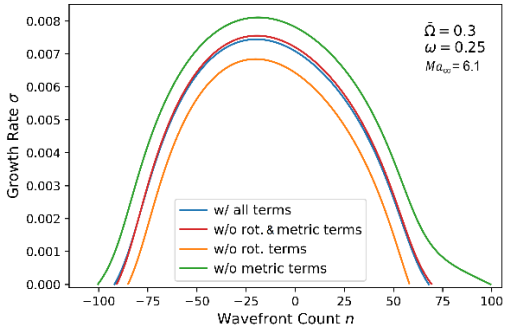

Figure 3: Growth-rate curves as a function of the wavefront count *n* for the 2nd-Mode.

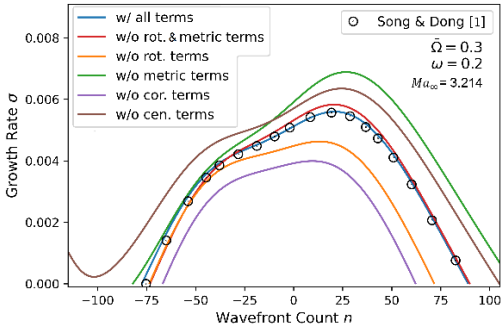

Figure 4: Growth-rate curves as a function of the wavefront count *n* for the 1st-Mode.

[1] Song, R. and Dong, M. (2023). Linear instability of a supersonic boundary layer over a rotating cone. Journal of Fluid Mechanics, 955:A31.

[2] Dechamps, X. and Hein, S. (2018). Extension of the pse code NOLOT for transition analysis in rotating reference frames. In Dillmann, A., Heller, G., Krämer, E., Wagner, C., Bansmer, S., Radespiel, R., and Semaan, R., editors, New Results in Numerical and Experimental Fluid Mechanics XI, pages 179–188, Cham. Springer International Publishing

Mitteilung

Projektgruppe/Fachkreis: Transition

Delay of laminar-turbulent transition by rotating cylindrical roughness elements in a flat-plate boundary layer

T. Römer, C. Wenzel, U. Rist
Institut für Aerodynamik und Gasdynamik der Universität Stuttgart
Pfaffenwaldring 21, 70569 Stuttgart, roemer@iag.uni-stuttgart.de

Delaying laminar–turbulent transition in boundary layers is of great interest and practical importance, as it can reduce surface friction by up to an order of magnitude. It has been the prevailing opinion for years that three-dimensional (3D) surface roughness elements can solely promote the transition process in Blasius boundary layers. Fransson et al. [2] showed, however, that boundary layer streaks induced by cylindrical roughness elements are able to control the Tollmien–Schlichting (TS) instabilities up to a complete transition delay, indeed. The mechanism is attributed to a negative spanwise production in the perturbation kinetic energy (PKE) budget, brought by the spanwise modulated velocity streaks [1]. In a numerical investigation from Wu et al. [5], it has been further observed that also counter rotating cylindrical roughness elements are capable to control the TS instabilities. However, the inviscid inflectional mode caused by the distortion of the cylinder in the boundary layer at medium rotation speed can provoke transition. In this talk, it is shown by experimental investigations that by actively rotating a cylinder pair, the boundary layer primary instability can be stabilized and the laminar-turbulent transition can be delayed in a realistic flow configuration [3].

The experimental setup is given in the top figure, highlighting the flow field around the pair of rotating cylinders via a dye visualization. Two cylinders, each with a height $k = 7.4\,\mathrm{mm}$ and a diameter of $d = k/2$, are placed at a distance of $x = 1400\,\mathrm{mm}$ behind the leading edge with a spanwise spacing of $\lambda/k = 2$. Between the two cylinders at $(x, y, z) = (1400, 0, 0)\,\mathrm{mm}$ the (x_k, y_k, z_k)-coordinate system (non-dimensionalized by k) has its origin. The free-stream velocity is $U_e = 0.1\,\mathrm{m\,s^{-1}}$, resulting in a displacement thickness at the streamwise cylinder position of $\delta_1/k = 0.87$. The roughness Reynolds number $Re_{kk} = u(k)k/\nu$ is 461, where $u(k)$ is the undisturbed boundary layer velocity at roughness height k and ν is the kinematic viscosity. The cylinders rotate counterwise, inducing

a high-momentum fluid between them. The rotation speed is given by $\Omega_u = \Omega d/(2u(k))$, where Ω is the angular velocity.

For the rotating cylinders, the streak amplitude A_{st} increases, see Figure 1 (left). A_{st} is defined as in Shahinfar et al. [4]: $A_{\mathrm{st}}(y_k) = (\max_z(\bar{u}) - \min_z(\bar{u}))/(2U_e)$. The maximum/minimum of $\bar{u}$ is calculated at constant $z_k = 0$ position. According to the hypothesis of Fransson et al. [2], a higher streak amplitude is destined to stabilize the boundary layer. Figure 1 (right) shows the evaluated intermittency factor γ at different streamwise positions x_k downstream of the rotating cylinders; if $\gamma = 0$, the flow is laminar, $\gamma = 1$ indicates a fully turbulent flow. Compared to a TS wave disturbed boundary layer (black line), the intermittency function indicates a transition delay up to a rotation speed of $\Omega_u = 0.343$. The mechanism for the transition delay is in the amplified streaks induced by the rotating cylinders, which are able to attenuate the TS-like mode [5].

The advantage of this active transition delay mechanism lies in the controllability of the laminar-turbulent transition that can be adjusted by the rotation speed of the cylinders.

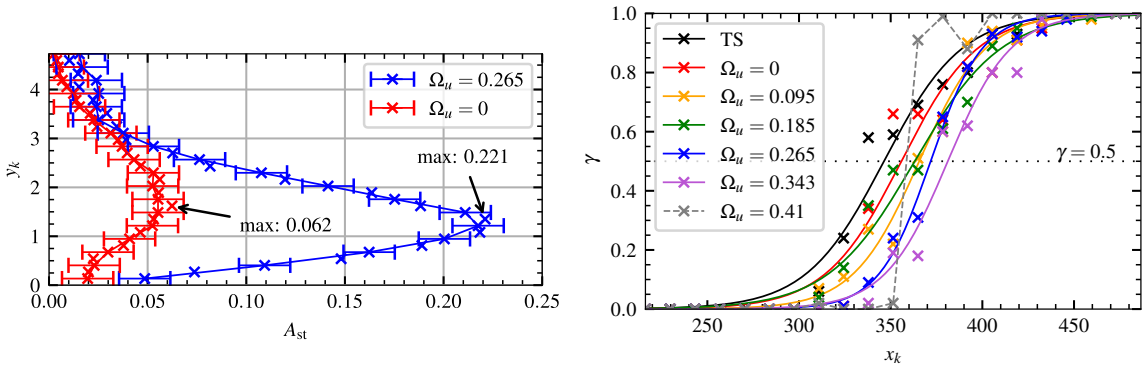

Figure 1: Left: Streak amplitude A_{st} at $x_k = 216$. Right: Intermittency function downstream of the cylinders. Measurements were carried out using a hot-film probe.

References

[1] C. Cossu, L. Brandt. On Tollmien-Schlichting-like waves in streaky boundary layers. *Eur J Mech B/Fluids*, 23(6):815, 2004.

[2] J. H. M. Fransson, A. Talamelli, B. Luca and C. Cossu. Delaying transition to turbulence by a passive mechanism. *Phys Rev Lett*, 96(6):064501, 2006.

[3] T. M. Römer, K. A. Schulz, Y. Wu, C. Wenzel, and U. Rist. Delay of laminar–turbulent transition by counter–rotating cylindrical roughness elements in a laminar flat plate boundary layer. *Exp in Fluids*, 64(42), 2023.

[4] S. Shahinfar, S. S. Sattarzadeh, J. H. M. Fransson and A. Talamelli. Revival of Classical Vortex Generators Now for Transition Delay *Phys Rev Lett*, 109(7):074501, 2012.

[5] Y. Wu, A. G. Axtmann and U. Rist. Linear stability analysis of a boundary layer with rotating wall–normal cylindrical roughness elements. *J Fluid Mech*, 915:A132, 2021.

Mitteilung

Fachgruppe: Turbulenz und Transition

Compressibility Effects on Drag Reduction in Turbulent Boundary Layers through Spanwise Traveling Waves

Xiao Shao, Matthias Meinke, Wolfgang Schröder
[1]Institute of Aerodynamics and Chair of Fluid Mechanics, RWTH Aachen University, Wüllnerstr. 5a, 52062 Aachen, Germany
E-Mail: X.Shao@aia.rwth-aachen.de

Turbulent boundary layer drag reduction plays a vital role in mitigating energy requirements in high Reynolds number flows. Various drag reduction techniques have been developed in the past to reduce friction drag. In addition to passive drag reduction techniques such as riblets, active techniques that involve control systems offer the advantage of adjustable actuation parameters according to the prevailing flow conditions. Since active methods require external energy input, they are not only evaluated based on the drag reduction but also on the achievable net power savings, which is a crucial parameter for assessing the flow control efficiency. One particularly promising approach in active flow control is the utilization of spanwise traveling waves (STW) with wall deformation. Extensive research [1-4] has demonstrated the efficacy of STW in controlling near-wall turbulent structures and reducing viscous drag. However, a majority of these investigations have been limited to incompressible or low Mach number turbulent boundary layers. In practical scenarios, high-speed transportation vehicles such as aircraft operate under compressible flow conditions. Therefore, this project is dedicated to a comprehensive understanding of the influence of compressibility on the efficiency of drag reduction (Δc_d) and net power saving (ΔP_{net}) for compressible, turbulent flat plate flow.

Turbulence scale-resolving numerical simulations for actively controlled turbulent boundary layer flow are conducted by using the multiphysics software framework m-AIA, which is continuously developed at the Institute of Aerodynamics of RWTH Aachen University. Further details on the numerical method, boundary conditions, and the validation for active control simulations can be found in studies for flat plate TBL flows [2, 4] and turbulent airfoil flows [1, 3].

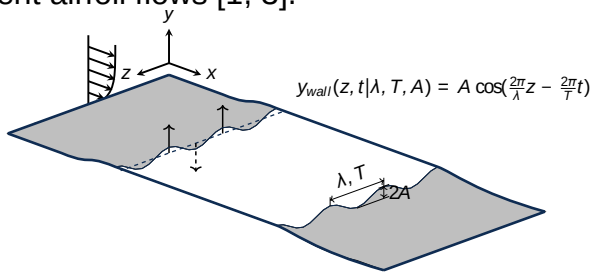

Fig. 1 Schematic of span wise actuation for turbulent flat plate flow. The STW are characterized by the actuation parameters wave length λ, amplitude A, and time period T.

The setup for the actuated turbulent boundary layer, as depicted in Fig. 1, can be conceptualized as an energy system. When compared to non-actuated flow, the generation of spanwise traveling waves incurs an additional cost in terms of power needed to induce the vertical surface motion. ΔP_{net} represents the difference between the effective power saving due to the reduced viscous drag Δc_d and the power input required for STW excitation ($P_{control}$). True energy savings are achieved when the viscous drag reduction exceeds the power required for the surface actuation.

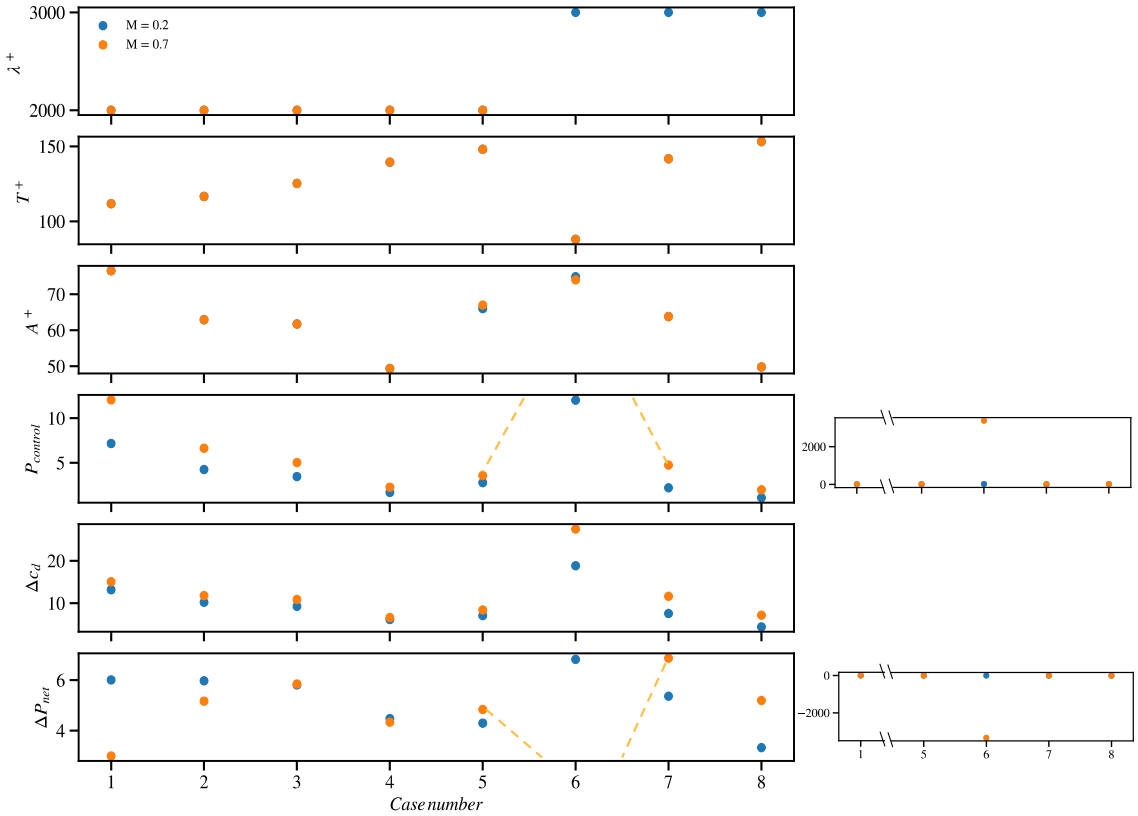

Fig. 2 Results for $P_{control}$, Δc_d, and ΔP_{net} versus inner scale actuation parameters (λ^+, T^+, A^+) for $M = 0.2$ and $M = 0.7$, where $\lambda^+ = \lambda\, u_\tau/\nu$, $T^+ = T\, u_\tau^2/\nu$ and $A^+ = A\, u_\tau/\nu$.

The effects of the STW actuation on the turbulent boundary layers at subsonic, i.e., $M_{inlfow} = 0.2$ and transonic, i.e., $M_{inlfow} = 0.7$ (for which the local Mach number reaches 1 for actuation cases) Mach numbers are considered. Latin hypercube sampling is employed to obtain parameters settings within the predefined range of actuation parameters determined from the incompressible cases in [2]. Sixteen cases were simulated, comprising eight sets of distinct actuation parameters, each corresponding to two different Mach numbers, as shown in Fig. 2. The comparison of the low Mach number results with those for the transonic cases, shows that $P_{control}$ for the transonic flow is consistently higher, but also show larger drag reduction Δc_d. However, the net power saving ΔP_{net} does not always follow the pattern of $P_{control}$, especially in the case 6 which employs the smallest T^+. Case 6 exhibits the highest $P_{control}$, Δc_d and ΔP_{net} at $M = 0.2$, while it yields a notably large negative ΔP_{net} at $M = 0.7$, which is obviously caused by the effect of flow compressibility. Detailed analysis of the turbulence statistics, turbulent flow structures, and multivariate empirical mode decomposition to investigate the influence of compressibility on this STW excitation method will be presented in the conference presentation.

[1] Albers M, Meysonnat P S, Schröder W. Actively reduced airfoil drag by transversal surface waves[J]. Flow, Turbulence and Combustion, 2019, 102: 865-886.
[2] Albers M, Meysonnat P S, Fernex D, et al. Drag reduction and energy saving by spanwise traveling transversal surface waves for flat plate flow[J]. Flow, Turbulence and Combustion, 2020, 105(1): 125-157.
[3] Albers M, Schröder W. Lower drag and higher lift for turbulent airfoil flow by moving surfaces[J]. International Journal of Heat and Fluid Flow, 2021, 88: 108770.
[4] Mäteling E, Albers M, Schröder W. How spanwise travelling transversal surface waves change the near-wall flow[J]. Journal of Fluid Mechanics, 2023, 957: A30.

Mitteilung

Fachgruppe: Turbulenz und Transition

Numerical modeling and simulation of two-phase internal flow instabilities using Smoothed Particle Hydrodynamics (SPH)

Rishindra Vallem Marten Klein Heiko Schmidt

Lehrstuhl Numerische Strömungs- und Gasdynamik, Brandenburgische Technische Universität (BTU) Cottbus-Senftenberg, Siemens-Halske-Ring 15A, D-03046 Cottbus
marten.klein@b-tu.de

Various engineering applications exhibit complex internal two-phase flows. Some relevant examples are found in aviation in cases where lubrication and cooling needs to be provided by a single but robust system that should also be lightweight. Air inclusions in oil supply lines, however, give rise to intricate flow dynamics that pose an enormous challenge to numerical modeling of shaft bearings or electric motors, among other cases. Smoothed Particle Hydrodynamics (SPH) offers a numerically efficient treatment of such two-phase flows [1]. SPH has demonstrated advantages in modeling highly dispersed flows, but has also been applied to non-dispersed cases [2]. However, the qualitative and quantitative capturing of interfacial instabilities in non-dispersed flows are not yet generally established [3].

In this study, a stratified two-dimensional internal liquid-gas flow is investigated as a canonical problem for flows occurring in oil supply lines. These applications show uniform stratified flow, wavy flow, elongated bubble flow, and slug flow regimes [4,5,6]. The latter two exhibit multiscale features due to emerging turbulence and break-up of the interface. Slug flow is of high technical relevance due to violent fluctuations in mass flow rate, pressure, and temperature, which is undesirable [7]. Despite the overall complexity of the flow, the primary mechanism is given by a developing Kelvin–Helmholtz instability (KHI). Capturing of the linear and non-linear growth of the KHI is hence a crucial aspect for modeling. The commercial SPH software *PreonLab*® is used to assess the capabilities of SPH within a user-friendly tool.

Figure 1 shows a sketch of the two-dimensional KHI set-up investigated. An incompressible SPH formulation, the so-called density-invariant SPH approach (ISPH–DI) [8], is adopted. Previous KHI studies performed with SPH were conducted at low density ratios, $\rho_1 / \rho_2 \leq 10$ [9,10], which contrasts air-water (air-oil) flows with $\rho_1 / \rho_2 \approx 800$. The flow is characterized by the Richardson number *Ri*, which is defined as the ratio of stabilizing buoyancy and surface tension effects to destabilizing velocity shear. First, a reduced KHI case was set up for $\rho_1 / \rho_2 = 2$ and then a more complex one for $\rho_1 / \rho_2 = 800$. The initial density profile $\rho_0(y)$ is discontinuous, while a smooth hyperbolic tangent profile is prescribed for the streamwise velocity $U_0(y)$. The bulk velocity difference is $\Delta U = U_1 - U_2 = 1$ m/s. The sinusoidal velocity perturbation $V_0(x,y) = A \sin(kx) \exp(-y^2/c^2)$ is prescribed at the interface location $y = 0$ m. The shear instability is seeded with the amplitude $A = 0.01\ \Delta U$, the layer width $c = 0.2$ m, and the wavenumber $k = 2\pi$ m^{-1}.

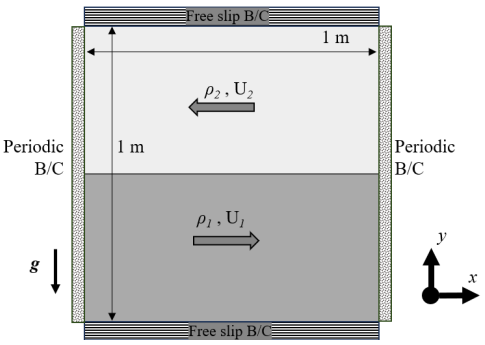

Figure 1: Sketch of the KHI set-up

Figure 3 shows the temporal evolution of the KHI in SPH for a low-density-ratio case. The dimensionless time is $t^* = t\ \Delta U / (2\lambda)$, where $\lambda = 2\pi / k$ is the wavelength. The flow evolution is quantitatively analyzed by the growth rate in the linear regime, where the linear stability theory (LST) applies, and in the nonlinear (turbulent) flow regime, in which self-similarity properties of the horizontally averaged mean streamwise velocity profiles $\bar{U}(y,t)$ are investigated. Next, Figure 4 shows the SPH simulation of the growth rate of the KHI for the prescribed

$V_0(x,y)$. A clear exponential growth can be observed in accordance with the LST. The growth rate itself is slightly smaller in the numerical simulations in line with other studies [10,11]. The nonlinear regime sets in at approximately $t^* = 2$. Last, Figure 5 shows the SPH mean streamwise velocity profiles transformed into similarity coordinates. The momentary mean streamwise velocity $\bar{U}(y,t)$ is obtained by horizontal averaging of the momentary flow solution. Self-similarity properties are assessed by similarity coordinates $\bar{U} / \Delta U$ and ξ such that $\bar{U} / \Delta U = f(\xi)$. ξ ranges from –0.5 to +0.5 between the locations where the bulk mean velocity $\bar{U}(y)$ ranges from $(U_1 - 0.1\,\Delta U)$ to $(U_1 - 0.9\,\Delta U)$. The simulation results collapse for large t^* demonstrating that the SPH approach is able to capture the statistical mean state evolution for a shear-dominated ($Ri = 0$), low-density-ratio case. For the high-density-ratio case, and including gravity and surface tension, Ri was varied from 0.3 (unstable) to 2 (stable). Instabilities started to grow out of bounds for $Ri < 1$, whereas the instability ceased for $Ri > 1$. These results agree with theory.

In the contribution to the STAB workshop, the KHI results will be analyzed more comprehensively and compared with LST and reference data, including a landscape of growth rates. Grid resolution effects will be discussed to some extend with respect to the particle cover and a given SPH kernel. Last, preliminary results towards the simulation of slug flow in channels will also be presented. Forthcoming research is devoted to extending the case set-up to three-dimensional transient flow in a channel with lateral inflow/outflow boundary conditions.

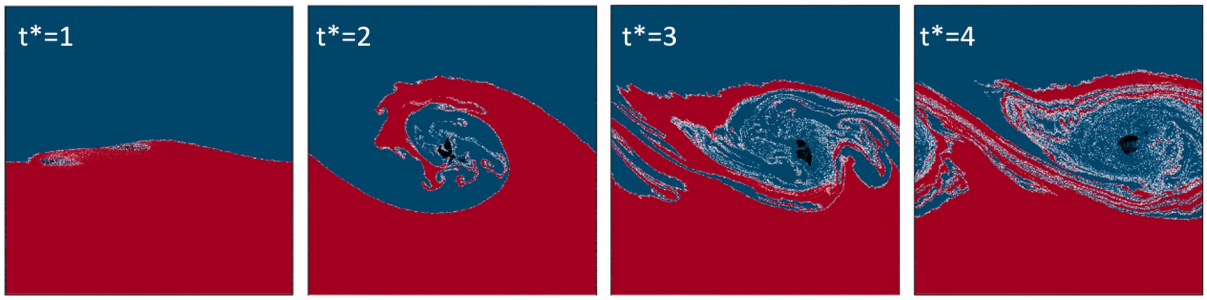

Figure 1: SPH simulation of the temporal evolution of the KHI at $Ri = 0$ and $\rho_1 / \rho_2 = 2$ showing ρ_1 in red, and ρ_2 in blue. The interface is white. Regions with insufficient SPH particle density are black.

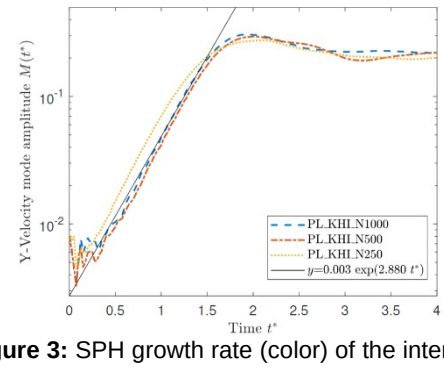

Figure 3: SPH growth rate (color) of the interfacial V velocity in comparison to LST (black) using N = 250, 500, 1000 SPH particles along each axis.

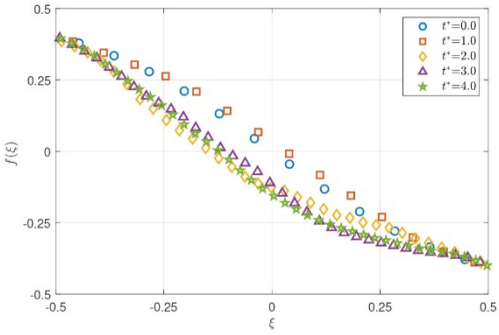

Figure 4: Normalized mean streamwise velocity $f(\xi)$ as function of the vertical similarity coordinate ξ for various non-dimensional times t^*.

References

[1] Monaghan, J. J. (1992). *Annu. Rev. Astron. Astrophys.* **30**:543–574
[2] Wang, Z. B., Chen, R., Wang, H., Liao, Q., Zhu, X. & Li, S. Z. (2016). *Appl. Math. Model.* **40**:9625–9655.
[3] Douillet-Grellier, T., De Vuyst, F., Calandra, H. & Ricoux, P. (2018). *Comput. Fluids* **177**:101–122.
[4] Taitel, Y. & Dukler, A. E. (1976). *AIChE J.* **22**:47–55.
[5] Vallée, C., Höhne, T., Prasser, H. M. & Sühnel, T. (2007). *FZD Tech. Rep. 485,* TU Dresden, Germany.
[6] Lu, M. (2015). *Experimental and computational study of two-phase slug flow.* PhD thesis, Imperial College, London, UK.
[7] Pedersen, S., Durdevic, P., & Yang, Z. (2017). *Int. J. Multiphase Flow* **88**:270–284.
[8] Shao, S. & Lo, E. Y. (2003). *Adv. Water Res.* **26**:787–800.
[9] Shadloo, M. S. & Yildiz, M. (2011). *Int. J. Num. Methods Eng.* **87:**988–1006.
[10] Tricco, T. S. (2019). *Mon. Not. Royal Astronom. Soc.* **488**:5210–5224.
[11] Berlok, T. & Pfrommer, C. (2019). *Mon. Not. Royal Astronom. Soc.* **485**:908–923.

Mitteilung

Fachgruppe: Turbulenz und Transition

Sensitivity study of Richardson number in flows with mean-streamline curvature

Srinivas L. Vellala and Tobias Knopp
DLR, Institut für Aerodynamik und Strömungstechnik,
Bunsenstraße 10, 37073 Göttingen, laxmi.vellala@dlr.de

Flows with significant mean-streamline curvature effects are relevant in many applications, e.g., the curved wake flows above the flap of a high-lift system and vortical flows around delta-wing type configurations. In such flows, mean-streamline curvature is known to cause considerable changes in the turbulence structure of shear layers. [1] More insight into a quantification of effects of curvature is important for devising modifications to RANS turbulence models.

Previously, [2] explored a grid-point local and general formulation of the gradient Richardson number, which is used to characterize and quantify rotation and mean-streamline curvature effects in a fluid flow. Originally, Richardson number is a dimensionless number that describes the ratio of buoyancy to the flow shear. Bradshaw [1] suggested the gradient Ricardson number to characterize effects of rotation and curvature: $Ri_{Br} = 2S(S+1)$. Here S = $(U_\phi/r)/(\partial U_\phi/\partial r)$ is the ratio of curvature (U_ϕ/r) to shear. (Here U_ϕ is the circumferential velocity and r is the radial direction). The classical formulation was converted into a generalised formulation using grid-point local quantities such as vorticity $|\Omega|$, strain-rate |S| and directional information n_Ω , which is important to describe the sign of Ri for the amplification or damping of the turbulence due to curvature [2].

$$Ri_{Bradshaw} = \frac{2\left(\frac{U_\phi}{r}\right)\left(\frac{U_\phi}{r}+\frac{\partial U_\phi}{\partial r}\right)}{\left(\frac{\partial U_\phi}{\partial r}\right)^2} \rightarrow Ri_{local} = \frac{-n_\Omega|\Omega|\,(|S|-n_\Omega|\Omega|)}{\left(\frac{1}{2}|S|+\frac{1}{2}n_\Omega|\Omega|\right)^2}$$

[2] used the above formulation to study a U-duct test case (see Fig. 1). The present work extends [2] by an in-depth analysis of U-ducts with varying radius and thus changing the ratio of curvature to shear. This helps to understand the behaviour of Ri_{local} and n_Ω proposed by [2] for moderate to strong curvature.

Five cases of U-ducts with inner radius at the bend r as a function of half-channel height R from r = R/2 (strong curvature) to 20R (moderate curvature) were simulated using the DLR-TAU code with the negative Spalart-Almaras(SA-neg) turbulence model with 'SARC' rotational correction. Here, the inner wall of the bend acts as a convex wall $(U_\phi/r > 0, \partial U_\phi/\partial r > 0)$, where curvature and shear have the same sign, and the outer wall acts as a concave wall $(U_\phi/r > 0, \partial U_\phi/\partial r < 0)$, where curvature and shear have opposite sign. Note that, $\Omega_z(r) = U_\phi/r + \partial U_\phi/\partial r$ gives the distinction between convex and concave curvatures. A nondimensional parameter r_b introduced by Shur et al. [4] estimates convex and concave curvature regions accurately. This parameter is used in n_Ω to construct Ri_{local}.

Theoretically, Richardson number as a function of S forms a parabola. Ri < 0 occurs only when $-1 \leq S \leq 0$ (see Fig. 2). Curvature is destabilizing, when Ri < 0 and stabilizing, if Ri > 0. Hence, negative Ri amplifies turbulence and positive Ri suppresses turbulence.

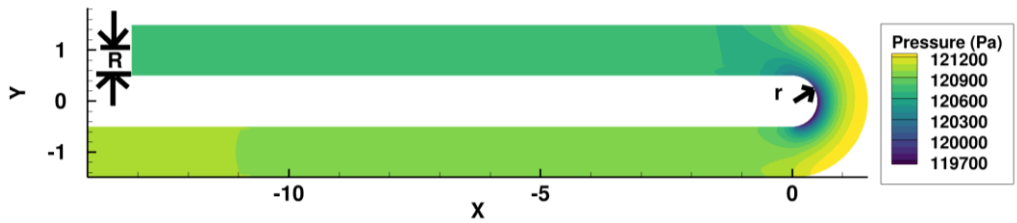

Figure 1: Pressure contours of U-turn test case with inner bend radius r = R.

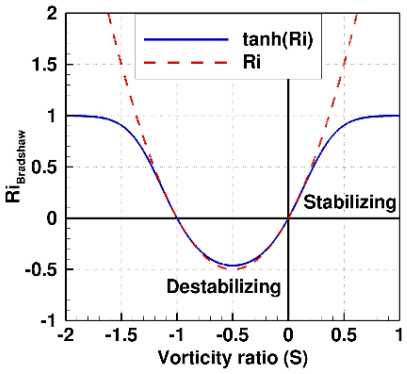

Figure 2: Behaviour of Richardson number showing stable/unstable zones.

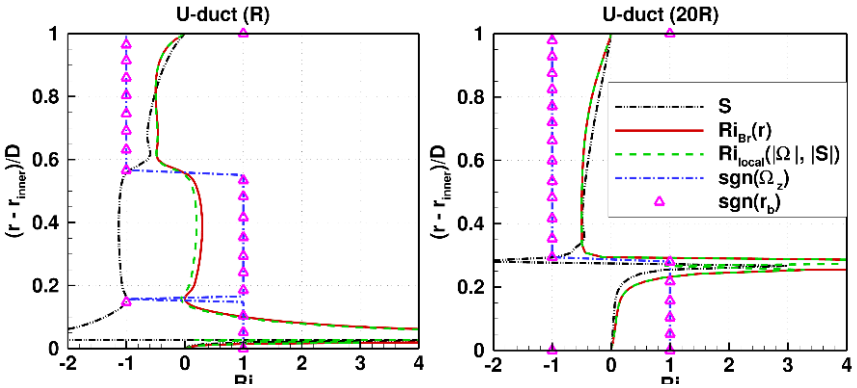

Figure 3: Spanwise line plots of Ri at the 90° bend for pipe with inner radii of the bend r = R (left), and r = 20R (right).

Figure 3 shows that non-dimensional parameter r_b captures the behaviour of $\Omega_z(r)$ very well. As a result, good agreement between Ri_{local} and $Ri_{Br}(r)$ can be observed. Here, Ri > 0 near the convex wall and Ri < 0 for the concave wall, as expected. Thus, convex curvature amplifies turbulence and concave curvature regions suppress turbulence.

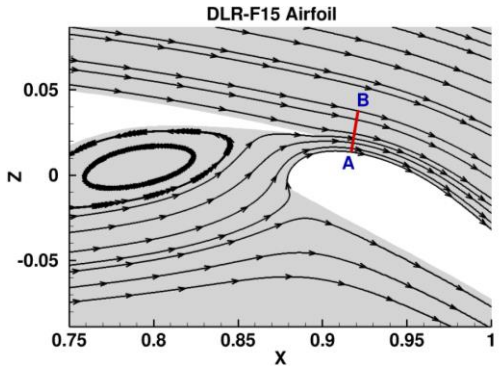

Figure 4: Streamlines around DLR F15 airfoil and line segment AB above the flap.

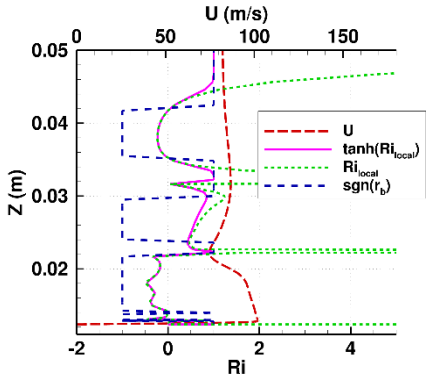

Figure 5: Horizontal velocity, local Ri on the wall-normal line segment AB above the flap.

Finally, the local Ri is applied to the curved wake flow around the DLR F15 airfoil (see Fig 4). The line segment AB on the flap covers the boundary layer of the flap, the wake flow of the main wing, and the jet emerging from the gap between main-wing and flap. Figure 5 shows that Ri_{local} and sgn(r_b) predict the regions of destabilizing and stabilizing flow correctly. Note that, in the regions with low shear or near the point where shear switches in sign, very high values of Ri are observed in figures 3 and 5. It is necessary to modify Ri to make it a quantitative tool to be used in further modelling of components of turbulence budget. As a remedy, a suitably calibrated hyperbolic tangent (tanh) function is used to deal with extreme values (see Figures 2 and 5), which is described in the final presentation.

Moreover, for the final presentation, the local Richardson number will be used to modify the production term of the length scale equation of the SSG/LRR-ω RSM, increasing/decreasing turbulence by a factor of around two in concave/convex regions respectively, analogous to magnitude of increase/decrease of the production term found from SA-RC.

References :

[1] Bradshaw, P., “The analogy between streamline curvature and buoyancy in turbulent shear flows,” Journal of Fluid Mechanics, Vol. 36, No. 177, 1969.

[2] Ströer, Philip, and Tobias Knopp. "General Formulation of the Gradient Richardson Number for RANS Modelling." AIAA SciTech 2023 Forum. AIAA paper 2023-1801, 2023.

[3] Durbin, Paul A. "Some recent developments in turbulence closure modeling." Annual Review of Fluid Mechanics Vol., 50, pp. 77-103, 2018.

[4] Shur, Michael L., Michael K. Strelets, Andrey K. Travin, and Philippe R. Spalart. "Turbulence modeling in rotating and curved channels: assessing the Spalart-Shur correction." AIAA journal Vol. 38, No. 5, pp. 784-792, 2000.

Mitteilung

Fachgruppe: Turbulenz und Transition

Near-wall dynamics of laminar separation bubbles at low inflow turbulence intensities

Tudor V. Venenciuc[1,*], Christian Klein[2], Rainer Hain[1], Christian J. Kähler[1]
1: Institute of Fluid Mechanics and Aerodynamics, University of the Bundeswehr Munich, Neubiberg 85577, Germany
2: Institute of Aerodynamics and Flow Technology, German Aerospace Center (DLR), Bunsenstraße 10, Göttingen 37073, Germany
* Correspondent author: tudor-victor.venenciuc@unibw.de

Laminar separation bubbles (LSB) form at aerodynamically low Reynolds numbers (Re_c) due to adverse pressure gradients that induce flow separation. In the free shear layer, the Kelvin-Helmholtz instability mechanism amplifies perturbations until their amplitudes reach such a high value that vortices are formed. The momentum entrainment of the transitional flow can force a reattachment. The unstable flow causes variations in drag, pitch and lift, which can be detrimental to the efficient operation of Unmanned Aerial Vehicles (UAV), gliders, and small to medium sized turbine blades. Studying the phenomenon experimentally is challenging, due to its relatively small size, surface curvature of foils and its sensitivity to chaotic or deterministic disturbances. Non-invasively analyzing an LSB from the near-wall perspective can be achieved by applying an artificial heat-flux on a surface and studying the footprints of coherent structures in the thermal field with infrared thermography or temperature sensitive paint (TSP), provided the natural convection does not greatly influence the flow. The aspect of the low bubble height and surface curvature can thus be circumvented and near-wall flow information can be accessed with a level of detail that can be provided only by numerical simulations.

The Tollmien-Schlichting and the Kelvin-Helmholtz instability behavior can be accurately predicted by solving the Orr-Sommerfeld equation or, in the case of inviscid flows, the Rayleigh equation (Schlichting and Gersten (2017)) up until the influence of the non-linear terms cannot be neglected anymore. The secondary instabilities that cause the degradation of the Kelvin-Helmholtz roll-up vortices can not only define the spanwise and streamwise vorticity content in the aft portion of an LSB but also that of the turbulent boundary layer (Zhang et al. (2009)). Which secondary instabilities are responsible for the coherent structure deformations has been shown to depend on the free-stream turbulence level (Jones et al. (2008)) and their influence is far more complicated to predict and must thus be simulated or experimentally analyzed. Although knowledge of the free-shear and higher regions of the boundary layer is abundant, most studies that provide detailed insight of the most complex near-wall flow mechanisms at low turbulence levels stem from numerical simulations. The purpose of the present study is to assess which coherent structures impact the surface of a foil in the low turbulence environment provided by a towing tank. An artificial heat flux is created by spraying electrically conductive paint onto a groove milled on the suction side of an SD 7003 foil (see figure 1). The thermal footprints are visualized by using Europium based TSP and the single-shot lifetime

method. The influence of the heat flux on the transition behavior is assessed using 2D2C-PIV to be nearly non-existent.

The experiments are conducted at Re_c=6·10^4 and 8·10^4 and an angle of attack of α=6°. The applied heating power at the lower Re_c is 1764 W/m^2 and 2545 W/m^2 at the higher. Spectral proper orthogonal decomposition (SPOD) analysis of the thermal fluctuations displays the footprints of the Kelvin-Helmholtz instabilities with temporary high levels of span-wise coherence (see figure 2). Instantaneous thermal snapshots display the propagation of simultaneously emerging V-shaped footprints in the stream-wise direction. Examples are depicted in figure 3. Some of the snapshots depict span-wise coherent footprints, which can only be assumed to be caused by Kelvin-Helmholtz vortices, in the same region as the V-shaped footprints, which implies that these are two distinct phenomena. Quasi-simultaneous PIV and TSP measurements confirm the assumption.

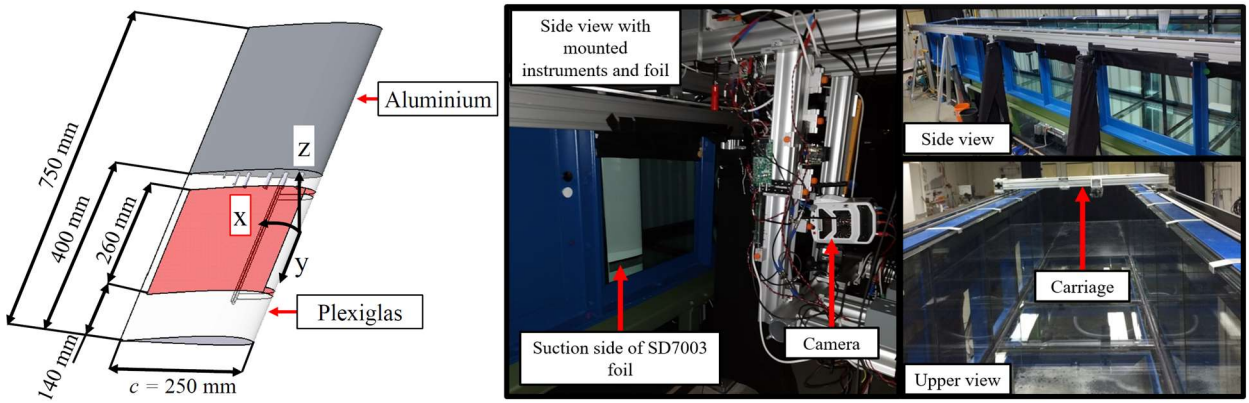

Figure 1. Left: CAD model of the SD-7003 foil equipped with the heating element (red region). Right: Images depicting the towing tank and the experimental setup for the TSP measurements. The foil is mounted vertically in the tank.

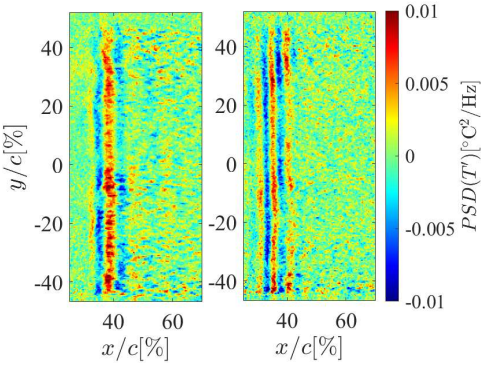

Figure 2. First SPOD mode spatial reconstruction at a frequency of 6.25 Hz at Re_c=6·10^4 (left) and 12.81 Hz at Re_c=8·10^4 (right)

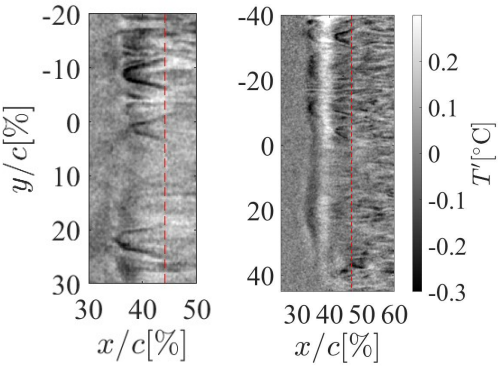

Figure 3. High-pass filtered temperature snapshots at Re_c=6·10^4 (left) and Re_c=8·10^4 (right). The red lines indicate the time averaged reattachment location

Jones L, Sandberg R, Sandham N (2008) Direct numerical simulations of forced and unforced separation bubbles on an airfoil at incidence. Journal of Fluid Mechanics 602:175–207.

Schlichting H, Gersten K (2017) Boundary-Layer Theory. Springer-Verlag, Berlin Heidelberg, ninth edition, 2017.

Zhang W, Hain R, Kähler C (2008) Scanning PIV investigation of the laminar separation bubble on a SD7003 airfoil. Experiments in Fluids 45, 725-743.

Mitteilung:
Fachgruppe: Versuchsanlagen

Comissioning of a Ludwieg tube at DLR Göttingen.

Qi Xuan Goh, Divek Surujhlal
DLR Göttingen, Bunsenstraße 10, Göttingen

The HHK4 is a Ludwieg tube that has been relocated from TU Dresden to DLR Göttingen and is currently being commissioned for sensor calibration and student work. A Ludwieg tube is a cheap and efficient device used to produce supersonic/hypersonic freestreams for aerodynamic ground testing [1]. The layout of the Ludwieg tube is shown in Figure 1. In the reservoir, the test gas is compressed to a high pressure. At the exit of the reservoir is a fast-acting valve which opens for a short amount of time. At the opening, test gas will be expanded through the converging-diverging nozzle with a throat cross sectional area A*, and into the test section of cross sectional area A_1. The Mach number of the freestream flow in the test section is governed by the area ratio A* / A_1. Simultaneously, at the opening of the valve, an expansion wave travels upstream in the reservoir, after which it will reflect at the end wall and travel downstream towards the nozzle again. Upon reaching the nozzle, the valve is closed. The duration for the valve to be open is given by t_{shot}, and is calculated using Equation 1, where L is the length of the reservoir and a_{tube} is the speed of sound in the reservoir.

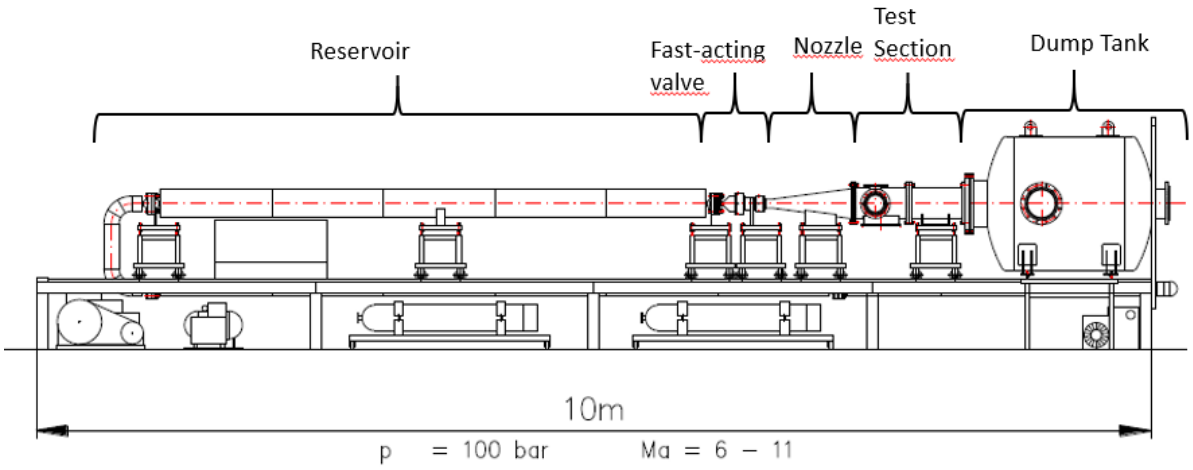

Figure 1: Schematic layout of the Ludwieg tube HHK 4

The reservoir of the HHK4 is 24 m in length and can withstand a reservoir pressure up to 100 bar and a reservoir temperature up to 1000 K. Similarly-constructed tunnels [2] were shown to produce a Reynolds number between $2{,}4 \times 10^5$/m and $5{,}8 \times 10^6$/m. Freestream Mach numbers in the range 6 – 11 can be produced with different nozzles, with an exit diameter of 250mm [3]. Compared to other well-known Ludwieg tubes, i.e, HDT in Oxford [4], BAM6QT in Purdue [5], HLB in Braunschweig [6] and the RWG in Göttingen [7] the HHK 4 has a rather small Reynolds number range, but a large range of total pressure and Mach numbers.

$$t_{shot} = \frac{2L}{a_{tube}} \tag{1}$$

As the free stream temperature T_∞ at the nozzle is expected to be around 40-50 K, the total temperature in the reservoir has to be adjusted accordingly. A high total temperature will have a disadvantage as it increases the speed of propagation of the expansion wave in the reservoir, resulting in a shorter test time. As seen below, a lower Mach number requires a lower total temperature, meaning a longer test time to collect more data. (Figure 2).

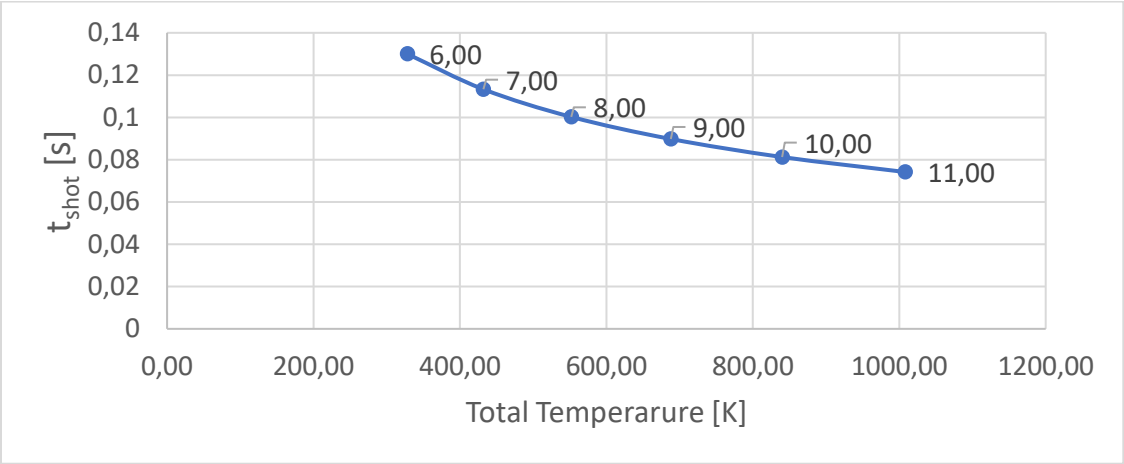

Figure 2: Reservoir total temperature plotted against the resulting t_{shot}. Freestream Mach numbers are labelled at each datapoint.

The free stream pressure at the test section should be able to be measured and a calibration rake consisting of pitot pressure probes is in the design phase. The calibration rake will be mounted in the test section, so the pitot pressure along horizontal and vertical axes of the nozzle can be measured. By November, it is expected that the Ludwieg tube be functioning and able to produce some preliminary data.

References

[1] Tropea C, L. Yarin A, F. Foss J. Springer handbook of experimental fluid mechanics. Berlin: Springer; 2007.

[2] Friehmelt H, Koppenwallner G, Mueller-Eigner R. Calibration and first results of a redesigned Ludwieg expansion tube. In: 5th International Aerospace Planes and Hypersonics Technologies Conference. Reston, Virigina: American Institute of Aeronautics and Astronautics; 1993.

[3] Müller-Eigner R. Betriebsanleitung HHK 4.

[4] Wylie S, Doherty L, McGilvray M. Commissioning of the Oxford High Density Tunnel(HDT) for Boundary Layer Stability Measurements at Mach 7.

[5] C. Berridge D, A.C. Ward C, P:K: Luersen R, Chou A, D. Abney A, P.Schneider S. Boundary-Layer Instability Measurements in a Mach 6 Quiet Tunnel.

[6] Estorf M., Wolf T., Radespiel R. Experimental and numerical investigations on the operation of the Hypersonic Ludwieg Tube Braunschweig.

[7] Ludwieg, Hubert, Th. Hottner and Helmut Grauer-Carstensen. “Der Rohrwindkanal der Aerodynamischen Versuchsanstalt Goettingen (The Ludwig-Tube (Wind Tunnel) of the Gottingen Aerodynamic Facility)” (1969).

Mitteilung

Projektgruppe/Fachkreis: Windenergie

Automatic Reconstruction of the Measured Surface of Wind Turbine Blades from the WindForS Complex Terrain Testfield on the Albtrauf for CFD Modeling

L. Gagnon, T. Lutz
Universität Stuttgart, Institut für Aerodynamik und Gasdynamik
70569 Stuttgart, gagnon@iag.uni-stuttgart.de

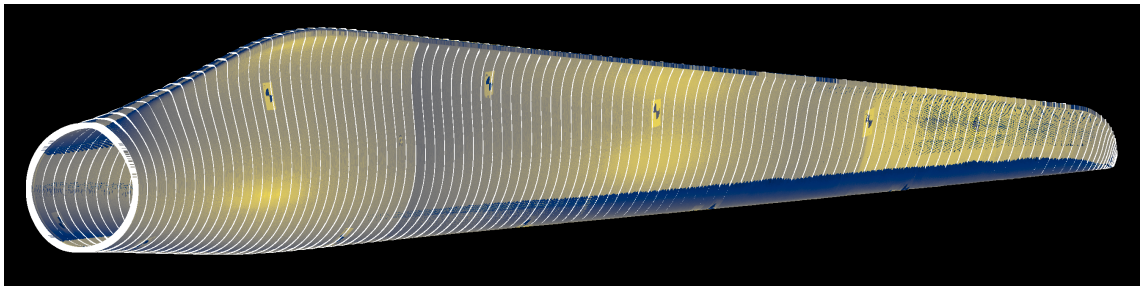

Abstract: The WindForS complex terrain test field on the Albtrauf is equipped with two research wind turbines. It serves as the basis for the WINSENTvalid project for which the work presented here is carried out. WINSENTvalid aims to validate the numerical methods [1, 2] developed in the previous project WINSENT using data collected from these turbines. As a result, state-of-the-art models for complex terrain wind energy site flow modeling and wind turbine design will be improved. As IAG focuses on high-fidelity CFD tool validation using the WindForS test field sensor data, detailed analysis of 3D turbine blade geometries is critical to this validation. These geometries, coupled with meteorological mast data, facilitate the identification of modeling inaccuracies. They will be used in comprehensive turbine simulations that include forest, terrain, and structural models. Investigations of various environmental factors will provide insight into turbine efficiency, wake length, and loading.

For this study, the three blades of a wind turbine were scanned with a Leica ScanStation P20 while lying on the ground in light wind conditions. Due to site constraints and equipment availability, multiple scans per blade were required. The individual scan boundaries can be seen by the jumps in the colors of the intensity field (variation in the returned signal strength from the scanned surfaces) in the figure above. These scans were then aligned using a combination of methods to ensure alignment first in 3D and then for individual blade slices.

Beyond the overall goals of the WINSENTvalid project, this work focuses on the accurate reconstruction of the wind turbine blade surface mesh. The goal was to obtain the blade geometries as cross-sections along the spanwise direction of the blade, while minimizing errors due to the scanning process, alignment discrepancies, and varying spanwise point positions on each blade.

The 3D point clouds underwent an initial cleaning based on specified criteria. A custom Python class was developed to manage the 3D point clouds. It creates a curve for each cloud slice using a savgol-filtered airfoil [3] and then iteratively realigns the clouds. Subsequent 2D splines (created by a least-squares fit with smoothing) use a consistent knot distribution in parametric space to ensure consistency of the subsequent 3D alignment.

The control points of these 2D splines were then 3D-smoothed by distributing their control points on another smoothed spline, this time in the spanwise direction. Leading and trailing blade edges were determined based on curvature peaks, which were then spanwise-smoothed before being used as input in subsequent runs of the cloud slicing and smoothing algorithm. The specific methodological details are omitted for brevity and the resulting point distribution of the surface mesh were shown in the first figure.
Of the 108 profiles that were automatically generated from the scan, Fig. 1 shows segment 32, when starting from the root. The differences between the subsampled cloud (which was slightly filtered to minimize spanwise discrepancies) and the 3D smoothed airfoil are shown along with the pressure coefficient distribution on the airfoil, which was computed using nonviscous XFOIL. The robustness of the Python class allowed to avoid blade-specific parameter adjustments for the 3 blades of the turbine, which had small geometrical differences and non-negligible differences in the number of cloud points. The URANS simulation of the single 3D wind turbine blade in rotation is presented and the effects of smoothing and its parameters are analyzed.

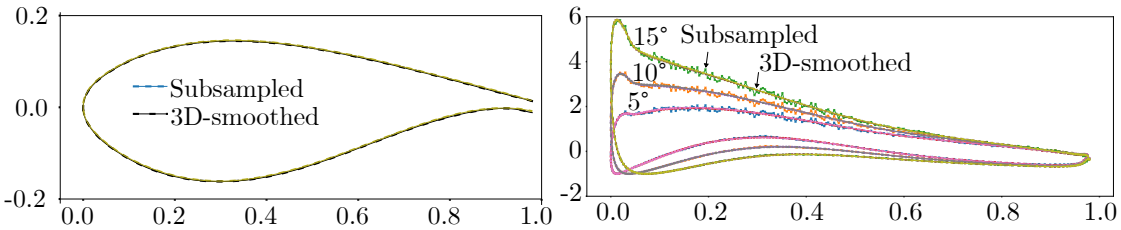

Figure 1: Blade segment 32 of 108. Left: Subsampled and 3D-smoothed airfoils. Right: Pressure distribution on subsampled and 3D-smoothed airfoils at different angles of attack.

While every effort has been made to match actual blade geometries, the resolution of the mesh (based on standard URANS meshing guidelines) is inherently variable across the blade span. Small variations on the blade surface, whether due to design details or subsequent modifications, are not retained individually. Instead, they are incorporated as an influence on the averaged and smoothed point distribution. Nevertheless, this work highlights the nature of the differences between the designed and built blade geometries. It also evaluates the impact of these differences on the aerodynamic properties of the wind turbines as evaluated by the URANS CFD models, and the potential cost in accuracy resulting from neglecting them.

The authors gratefully acknowledge the funding of the project WINSENTvalid (code no. 03EE2048C) by the German Federal Ministry for Economic Affairs and Climate Action (BMWK).

References

[1] G. Guma, P. Bucher, P. Letzgus, T. Lutz, and R. Wüchner. High-fidelity aeroelastic analyses of wind turbines in complex terrain: fluid–structure interaction and aerodynamic modeling. *Wind Energy Science*, 7(4):1421–1439, 2022.

[2] P. Letzgus, G. Guma, and T. Lutz. Computational fluid dynamics studies on wind turbine interactions with the turbulent local flow field influenced by complex topography and thermal stratification. *Wind Energy Science*, 7(4):1551–1573, 2022.

[3] A. Savitzky, and M. J. E. Golay. Smoothing and Differentiation of Data by Simplified Least Squares Procedures. *Analytical Chemistry*, 36(8):1627–1639, 1964.

Mitteilung

Fachgruppe: Windenergie

Vorhersage der Lärmreduktion durch Grenzschichtabsaugung
an Windenergieanlagen

Sabrina Haubold, Thorsten Lutz, Andrea Beck
Institut für Aerodynamik und Gasdynamik, Universität Stuttgart
Pfaffenwaldring 21, 70569 Stuttgart
sabrina.haubold@iag.uni-stuttgart.de

Einer der limitierenden Faktoren für die Ausweitung der Stromversorgung durch Windenergie ist der strömungsbedingte Lärm, der an den Anlagen entsteht. Die Notwendigkeit der Einhaltung von Lärmgrenzwerten wirkt sowohl einschränkend auf die Standortwahl als auch auf den Betrieb bei unterschiedlichen Wetterbedingungen. Daher ist das Interesse an Möglichkeiten zur Schallabminderung mit verhältnismäßig geringen Einbußen in der Effizienz nach wie vor groß. Ziel ist hierbei vor allem, eine der dominanten aeroakustischen Quellen, den Hinterkantenschall, zu reduzieren. Dieser entsteht aufgrund einer Streuung von turbulenten Druckfluktuationen innerhalb der Grenzschicht in Schallwellen beim Überschreiten der scharfen Profilhinterkante. Ein Nachteil von passiven Maßnahmen wie Serrations ist, dass sie oft nur für ihren Auslegungspunkt die optimale Lärmreduktion erreichen können und ihre Effektivität unter anderen Betriebsbedingungen abgemindert wird. Da eine Windenergieanlage jedoch während ihrer Laufzeit einem breiten Spektrum an Umgebungsbedingungen ausgesetzt ist, macht dies die Attraktivität von aktiven Maßnahmen aus, welche eine gewisse Regelbarkeit mit sich bringen.
Aktive Maßnahmen arbeiten mit dem Einbringen oder Entziehen von Energie aus der Strömung, zum Beispiel in Form von Ausblasung oder Absaugung an der Profiloberfläche. Für den Aspekt der Schallreduktion ist vor allem die Beeinflussung der Profilgrenzschicht stromauf der Hinterkante relevant. Das Breitbandspektrum der Hinterkantenschallquelle steht im Verhältnis zu der turbulenten kinetischen Energie, sowie den turbulenten Längenskalen in der Grenzschicht. Die abgestrahlte Frequenz einer turbulenten Struktur ist höher, je kleiner sie und je höher ihre Konvektionsgeschwindigkeit ist. Die niedrigsten Frequenzen im Schallspektrum entstehen dementsprechend an den größten und langsam strömenden Strukturen. Da die größten Wirbel in der Grenzschicht den größten Teil der turbulenten kinetischen Energie in sich tragen, besitzt das Schallspektrum dort sein Maximum. Durch eine aktive Beeinflussung der turbulenten Grenzschicht kann also direkt der aeroakustische Quellmechanismus modifiziert werden.

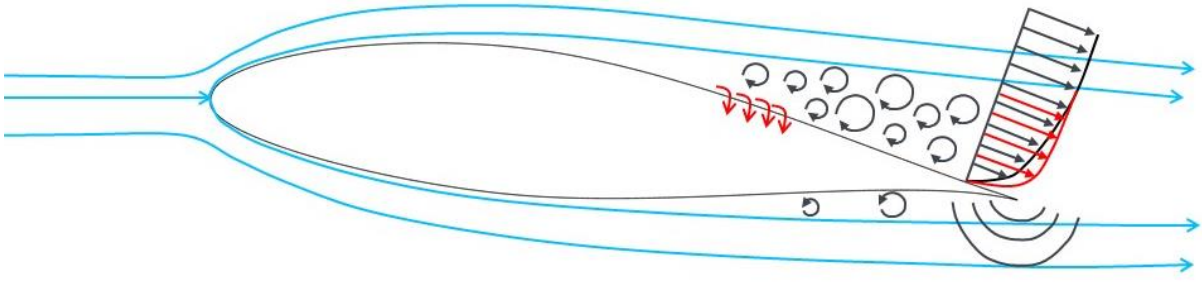

Abb. 1: Prinzip der Hinterkantenschallabminderung mittels Grenzschichtbeeinflussung durch Absaugung

In dieser Arbeit wird eine flächige Grenzschichtabsaugung durch ein poröses Blech betrachtet. Die Absaugung stromauf der Hinterkante reduziert dabei die Grenzschichtdicke und verhindert Strömungsablösungen, wodurch die integrale Längenskala in der turbulenten Grenzschicht reduziert wird. Außerdem besitzt die Grenzschicht nach der Absaugung eine geringere turbulente kinetische Energie, was sich auf die maximalen Schalldruckpegel im Hinterkantenlärmspektrum auswirkt. Gleichzeitig ergeben sich höhere Konvektionsgeschwin-digkeiten

nahe der Wand, welche eine Verschiebung im Spektrum in Richtung höherer Frequenzen erzeugen. Diese Verschiebung ist vorteilhaft, da höherfrequente Schallsignale aufgrund von atmosphärischer Dämpfung mit der Distanz von der Quelle schneller abklingen. Ein positiver Nebeneffekt der Absaugung ist eine Verbesserung der aerodynamischen Güte aufgrund der Widerstandsreduktion, was einen gewissen Teil der für die Absaugung zusätzlich benötigten Leistung ausgleichen kann.
Für die Auslegung einer solchen Grenzschichtabsaugung ist es nötig, zuverlässige und dennoch recheneffiziente Vorhersagetools zur Verfügung zu haben. Eine hybride Methode mittels des semi-empirischen TNO-Modells nach Blake [1] und Parchen [2] besitzt in dieser Hinsicht gute Eigenschaften. Hier wird aus den RANS gemittelten Turbulenzdaten und einigen empirischen Parametern ein Spektrum der Wanddruckfluktuationen berechnet, welches die aeroakustische Quelle darstellt. Die Schallausbreitung wird in diesem Modell ebenfalls über eine analytische Gleichung ermittelt, wodurch die Vorhersage gegenüber einer CAA Rechnung deutlich schneller ausfällt. Für das grundlegende TNO-Modell wurden bereits viele Erweiterungen und Verbesserungen entwickelt, um die Genauigkeit der Vorhersage und Anwendbarkeit für unterschiedliche Fälle zu erhöhen. Eine vor kurzem von Hornung [3] entwickelte Erweiterung ermöglicht eine bessere Vorhersage der Erhöhung des Hinterkantenschalls durch ansteigende Anstellwinkel und beginnende Strömungsablösung.
In dem IAGNoise+ Vorhersagetool, basierend auf der Arbeit von Kamruzzaman [4], sind sowohl das ursprüngliche TNO-Modell, als auch die neue erweiterte Version implementiert. Da die hier betrachtete Grenzschichtabsaugung auf die gleichen Mechanismen Einfluss nimmt, welche für die Schallzunahme durch höhere Anstellwinkel verantwortlich sind, wäre auch für die Vorhersage dieser Schallminderungsmaßnahme eine erhebliche Verbesserung zu erwarten. Diese These wurde im Vergleich mit Windkanalergebnissen für ein NACA64$_3$418 mit und ohne Grenzschichtabsaugung verifiziert und die Ergebnisse zeigen gute Vorhersagequalitäten des Tools in seiner aktuellen Iteration [5]. Anschließend daran werden Ergebnisse von Large Eddy Simulationen vorgestellt, welche einen tieferen Einblick in die Strömungsphysik bieten und die noch sichtbaren Abweichungen in der Vorhersage erklären sollen.

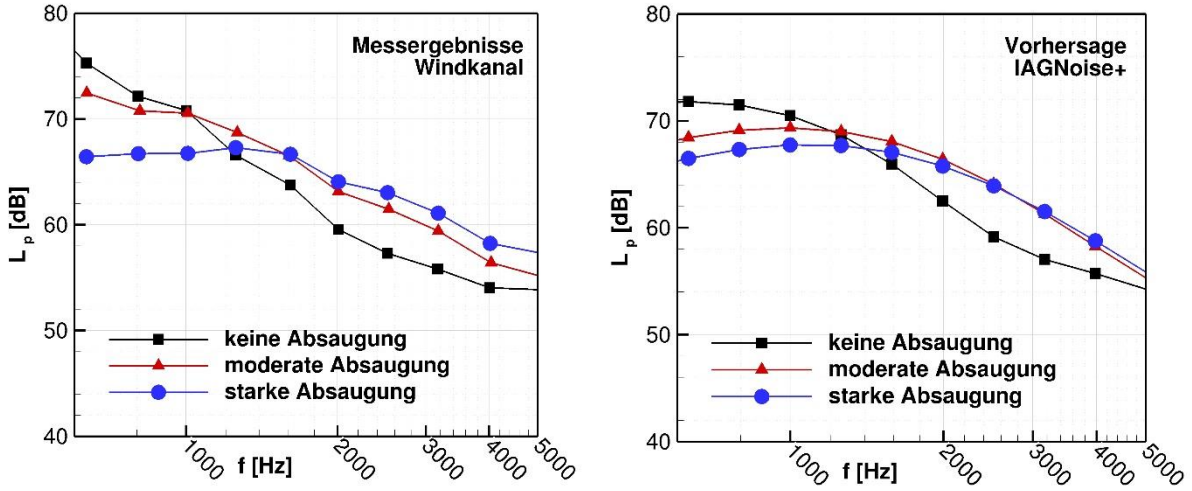

Abb. 2: Absaugungseinfluss auf Hinterkantenschallspektrum eines NACA 64$_3$-418 Profils bei α=6°, Windkanalmessung (links) vs. RANS-TNO-basierte Vorhersage mit IAGNoise+ (rechts) veröffentlicht in [5].

Literatur :

[1] W.K. Blake, Mechanics of flow-induced sound and vibration, Vol. I and II, in Applied Mathematics and Mechanics, Academic Press, 1986, http://dx.doi.org/10.1121/1.396227.
[2] R. Parchen, “Progress report DRAW: a prediction scheme for trailing edge noise based on detailed boundary layer characteristics”, Delft: TNO Institute of Applied Physics, 1998.
[3] C. Hornung, T. Lutz, E. Krämer: "A model to include turbulence-turbulence interaction in the prediction of trailing edge far field noise for high angles of attack or slightly separated flow", Journal of Renewable Energy, 136, 945–954, 2019. doi: http://doi.org/10.1016/j.renene.2018.12.093.
[4] M. Kamruzzaman, D. Bekiropoulos, A. Wolf, T. Lutz, E. Krämer, Rnoise: a RANS based airfoil trailing-edge noise prediction model, AIAA Conf. (2014) 1e22, https://doi.org/10.2514/6.2014-3305.
[5] S. Haubold, F. Seel, T. Lutz, A. Beck and E. Krämer, “Study on the Capabilities of a TNO-Based Trailing Edge Noise Prediction Tool Applied to Boundary Layer Suction on a NACA 64-418 Airfoil,” , Proceedings of the 10th International Conference on Wind Turbine Noise, Dublin, 2023.

Mitteilung

Fachgruppe: Wind Energy

Wall Pressure of Separated Flows: Flat Plate and Airfoil

Arnaud Le Floc'h, Alexandre Suryadi, Michaela Herr
DLR Institute of Aerodynamics and Flow Technology, Department of Wind Energy
Lilienthalplatz 7, 38108 Braunschweig, Germany
arnaud.lefloch@dlr.de, alexandre.suryadi@dlr.de, michaela.herr@dlr.de

When almost a third of the electricity produced in Germany already comes from wind energy, and with the target of 2030 to develop it into a leading contributor in the energy mix (More & Murray, 2023), development of a larger capacity productions using wind power is a priority. Facing on-site environmental conditions, it is necessary to improve the performance and reliability of wind turbines from the design-chain standpoint and the operational standpoint with the use of on-board sensors and AI-lead real time monitoring.

One of the environmental conditions is the proximity of wind parks near residential areas need to comply with the noise regulations. With poor design and imprecise monitoring, the flow may separate from the blade's surface, reducing the wind turbine's efficiency and amplifying its noise emission. Therefore, tracking flow separation on wind turbine blades is thus essential not only aerodynamically but also acoustically. The first step in tracking flow separation is to better understand the physics of separated flows and the mechanisms driving the wall-pressure fluctuations beneath a separating turbulent boundary layer. In this study we aim to derive the flow separation topology from wall-pressure measurements. One of the reasons behind this is practicability. Wall pressure sensors are easily mountable on a wind turbine blade and are relatively nonobstructive to the boundary layer.

Two databases are available for the present study. (1) The velocity field of a family of turbulent separation bubbles was recently measured using 2D-2C PIV in the boundary layer wind tunnel of ÉTS Montréal-University of Québec (Le Floc'h, 2021). Three distinct turbulent separation bubbles were investigated at $Re_\theta = 5000$: (a) Large with a 41 cm long recirculation region, (b) Medium, 11 cm long, and (c) Small with no backflow. (2) In investigating flow separation noise, the wall pressure of the DU96-W-180 was measured at the Acoustic Wind tunnel Braunschweig (AWB) at DLR-Braunschweig (Suryadi & Herr, 2015). The airfoil's angle of attack was set up to 14.7°, where massive flow separation has happened but the airfoils is still below the stall angle. Assuming the same phenomena can take place either near the trailing edge of an airfoil at high angle of attack or on a flat plate due to the presence of an adverse pressure gradient, then the same flow physics will produce the same results for both configurations. This paper investigates the relevant similarities of flow separation between the flat plate and the airfoil at high angle of attack.

Figure 1 depicts the two oil films for the Large TSB and the airfoil at an angle of attack of 12 degrees. The skewness of wall-pressure distributions associated with the oil films in Figure 1 are presented in Figure 2. Skewness is typically a measure of asymmetry of a probability density function. The skewness presented in Figure 2 is a measure of the length of each density function *tail*. Namely, the more predominant pressure sign will have a longer tail, which results in a larger skewness magnitude. Interestingly, the two skewness distributions indicate the same pattern near the separation region (highlighted region in Figure 2): a predominantly positive wall pressure fluctuation is subsequently followed by a negative one. Skewness was utilized in a study of flow separation of a linear compressor cascade, which links positive pressure fluctuations to separation onset (Zambonini & Ottavy, 2015). They also illustrated the fact that the low frequency dominates precisely in the upstream portion of the separated region (Le Floc'h, 2021).

In the final paper, a detailed review of the skewness of pressure and velocity in the family of TSBs will be provided, and analogies between flat plate and airfoil should be drawn with re-

spect to the airfoil incidence and the associated amount of predicted backflow. Such results will be valuable for the noise modeling of separated flows on the DLR wind turbine project.

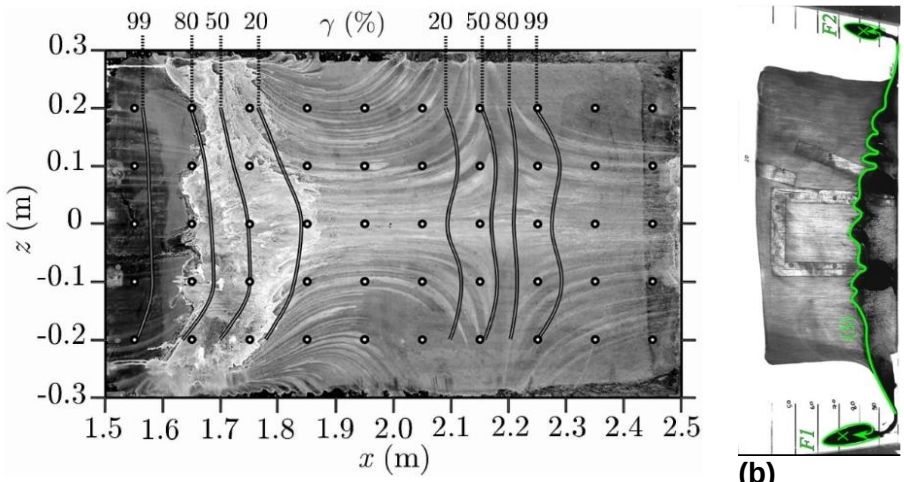

Figure 1(a) Oil film visualization on a flat plate, flow goes from left to right. Iso-lines of γ(%), the forward flow fraction (Simpson, Chew, & Shivaprasad, 1981), are superimposed; (b) on a DU96-W-180 airfoil, flow goes from left to right. Separation line is highlighted in green.

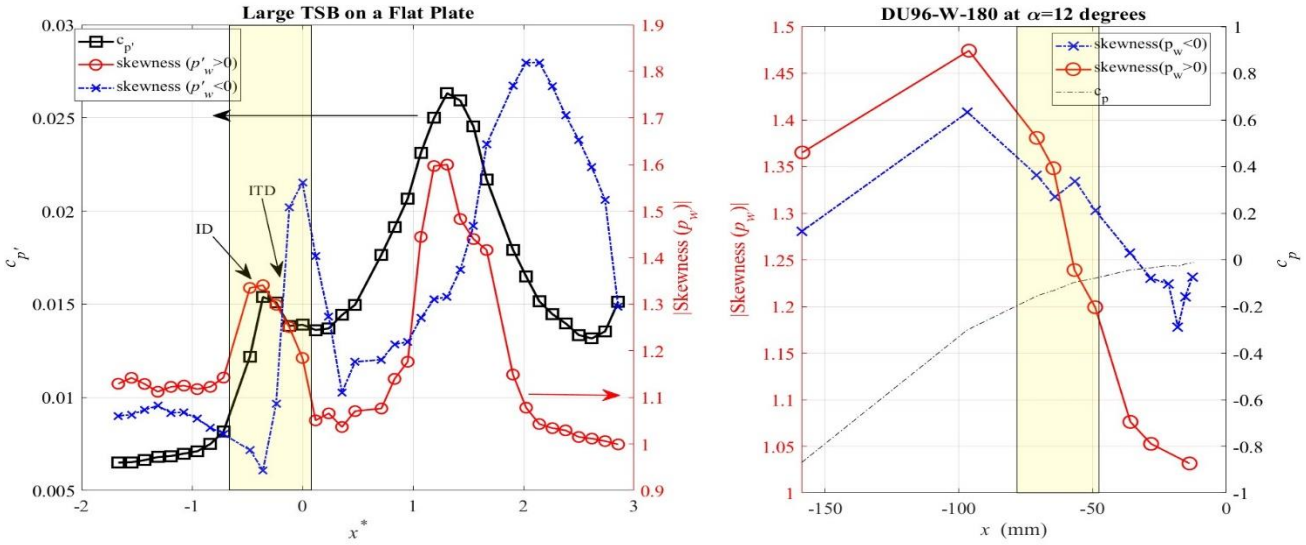

Figure 2 Comparison of wall-pressure skewness between the flat plate and trailing edge separations shown in Figure 1. The onset of separation is identified by the fluctuating pressure coefficient C_p, for the flat plate and by the mean pressure coefficient c_p for the DU96-W-180

References

Le Floc'h, A. (2021). *Experimental analysis in a family of turbulent separation bubbles.* PhD thesis, Université du Québec.

More, R., & Murray, M. (2023, June 7). *Wind returns to top of list of German power sources.* Retrieved from Reuters: https://www.reuters.com/business/energy/wind-returns-top-list-german-power-sources-2023-06-07/

Simpson, R., Chew, Y.-T., & Shivaprasad, B. (1981). The structure of a separating turbulent boundary layer. Part 2. Higher-order turbulence results. *Journal of Fluid Mechanics*, 53-73.

Suryadi, A. (2019). Kinematic and Acoustic Similarities of Separated Turbulent Boundary Layers. *AIAA Journal*, 2435-2446.

Suryadi, A., & Herr, M. (2015). *Wall pressure spectra on a DU96-W-180 profile from low to pre-stall angles of attack.*

Zambonini, G., & Ottavy, G. (2015). Unsteady Pressure Investigations of Corner Separated Flow in a Linear Compressor Cascade. *ASME Proceedings Paper*, (pp. 1-14). Montréal, Canada.

Mitteilung

Fachgruppe: Windenergie

Numerical investigations on propagation of wind gust modeled from stochastic description of field data

Neeraj Paul Manelil[1], Johannes Nicolaas Theron[1], Leo Höning[1], André Fuchs[2], Bernhard Stoevesandt[1]

[1] *Fraunhofer Institute for Wind Energy Systems, Department Aerodynamics, CFD and stochasti Dynamics, Küpkersweg 70, 26129 Oldenburg, Germany*

[2] *Institute of Physics and ForWind, University of Oldenburg, Küpkersweg 70, 26129 Oldenburg, Germany*

Keywords: Wind turbine, Gust, LES, Atmospheric boundary layer

Design regulations and certification standards require wind turbines to be engineered to withstand dynamic loading induced by extreme environmental events such as wind gusts. In this context, a realistic description of wind gusts becomes a priority for the aero-elastic analysis of wind turbine loads. The present work focuses on a new stochastic measurement-based description of wind turbine gusts, followed by computational fluid dynamics (CFD) simulations of its propagation through atmospheric boundary layers.

The deterministic portrayal of extreme operational gusts, as prescribed in the IEA standard [4], has been acknowledged as unrealistic due to the lack of corresponding realistic observations [1]. Thus, the establishment of a measurement-informed gust description becomes crucial. To address this, the current study adopts an entropy-based stochastic method outlined in [3] to define the temporal shape of the gust. An additional point of concern regarding gust characterization pertains to its spatial distribution. While the Extreme Operational Gust (EOG) description assumes a uniform gust impact across the entire turbine rotor disk area, wind measurements of gusts along a vertical from the ground challenge this assumption. The inherent asymmetry introduced by the atmospheric boundary layer is expected to induce non-uniformity within the gust. This particular aspect forms the focus of investigation, executed through the implementation of computational fluid dynamics (CFD) simulations. These simulations delve into the propagation of a wind gust across a computational domain spanning 1000 meters in the downwind direction. Unsteady Large Eddy Simulation (LES) simulations are conducted using the open-source CFD solver OpenFOAM, with the selection of solvers and schemes kept consistent with description in [2].The gust is incorporated into the computational domain through the inclusion of a body force source term within the injection zone (see Fig. 1), as described in [6]. These body forces are evaluated based on predefined spatio-temporal description of gust. When incorporating the gust within the LES model, special care is taken to uphold mass conservation across the injection zone, given the in-compressible nature of the flow solver employed in the simulations[5].

Figure 1 illustrates the instantaneous iso-velocity surface corresponding to a velocity magnitude of 12 m/s after 46 seconds of flow simulation. In the x-z plane, the gust is characterized as a circular region with a diameter of 240 meters, featuring a 30% velocity excess over the mean flow velocity of 10 m/s. This spatial

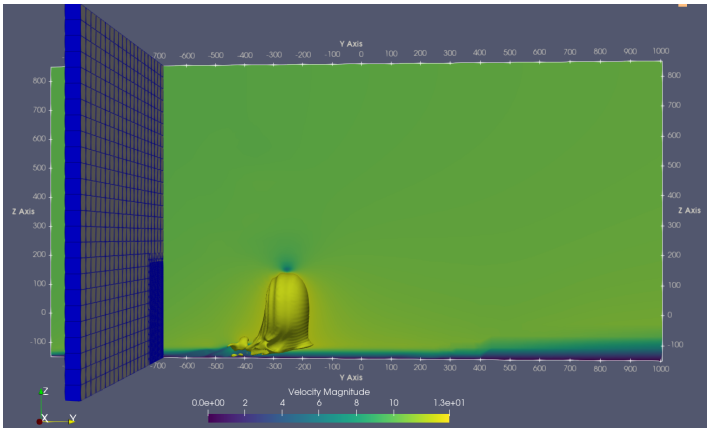

Figure 1: Instantaneous iso-surface of velocity magnitude after 40 seconds of flow simulation

depiction ensures that, in the absence of a boundary layer, the gust would uniformly impact the rotor area of the IEA 15MW wind turbine. However, the results depicted in Fig. 1 unmistakably indicate a complex interaction between the gust and the boundary layer. The region of gust adjacent to the boundary layer exerts a strong shear, leading to separation, while the region farther away from the boundary layer is observed to accelerate as the gust traverses the computational domain. This non-uniformity in the gust's behavior is directly attributed to the influence of the boundary layer. This phenomenon could result in a partially non-uniform gust strike on the wind turbine, which could have more critical implications due to the greater force imbalance in the turbine rotor plane. This is a departure from the uniform gust described in [4]. The results derived from this study emphasize the necessity of a three-dimensional gust description, especially for large MW scale wind turbines where the assumption of a uniform wind gust is invalid. Looking ahead, the future scope of this research will encompass the estimation of aero-elastic loads on a 15MW wind turbine under diverse scenarios involving partial wind gust loads.

References

[1] Wim Bierbooms and Po-Wen Cheng. Stochastic gust model for design calculations of wind turbines. *Journal of Wind Engineering and Industrial Aerodynamics*, 90(11):1237–1251, 2002.

[2] Bastian Dose, Hamid Rahimi, Iván Herráez, Bernhard Stoevesandt, and Joachim Peinke. Fluid-structure coupled computations of the nrel 5 mw wind turbine by means of cfd. *Renewable energy*, 129:591–605, 2018.

[3] André Fuchs, Corentin Herbert, Joran Rolland, Matthias Wächter, Freddy Bouchet, and Joachim Peinke. Instantons and the path to intermittency in turbulent flows. *Physical Review Letters*, 129(3):034502, 2022.

[4] IEC-Standard. *61400-21. Measurement and Assessment of Power Quality of Grid Connected Wind Turbines.* 2002.

[5] Stuart Edward Norris, John Edward Cater, Karl Alexander Stol, and CP Unsworth. Wind turbine wake modelling using large eddy simulation. In *Proceedings of the 17th Australasian Fluid Mechanics Conference. University of Auckland*, 2010.

[6] Niels Troldborg, Jens N Sørensen, Robert Mikkelsen, and Niels N Sørensen. A simple atmospheric boundary layer model applied to large eddy simulations of wind turbine wakes. *Wind Energy*, 17(4):657–669, 2014.

Namensverzeichnis der Autoren und Koautoren